

---

Study of the shape and alignment of lensed CMB and large  
scale structure inferred from the CMB using Minkowski  
Tensors

---

A thesis  
submitted for the degree of  
**Doctor of Philosophy**

in

The Department of Physics,  
Pondicherry University,  
Puducherry - 605 014, India



by

Priya Goyal  
Indian Institute of Astrophysics,  
Bangalore - 560 034, India



August 2021



Study of the shape and alignment of lensed CMB  
and large scale structure inferred from the CMB  
using Minkowski Tensors

Priya Goyal  
*Indian Institute of Astrophysics*



Indian Institute of Astrophysics  
Bangalore - 560 034, India



---

Title of the thesis : **Study of the shape and alignment of lensed CMB and large scale structure inferred from the CMB using Minkowski Tensors**

Name of the author : **Priya Goyal**

Address : Indian Institute of Astrophysics  
II Block, Koramangala  
Bangalore - 560 034, India

Email : priya.goyal@iiap.res.in

Name of the supervisor : **Prof. Pravabati Chingangbam**

Address : Indian Institute of Astrophysics  
II Block, Koramangala  
Bangalore - 560 034, India

Email : prava@iiap.res.in

---



## Declaration of Authorship

I hereby declare that the matter contained in this thesis is the result of the investigations carried out by me at the Indian Institute of Astrophysics, Bangalore, under the supervision of Prof. Pravabati Chingangbam. This work has not been submitted for the award of any other degree, diploma, associateship, fellowship, etc. of any other university or institute.

Signed: Priyagoyal

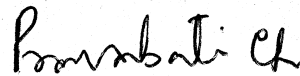
Date: 5<sup>th</sup> January, 2022





# Certificate

This is to certify that the thesis entitled '**Study of the shape and alignment of lensed CMB and large scale structure inferred from the CMB using Minkowski Tensors**' submitted to the Pondicherry University by Ms. Priya Goyal for the award of the degree of Doctor of Philosophy, is based on the results of the investigations carried out by her under my supervision and guidance, at the Indian Institute of Astrophysics. This thesis has not been submitted for the award of any other degree, diploma, associateship, fellowship, etc. of any other university or institute.



Signed:

Date: 5<sup>th</sup> January, 2022



# List of Publications

## Refereed Publications

1. *Morphology of CMB fields-Effect of weak gravitational lensing*

**Priya Goyal**, P. Chingangbam & S. Appleby, JCAP02(2020)020,

DOI:10.1088/1475-7516/2020/02/020, arXiv:1911.04740 [astro-ph.CO].

*Chapter 4*

2. *Local patch analysis for testing statistical isotropy of the Planck convergence map,*

**Priya Goyal**, Pravabati Chingangbam, JCAP08(2021)006,

DOI:10.1088/1475-7516/2021/08/006, arXiv:2104.00418 [astro-ph.CO]

*Chapters 5*

## Under Preparation

3. *Geometric meaning of statistical isotropy of smooth random fields: application to cosmological fields,*

P. Chingangbam, **Priya Goyal**, K. P. Yogendran, & Stephen Appleby 2021, in preparation

*Chapter 6*

4. *The information content of Minkowski tensors of cosmological random fields - a comparison with scalar Minkowski functionals,*

P. Chingangbam, **Priya Goyal** & Fazlu Rahman 2021, in preparation.

*Chapter 7*



# Presentations

1. Oral presentation titled "Effect of gravitational lensing on morphology of CMB fields" in Workshop on Geometrical and Topological Methods for Cosmological Data , 20-23 July, 2019, NISER, Bhubaneswar, India.
2. Poster presentation titled "Effect of weak gravitational lensing on morphology of CMB fields" in CosmoGold IAP 2019, 24-28 June, 2019, IAP, Paris.
3. Participant in a school and workshop, "Cosmology- The Next Decade" , 3 - 25 January, 2019, ICTS, Bangalore, India.
4. Participant in a school and workshop, "Frontiers in 21cm Cosmology" , 10-18 December, 2018, kodaikanal Solar Observatory, IIA, India.
5. Oral presentation titled "Effect of lensing on morphology of CMB B-mode polarization" in Introductory School on Galaxy Formation, 13-16 March, 2018, NISER, NISER, Bhubaneswar, India.
6. Poster presentation titled "Effect of lensing on morphology of CMB B-modes" in 14th Young Astronomers Meet, 11-15 September, 2017, IUCAA, Pune, India.



# *Acknowledgements*

First of all, I would like to express my sincere gratitude and deep regards to my supervisor Dr. Pravabati Chingangbam for her invaluable guidance, encouragement and constant support throughout my research. Her perspectives, expertise in the subject and immense knowledge has helped me a lot during my PhD. I thank her for being extremely patient with me and giving me enough time and independence, to think and grow during this journey. I could not have imagined having a better advisor and mentor for my research work.

My sincere thanks to my doctoral committee members Dr. G. Ramesh Babu and Dr. Mousumi Das and the staff at the Pondicherry University for their timely help, feedback and suggestions.

I am extremely grateful to Prof. Changbom Park at Korea Institute for Advanced Study, Seoul for the hospitality provided during my visits there. I thank Prof. Park and my collaborator Stephen Appleby for their insightful comments and suggestions about my research work. I would also like to thank Dr Patta Yogendran for all the useful discussions and his feedback. I also thank Dr. Subinoy Das for his advice on both research as well as on my future course of journey.

I am thankful to IIA for providing me an excellent academic environment and the necessary facilities for my research work during my PhD tenure.

I am deeply grateful to Prof. T.R. Seshadri for motivating and inspiring me to explore our beautiful and mysterious Universe.

I thank my friend Sunil for keeping me motivated and always pushing me to go out of my comfort zone to achieve greater things in life. A very special thanks

to Chinthak, Maninder and Prolay, my PhD batchmates and friends for their unconditional support and encouragement. I extend my gratefulness to the members of my Bhaskara family Manoj, Panini, Prasanna, Ritesh, Prerna, Ekta, Priyanka, who played their part in this journey, academically and otherwise, making it a memorable experience. I would like to offer my sincere thanks to Rishabh for his unwavering support and belief in me. I also thank my academic group members Joby, Fazlu, Vidhya and Akanksha for their timely help and support. Many thanks to Kshama, Deepak, Raghubar, Amit, Shejeela, Manika, Sharmila, Partha for being a part of this challenging voyage. Lastly, my heartfelt regards to my forever friends, Minal and Kirtima for tolerating me, loving me, and supporting me throughout.

I will also thank my family members and my teachers for always supporting and encouraging me. Last, but not the least, I acknowledge with pleasure the unconditional love and support of my parents for making me what I am today. No words will be enough to honour their sacrifices in my whole journey, till date. I thank them from the bottom of my heart for everything.



*Dedicated to*  
*my*  
*grandparents*



# Abstract

The large scale structure in the universe causes arcminute angular scale deflections of the paths of CMB photons, leading to blurring of the acoustic peaks and correlations between different modes. This effect can be exploited to reconstruct the matter distribution in the universe, or equivalently the lensing potential map, integrated along the line of sight. The aim of this thesis is to carry out a careful investigation of the imprint of the large scale structure on the CMB fields, and the morphology of the matter distribution inferred from the observed CMB data. This thesis begins with an introduction to the field of CMB lensing and CMB lensing reconstruction. Then in the third chapter we introduce the morphological descriptors, namely Minkowski functionals and Minkowski Tensors used in our analysis. As the first step we study the effect of gravitational lensing on the morphology of the intensity patterns of the CMB temperature and polarization fields using Minkowski tensors (MT). We calculate the distortion of the CMB patterns at different angular scales which are manifested as magnification and shearing, by measuring the alignment and shape parameters,  $\alpha$  and  $\beta$  that are constructed from the MTs. We demonstrate that lensing makes all structures of the fields increasingly more anisotropic as we probe down to smaller scales. Further, we find that lensing does not induce statistical anisotropy of the fields, which shows consistency with the isotropic distribution of matter on large scales. This work constitutes the fourth chapter of this thesis. Next, in the fifth chapter we test the statistical isotropy of the universe using the reconstructed lensing potential data from a global as well as local perspective. This analysis is vital in the wake of the detection of CMB anomalies in the data of concluded and ongoing CMB missions. From the global analysis we find that the matter distribution is consistent with statistical isotropy of the universe. From the local analysis we identify several anomalous sky patches in the observed matter distribution which exhibit levels of alignment that are significantly higher than expected from isotropic fields having the same power spectrum. In the last

part of the work we clarify the geometrical meaning of statistical isotropy and extend the analytic calculation of MTs to anisotropic Gaussian random fields. We also calculate the signatures of local type primordial non-Gaussianity on the MTs. Our results will be useful for accurate searches for non-Gaussianity and departure from isotropy using high precision cosmological datasets.

# Contents

<b>Abstract</b>	<b>i</b>
<b>List of Figures</b>	<b>vii</b>
<b>List of Tables</b>	<b>xiii</b>
<b>1 Introduction</b>	<b>1</b>
1.1 Background cosmology . . . . .	7
1.2 First order perturbed universe . . . . .	12
1.2.1 Perturbation equations . . . . .	12
1.2.2 Setting the initial conditions: Inflation . . . . .	15
1.3 CMB anisotropies . . . . .	16
1.4 Structure formation . . . . .	23
1.5 Real space statistics . . . . .	27
1.6 Goal of the Thesis . . . . .	29
<b>2 Gravitational lensing of Cosmic Microwave Background</b>	<b>32</b>
2.1 Introduction . . . . .	32
2.2 The lensing potential and its power spectrum . . . . .	37
2.3 CMB lensed power spectrum . . . . .	43
2.4 Lensing reconstruction . . . . .	47
2.5 CMB lensing observations . . . . .	50
<b>3 Geometrical and Topological Observables for smooth random fields</b>	<b>54</b>
3.1 Introduction . . . . .	54
3.2 Review of smooth random fields . . . . .	55
3.3 Minkowski functionals and Minkowski tensors for a single structure	57
3.3.1 Minkowski functionals . . . . .	58
3.3.2 Minkowski tensors . . . . .	59
3.3.3 Alignment and shape parameters: $\alpha$ and $\beta$ . . . . .	61
3.4 Minkowski functionals and Minkowski tensors for smooth random fields. . . . .	63

3.4.1	Analytical expressions for MFs of a Gaussian field . . . . .	65
3.4.2	Minkowski tensors of smooth random fields . . . . .	66
3.5	Numerical computation of Minkowski functionals and Minkowski tensors . . . . .	67
3.5.1	Minkowski functionals . . . . .	67
3.5.2	Discretization error for $V_1$ and $V_2$ . . . . .	69
3.5.3	Methods for $\mathcal{W}_1$ and $\mathcal{W}_2$ numerical computation . . . . .	70
<b>4</b>	<b>Morphology of CMB fields-effect of weak gravitational lensing</b>	<b>74</b>
4.1	Introduction . . . . .	74
4.2	$\alpha$ and $\beta$ for CMB fields . . . . .	76
4.2.1	$\alpha$ and $\beta$ for Gaussian isotropic fields in $\Lambda$ CDM cosmology . . . . .	77
4.2.2	Sensitivity of $\alpha$ and $\beta$ to variation of cosmological parameters . . . . .	80
4.2.3	Sensitivity of $\alpha$ and $\beta$ to Hemispherical anisotropy . . . . .	84
4.3	Effect of weak lensing on the morphology of CMB fields . . . . .	86
4.3.1	Simulation of lensed CMB maps . . . . .	86
4.3.2	Morphological changes induced by lensing . . . . .	88
4.4	Conclusion and discussion . . . . .	95
<b>5</b>	<b>Local patch analysis for testing statistical isotropy of the Planck convergence map</b>	<b>99</b>
5.1	Introduction . . . . .	99
5.2	Data and Methodology . . . . .	100
5.2.1	The Planck convergence map: Observed data and Simulations . . . . .	101
5.3	Analysis and results . . . . .	103
5.3.1	Understanding the effects of bandpass filter and masking on $\alpha$ using ideal simulations . . . . .	104
5.3.2	Quantifying the statistical significance of $\alpha$ and error bars . . . . .	106
5.3.3	Global analysis . . . . .	108
5.3.4	Local patch analysis . . . . .	111
5.4	Conclusion . . . . .	119
<b>6</b>	<b>Contour Minkowski tensor for Gaussian <i>anisotropic</i> fields</b>	<b>121</b>
6.1	Introduction . . . . .	121
6.2	Mapping of a single arbitrary curve to an ellipse, uniqueness and shape anisotropy parameter . . . . .	122
6.2.1	Distribution of many curves and their relative alignment . . . . .	124
6.3	Comparison with shape finders . . . . .	126
6.4	Ensemble expectation value of $\widetilde{\mathcal{W}}_1$ for Gaussian anisotropic fields . . . . .	129
6.4.1	Ensemble expectation of $\widetilde{\mathcal{W}}_1$ . . . . .	130
6.5	Conclusion . . . . .	133

---

<b>7</b>	<b>Constraining primordial non-Gaussianity using Minkowski tensors and Betti numbers</b>	<b>135</b>
7.1	Review of primordial non-Gaussianity . . . . .	136
7.2	Simulation of non-Gaussian CMB maps . . . . .	138
7.3	Prospects of using Minkowski tensors and Betti numbers to constrain primordial non-Gaussianity . . . . .	140
7.4	Summary and future work . . . . .	141
<b>8</b>	<b>Summary, conclusions, and caveats</b>	<b>144</b>
8.1	Key results and conclusions . . . . .	144
8.2	Future work . . . . .	146
	 <b>Bibliography</b>	 <b>148</b>





# List of Figures

1.1	Thomson scattering of radiation with a quadrupole anisotropy generates linear polarization. Blue colors (thick lines) represent hot and red colors (thin lines) cold radiation. (Wayne Hu, M. White 1997) . . . . .	17
1.2	Recent measurements of the CMB temperature anisotropy and polarization. The two models, the thin, nearly overlapping grey lines, are from Planck (dashed line) and ACT plus WMAP (A20, solid line). The primordial BB signal with $r = 0$ is also shown with the dot-dashed line. For Planck, 2018 results (Planck Collab. V et al. 2019) are shown. For SPT, Henning et al.(2018) for 150 GHz $TT < 2000$ , TE and EE, and Sayre et al. (2019) for BB are shown here. For $\ell > 2000$ , the plot shows the SPT spectrum from George et al. (2015), corrected for point source emission. It is visually indistinguishable from the more precise but uncorrected spectrum in Reichardt et al. (2020). For Polarbear/Simons Array, figure show EE from Adachi et al. (2020) and BB from pipeline A in POLARBEAR Collaboration et al. (2017). For BICEP2/Keck, Ade et al. (2018) is used. All error bars are one sigma, and points with no lower bound in TT and EE have been dropped at high $\ell$ . This figure is taken from Choi <i>et al.</i> (2020). . . . .	22
2.1	Current upper limits on B-modes from CMB experiments. Image Credit: Kuo Group:CMB Polarization Experiment Team . . . . .	37
2.2	Weak lensing geometry for a source (the CMB) at comoving distance $\chi^*$ lensed by a potential $\Psi$ at distance $\chi$ , assuming a flat universe. The lensing deflection by an angle $\delta\beta$ changes the observed angle of the source by an angle $\delta\theta$ . . . . .	39
2.3	The power spectrum of the deflection angle (given in terms of the lensing potential $\phi$ by $\nabla\phi$ ) for a concordance $\Lambda$ CDM model. The linear theory spectrum (solid) is compared with the same model including non-linear corrections (dashed) from HALOFIT (Smith et al. 2003). . . . .	42

2.4	Top panel in left: the lensed temperature power spectrum (green) and the unlensed spectrum (red). Bottom: the fractional change in the power spectrum due to lensing. Top panel in right plot: lensed $E$ -mode polarization power spectra overlaid on unlensed $E$ -mode spectrum, with bottom panel showing the residual in this case. Both plots are for a typical concordance $\Lambda$ CDM model with Planck 2018 (Planck Collaboration <i>et al.</i> 2020c) cosmological parameters. . . . .	45
2.5	Recent measurements of the CMB temperature and polarization anisotropy power spectra from various CMB experiments. This figure has been taken from Choi <i>et al.</i> (2020). . . . .	50
2.6	Mollweide projection in Galactic coordinates of the lensing-deflection reconstruction map from Planck Collaboration <i>et al.</i> (2020a) baseline minimum-variance (MV) analysis. Map represents the Wiener-filtered displacement-like scalar field with multipoles $\hat{\alpha}_{LM}^{MV} = \sqrt{(L(L+1))} \hat{\phi}_{LM}^{MV}$ , corresponding to the gradient mode (or $E$ -mode) of the lensing deflection angle. Modes with $L < 8$ have been filtered out.. This figure and caption has been taken from Planck Collaboration <i>et al.</i> (2020a). . . . .	52
2.7	Planck 2018 lensing power-spectrum band powers (pink boxes) over the aggressive multipole range. The 2015 analysis band powers (green) were calculated assuming a slightly different fiducial model and have not been (linearly) corrected to the 2018 model. Also shown are recent measurements by the ACT-Pol (Sherwin <i>et al.</i> 2017), SPTpol (Story <i>et al.</i> 2015), and SPT-SZ (Simard <i>et al.</i> 2018) collaborations. The SPT-SZ measurement is not completely independent, since the SPT-SZ reconstruction also uses temperature data from Planck, but with subdominant weight over the smaller sky area used. The black line shows the lensing potential power spectrum for the $\Lambda$ CDM best-fit parameters to the Planck 2018 likelihoods (Planck TT,TE,EE+lowE, which excludes the lensing reconstruction). This figure and caption has been taken from Planck Collaboration <i>et al.</i> (2020a). . . . .	52
3.1	Examples of simply and doubly connected region. This figure demonstrates that a connected region or hole can be associated with a closed curve and hence count of structures is equivalent to count of closed curves. . . . .	58
3.2	$\alpha$ and $\beta$ values for structures of different shapes and different spatial arrangement. . . . .	62
3.3	This figures shows the excursion set at three chosen $\nu$ values of CMB temperature field on a 2-D surface of a sphere. Excursion set consist of red regions in the three panels. Red region in the top panel represents a multiply connected region with many holes. The threshold value for the three excursion sets (from left to right) are $\nu = -1.5, 0, 1.5$ . Excursion sets vary systematically as a function of threshold, and their geometrical and topological properties are captured by MFs and MTs. . . . .	64
3.4	The three scalar Minkowski functionals for a Gaussian random field. . . . .	66

- 4.1 Maps of unlensed  $T$  (left),  $E$  (middle), and  $B$  (right) with tensor-to-scalar ratio  $r = 0.1$ . All maps are smoothed with  $\text{FWHM}=1^\circ$ . We have not put the colour scale since we wish to only draw visual attention to the fact that  $E$  mode has the highest number of structures per unit area, while  $B$  mode has the lowest. As a consequence  $\alpha$  is expected to be largest for  $E$  mode and lowest for  $B$  mode, at all threshold values. This expectation is corroborated by the top left panel of figure 4.2. . . . . 78
- 4.2 *Top left:*  $\alpha$  versus  $\nu$  for unlensed  $T$ ,  $E$  and  $B$  fields for the same smoothing angle  $\text{FWHM}=20'$ . *Bottom left:* Variation of  $\alpha$  at  $\nu = 0$  as a function of the smoothing angle. Both the plots are average over 500 maps. *Top right:*  $\beta$  versus  $\nu$  for  $T$ ,  $E$  and  $B$  fields same smoothing scale as for  $\alpha$ . *Bottom right:* Variation of  $\beta$  at  $\nu = 0$  as a function of the smoothing angle. The plots for  $\beta$  are average over 200 maps. . . . . 79
- 4.3 Deviations of  $\alpha$  (left column) and  $\beta$  (right column) for different cosmological models (listed in Table 4.1) from the ‘fiducial’  $\Lambda\text{CDM}$  model, for  $T$  (top),  $E$  (middle) and  $B$  mode (bottom) fields. The smoothing scale used is  $\text{FWHM}=20'$ . The upper panels in each plot show the effect of varying the matter density fraction, while the lower panels show the effect of varying  $n_s$ . For  $B$ -mode there is only one panel since we have fixed the tensor spectral index to be one. We have assumed a flat universe for all the cases. . . . . 82
- 4.4 *Left:*  $\Delta\alpha^A$  for temperature field with input hemispherical anisotropy corresponding to  $A = 0.1$  and  $0.5$ , for three different smoothing scales at  $\text{FWHM}=10'$ ,  $60'$  and  $180'$ . All plots are average over 500 maps. We can see that the deviation in  $\alpha$  becomes distinguishable as we increase the smoothing scale. *Right:*  $\Delta\beta^A$  for the same fields, values of  $A$ , and smoothing scales as for  $\alpha$ . We have not added error bars since they are roughly one order of magnitude larger than the mean values, and hence they make the mean values difficult to discern visually. . . . . 85
- 4.5 *Left:* We show here the lensing geometry.  $\hat{n}$  denotes the direction of observed lensed CMB and  $\hat{n}'$  denotes the corresponding unlensed CMB direction. *Right:* We show the unit vectors  $e_\theta, e_\phi, e'_\theta, e'_\phi$  and angle  $\gamma$  the spherical coordinate system is to be rotated to take into account the different direction of the coordinate vectors at the two points. . . . . 87
- 4.6 *Left:* Difference between lensed and unlensed angular power spectra for  $T$  used in our simulations. *Middle:* same for  $E$ . *Right:*  $D_\ell$  for primordial  $B$  with  $r = 0.1$  (blue) and  $r = 0.01$  (green), and lensed  $B$  corresponding to  $r = 0$  (red). We have used two different scales on the  $x$ -axis, with a dotted line serving as demarcation, in order to highlight the low  $\ell$  region. . . . . 89

- 4.7 *Top panels:* Deviations  $\Delta\alpha$  between lensed and unlensed  $T$  (left),  $E$ -mode (right). *Bottom left panels:*  $\Delta\alpha$  for  $B$ -mode. All plots are average over 500 maps and the error bars are the standard deviation obtained from these maps. Note that the smoothing angles are different for the different fields. *Bottom right:*  $\Delta\alpha$  at  $\nu = 0$  as a function of smoothing angle, for  $B$ -mode, normalized by the magnitude of unlensed  $\alpha$  at  $\nu = 0$ . The range of the  $x$ -axis that is probed is between FWHM=2' to 270'. This range is subdivided into three different scales so as to highlight the behaviour at different scales. The locations of the scale transitions at FWHM=10' and 180' are marked by vertical dotted lines. Note the peak at FWHM $\sim$  5'. . . . . 90
- 4.8 *Left panels:* PDFs of  $\beta$  for  $T$  (top),  $E$  (middle) and  $B$  (bottom), at  $\nu = 0$  for FWHM=20' for unlensed (green) and unlensed (red) cases. *Right panels:* The difference between lensed and unlensed PDFs for the three fields shown in the right panels. All plots are average over 200 maps and error bars are the standard deviations obtained from them. . . . . 93
- 4.9 *Left panels:* Mean values of  $\beta$  for  $T$  (top),  $E$  (middle) and  $B$  (bottom) for FWHM=20' for unlensed (green) and unlensed (red) cases. *Right panels:* The difference between lensed and unlensed mean  $\beta$  values for the three fields shown in the top panels. All plots are average over 200 maps and error bars are the standard deviations obtained from them. . . . . 96
- 5.1 Mean values of  $\alpha$  and standard deviation obtained from isotropic Gaussian simulations of the convergence map for different resolutions  $N_{\text{side}} = 64, 128, 256$  and 512. Different colors here represent  $\alpha$  calculated for full sky (blue), masked (orange), bandpass filtered (red), and masked plus band pass filtered (green). . . . . 105
- 5.2 *Left:*  $P(\alpha)$  for some selected values of  $\nu$  for  $N_{\text{side}} = 512$ . *Right:*  $2\sigma_\alpha$  (red triangle),  $\delta_-^{(2)}$  (green square) and  $\delta_+^{(2)}$  (blue circle), for the same  $N_{\text{side}}$  as the left panel. . . . . 107
- 5.3 *Top row:* Upper panels show  $\alpha$  while lower panels show  $\tilde{\chi}^{(2)}$  for the Planck convergence map (blue stars) and FFP10 simulations (red triangles), without Wiener filtering, for different values of  $N_{\text{side}}$ . *Bottom row:* Same as first row but for Wiener filtered maps. . . . . 109
- 5.4 *Left:* An example of a patch of the  $\kappa$  map. *Right:* Map showing values of  $\alpha$  for sky patches at  $\nu = -0.5$ , with each patch being one of the 192 pixels given by  $N_{\text{side}}^{\text{local}} = 4$ . The value of  $N_{\text{side}}^{\text{global}}$  is 256 and the valid pixel fraction is  $p_{\text{frac}} = 0.6$ . . . . . 112
- 5.5  $\tilde{\chi}$  values for outlier patches versus threshold. . . . . 115

- 5.6 *Top:* Maps of showing outlier patches for  $N_{\text{side}}^{\text{local}} = 2$  for  $N_{\text{side}}^{\text{global}} = 128$  (left) and  $N_{\text{side}}^{\text{global}} = 256$  (right). The colors indicate the corresponding values of  $\tilde{\chi}$ . Dark blue corresponds to  $-3 < \tilde{\chi} < -2$ , yellow corresponds to  $2 < \tilde{\chi} < 3$  and maroon to  $\tilde{\chi} > 4$ . Patches are numbered in Healpix ring format. *Bottom:* Same as the top row but for  $N_{\text{side}}^{\text{local}} = 4$ . All maps are shown using Mollweide projection in Galactic coordinates. . . . . 118
- 6.1 Schematic diagram for mapping from a distribution of curves (left panel) to a distribution of ellipses (a) in the middle panel to a single unique ellipse in the right panel. . . . . 125
- 6.2 *Top:* Iso-contours for two functions given by eq. 6.12 with peak locations arranged linearly (left) and non-linearly (right). *Bottom:*  $F$ ,  $\alpha$  and  $\beta$  for individual structures after fragmentation versus threshold, for the corresponding function in the panel above. The percolation thresholds are indicated by the black dashed lines. . . . 128
- 7.1 Comparison of  $S/N$  between MTs and SMFs (trace of MTs) for the temperature and  $E$ -mode polarization field. . . . . 142



# List of Tables

1.1	This table summarizes the different phase transitions in the universe with the corresponding energy scale at which they occurred in history of the universe. . . . .	5
4.1	Models with different values of cosmological parameters for which we compute $\alpha$ . The input for the amplitude of primordial power spectrum and reionization history is the same in all the models. We assume curvature parameter, $\Omega_k$ , is zero for all models. All models other than the fiducial one have unrealistic parameter values so as to magnify their effect in $\alpha$ and $\beta$ . . . . .	81
5.1	Table showing the numbers of patches and their angular size. and number of pixels in each patch, for the values of $N_{\text{side}}^{\text{global}}$ and $N_{\text{side}}^{\text{local}}$ considered in our local analysis. . . . .	112
5.2	Table showing the numbers of anomalous patches, and their identification numbers. Patches shown in pink have positive value of $\tilde{\chi}^{(2)}(\nu)$ , while those in blue have negative values of $\tilde{\chi}^{(2)}(\nu)$ at all anomalous thresholds. The patches that are <i>not</i> common between $N_{\text{side}}^{\text{global}}=128$ and 256 are highlighted by the black boxes. . . . .	114





# Chapter 1

## Introduction

During the last several decades, cosmology has progressed from being a speculative science to one of the most successful fields of physics. This rapid growth is driven by an exemplary interplay between experiment and theory. A wide variety of observations of supernovae, galaxy distribution, galaxy clustering, strong lensing, galaxy weak lensing, cosmic microwave background (CMB) anisotropies have unveiled a wealth of cosmological information (about its content and the geometry) across different length scales and different epochs in the universe. To observe the universe in its full glory, multiwavelength observations, i.e., observations across the entire electromagnetic spectrum (from x-rays to radio regime), have been instrumental. Baryonic matter in the universe is constituted by stars, gas (in the molecular, neutral, ionized state), and dust. Each of these components emits at different wavelengths depending on the kind of interactions they have and also on their distance from the observer. For example, dust in our galaxy or the intergalactic medium is mostly mapped in infrared wavebands. With the advancement in technology and our theoretical understanding, we have been able to look back into the universe at much greater distances. Continuous efforts are made to explore important phases in the history of the universe like dark ages,

reionization, the peak of star formation, dark energy domination era, etc. Observations of CMB temperature and polarization anisotropies provide the earliest snapshot of our universe. Measurements of CMB anisotropies on large scales represent the primordial seed fluctuations in their most pristine form. However, on small scales, this primordial picture is distorted by the interactions of the CMB photons with matter inhomogeneities encountered during their travel from the last scattering surface to the observer. These secondary effects are a useful source of information on the universe's large-scale structure. One of these effects is gravitational lensing of CMB photons, causing small but coherent deflections of the observed CMB temperature and polarization anisotropies, with a typical amplitude of two arcminutes. One of the critical goals of this thesis is to capture the effect of lensing on the morphology of CMB fields using real space statistical tools such as Minkowski Tensors (MTs). Also, specific statistical signatures of lensing enable the reconstruction of the gravitational potential integrated along the line of sight from observed CMB maps. We also investigate the assumption of statistical isotropy of the universe by employing MTs on the convergence or lensing potential field inferred from lensed CMB observations.

Cosmological data encodes information about the origin and evolution of our universe in a non-trivial way. This information needs to be extracted by using various statistical tools. Cosmology is intrinsically related to statistics, as theories of the origin and evolution of the universe do not predict, for example, that a particular galaxy will form at a specific point in space and time or that a specific patch of the cosmic microwave background will have a given temperature: any theory predicts the average statistical properties of our universe, and we only observe one particular realization of that statistical ensemble. Statistical methods like Bayesian inference, chi-square, the goodness of fit, confidence regions, likelihood analysis, Fisher matrix approach, Monte Carlo methods have been extensively used to infer cosmological parameters and compare different models. CMB fluctuations have been analyzed so far using statistical tools such as power spectrum, bispectrum,

trispectrum, skewness, kurtosis, scalar Minkowski Functionals (SMFs), and so on. Low angular resolution and high noise levels in CMB experiments have limited the use of real space statistics to analyze the CMB data. However, improvements in sensitivity and small beam sizes of many recent and upcoming experiments will enable high signal-to-noise measurements of CMB anisotropies up to very small angular scales. Real space statistical tools can then be employed to gain complementary information about the underlying physical phenomenon. We use in our analysis the Minkowski Tensors and the shape and alignment parameters inferred from Contour Minkowski Tensor (CMT) to investigate the effect of weak gravitational lensing on CMB fields.

The CMB temperature and polarization anisotropies have been measured to very high precision. They are consistent with the standard six-parameter  $\Lambda$ CDM model, with purely adiabatic, Gaussian initial fluctuations, as predicted by simple inflationary models. In this standard picture, observed galaxies form in matter overdensities that grow due to gravitational instabilities in an expanding universe and seeds of which are the primordial inhomogeneities generated during an inflationary epoch. Observations suggest that the universe is now composed of about 5% ordinary matter, 27% dark matter, and 68% dark energy. Although there is consensus in the community about the standard  $\Lambda$ CDM or the concordance cosmological model of the universe, the nature of dark matter and dark energy is yet unknown. The CMB observations have proved to be a precious window to explore and understand our universe since the time of its first detection by Penzias and Wilson in 1965 (Penzias and Wilson 1965). The cosmic microwave background (CMB) is the primordial microwave radiation that fills the universe. It is predicted to be the afterglow of Big Bang (GAMOW 1948; Alpher and Herman 1948). About  $10^{-36}$  seconds after the Big Bang, the universe went through a phase of exponential expansion. This is the cosmic inflation introduced (Guth 1981; Linde 1982) to explain the homogeneity and isotropy of CMB (horizon-problem) and other problems like the flatness problem. Quantum fluctuations in the scalar field inflaton

form the primordial seeds, which eventually evolve into the anisotropies observed in the CMB and the large-scale structures in the universe. Further at the end of an inflationary phase, the energy density of the inflaton field decays to form the standard model particles, a process referred to as the *reheating*. Consequently, fluctuations in the initial energy density were transferred into fluctuations in the particle density.

The early universe was in a hot, dense state, with all the particles being relativistic and in thermal equilibrium with each other. When the universe's temperature was above 200GeV, unbounded quarks, gluons, and dark matter (DM) were the main constituents of the universe. These different constituents decoupled from plasma at different epochs in the history of the universe. Table 1.1 summarizes the various phase transitions our universe underwent at different energy scales. As the universe expanded, the temperature and the density of the cosmic plasma dropped further. This led to the decoupling of different particles from the cosmic soup at different stages in the thermal history of the universe. For instance, when the temperature falls below 1.4MeV, the weak interaction rate becomes slower than the universe's expansion rate, which led to the decoupling of neutrinos. After this, neutrinos did not interact with the remaining world and continued freely on their cosmic journey. At a later stage, electrons, protons, photons, few neutrons formed the components of plasma. The count of photons with energies higher than the binding energy of Deuterium (2.2MeV) was significant to prevent the survival of any deuterium nuclei that formed. Only when the temperature dropped below 0.08MeV, Deuterium nuclei could survive. Then the Big bang nucleosynthesis (BBN) leads to the formation of light nuclei, He<sup>4</sup>, with the traces of Deuterium, He<sup>3</sup>, and Lithium, Li<sup>7</sup> in the universe.

At  $z > 1100$ , the cosmic plasma consisted of photons, electrons, and protons in thermal equilibrium. They were tightly coupled to each other via Thomson and Coulomb scattering. High interaction rates due to high density of particles did

TABLE 1.1: This table summarizes the different phase transitions in the universe with the corresponding energy scale at which they occurred in history of the universe.

Inflation	$T \sim 10^{16}$ Gev	$10^{-36}$ s
Electroweak Phase Transition	$T \sim 100$ Gev	$t \sim 20$ ps
QCD Phase Transition	$T \sim 150$ Mev	$t \sim 20$ $\mu$ s
Neutrino Decoupling	$T \sim 1$ Mev	$t \sim 1$ s
Electron-Positron Annihilation	$T < m_e \sim 0.5$ Mev	$t \sim 10$ s
Big Bang Nucleosynthesis	$T \sim 50$ - $100$ kev	$t \sim 10$ min
Matter-Radiation Equality	$T \sim 0.8$ ev $\sim 9000$ K	$t \sim 60000$ yr
Recombination + Photon Decoupling	$T \sim 0.3$ ev $\sim 3000$ K	$t \sim 380000$ yr
Dark ages		$t \sim 380$ kyr – 400 Million yr
Reionization		$t \sim 400$ Million yr-present
CMB lensing efficiency peaks at		$z \sim 2$

not allow for the formation of neutral atoms until about  $z \sim 1100$ . However, once the temperature falls below 0.3eV, protons and electrons combine to form neutral hydrogen atoms. The photons then decoupled and started free streaming; this epoch is referred to as the **Recombination epoch**. This is the CMB radiation that we receive and measure today, providing us the earliest snapshot of our universe. The CMB is a fossil from  $\approx 380$ kyrs after the Big Bang when photons decoupled from the matter and the mean free path of photons exceeded the Hubble horizon at that epoch. The CMB photons we receive today represents a redshifted snapshot (the redshift of the CMB is  $z_{CMB} \sim 1100$ ) of the universe at the last scattering surface. The CMB is almost spatially isotropic and uniform, with tiny fluctuations of the order  $10^{-5}$  across the sky. These tiny departures from average temperature are sourced by the inhomogeneities in the photo-baryonic plasma present at the time of decoupling.

After decoupling, the mean free path of photons becomes large enough to be considered to be freely propagating in the intergalactic medium. In reality, CMB photons interact with matter distribution as they travel from the last scattering surface to the observer today. These interactions alter the frequency, energy, or direction of propagation of CMB photons. They are referred to as secondary anisotropies since they do not originate in the primordial Universe before decoupling. There are two broad categories of interaction between CMB photons and cosmic structures

- Gravitational effects: Integrated Sachs Wolfe (ISW) effect, gravitational lensing of CMB photons, the Rees-Sciama effect (RS).
- Scattering of CMB photons of electrons: Kinetic Sunyaev Zeldovich (KSZ) effect, thermal SZ effect, polarization due to reionization, Ostriker-Vishniac (OV) effect

More detailed discussion on CMB secondary anisotropies can be found in a review by Aghanim *et al.* (2008).

The focus of this thesis is the gravitational lensing of CMB photons. Gravitational lensing causes small but coherent deflections of the observed CMB temperature and polarization anisotropies, with a typical amplitude of two arcminutes. Specific statistical signatures of lensing in the observed CMB maps enable the reconstruction of the gravitational potential integrated along the line of sight. It opens a unique window on underlying physics aspects that affect the structure formation in the universe, such as dark matter, gravity theories and neutrino sector. CMB lensing physics, its consequences, and matter distribution reconstruction from CMB will be discussed in detail in the next chapter of the thesis.

The remaining part of this chapter describes the modeling of the background universe together with its constituents and the first-order perturbed universe in section 1.1 and section 1.2, respectively. The mathematical description and physics of the CMB temperature and polarization anisotropies are discussed in section 1.3. Then, section 1.4 sketches how the cosmic structures form and evolve from the initial conditions set by inflation. In section 1.5 we briefly discuss the real space statistics, their usefulness, and their applications in cosmology. Finally, we end this chapter by outlining the main objectives of this thesis work in section 1.6.

## 1.1 Background cosmology

Einstein's General Theory of Relativity (GTR) is the metric theory of gravitation, according to which gravitational force experienced by objects in the universe is the manifestation of space-time curvature. Einstein's field equations binds the curvature of space-time to the energy-momentum content of the universe

$$\mathcal{R}_{\mu\nu} - \frac{1}{2}g_{\mu\nu}\mathcal{R} = 8\pi G\mathcal{T}_{\mu\nu} + \Lambda g_{\mu\nu}, \quad (1.1)$$

where  $\mathcal{R}_{\mu\nu}$  is the Ricci curvature tensor, which is given in terms of second-order derivatives of the metric tensor,  $g_{\mu\nu}$  and  $\mathcal{R}$  is the Ricci scalar, obtained by contracting Ricci tensor.  $\Lambda$  is the famous cosmological constant, the energy density of space, or vacuum energy.  $\mathcal{T}_{\mu\nu}$  represents the energy-momentum tensor for a homogeneous and perfect fluid,

$$T_{\mu\nu} = (\rho + p) u_\mu u_\nu + p g_{\mu\nu}, \quad (1.2)$$

here  $\rho$  represents the energy density and  $p$  the pressure of the cosmic fluid.

One of the solutions of Einstein's field equations, that describes our homogeneous and isotropic universe is given by,

$$ds^2 = a^2(t)[-d\tau^2 + d\chi^2 + f_K^2(\chi)d\omega^2]. \quad (1.3)$$

It is known as **Friedmann Robertson Walker metric (FRW)**. Here,  $a(t)$  scale factor tells us how the distance between two points scales with coordinate time  $t$ .  $\chi$ , the radial coordinate is known as the comoving distance, and  $d\omega$  is the solid angle element. The function  $f_K(\chi)$  is called the comoving angular diameter distance that depending on the curvature (value of  $K$ ) of the spatial hypersurfaces is given by,

$$f_K(\chi) = \begin{cases} K^{-1/2} \sin(K^{1/2}\chi), & \text{for } K > 0, \text{ closed,} \\ \chi, & \text{for } K = 0, \text{ flat,} \\ |K|^{-1/2} \sinh(|K|^{1/2}\chi), & \text{for } K < 0, \text{ open.} \end{cases} \quad (1.4)$$

The conformal time ( $\tau$ ) is defined by  $d\tau = \frac{dt}{a(t)}$ .

The fundamental assumption underlying this metric solution is the validity of the **Cosmological Principle**, which states that the universe is spatially homogeneous and isotropic on large scales. This is one of the main assumptions of the standard theory of cosmology,  $\Lambda$ CDM (based on cold dark matter and a cosmological constant). Homogeneity implies translational invariance, while isotropy is equivalent to rotational invariance of the statistical observables like the density of the universe. As a consequence of this assumption, scale factor  $a(t)$  in the FLRW metric above is only the function of time and not of the position. Observations suggest that this assumption is valid on scales  $> 100$  Mpc.



The time evolution of the scale factor is determined by solving the following Friedmann equations (obtained by substituting FLRW metric in Einstein's field equation)

$$\left(\frac{\dot{a}}{a}\right)^2 = \frac{8\pi G\rho}{3} - \frac{K}{a^2} + \frac{\Lambda}{3}, \quad (1.5)$$

$$\frac{\ddot{a}}{a} = -\frac{4\pi G}{3}(\rho + 3p) + \frac{\Lambda}{3}. \quad (1.6)$$

In the above equations  $\rho$  and  $p$  are total energy density and total pressure, i.e., sum of the contributions from different constituents of the universe,  $\Lambda$  is the cosmological constant. And there are two commonly used choices of  $a$  and  $K$  given by,

- $K = +1, 0$  or  $-1$  depending on whether the shape of the universe is a closed 3-sphere, flat (i.e. Euclidean space) or an open 3-hyperboloid, respectively. If  $K = +1$ , then  $a$  is the radius of curvature of the universe. If  $K = 0$ , then  $a$  may be fixed to any arbitrary positive number at one particular time. If  $K = -1$ , then (roughly) one can say that  $a$  is the radius of curvature of the universe.
- $a$  is the scale factor which is taken to be 1 at the present time.  $K$  is the current spatial curvature (when  $a = 1$ ). If the shape of the universe is hyperspherical and  $R_t$  is the radius of curvature ( $R_0$  at the present), then  $a = \frac{R_t}{R_0}$ . If  $K$  is positive, then the universe is hyperspherical. If  $K = 0$ , then the universe is flat. If  $K$  is negative, then the universe is hyperbolic.

Eqns 1.5-1.6 are consistent with the first choices of  $a$  and  $K$ . The ratio of the time derivative of the scale factor with itself, i.e.,  $\frac{\dot{a}}{a}$ , is known as the Hubble parameter  $H(a)$ . The Hubble parameter today or the Hubble constant is often expressed in terms of the dimensionless constant  $h$ ,  $H(a = 1) = H_0 = h100 \text{ km}/(\text{s Mpc})$ . Measurements of  $H_0$  determine the current value of expansion i.e.  $\dot{a}$ . The expansion of space leads to a redshift of wavelength of the photons. A photon

emitted at a time  $t_{em}$  with wavelength  $\lambda_{em}$  will be observed at a time  $t_{obs}$  with a wavelength  $\lambda_{obs}$  given by

$$\frac{a(t_{obs})}{a(t_{em})} = \frac{\lambda_{obs}}{\lambda_{em}} \equiv 1 + z, \quad (1.7)$$

where  $z$  is the cosmological redshift, which has value zero today ( $z(t_0) = 0$ ). For the flat universe, i.e., for  $K = 0$ , critical energy density of the universe  $\rho_{critical}$  is defined as

$$\rho_{critical}(t) = \frac{3H^2(t)}{8\pi G}, \quad (1.8)$$

here  $H$  is the Hubble parameter. The value of critical density today is  $\mathcal{O} \sim 10^{-26} \text{ kg m}^{-3}$ . The critical density is useful to define dimensionless density parameters,

$$\Omega_i(t) = \frac{\rho_i(t)}{\rho_{critical}(t)}. \quad (1.9)$$

The components of the universe are assumed to be barotropic, that is, their pressure is given as an explicit function of their energy density, termed as the Equation of state (EOS):  $p = w(\rho) \rho$ , and the sound speed as  $c_s^2 = \delta p / \delta \rho$ . From the conservation of the stress energy tensor,  $\nabla_\mu T_{\mu\nu} = 0$ , we can show that the time evolution of the energy density obeys

$$\dot{\rho} + 3H(\rho + p) = 0. \quad (1.10)$$

This is the so-called continuity equation. For a constant  $w$ , the energy density scales as  $\rho \propto a^{-3(1+w)}$ . The cosmic fluid consist of the following different species classified according to their contribution to pressure,

- **Matter:** This is composed of two varieties: baryonic matter (i.e., ordinary matter) and dark matter (DM). The former corresponds to ordinary matter,

which we observe (stars, dust, gas, galaxies), while the latter only interacts gravitationally with the former. The nature of DM is still a cosmic mystery. There are different models for DM, for example, cold dark matter (CDM), warm dark matter (WDM), or hot dark matter (HDM). They differ in the physical properties of the fluid (from non-relativistic CDM to relativistic HDM). In the concordance model, we consider a CDM fluid. Gas of non-relativistic particles of baryons and dark matter can be assumed to be pressure-less  $|p| \ll \rho$  with EOS parameter,  $w \approx 0$ . Hence, their energy density dilutes with cosmic expansion as  $\rho \propto a^{-3}$ .

- **Radiation** : Relativistic species for which  $p = \frac{1}{3}\rho$ , like for photons, neutrinos and other massive particles until they are relativistic, energy density falls as  $\rho \propto a^{-4}$ .
- **Dark energy or cosmological constant ( $\Lambda$ )**: The question of the true nature of dark energy is not yet settled; there are plenty of models which can cause accelerated expansion of the universe. Cosmological constant with negative pressure and constant EOS parameter,  $w = -1$  is one of the possible explanations. In this case, the energy density will be constant and will not dilute with cosmic expansion,  $\rho \propto a^0$ .

Friedmann equation 1.5 can be rewritten in a useful form as

$$H^2(z) = H_0^2[\Omega_{m0}(1+z)^3 + \Omega_{r0}(1+z)^4 + \Omega_{K0}(1+z)^2 + \Omega_{\Lambda0}], \quad (1.11)$$

where subscript '0' denotes the evaluation of a given quantity today. Here,  $\Omega_{r0}$  is the radiation density today (when  $a = 1$ ),  $\Omega_{m0}$  is the matter (dark plus baryonic) density today,  $\Omega_{K0} = 1 - \Omega_0$  is the "spatial curvature density" today, and  $\Omega_{\Lambda0}$  is the cosmological constant or vacuum density today. Depending on the underlying cosmological model and the proportion of different components, the history of the universe will drastically change.

The cosmological parameters obtained from measuring CMB temperature and polarization anisotropies by recently concluded Planck mission (Planck Collaboration *et al.* 2020c) are: dark matter density  $\Omega_c h^2 = 0.120 \pm 0.001$ , baryon density  $\Omega_b h^2 = 0.0224 \pm 0.0001$ , dark energy density  $\Omega_\Lambda = 0.689 \pm 0.006$ , Hubble constant  $H_0 = (67.4 \pm 0.5) \text{ Km s}^{-1} \text{ Mpc}^{-2}$ . The joint constraint with BAO measurements on spatial curvature is consistent with a flat universe,  $\Omega_K = 0.001 \pm 0.002$ . These values are consistent with the standard spatially-flat 6-parameter  $\Lambda$ CDM cosmology having a power-law spectrum of adiabatic scalar perturbations. These inferred values of cosmological parameters are in good agreement with BAO, SNe, and some galaxy lensing observations, but in slight tension with the Dark Energy Survey's combined-probe results, including galaxy clustering (which prefers lower fluctuation amplitudes or matter density parameters) and in significant,  $5\sigma$  (Riess *et al.* 2021), tension with local measurements of the Hubble constant (which prefer a higher value).

## 1.2 First order perturbed universe

### 1.2.1 Perturbation equations

The universe is homogeneous and isotropic only on large scales ( $> 100\text{Mpc}$ ). However, on small scales, we see the violation of this basic assumption in cosmology. Observations of the galaxy distribution and the CMB fluctuations pattern implies that the universe is far from being homogeneous, having a complex structure and rich hierarchy composed of stars, globular clusters, galaxies, galaxy clusters, filaments and voids. These structures are believed to be originated from primordial fluctuations through gravitational instability. For small perturbations, the metric tensor can be split into a background metric for homogeneous and isotropic

universe  $g_{\mu\nu}^{bg}$  plus the small perturbations,  $h_{\mu\nu}$ , sourced by density fluctuations

$$g_{\mu\nu} = g_{\mu\nu}^{bg} + h_{\mu\nu}, \quad \text{with } |h_{\mu\nu}| \ll 1. \quad (1.12)$$

These metric perturbations can be classified into scalar, vector, and tensor perturbations. At first order, these perturbations are decoupled from each other and evolve independently and hence, can be studied individually. The general perturbed metric is given by,

$$ds^2 = (1 + 2\Psi)dt^2 + a^2(t)[(1 - 2\Phi)\gamma_{ij} + 2h_{ij}]dx^i dx^j, \quad (1.13)$$

where  $\Psi$  and  $\Phi$  are the Bardeen potentials,  $\gamma_{ij}$  is the spatial part of Friedmann Robertson walker metric and  $h_{ij}$  is a traceless, divergenceless symmetric tensor. The Bardeen potentials correspond to the scalar metric perturbations, while  $h_{ij}$  describes the tensor perturbations. Inflation tends to produce both vector and tensor perturbations. However, the vector perturbation sourced by inflation would die out due to the expansion of the universe and hence not included in the perturbed metric (based on standard inflationary paradigm) above. The density perturbations can generate scalar perturbations while it does not generate tensor perturbations at first order. The tensor-to-scalar ratio,  $r$ , parameterizes the ratio of the amplitude of the tensor and scalar fluctuations.

We need a formalism to determine the evolution of perturbations/anisotropies of each constituent of the universe. Each species is coupled to every other species by various types of interactions like gravitational, electromagnetic; for example, photons are affected by gravity and are coupled to electrons by Compton scattering. The electrons are tightly coupled to protons via Coulomb interaction. Thus, to solve photons or dark matter perturbations, one must simultaneously solve the perturbation equation for all the other components. The Boltzmann equation describes the evolution of perturbations in photon, neutrino, dark matter, proton,

and electron distributions. It is given by,

$$\frac{df(\vec{x}, \vec{p}, t)}{dt} = C[f], \quad (1.14)$$

where  $f$  is the phase space distribution of particles in consideration, which is the distribution of position ( $\vec{x}$ ), momentum ( $\vec{p}$ ), and time  $t$ . The right-hand side  $C[f]$  takes into account all possible collision terms or relevant interactions for each species. The Einstein equation and the Boltzmann equation are solved simultaneously to find the distribution of anisotropies of CMB temperature and polarization. These equations are numerically solved using the publicly available codes like, `Cosmological Initial Conditions and Microwave Anisotropy Codes (COSMICS)` (Bertschinger 1995), `CMBFast` (Seljak and Zaldarriaga 1996; Zaldarriaga *et al.* 1998), `Code for Anisotropies in Microwave Background (CAMB)` (Lewis *et al.* 2000), `Cosmic Linear Anisotropy Solving System (CLASS)` (Lesgourgues 2011). These codes simulate the evolution of linear perturbations in the universe and compute CMB and large-scale structure observables like transfer functions, matter power spectrum, CMB angular power spectra. The power spectrum of the CMB field in terms of the radiation transfer function is given as

$$C_\ell^{XY} = \int dk k^2 P_\Phi(k) |\Delta_\ell^X(k) \Delta_\ell^Y(k)|, \quad (1.15)$$

for  $X, Y = T, E, B$ . Here  $\Delta_\ell^X$  is the radiation transfer function which encapsulates the information about the physics that has led to evolution of primordial fluctuations to present day anisotropies. And,  $P_\Phi(k)$  is the power spectrum of primordial gravitational potential as predicted by inflation.

## 1.2.2 Setting the initial conditions: Inflation

The seeds of the perturbations described above were laid during the inflationary epoch in the universe's early moments. The early universe went through a phase of exponential expansion, about  $10^{-36}$  seconds after Big Bang. The simplest inflation models consider this expansion driven by a scalar field inflaton that filled the entire universe. Quantum fluctuations were generated in the inflaton field during this phase. Inflation generates perturbations, which are stretched by the rapid expansion, beyond the Hubble horizon scale,  $cH^{-1}$ . After crossing the horizon, the amplitude of the fluctuations remains constant. At some later time, they re-enter the horizon and start evolving. These form the primordial seeds, which later evolve into CMB anisotropies and the large scale structure, we see today in the universe. The simplest inflationary models predict two types of perturbations: scalar and tensor metric perturbations. The scalar or density perturbations grow via gravitational instability and lead to structure formation, while the latter can influence the CMB anisotropies. Some models of inflation also predict an almost scale-invariant power spectrum of primordial density perturbations. We can define the power spectrum of the primordial comoving curvature perturbation,  $\mathcal{R}$  as

$$\mathcal{P}_{\mathcal{R}}(k) = \frac{k^3 P_{\mathcal{R}}(k)}{2\pi^2} = \mathcal{A}_s \left( \frac{k}{k_*} \right)^{n_s - 1}, \quad (1.16)$$

where  $n_s$  is the scalar spectral index which is close to one, thereby ensuring a scale-invariant spectrum.  $\mathcal{A}_s$  is the amplitude of the primordial scalar fluctuations evaluated at the pivot scale  $k_*$  (commonly taken to be  $0.05 \text{ Mpc}^{-1}$  or  $0.002 \text{ Mpc}^{-1}$ ). Another robust prediction from the inflationary scenario is the generation of a stochastic background of primordial gravitational waves that are also expected to be nearly scale-invariant power spectrum. We can define the scale-invariant power spectrum of tensor fluctuations as

$$\mathcal{P}_{\mathcal{R}}(k) = \mathcal{A}_t \left( \frac{k}{k_*} \right)^{n_t}, \quad (1.17)$$

The tensor and scalar fluctuations are related through the tensor-to-scalar ratio  $r \equiv \frac{A_t}{A_s}$ , which represent a valuable probe of the inflation physics since it directly sets the energy scale for inflation, given by the inflaton potential  $V$  as (Lyth 1997),

$$V^{1/4} \approx \left( \frac{r}{0.01} \right)^{1/4} 10^{16} \text{ Gev.} \quad (1.18)$$

### 1.3 CMB anisotropies

The cosmic microwave background radiation illuminates our entire universe since 380000yrs after the Big Bang. The CMB is uniform and isotropic with the thermal blackbody frequency spectrum corresponding to the mean temperature of about  $\sim 2.725$  K. The first measurement of the CMB frequency spectrum over the frequency range  $\nu \in [50, 650]$  GHz has been reported by the Far-InfraRed Absolute Spectrophotometer (FIRAS) instrument (Mather *et al.* 1994) on board of the Cosmic Background Explorer (COBE) satellite in the early nineties, showing that it has a Planckian shape with the corresponding brightness temperature of about  $T = 2.725 \pm 0.001$  K (Fixsen *et al.* 1996). Although the FIRAS measurement showed excellent agreement between the CMB spectrum and a perfect blackbody spectrum, there are various physical mechanisms like Silk damping of small scale perturbations (Silk 1968), decay and annihilation of relic particles (McDonald *et al.* 2000), primordial magnetic fields (Miyamoto *et al.* 2014), etc., which can cause spectral deviation of CMB from the blackbody spectrum. It has now become a focus of attention as a probe of the thermal history of the Universe. The type of distortion depends on the epoch and the process of energy injection. Two future missions, PIXIE and PRISM, have been proposed for precise measurement of the CMB distortions, as these measurements hold the key to our understanding of early universe physics. Less than 10% of CMB radiation is linearly polarized (Coulson *et al.* 1994; Hu and White 1997). This linear polarization is generated by Thomson



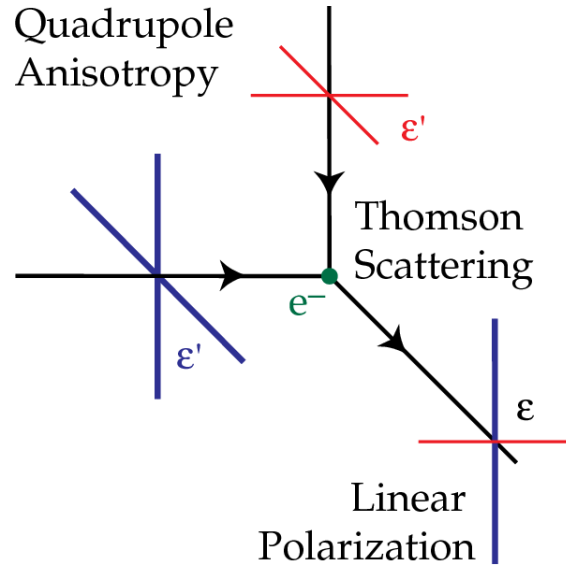


FIGURE 1.1: Thomson scattering of radiation with a quadrupole anisotropy generates linear polarization. Blue colors (thick lines) represent hot and red colors (thin lines) cold radiation. (Wayne Hu, M. White 1997)

scattering of CMB photons having a quadrupolar pattern in their intensity, off free electrons during the late stages of recombination epoch (Rees 1968). The presence of quadrupole anisotropy in photon intensity distribution is one of the necessary conditions for polarising CMB photons. Before the recombination era, the mean free path of photons was small relative to the Hubble scale, and the interaction rate between photons and electrons was so high that it erased any anisotropies in the photon distribution. While after the recombination, there was no Thomson scattering of CMB photons off electrons due to decoupling. Therefore, CMB photons could get polarized during the recombination phase. CMB polarization is often described in terms of  $E$ -modes and  $B$ -modes constructed using Stoke's parameters  $Q$  and  $U$ , and are rotationally invariant, unlike  $Q$  and  $U$ .  $E$ -mode polarization arises from velocities and has more structure at small scales. CMB  $E$ -mode polarization was detected first by DASI (Kovac *et al.* 2002) in 2002 after a lot of experimental efforts.  $B$ -mode polarization has mainly two sources: primordial gravitational waves, i.e., waves generated during the inflation era (which is dominant at low multipole range) (Crittenden *et al.* 1993; Seljak and Zaldarriaga 1997) and weak gravitational lensing of CMB photons by large scale structures

in the universe (which is dominant at high multipole range). Lensed  $B$ -modes have been detected by multiple experiments at very small scales, while primordial  $B$ -modes are still beyond the detection limits of the current ongoing missions. Further, these polarization signals get modified during the epoch of reionization and by the interaction of CMB photons with Large scale structure (LSS) in the universe.

The CMB photons carry information about the inhomogeneities in density, velocity, and gravitational potential fields imprinted by inflation into the photo-baryonic plasma. These tiny inhomogeneities in the plasma source the tiny fluctuations in the CMB temperature across the sky. These fluctuations are the so-called primary CMB temperature anisotropies, which provide a snapshot of the universe at the time of decoupling. These intrinsic/primary anisotropies are of the order of  $\sim 10^{-5}$ . COBE satellite in 1992 detected anisotropy in CMB temperature field at the level of  $10^{-5}$  around the mean value (Smoot *et al.* 1992). Since their first detection, CMB anisotropies have been the subject of greater interest and have provided a solid ground for testing our theories of structure formation and the early universe.

CMB anisotropy measurements constitute measuring anisotropies in three observables, temperature ( $\hat{n}$ ) and, stokes parameters  $Q(\hat{n})$ ,  $U(\hat{n})$ , along each line of sight  $\hat{n}$ . The fluctuation in temperature is expressed as,

$$\Theta(\hat{n}) \equiv \frac{\Delta T}{T_0}(\hat{n}) = \frac{T(\hat{n}) - T_0}{T_0}, \quad (1.19)$$

where  $T_0$  is the mean temperature across the whole sky. Scalar CMB temperature anisotropy field  $\Theta(\hat{n})$  can be decomposed in terms of spherical harmonics  $Y_{\ell m}$ 's as

$$\Theta(\hat{n}) = \sum_{\ell m} a_{\ell m} Y_{\ell m}(\hat{n}) \quad \text{where} \quad a_{\ell m}^T = \int d\Omega \Theta(\hat{n}) Y_{\ell m}^*(\hat{n}). \quad (1.20)$$

We cannot make predictions about any particular  $a_{\ell m}$ , but different theories predict the probability distribution from which they are drawn. Considering CMB temperature field to be a Gaussian random field, the harmonic coefficients are complex Gaussian random variables with zero mean, and a non-zero variance, i.e.,

$$\langle a_{\ell m} \rangle = 0 \quad ; \quad \langle a_{\ell m} a_{\ell' m'}^* \rangle = \delta_{\ell\ell'} \delta_{mm'} C_\ell, \quad (1.21)$$

where  $\langle . \rangle$  denotes an ensemble average over the sky realizations, and  $C_\ell$  is the angular power spectrum. The covariance matrix of the harmonic coefficients is diagonal as a consequence of the fundamental assumption of homogeneity and isotropy of the universe. Any preferred direction in the sky will introduce off-diagonal elements in the covariance matrix, breaking the statistical isotropy of the temperature field.

The CMB polarization is described in terms of Stokes parameters  $Q(\hat{n})$  and  $U(\hat{n})$  defined on the sphere in a particular frame of reference. These parameters are not scalar quantities, they transform as the components of a symmetric trace free  $2 \times 2$  tensor under rotation by an angle  $\gamma$  as,

$$\begin{pmatrix} Q & U \\ U & -Q \end{pmatrix} \Rightarrow \begin{pmatrix} \cos \gamma & \sin \gamma \\ -\sin \gamma & \cos \gamma \end{pmatrix} \begin{pmatrix} Q & U \\ U & -Q \end{pmatrix} \begin{pmatrix} \cos \gamma & \sin \gamma \\ -\sin \gamma & \cos \gamma \end{pmatrix},$$

or the linear combination of  $Q$  and  $U$  transforms like a spin-2 field,

$$(Q \pm iU)'(\hat{n}) = e^{\mp 2i\gamma} (Q \pm iU)(\hat{n}). \quad (1.22)$$

We may therefore expand these quantities in the appropriate spin weighted basis (Zaldarriaga and Seljak 1997),

$$(Q + iU)'(\hat{n}) = \sum_{\ell m} a_{2,\ell m} {}_2Y_{\ell m}(\hat{n}), \quad (1.23)$$

$$(Q - iU)'(\hat{n}) = \sum_{\ell m} a_{-2,\ell m} {}_{-2}Y_{\ell m}(\hat{n}). \quad (1.24)$$

The CMB polarization is described in terms of  $E$ -mode and  $B$ -mode respectively. For both the  $E$ -mode and  $B$ -mode, the polarization varies along direction parallel to the wave vector,  $\mathbf{k}$ . For the case of a pure  $E$ -mode, the polarization is parallel or perpendicular to  $\mathbf{k}$ . For a pure  $B$  mode, the polarization is rotated by  $45^\circ$  with respect to  $\mathbf{k}$ .  $E$ -mode and  $B$ -mode multipoles are defined in terms of coefficients  $a_{\pm 2,lm}$  as,

$$E_{lm} \equiv \frac{-1}{2} [a_{2,lm} + a_{-2,lm}], \quad (1.25)$$

$$B_{lm} \equiv \frac{-1}{2i} [a_{2,lm} - a_{-2,lm}]. \quad (1.26)$$

We can now define the  $E$ -mode and  $B$ -mode polarization sky map as

$$E(\hat{n}) \equiv \sum_{lm} E_{lm} Y_{lm}(\hat{n}), \quad (1.27)$$

$$B(\hat{n}) \equiv \sum_{lm} B_{lm} Y_{lm}(\hat{n}). \quad (1.28)$$

It can be shown that scalar perturbations in the density only generate gradient-like polarization patterns at first order, while curl-like polarization requires tensor-like perturbations. Tensor-like perturbations in the metric describe gravitational waves. It is believed that a background of gravitational waves was generated during inflation, which would imprint  $B$ -mode polarization in CMB. However, this primordial component is yet to be detected in CMB experiments.

The CMB fluctuations are statistically isotropic and follow a Gaussian distribution. The power spectrum of the CMB fields are calculated as,

$$C_\ell^{XY} = \frac{1}{(2\ell + 1)} \sum_{m=-\ell}^{\ell} a_{\ell m}^X a_{\ell m}^{*Y}, \quad (1.29)$$

where  $X, Y = T, E, B$ . CMB fluctuations are described using four combinations only i.e  $TT, EE, BB$  and  $TE$ . This is because the  $B$ -mode field has odd parity, hence the cross correlation between  $B$ -mode and  $T$  or  $E$ -mode vanishes. A more

conventional form of power spectrum,  $D_\ell$ , can be defined as

$$D_\ell^{XY} = \frac{\ell(\ell+1)}{2\pi} C_\ell^{XY}. \quad (1.30)$$

The CMB power spectrum can be modeled using perturbation theory and has been measured to high precision by several experiments from the largest scales down to arcminute scales. Figure 1.2 (Choi *et al.* 2020) shows the recent measurements of CMB temperature and polarization power spectra from various CMB experiments.

By looking at  $C_\ell^{TT}$  or  $D_\ell^{TT}$ , we can appreciate the wealth of information contained here. At low  $\ell$ , we see a scatter in the data points compared to the theory. This arises from the cosmic variance. Since, we only have one universe, which is a unique realization of a Gaussian random process, and we only have one sky, to make measurements. There is the fundamental uncertainty in the knowledge we may get about the  $C'_\ell$ s. This uncertainty is known as a cosmic variance. At these scales, the number of modes available for  $C_\ell$  estimation is limited. For a given  $\ell$ , the number of modes is  $(2\ell+1)$ . For independent Gaussian realizations, the error scales as

$$\frac{\Delta C_\ell}{C_\ell} = \sqrt{\frac{2}{2\ell+1}}. \quad (1.31)$$

From the  $C_\ell$  we can distinguish three main features sourced by different physical effects:

- the Sachs-Wolfe plateau (almost flat region) at  $\ell \lesssim 100$ , that traces the initial conditions (which have not had enough time to evolve on such big scales).
- a prominent primary peak around  $\ell \sim 220$  followed by a series of acoustic peaks of varying amplitude. These wiggles are the baryon acoustic oscillations (BAO) sourced by the sound waves in the photon-matter plasma before recombination (driven by the competing force of gravity and pressure).

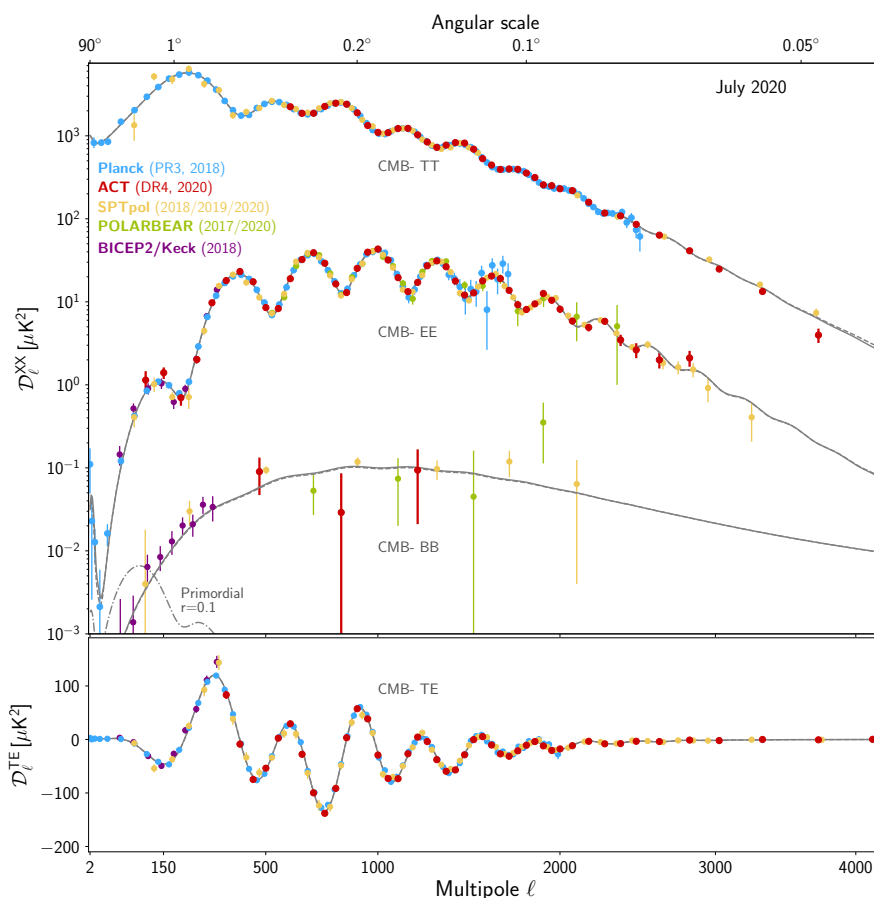


FIGURE 1.2: Recent measurements of the CMB temperature anisotropy and polarization. The two models, the thin, nearly overlapping grey lines, are from Planck (dashed line) and ACT plus WMAP (A20, solid line). The primordial BB signal with  $r = 0$  is also shown with the dot-dashed line. For Planck, 2018 results (Planck Collab. V et al. 2019) are shown. For SPT, Henning et al. (2018) for 150 GHz  $TT < 2000$ , TE and EE, and Sayre et al. (2019) for BB are shown here. For  $\ell > 2000$ , the plot shows the SPT spectrum from George et al. (2015), corrected for point source emission. It is visually indistinguishable from the more precise but uncorrected spectrum in Reichardt et al. (2020). For Polarbear/Simons Array, figure show EE from Adachi et al. (2020) and BB from pipeline A in POLARBEAR Collaboration et al. (2017). For BICEP2/Keck, Ade et al. (2018) is used. All error bars are one sigma, and points with no lower bound in TT and EE have been dropped at high  $\ell$ . This figure is taken from Choi *et al.* (2020).

- overall damping of the spectrum for  $\ell \gtrsim 1000$  caused by photon diffusion at recombination. This process of fall in the power at small scales is referred to as the Silk damping.

Acoustic peak amplitudes and their locations are sensitive to different cosmological parameters, which are then constrained using CMB observations.

## 1.4 Structure formation

Initial density fluctuations grow due to gravitational instability. This leads to under-dense and over-dense regions in matter density distributed across the different spatial location and redshifts in the universe. We can analytically model the evolution and structuring of matter at large scales. An analytical description of the matter density evolution at linear and quasi-linear scales can be obtained using first order perturbation theory. However, at small scales where the matter density becomes highly non-linear, we must combine semi-analytical approaches and simulations to understand the matter density evolution further.

The fluctuation from the mean density of the universe is described using the density contrast  $\delta$ , which is defined as,

$$\delta(\vec{x}, a) = \frac{\rho(\vec{x}, a) - \bar{\rho}(a)}{\bar{\rho}(a)}, \quad (1.32)$$

where  $\vec{x}$  is a 3-D position vector and bar indicate mean quantities. In an expanding universe the velocity can be written as

$$\mathbf{v} = H\mathbf{x} + a\mathbf{u}, \quad (1.33)$$

Here  $\mathbf{v}$  is the sum of the Hubble flow plus a peculiar velocity term. In the Newtonian limit (densities and velocities are assumed to be small, i.e.  $\delta \ll 1$  and  $v \ll c$ ), the evolution of matter fluctuations in the cosmic mean density can be studied using three non-linear coupled differential equations (on a homogeneously expanding background)

- The continuity equation, which describes conservation of mass,

$$\dot{\delta} + \nabla[(1 + \delta)\mathbf{u}] = 0. \quad (1.34)$$

- the Euler equation, describing conservation of momentum

$$\mathbf{u} + H\mathbf{u} + (\mathbf{u}\nabla)\mathbf{u} = -\nabla\Psi - \frac{1}{\rho}\nabla p. \quad (1.35)$$

- the Poisson equation, which relates the mass density to the gravitational potential

$$\nabla^2\Psi = 4\pi G \bar{\rho} \delta a^2. \quad (1.36)$$

$\Psi$  is the gravitational potential and  $p$  is the pressure. For components with non-zero (non-negligible) pressure, an equation of state must be added to close this set of equations.

To study the evolution of the density field these equations are linearized assuming small perturbations ( $\delta \ll 1$ ). Finally we get second order linear differential equation for the density contrast

$$\ddot{\delta} + H \dot{\delta} - \frac{3}{2}\Omega_{m0} H^2 \delta = 0, \quad (1.37)$$



where  $\Omega_{m0} = \Omega_m(z = 0)$ . Solution of this equation yields,

$$\delta(\vec{x}, a) = \frac{D_+(a)}{D_+(a_0)} \delta(\vec{x}, a_0), \quad (1.38)$$

Here  $D_+$  is the linear growth function. For a matter-dominated universe, which is the picture before dark energy starts to dominate the energy budget of the universe, one can solve for  $D_+(a)$  exactly and obtain  $D_+(a) = a$ . In the presence of dark energy we have  $D(a) < a$ , and the exact solution for D must be evaluated numerically.

The density contrast has zero mean, i.e.,  $\langle \delta(\vec{x}, a) \rangle = 0$ , by construction. Inflation sets the initial conditions for the matter perturbations and its power spectrum. Hence, the matter power spectrum  $P_\delta(k, a)$  is assumed to start out nearly scale-invariant  $P(k, a_{initial}) \equiv \mathcal{P}_{\mathcal{R}}(k) \propto k^{n_s - 1}$ , where  $n_s \approx 1$ . The subsequent evolution of this primordial spectrum can be expressed in term of a matter transfer function  $T(k, a)$ ,

$$P(k, a) = T^2(k, a) P(k, a_{initial}). \quad (1.39)$$

The transfer function accounts for all the interactions between different components and the effects at play on all scales. The matter power spectrum normalization is determined from observations and it is commonly expressed in terms of the variance on scales of  $8 \text{ Mpc } h^{-1}$  as

$$\sigma_8^2 = 4\pi \int \frac{k^2 dk}{(2\pi)^3} \tilde{W}^2(k, R = 8) P_{\delta\delta}(k), \quad (1.40)$$

where  $\tilde{W}^2(k, R = 8)$  is the Fourier transform of top-hat window function with radius  $R = 8 \text{ Mpc } h^{-1}$  and  $P_{\delta\delta}(k)$  is the matter power spectrum defined as a function of scale  $k$ .  $\sigma_8$  is called the amplitude of matter fluctuations.

As the structures grow via gravitational instability, non-linear terms in the perturbation evolution equations shown above become important. The non-linear evolution can in principle be modeled using perturbation theory, i.e., by considering the next to leading order terms in  $\delta$ . However, this approximation is no longer valid for  $\delta \rightarrow 1$ . The *halo model* which is a semi-analytical approach, has proven useful to address non-linear clustering (Cooray and Sheth 2002). The basic idea is that at late times all the matter cluster in virialized DM halos, and the galaxy distribution can be modeled by an appropriate method that can assign galaxies to these DM halos. The basic assumption of the halo model is that the average halo properties, such as its density profile and its baryon content, only depend on the halo mass.

These DM halos provide the gravitational potential wells for forming large scale structures of the universe consisting of galaxies, galaxy clusters, superclusters. This large scale structure distributed across the universe interacts with CMB photons in various ways leaving their imprint in the CMB frequency spectrum and its anisotropies. CMB secondary anisotropies on small angular scales encode important information about the late time interaction of CMB photons with large-structure in the Universe. One of the most rudimentary of these interactions is the gravitational effect of the large-scale structure potentials deflecting the photons, an effect referred to as the Gravitational Lensing of the CMB. The effect of lensing on CMB and its formalism will be discussed in detail in the next chapter of this thesis.

## 1.5 Real space statistics

The wealth of cosmological information in CMB temperature and polarization anisotropies is captured using different statistical observables. Conventional statistical tools employed for analyzing cosmological data are the hierarchy of  $n$ -point functions, fractals, skewness, kurtosis, Minkowski functionals, power spectrum, bispectrum. These measures capture different aspects of the properties like non-Gaussianity, statistical isotropy, etc., of the cosmological fields. Another promising approach to gain insights into the underlying physical processes is studying the geometry and topology of excursion sets of smooth random fields. Betti numbers, Minkowski functionals, and Minkowski tensors are the geometrical and topological quantities used to study the morphology of cosmological random fields. These real space statistical measures provide alternative methods, complementary to the traditional approach, to constrain cosmological parameters. Moreover, above all, morphological statistics incorporate correlation functions of arbitrary order. Hence, they are sensitive to the signatures of non-Gaussianity in any random field.

The genus, which is one of the Minkowski functionals, has been used extensively for analyzing the large scale structure and CMB data (Gott *et al.* 1986; Mecke *et al.* 1994; Vogeley *et al.* 1994; Hikage *et al.* 2003). Other scalar Minkowski functionals have also been applied to investigate statistical properties like the signature of primordial non-Gaussianity in CMB (Novikov *et al.* 2000; Shandarin *et al.* 2001; Ducout *et al.* 2012; Buchert *et al.* 2017; Planck Collaboration *et al.* 2020d) or LSS data (Pratten and Munshi 2012; Shirasaki *et al.* 2012), to trace the level of residual foreground contamination in CMB observed maps (Chingangbam and Park 2013; Santos *et al.* 2016), modified theories of gravity. Betti numbers, which are the number of connected regions and holes and whose difference give the genus (the third scalar Minkowski Functional), have also been utilized for

analyzing cosmological fields (Chingangbam *et al.* 2012; Park *et al.* 2013; Pranav *et al.* 2019).

Vector- and tensor-valued generalizations of the scalar Minkowski Functionals on two- and three-dimensional Euclidean space have been constructed in Alesker (1999); Schroder-Turk *et al.* (2010). They are collectively known as Tensor Minkowski functionals or Minkowski Tensors (henceforth MTs). In comparison to scalar Minkowski functionals, they carry additional information related to intrinsic anisotropy and alignment of structures (Schroder-Turk *et al.* 2010; Schröder-Turk *et al.* 2013). Of these, rank-1 Minkowski tensors have been used to study the substructure of galaxy clusters (Beisbart *et al.* 2001a,b). Rank-2 Minkowski tensors can be further sub-classified into translation covariant and translation invariant ones. Translation covariant MTs have been used to study the substructure of spiral galaxies in Beisbart *et al.* (2002).

The *translation-invariant rank-2 MTs* have been recently introduced to cosmological applications. They were first applied to analyze the CMB in Ganesan and Chingangbam (2017). The definition of MTs was generalized to smooth random fields on curved two-dimensional manifolds, in particular spaces of constant curvature such as the sphere, in Chingangbam *et al.* (2017b). They have also been applied to search for departure from statistical isotropy of the CMB (Ganesan and Chingangbam 2017; Joby *et al.* 2019; Kochappan *et al.* 2021). They have also been applied to analyze fields of the epoch of reionization Kapahtia *et al.* (2018); Kapahtia *et al.* (2019); Kapahtia *et al.* (2021). Most recently, they have been used to study the effect of redshift-space distortion on matter distribution in the universe (Appleby *et al.* 2018a,b; Appleby *et al.* 2019). We will be using these real space geometrical observables, specifically the Contour Minkowski Tensor (CMT), for investigating the effect of gravitational lensing on CMB fields.

## 1.6 Goal of the Thesis

This thesis aims to probe the evolution of the universe and its properties by analyzing the morphology of cosmological fields. We used the method that relies on novel morphological descriptors known as Minkowski tensors (MTs). One of the translational invariant MTs, the contour Minkowski tensor (CMT), captures the information on the shape and alignment of the structures in the excursion sets of the smooth random fields. The CMT is particularly useful in the context of the CMB and Large scale structure (LSS). We can probe departures from isotropy and Gaussian statistics by studying the topology and geometry of CMB fields or the matter density field using CMT. Hence, we can infer the critical time and length scales related to the underlying physics causing these deviations from the standard picture.

The specific questions that we address and the structure of the thesis are outlined below.

- As a first step towards our goal we have studied cross correlation between CMB and large scale structure. We studied the morphology changes induced in the CMB fields, namely temperature fluctuations and E and B modes of polarization, which are sourced by gravitational lensing of CMB photons by large scale structures in the Universe. We use the contour Minkowski Tensors to quantify the distortion induced by lensing in the shapes of connected and hole regions, and their relative alignment, which gives a measure of departure from statistical isotropy.
- We test the statistical isotropy of the universe by employing Contour Minkowski Tensor and hence computing  $\alpha$  parameter for the large scale matter distribution reconstructed using observations of lensed CMB fields by Planck mission. We compute the alignment parameter,  $\alpha$ , for the convergence ( $\kappa$ )

map over full sky and also in small patches of the sky. From the local analysis we have identified anomalous regions in the sky with high statistical significance.

- We are interested in understanding the geometrical meaning of statistical isotropy that is manifest in excursion sets of smooth random fields in two dimensions. We extend the results of Chingangbam *et al.* (2017b) focusing on the contour Minkowski tensor. We give an explicit construction for mapping any arbitrary shaped simple closed curve to an ellipse that is unique upto translations of its centroid. We also carry out a comparison of the shape parameters defined using the contour Minkowski tensor with the filamentarity parameter defined using two scalar Minkowski functionals - area and contour length, and demonstrate that they contain complementary shape information. Then we discuss the derivation of analytic expression for the contour Minkowski tensor for Gaussian anisotropic random fields.
- The last part of the thesis will focus on analyzing the prospects of constraining primordial non-Gaussianity in CMB fields using MTs and Betti numbers. MTs being tensorial generalization of the scalar Minkowski Functionals (MFs) contain more independent degrees of freedom. Hence, we expect that they can provide tighter constraints on primordial non-Gaussianity parameter  $f_{NL}$  in comparison to SMFs.

### Outline of the thesis:

The chapter-wise plan of the thesis is given below

- In chapter 2, we sketch the CMB weak lensing formalism, and describe the deflection angle and the lensing potential. We then qualitatively describe the effect of lensing on CMB temperature and polarization angular power

spectrum and discuss the construction of quadratic estimator for lensing potential.

- In chapter 3, we present a brief overview of the statistical tools used in this thesis work. We present definitions and the recipe for the numerical computation of the scalar Minkowski functionals and Minkowski tensors relevant for this thesis.
- In chapter 4, we investigate the effect of weak lensing on the morphology of CMB fields using shape and alignment parameters,  $\beta$  and  $\alpha$ , respectively. These shape parameters are obtained from the Contour Minkowski tensor.
- In chapter 5, we test the statistical isotropy of the Planck convergence field or the lensing potential field, inferred from lensed CMB observations by Planck mission.
- In chapter 6, we extend the analytic derivation of the CMT from the case of Gaussian isotropic field to the case of Gaussian anisotropic field. We discuss the geometrical meaning of statistical isotropy of the excursion sets of smooth random fields in two dimensions. We demonstrate mapping of arbitrary shaped simple closed curve to an ellipse and further discuss the distribution of many such curves and their relative alignment.
- In chapter 7, we discuss our ongoing project on the comparison of the information content in the Minkowski Tensors and the scalar Minkowski functionals. We formulate the problem and present the preliminary results obtained, and discuss our future work.
- In chapter 8, we summarize our key results focusing on the novel aspects, and then discuss directions of future studies.

# Chapter 2

## Gravitational lensing of Cosmic Microwave Background

Gravitational lensing of the CMB by the intervening matter distribution in the universe imprints valuable information in the temperature and polarization anisotropies. CMB lensing has become an essential probe in cosmology and astrophysics. In this chapter, we briefly describe the CMB lensing phenomenon and its consequences.

### 2.1 Introduction

CMB photons encounter the intervening cosmic web formed mostly by dark matter and baryonic matter as they traverse from the last scattering surface to us today. This structure distorts space and time according to the prediction of General Relativity (GR). In GR for a point mass deflected by mass  $M$  at an distance



of closest approach  $R$ , deflection angle is given by  $\frac{4\Psi(R)}{c^2}$ . Here,  $\Psi$  is the gravitational potential due to mass  $M$  at the distance of closest approach, and  $c$  is the velocity of light. The amount of deflection predicted by GR is twice that of the Newtonian prediction. The CMB photons geodesic are deflected multiple times by the interceding structure (Blanchard and Schneider 1987). The root mean square (RMS) depth of the potential well at last scattering is of order  $\mathcal{O}(10^{-5})$  (Lewis and Challinor 2006). Each such potential then gives a deflection  $\delta\beta \sim 10^{-4}$  radians. The scale corresponding to the peak of the matter power spectrum, i.e.,  $\sim 300$  Mpc (comoving), gives the characteristic size of the potential well. The comoving distance to the last scattering surface is about 14000 Mpc, so the number of potential wells passed through is  $\sim 50$ . If the potentials are uncorrelated, this will give an r.m.s. total deflection,  $50^{1/2} \times 10^{-4} \sim 7 \times 10^{-4}$  radians or two arcminutes. The deflection of the CMB photons is small, so CMB lensing can be studied well within the weak-lensing regime.

The gravitational lensing effect can be understood as a remapping of the unlensed CMB field by a line-of-sight averaged deflection field. Let the deflection caused by lensing for each sky direction  $\hat{n}$  be captured by deflection angle  $\vec{d}(\hat{n})$ , which is a vector field on the 2-D surface of a sphere. Then the observed CMB field value in some direction  $\hat{n}'$  can be expressed in terms of the field values in the original direction  $\hat{n}$  as,

$$T^{\text{L}}(\hat{n}') = T^{\text{UL}}(\hat{n} + \vec{d}). \quad (2.1)$$

CMB lensing is an achromatic effect, i.e., it does not modify the CMB blackbody frequency spectrum. However, it does alter the two and higher-point statistics (Seljak 1996; Zaldarriaga and Seljak 1998; Zaldarriaga and Seljak 1999) and generates non-Gaussianity in otherwise Gaussian primordial fluctuations. The deflection suffered by a CMB photon as it travels towards us from the last scattering surface is about three arcminutes, as discussed above. The deflection angles will be

correlated over the sky by an angle given by the angular size of a characteristic potential,  $\sim 300/7000 \sim$  two degrees, for a potential lying mid-way to the last scattering. Hence the deflections, although much smaller than the angular scale corresponding to the primary CMB acoustic peaks, are coherent over comparable scales. Consequently, lensing causes coherent distortions of the CMB cold and hot spots and broadens their size distribution. This results in redistribution of power among the acoustic scales in the CMB and shows up in the angular power spectrum as smoothing of the acoustic peaks (Seljak 1996; Metcalf and Silk 1997; Lewis and Challinor 2006). At smaller scales, where a local gradient well approximates the CMB, deflectors of small angular size produce small-scale distortions in the CMB, thereby transferring power from large scales in the CMB to the higher multipoles.

CMB lensing is an integrated effect and hence, sensitive to all the matter along the line of sight, thus acting as a complementary tracer of the large-scale structure in the universe. Matter distribution inferred from CMB lensing is described using integrated potential measure, i.e., lensing potential. The primordial CMB can be assumed to be a Gaussian random field (Komatsu *et al.* 2005), and the large-scale lensing potential field can also be well approximated by a Gaussian random field. However, the lensed CMB being a reprocessing of one Gaussian random field by another is not Gaussian. This non-Gaussianity or mode coupling in lensed fields enables us to extract information about the large scale matter distribution in the universe. The connected part of the four-point correlation function of CMB temperature and polarization anisotropy contains the relevant information about the lensing potential power spectrum. This fact has been the basis of the standard estimators for extracting gravitational lensing signal from CMB observations. There exist estimators both in harmonic space known as Quadratic estimators, (Hu 2001; Hu and Okamoto 2002; Okamoto and Hu 2003) and in configuration space like maximum likelihood estimators, (Hirata and Seljak 2003), to estimate the lensing potential or the projected density (convergence) of these structures, its

power spectrum, and cross-correlation with other observables. The CMB lensing potential provides a unique observable, in addition to the CMB temperature and polarization anisotropies, to study the properties of matter distribution, and hence another way to test our models of cosmological structure formation. Compared to galaxy surveys, CMB lensing has the advantage of directly tracing matter distribution, thus avoiding the uncertainties associated with a bias between the distributions of galaxies and mass (Zaldarriaga and Seljak 1999). Also, it traces the matter distribution at higher redshifts that cannot be reached by galaxy surveys or weak galaxy lensing and is sensitive to the largest observable scales in the universe (Zaldarriaga and Seljak 1999; Hu 2001, 2000).

Ultimately, they all observe the same available sky, i.e., the same underlying matter density field. This fact has led to various cross-correlation studies between CMB lensing and the large scale structure field. Also, it has been realized that this approach is powerful (Peiris and Spergel 2000) because many of the systematics disappear upon cross-correlating data sets. CMB lensing was first confirmed in the WMAP data by cross-correlating CMB observations (Hinshaw *et al.* 2007; Smith *et al.* 2007) with the WISE (Condon *et al.* 1998) galaxy data. With tremendous efforts and furtherance in our understanding of CMB physics combined with the advancement in technology has led to high resolution and detailed mapping of CMB anisotropies by various experiments such as ACT, PLANCK and the South Pole Telescope (SPT)\* on the horizon. We have now entered an era where robust detection and characterization of this effect has become a reality. Also, with upcoming and proposed large scale structure projects LSST†, SNAP‡, ADEPT§, DESTINY¶, etc, there will be many more datasets to cross-correlate with the CMB. The Planck results (Planck Collaboration *et al.* 2016, 2020a) have provided the most significant ( $\sim 40\sigma$ ) detection of gravitational lensing of CMB so far.

---

\*<http://spt.uchicago.edu>

†[http://www.lsst.org/lsst\\_home.shtml](http://www.lsst.org/lsst_home.shtml)

‡<http://snap.lbl.gov/>

§<http://universe.nasa.gov/program/probes/adept.html>

¶<http://destiny.asu.edu/>

In addition to being a useful cosmological signal, CMB lensing will act as a contaminant to detect the primordial  $B$ -mode polarization modes. The observed  $B$ -mode polarization signal has two components. The first is the primordial component sourced by gravitational waves generated during inflation which dominates at large angular scales ( $\ell \leq 100$ ). The amplitude of this component depends on the value of the tensor-to-scalar ratio,  $r$ .  $B$ -mode polarization in the CMB is a direct probe of the primordial gravitational wave. Thus detecting  $B$ -modes generated by GW is a 'smoking gun' evidence for inflation. The best current limits constrain the tensor-to-scalar ratio to  $r_{0.002} < 0.056$  (BICEP2 Collaboration *et al.* 2018; Planck Collaboration *et al.* 2020e), where  $r_{0.002}$  denotes  $r$  at the pivot scale  $0.002 \text{ Mpc}^{-1}$ . The second component, which is generated due to coupling between the  $E$  and  $B$ -mode (Zaldarriaga and Seljak 1998) caused by CMB weak lensing, dominates at small angular scales ( $\ell \sim 1000$ ). This implies that gravitational lensing can generate  $B$ -mode polarization, even if no primordial tensor fluctuations were present to generate primordial  $B$ -mode polarization. Lensed  $B$ -modes have been measured by various ground-based telescopes like SPTPOL (Hanson *et al.* 2013), BICEP2/KECK ARRAY V (Ade *et al.* 2015), POLARBEAR (and P. A. R. Ade *et al.* 2017), etc. Figure 2.1 shows current upper limits on  $B$ -modes from various experiments. In practice, cosmic variance, instrumental noise, and a high level of contamination from polarized foregrounds make the experimental detection of primordial  $B$ -modes extremely challenging. Measuring primordial  $B$ -modes is the major science goal for most of the planned CMB missions, such as satellite experiments like LiteBIRD (Hazumi *et al.* 2019; Sugai *et al.* 2020), as well as ground-based telescopes, such as the Simons Observatory (SO, Lee *et al.* (2019) and CMB-S4 (Abazajian *et al.* 2019). The estimated lensing potential from the lensed CMB alone, or the potential estimated from weak lensing surveys (Marian and Bernstein 2007), can be used to significantly delens the CMB (Knox and Song 2002; Hirata and Seljak 2003). This is important to recover the primordial signal from the total observed  $B$ -mode signal (Manzotti *et al.* 2017).

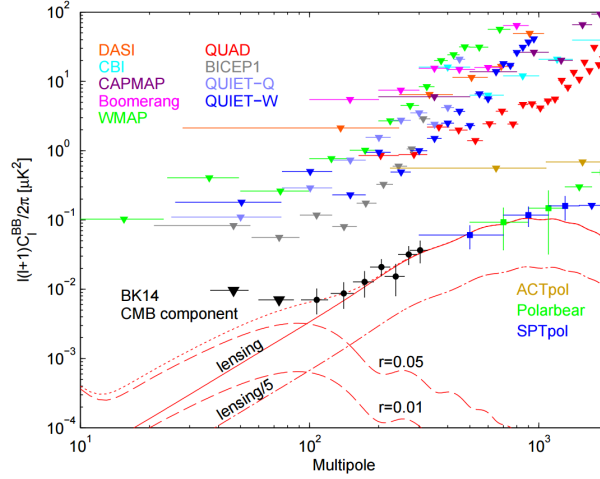


FIGURE 2.1: Current upper limits on B-modes from CMB experiments. Image Credit: Kuo Group:CMB Polarization Experiment Team

We will now review basic lensing formalism in the following sections.

## 2.2 The lensing potential and its power spectrum

We refer to Lewis and Challinor (2006) and Hanson *et al.* (2010) for a full review of the CMB lensing effect. It is now well known that gravitational potential bends the path of light. We will now estimate by how much the gravitational potentials in the universe deflects the CMB photons, so we start with a simple Newtonian calculation: for a photon approaching a point mass  $M$ , the gravitational potential encountered by the photon is given by:

$$\Psi = \frac{GM}{r}, \quad (2.2)$$

where  $G$  is Newton's constant and  $r$  is the distance between the photon and point mass  $M$ . The transverse acceleration of the photon due to the mass is,

$$\dot{v}_\perp = -\nabla_\perp \Psi = \frac{GM}{r^2} \cos \theta, \quad (2.3)$$

where  $\theta$  is the angle of the photon from the mass relative to its angle at a distance of closest approach  $R$ . Integration over the photon path for constant speed  $|v| = c$  gives a total (Newtonian) deflection angle:

$$\frac{\dot{v}_\perp}{|v|} = -\nabla_\perp \Psi = \frac{2GM}{c^2 R}. \quad (2.4)$$

In GR, we replace the derivative with the covariant derivative giving an acceleration of  $D_\chi \hat{v} = -\nabla \Psi$  where  $D_\chi$  is the covariant derivative along the photon world line. To get the deflection angle, we must also account for the curvature of space to give a local deflection angle of

$$\delta\beta = -2\delta_\chi \nabla_\perp \Psi, \quad (2.5)$$

where  $\delta_\chi$  is a small distance along the photon path. This GR result has an additional term due to the effect of space-time curvature. We now want to know how a deflection in a photon's path changes its observed angle on the sky. The angular diameter distance  $f_K(\chi)$  relates comoving distances to angles via,

$$f_K(\chi) = \begin{cases} K^{-1/2} \sin(K^{1/2}\chi), & \text{for } K > 0, \text{ closed,} \\ \chi, & \text{for } K = 0, \text{ flat,} \\ |K|^{-1/2} \sinh(|K|^{1/2}\chi), & \text{for } K < 0, \text{ open.} \end{cases} \quad (2.6)$$

Under the approximation of weak lensing and in the small angle approximation  $f_K(\chi^* - \chi) \delta\beta = f_K(\chi^*) \delta\theta$ . Solving for  $\delta\theta$  the deflection due to the source at  $\chi$  is

$$\delta\theta_\chi = \frac{f_K(\chi^* - \chi) \delta\beta}{f_K(\chi^*)} = \frac{f_K(\chi^* - \chi)}{f_K(\chi^*)} 2\delta_\chi \nabla_\perp \Psi. \quad (2.7)$$

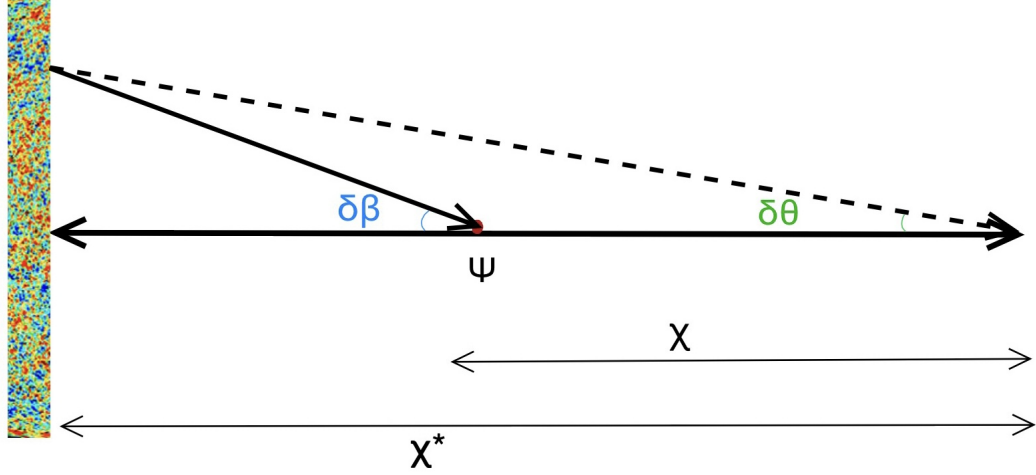


FIGURE 2.2: Weak lensing geometry for a source (the CMB) at comoving distance  $\chi^*$  lensed by a potential  $\Psi$  at distance  $\chi$ , assuming a flat universe. The lensing deflection by an angle  $\delta\beta$  changes the observed angle of the source by an angle  $\delta\theta$ .

The total deflection angle is the sum over all of the individual deflections due to gravitational potentials between the surface of last scattering and today:

$$\boldsymbol{\alpha} = -2 \int_0^{\chi^*} d\chi \frac{f_K(\chi^* - \chi)}{f_K(\chi^*)} \nabla_{\perp} \Psi(\chi \hat{\mathbf{n}}, \eta_0 - \chi), \quad (2.8)$$

where  $\eta_0 - \chi$  is the conformal time at which a photon was at position  $\chi \hat{\mathbf{n}}$ . Equation 2.8 requires the integral to be evaluated along the perturbed light path. However, since we are working at first order in  $\boldsymbol{\alpha}$  (small deflections), we can compute the integral over the unperturbed path of the photon. From the photons geodesic equation one has,

$$\chi = \eta_0 - \eta - \int_{\eta_0}^{\eta} d\eta' \Psi(\eta'). \quad (2.9)$$

The Born approximation is equivalent to setting  $\chi = \eta_0 - \eta$ , i.e. calculating the deflection along the unperturbed light path, so that the transverse derivative in equation 2.8 becomes the covariant derivative over the LOS  $\hat{\mathbf{n}}$ ,  $\nabla_{\perp} \rightarrow \nabla_{\hat{\mathbf{n}}}/f_K(\chi)$ . The validity of the Born approximation in the context of CMB lensing has been

recently investigated by Calabrese *et al.* (2015) by means of multiple planes ray-tracing techniques, and they have shown the differences to be small. We can now define the lensing potential  $\phi$  in terms of gravitational potential  $\Psi$  as:

$$\phi(\hat{\mathbf{n}}) \equiv -2 \int_0^{\chi^*} d\chi \frac{f_K(\chi^* - \chi)}{f_K(\chi^*) f_k(\chi)} \Psi(\chi \hat{\mathbf{n}}, \eta_0 - \chi), \quad (2.10)$$

which implies  $\boldsymbol{\alpha}(\hat{\mathbf{n}}) = \nabla_{\hat{\mathbf{n}}} \phi(\hat{\mathbf{n}})$  (from now on  $\nabla \equiv \nabla_{\hat{\mathbf{n}}}$ ). For the CMB, we can approximate recombination as instantaneous so that the CMB is described by a single source plane at  $\chi = \chi^*$ . Also we shall assume the universe to be flat, i.e.,  $f_K(\chi) = \chi$ . For scales on which the potential  $\Psi$  is Gaussian, the lensing potential will also be Gaussian. On smaller scales, non-linear evolution can introduce non-Gaussianity even for Gaussian primordial fields; however, on acoustic scales, this is a small correction and can be neglected for the zeroth-order picture. Therefore, its two-point function or power spectrum contains all the information needed to describe the lensed CMB statistics fully.

The lensing potential can be expanded into multipole moment (all-sky) or Fourier (flat-sky):

$$\phi(\hat{\mathbf{n}}) = \sum_{\ell m} \phi_{\ell m} Y_{\ell m}(\hat{\mathbf{n}}), \quad (2.11)$$

$$\phi(\hat{\mathbf{n}}) = \int \frac{d^2 \boldsymbol{\ell}}{(2\pi)^2} \phi(\boldsymbol{\ell}) \exp(i\boldsymbol{\ell} \cdot \hat{\mathbf{n}}), \quad (2.12)$$

where  $(\ell, m)$  and  $\boldsymbol{\ell}$  are conjugate to the real space unit vector  $\hat{\mathbf{n}}$  in all-sky and flat-sky, respectively. Now the assumption of linear evolution implies that the lensing potential is also Gaussian, and all the information about the field is carried by its power spectrum:

$$\langle \phi_{\ell m} \phi_{\ell' m'} \rangle = \delta_{\ell \ell'}^K \delta_{m m'}^K C_{\ell}^{\phi \phi}, \quad (2.13)$$

$$\langle \phi(\boldsymbol{\ell}) \phi(\boldsymbol{\ell}') \rangle = (2\pi)^2 \delta^D(\boldsymbol{\ell} - \boldsymbol{\ell}') C_{\ell}^{\phi \phi}. \quad (2.14)$$



The standard model of cosmology predicts the shape and amplitude of the CMB lensing power spectrum, which depends on geometrical factors and the metric perturbation evolution (Lewis and Challinor 2006):

$$C_\ell^{\phi\phi} = 16\pi \int d\log(k) \mathcal{P}_{\mathcal{R}} \left[ \int_0^{\chi^*} d\chi \mathcal{T}_{\Psi}(k; \eta_0 - \chi) j_\ell(k\chi) \frac{f_K(\chi^* - \chi)}{f_K(\chi^*)f_K(\chi)} \right]^2, \quad (2.15)$$

where  $j_\ell(k\chi)$  is the spherical Bessel function and  $\mathcal{T}_{\Psi}(k; \eta)$  is the linear theory transfer function. The gravitational potential at later epoch is given in terms of transfer function as,

$$\Psi(k; \eta) = \mathcal{T}_{\Psi}(k; \eta) \mathcal{R}(k), \quad (2.16)$$

where  $\mathcal{R}$  being the the primordial comoving curvature perturbation (set at the inflationary epoch) with the power spectrum  $\mathcal{P}_{\mathcal{R}}(k)$ .

We will now define another physical quantity known as convergence ( $\kappa$ ) which is useful in context of weak lensing. Shear and magnification are the two observable consequences of weak gravitational lensing. Shear (denoted by  $\gamma$ ) determines the area-preserving distortions of the images of galaxies or the structures (hot spots and cold spots) in the CMB map. The convergence ( $\kappa$ ) field, on the other hand, captures the magnification or demagnification of CMB hotspots and coldspots caused by gravitational lensing. Unlike the galaxy lensing scenario, where shear is the most crucial lensing observable, we can gain information from both shear and magnifications for the CMB. The  $\kappa$  field can be written in terms of matter density fluctuation (usually denote as  $\delta$ ) using Poisson's equation as,

$$\kappa = \frac{3}{2} \frac{H_0^2}{c^2} \Omega_{m0} \int_0^{\chi^*} d\chi \frac{\chi(\chi^* - \chi)}{\chi^*} \frac{\delta(\chi)}{a}, \quad (2.17)$$

where  $H_0$  is the Hubble constant, which quantifies the present expansion rate of the universe, and  $\Omega_{m0}$  is the dimension-less matter-density parameter.

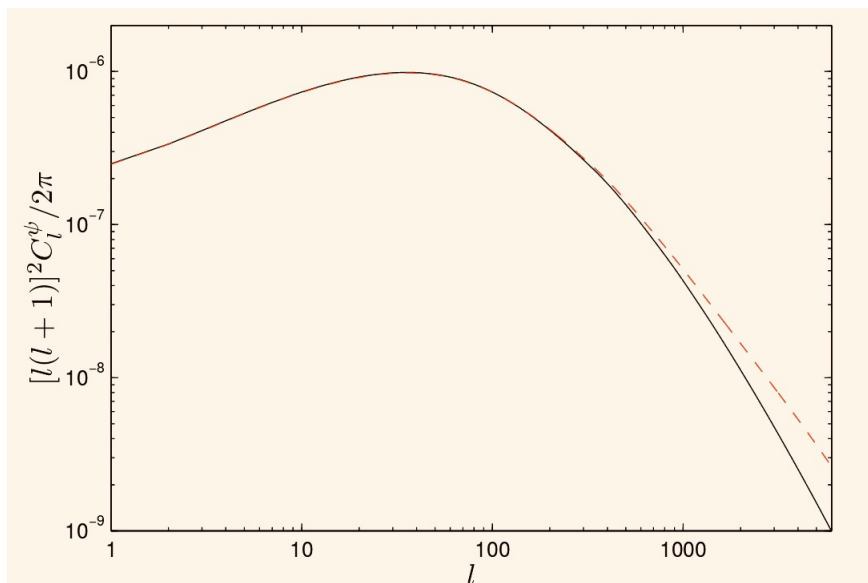


FIGURE 2.3: The power spectrum of the deflection angle (given in terms of the lensing potential  $\phi$  by  $\nabla\phi$ ) for a concordance  $\Lambda$ CDM model. The linear theory spectrum (solid) is compared with the same model including non-linear corrections (dashed) from HALOFIT (Smith et al. 2003).

The CMB lensing potential power spectrum, can be related to the deflection angle and to the convergence  $\kappa(\hat{n}) = \frac{-1}{2}\nabla^2\phi(\hat{n})$  power spectrum through,

$$C_\ell^{\alpha\alpha} = \ell(\ell+1) C_\ell^{\phi\phi}, \quad (2.18)$$

$$C_\ell^{\kappa\kappa} = \frac{[\ell(\ell+1)]^2}{4} C_\ell^{\phi\phi}. \quad (2.19)$$

begincenter

Figure 2.3 shows the deflection angle power spectrum for the case of the standard model. It has a peak at  $\ell \sim 60$ . The red curve represents non-linear corrections to the lensing potential or deflection angle. We can note that there is minimal effect on scales where the power peaks ( $\ell \sim 60$ ), but the non-linear evolution significantly increases the power on small scales. Hence, for doing precision cosmology, one should consider the non-linear evolution of the lensing potential at small scales. As already mentioned, the CMB lensing potential is an integrated measure of

the matter distribution in the universe, up to the last scattering surface. Hence, it has contributions out to relatively high redshifts. The CMB lensing potential has a broad kernel peaking at around  $z \sim 2$  but slowly varying from  $z \sim 1$  to  $z \sim 4$ . This provides us a novel way to study the time evolution and spatial distribution of the gravitational potential by correlating the weak lensing field with galaxy redshift distribution. These cross-correlation studies are valuable for combining information from two independent tracers of LSS while avoiding instrument-specific systematic errors (Bianchini *et al.* 2015).

## 2.3 CMB lensed power spectrum

As described earlier the lensing of CMB photons remaps unlensed temperature anisotropies  $\Theta(\hat{\mathbf{n}})$  in sky by the deflection angle  $\boldsymbol{\alpha}(\hat{\mathbf{n}})$ . By Taylor expanding in terms of the displacement field we get

$$\begin{aligned}
 \tilde{\Theta}(\hat{\mathbf{n}}) &= \Theta(\hat{\mathbf{n}} + \boldsymbol{\alpha}(\hat{\mathbf{n}})) \\
 &= \Theta(\hat{\mathbf{n}} + \nabla\phi(\hat{\mathbf{n}})) \\
 &= \Theta(\hat{\mathbf{n}}) + \nabla^a\phi(\hat{\mathbf{n}})\nabla_a\Theta(\hat{\mathbf{n}}) + \frac{1}{2}\nabla^a\phi(\hat{\mathbf{n}})\nabla^b\phi(\hat{\mathbf{n}})\nabla_a\nabla_b\Theta(\hat{\mathbf{n}}) \quad (2.20) \\
 &\quad + \mathcal{O}(\phi^3),
 \end{aligned}$$

Here the tilde denotes a lensed quantity. The Taylor expansion performed above simplifies the description of the lensing effect on CMB anisotropies, however it is not accurate on all scales, especially when looking at scales comparable to the deflections. In the flat-sky approximation equation 2.20 can be expressed in Fourier

domain as

$$\begin{aligned}\tilde{\Theta}(\boldsymbol{\ell}) &\approx \Theta(\boldsymbol{\ell}) - \int \frac{d^2\boldsymbol{\ell}'}{2\pi} \boldsymbol{\ell}' \cdot (\boldsymbol{\ell} - \boldsymbol{\ell}') \phi(\boldsymbol{\ell} - \boldsymbol{\ell}') \Theta(\boldsymbol{\ell}') \\ &\quad - \frac{1}{2} \int \frac{d^2\boldsymbol{\ell}_1}{2\pi} \int \frac{d^2\boldsymbol{\ell}_2}{2\pi} \boldsymbol{\ell}_2 \cdot [\boldsymbol{\ell}_1 + \boldsymbol{\ell}_2 + \boldsymbol{\ell}] (\boldsymbol{\ell}_1 \cdot \boldsymbol{\ell}_2) \Theta(\boldsymbol{\ell}_1) \phi(\boldsymbol{\ell}_2) \phi^*(\boldsymbol{\ell}_1 + \boldsymbol{\ell}_2 - \boldsymbol{\ell}).\end{aligned}\quad (2.21)$$

From here we see that lensing affects the unlensed multipoles by coupling different modes ( $\boldsymbol{\ell}'$ s). For a fixed realization of lenses, the effect of mode-coupling is to introduce off-diagonal components into the covariance matrix of observed temperature. Assuming that both  $\Theta(\boldsymbol{\ell})$  and  $\phi(\boldsymbol{\ell})$  to be isotropic, Gaussian random field which are uncorrelated, we get

$$\langle \tilde{\Theta}(\boldsymbol{\ell}), \tilde{\Theta}^*(\boldsymbol{\ell}') \rangle = \delta^D(\boldsymbol{\ell} - \boldsymbol{\ell}') \quad (2.22)$$

$$C_{\ell}^{\tilde{T}\tilde{T}} \approx (1 - \ell^2 R^\phi) C_{\ell}^{TT} + \int \frac{d^2\boldsymbol{\ell}'}{2\pi} [\boldsymbol{\ell}' \cdot (\boldsymbol{\ell} - \boldsymbol{\ell}')]^2 C_{|\boldsymbol{\ell} - \boldsymbol{\ell}'|}^{\phi\phi} C_{\ell'}^{TT}, \quad (2.23)$$

where  $R^\phi$  is half the total deflection angle power defined as

$$R^\phi \equiv \frac{1}{2} \langle |\nabla\phi|^2 \rangle, \quad (2.24)$$

$$\frac{1}{4\pi} \int \frac{d\ell}{\ell} \ell^4 C_{\ell}^{\phi\phi} \sim 3 \times 10^{-7}. \quad (2.25)$$

The lensed temperature power spectrum at first-order in  $C_{\ell}^{\phi\phi}$  differs from the unlensed spectra by a term proportional to  $R^\phi$  and by an integral term which has the form of a convolution of the unlensed temperature spectrum with the lensing potential power spectrum. This convolution smooths out the main peaks in the unlensed spectrum, which is the main qualitative effect on the temperature spectrum on large scales. The effect is shown in left plot of the figure 2.4. The bottom panel shows the fractional difference between lensed and unlensed CMB temperature power spectra and is several percent at  $\ell > 1000$ . On small scales where there is little power in the unlensed CMB, the convolution transfers power from large scales to small scales, increasing the small-scale power. Since weak lensing preserves the brightness but alter the photon's directions, the total variance of the temperature field is conserved even though the power is redistributed

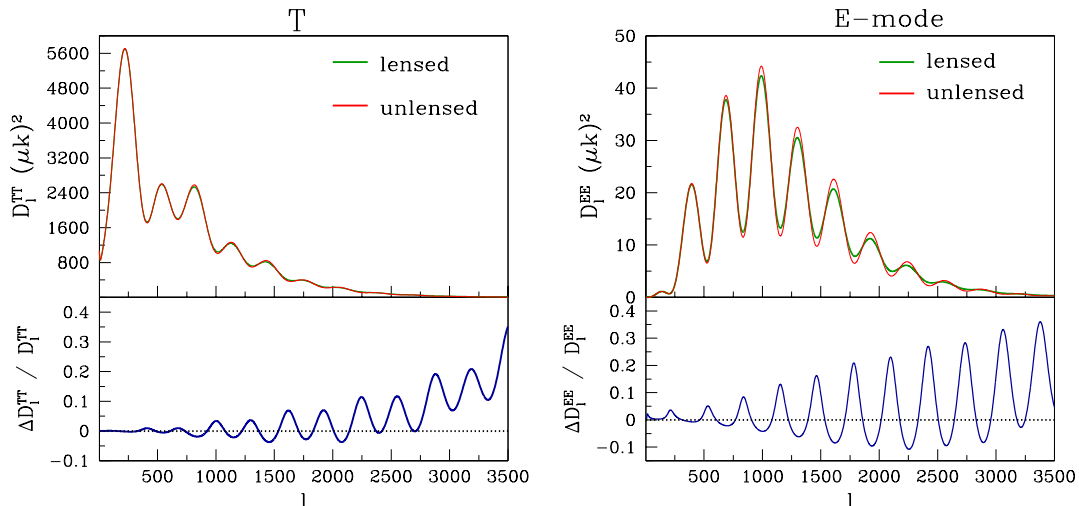


FIGURE 2.4: Top panel in left: the lensed temperature power spectrum (green) and the unlensed spectrum (red). Bottom: the fractional change in the power spectrum due to lensing. Top panel in right plot: lensed  $E$ -mode polarization power spectra overlaid on unlensed  $E$ -mode spectrum, with bottom panel showing the residual in this case. Both plots are for a typical concordance  $\Lambda$ CDM model with Planck 2018 (Planck Collaboration *et al.* 2020c) cosmological parameters.

among different scales. An exact calculation of the lensed spectra on the curved sky, which is based on real-space correlation function methods and is commonly adopted in modern Boltzmann codes, can be found in refs. (Challinor and Chon 2002; Challinor and Lewis 2005).

**Polarization power spectra:** The presence of a non-zero photon quadrupole at the last scattering surface generates a polarization signal in CMB. Linear polarization of CMB is described using Stoke's  $Q$  and  $U$  parameters or the so-called  $E$ -mode and  $B$ -mode. These are patterns in the sky, and they are defined by basically how they behave when we mirror them. So,  $E$ -modes stay the same, while  $B$ -modes changes sign under parity inversion. The lensing effect on the CMB polarization is also described as a remapping of the Stokes parameters  $Q \pm iU$  by the deflection field. Assuming no primordial  $B$ -modes, i.e.  $C_\ell^{BB} = 0$ , the lensed

power spectra to lowest order in  $C_\ell^{\phi\phi}$  are given by (Hu 2000),

$$C_\ell^{\tilde{T}\tilde{E}} \approx (1 - \ell^2 R^\phi) C_\ell^{TE} + \int \frac{d^2\ell'}{2\pi} [\ell' \cdot (\ell - \ell')]^2 C_{|\ell-\ell'|}^{\phi\phi} C_{\ell'}^{TE} \cos 2(\varphi_\ell - \varphi_{\ell'}), \quad (2.26)$$

$$C_\ell^{\tilde{E}\tilde{E}} \approx (1 - \ell^2 R^\phi) C_\ell^{EE} + \int \frac{d^2\ell'}{2\pi} [\ell' \cdot (\ell - \ell')]^2 C_{|\ell-\ell'|}^{\phi\phi} C_{\ell'}^{EE} \cos^2 2(\varphi_\ell - \varphi_{\ell'}), \quad (2.27)$$

$$C_\ell^{\tilde{B}\tilde{B}} \approx \int \frac{d^2\ell'}{2\pi} [\ell' \cdot (\ell - \ell')]^2 C_{|\ell-\ell'|}^{\phi\phi} C_{\ell'}^{EE} \sin^2 2(\varphi_\ell - \varphi_{\ell'}), \quad (2.28)$$

where  $\varphi_\ell$  and  $\varphi_{\ell'}$  are the angles between  $\hat{\mathbf{n}}$  and  $\boldsymbol{\ell}$  and  $\boldsymbol{\ell}'$  respectively. We can see from equation 2.28 that the lensing of pure  $E$ -modes generates  $B$ -mode polarization, even if the primordial  $B$ -mode component is absent. Lensing mixes these two distinct polarization modes in CMB. Qualitatively, lensing effect on  $C_\ell^{EE}$  and  $C_\ell^{TE}$  is similar to that on the temperature spectra: the unlensed spectra are convolved with the lensing potential spectra, resulting in blurring of spectral features and power transfer towards the damping tail of the power spectra. Since the acoustic peaks in  $C_\ell^{EE}$  are sharper than the temperature ones, the fractional changes in the lensed  $E$ -modes are  $\mathcal{O}(30\%)$  near the acoustic peaks (Lewis and Challinor 2006). Lensing must therefore be modelled in order to get accurate results when doing parameter estimation from polarized power spectra. Lensing causes power leakage from  $E$  to  $B$ - mode polarization, which acts as a contaminant in the search for gravitational induced  $B$ -modes on large angular scales. However, CMB lensing signal provides a unique observational probe of the large scale structure distribution. The lensing potential power spectrum has been reconstructed using observations of lensed CMB anisotropies from various CMB experiments. Its power spectrum contains a wealth of information about the late time structure formation of the universe, its expansion history, and in cross-correlation with other probes we can infer variety of astrophysical constraints as well.

## 2.4 Lensing reconstruction

As CMB photons travel from the last-scattering surface to us, their paths are deflected by the gravitational potential of matter. As explained earlier, these small coherent deflections are related to the gradient of the gravitational potential. They can be used to reconstruct the integrated gravitational potential along the line of sight, i.e., the lensing potential. Lensing correlates previously decoupled CMB temperature and polarization modes between different angular scales on the sky. This is a key property in searching for the lensing signal and reconstructing it. If the statistics of the unlensed CMB is known, it is possible to exploit the information contained in the four-point function of the lensed CMB to extract the lensing potential statistically. As we have discussed earlier, the main effects of lensing include introducing tiny deviations from Gaussianity in the CMB (when marginalized over realizations of the lenses) or statistical anisotropy (for a fixed distribution of the lenses). There are two main ways to detect the CMB lensing: one is to measure the smoothing of the acoustic peaks on small angular scales induced by lensing at the CMB power spectrum level (Reichardt *et al.* 2009; Keisler *et al.* 2011; Planck Collaboration *et al.* 2014b), while the second method involves measuring the mode-coupling induced in the CMB by lensing. Methods that directly reconstruct the deflection field or the lensing potential either employ a maximum likelihood approach (Hirata and Seljak 2003) or optimal quadratic estimators (Okamoto and Hu 2003). So far, all reconstructed lensing maps have employed the optimal quadratic estimator, which is derived under idealized observational conditions, i.e., the CMB and the lensing field being nearly perfect Gaussian field, with negligible mode-coupling induced by instrumental or foregrounds effect. Several papers have investigated the effect of several additional sources of mode-coupling, such as finite sky-coverage (Perotto, L. *et al.* 2010; Namikawa *et al.* 2013), higher-order mode-coupling induced by lensing itself (Kesden *et al.* 2003; Hanson *et al.* 2011), and foreground biases (Fantaye *et al.* 2012; Osborne *et al.* 2014).

Let us briefly review the optimal quadratic estimator in the flat-sky framework, which is based on the first order perturbative expansion, similar to Eqn. 2.20, but truncated at first order. The formally optimal (inverse-variance weighted lensing potential) estimator at lowest order in  $\phi$  has the following form

$$\bar{\phi}_L^{XY} = \int d^2\ell W_{\ell, \ell-L}^{XY} \bar{X}_\ell \bar{Y}_{\ell-L}^*, \quad (2.29)$$

where  $\bar{X}$  and  $\bar{Y}$  are the filtered T, E, or B CMB fields and  $W_{\ell, \ell-L}^{XY}$  is the weight function (unique for each XY pair, see Hu and Okamoto (2002) for the exact expression). This estimation technique amounts to taking a weighted sum of the covariance between  $\bar{X}_\ell$  and  $\bar{Y}_{\ell'}$  for all pairs of angular wavenumbers  $\ell$  and  $\ell'$  separated by  $\ell - \ell' = L$ . Covariance between  $\ell$  modes in  $\bar{X}$  and  $\ell'$  modes in  $\bar{Y}$  is imprinted by modes in the lensing potential  $\phi$  with angular wavenumber  $L$ . The input CMB multipoles used here are (Weiner) filtered to suppress modes which are dominated by noise and also to increase the sensitivity to lensing. In addition, the unlensed CMB power spectra appearing in the weight function are replaced with the lensed ones to cancel higher order biases (Hanson *et al.* 2011). Now, the lensing potential estimated with Eqn. 2.29 is a biased estimate of the true lensing potential  $\phi_L^{XY}$ :

$$\bar{\phi}_L^{XY} = \mathcal{R}_L^{XY} \phi_L^{XY}, \quad (2.30)$$

where  $\mathcal{R}_L^{XY}$  is the response function that normalizes the estimator. In practice, the response function is first calculated analytically, and then corrected perturbatively with simulations,  $\mathcal{R}_L^{XY} = \mathcal{R}_L^{XY, Analytic} \mathcal{R}_L^{XY, MC}$ . In the case of an isotropic filter, the response function is given by,

$$\mathcal{R}_L^{XY, Analytic} = \int d^2\ell W_{\ell, \ell-L}^{XY} W_{\ell, \ell-L}^{XY} \mathcal{F}_L^X \mathcal{F}_{\ell-L}^Y, \quad (2.31)$$

here  $\mathcal{F}_\ell^X = (C_\ell^{XX} + N_\ell^{XX})^{-1}$ . A fiducial cosmology is assumed to calculate both  $\mathcal{F}$  and  $W$  functions. Real systematic effects like coupling of modes at various angular scales due to masking and the inhomogeneous noise introduce spurious



signals that can mimic the effect of lensing. To circumvent these biases, a mean field (MF) correction term  $\bar{\phi}_{\mathbf{L}}^{XY, MF}$  which is estimated by averaging  $\bar{\phi}$  reconstructed from many input lensed CMB simulations, is removed from the estimated  $\bar{\phi}_{\mathbf{L}}^{XY}$ . Since the simulated lensing signal is uncorrelated from simulation to simulation, it averages to zero in this calculation; the common signal that remains after averaging is the MF bias. The final measure of the lensing potential is given by,

$$\hat{\phi}_{\mathbf{L}}^{XY} = \frac{1}{\mathcal{R}_{\mathbf{L}}^{XY}} (\bar{\phi}_{\mathbf{L}}^{XY} - \bar{\phi}_{\mathbf{L}}^{XY, MF}). \quad (2.32)$$

Finally, the different lensing estimators  $XY \in TT, EE, TB, EE, EB, ET, BT, BE$  are combined into a minimum variance estimate as

$$\hat{\phi}_{\mathbf{L}}^{MV} = \frac{1}{\mathcal{R}_{\mathbf{L}}^{MC}} \frac{\sum_{XY} \bar{\phi}_{\mathbf{L}}^{XY} - \bar{\phi}_{\mathbf{L}}^{XY, MF}}{\sum_{XY} \mathcal{R}_{\mathbf{L}}^{XY, Analytic}}. \quad (2.33)$$

The equation above is only a diagonal approximation of the minimum variance estimator. Maps and power spectra of the lensing potential are calculated from both the minimum variance and polarization only estimators.  $C_{\mathbf{L}}^{\hat{\phi}_{XY} \hat{\phi}^{MV}}$  is measured by forming cross- spectra of  $\hat{\phi}_{\mathbf{L}}^{XY}$  and  $\hat{\phi}_{\mathbf{L}}^{MV}$ . Although this estimate of  $C_{\ell}^{\phi\phi}$  has a minimal variance, it suffers from additive biases (Kesden *et al.* 2003) which must be subtracted to obtain an unbiased optimal estimate of lensing power spectra.

The amplitude of  $B$ -mode fluctuations is much smaller because the  $B$ -modes can only be generated by tensor fluctuations. Lensing generates  $B$ -modes at small angular scales, which are highly non-Gaussian. This is a key in searching for the lensing signal and reconstructing it. Here, in figure 2.5 shown are the power spectra of lensed CMB temperature and polarization anisotropies measured from various recent CMB experiments. We can see that the  $T$  and  $E$ -modes have been measured quite well. There is some scope for improvement at small scales or higher  $\ell$ -modes where lensing is the most important and  $B$ -modes are starting to be measured well, and the better we do in measuring lensed  $B$ -modes, the more we can hope to unearth the primordial  $B$ -mode signal. The lensing potential power spectrum

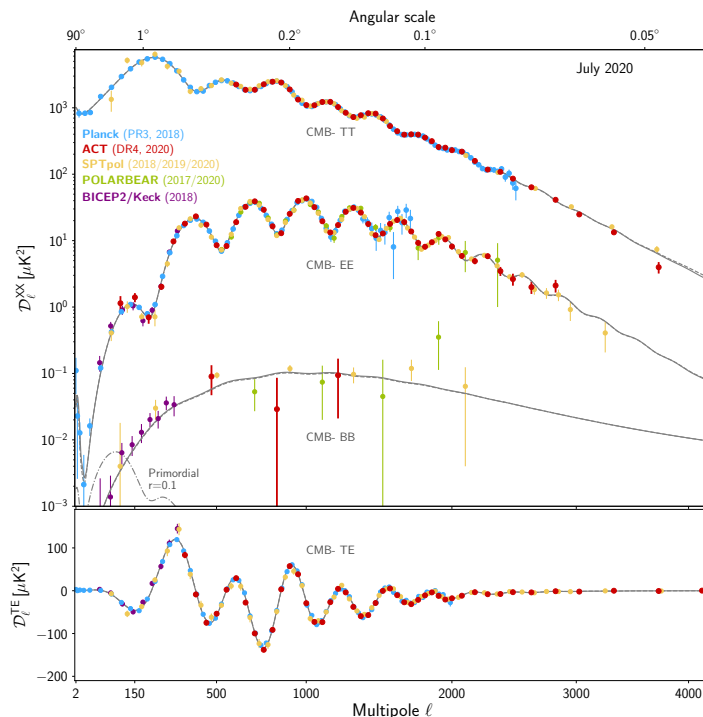


FIGURE 2.5: Recent measurements of the CMB temperature and polarization anisotropy power spectra from various CMB experiments. This figure has been taken from Choi *et al.* (2020).

has been reconstructed from many experiments. Its power spectrum contains a wealth of information about the late time structure formation of the universe, its expansion history, and cross-correlation with other probes; we can infer a variety of astrophysical constraints as well. How do we infer lensing potential power spectrum from data? It is all about searching for non-Gaussianity.

## 2.5 CMB lensing observations

In recent years, CMB lensing has entered the era of precision measurements. The first detections were made via cross-correlations with large-scale structures probed by galaxy surveys (Smith *et al.* 2007; Ho *et al.* 2008; Feng *et al.* 2012; Sherwin *et al.* 2012). The higher sensitivity and resolution, and low noise of recent CMB

instruments, such as the Atacama Cosmology Telescope (ACT), the South Pole Telescope (SPT), and PLANCK, have enabled an internal detection of lensing using CMB temperature data alone (Das *et al.* 2011; Keisler *et al.* 2011; van Engelen *et al.* 2012; Planck Collaboration *et al.* 2014a; Omori *et al.* 2017), polarization data only (Ade *et al.* 2014; BICEP2 Collaboration *et al.* 2016), and combinations of temperature and polarization data (Story *et al.* 2015; Planck Collaboration *et al.* 2020a; Wu *et al.* 2019). The most precise lensing amplitude measurement, at  $40\sigma$ , comes from Planck’s minimum-variance (MV) estimator that combines both temperature and polarization estimators; in that measurement, the temperature reconstruction contributes most of the signal-to-noise ratio (S/N). Figure 2.6 shows baseline Wiener-filtered minimum-variance lensing deflection estimate from the Planck temperature and polarization SMICA CMB maps. The characteristic scale of the lensing modes visible in the reconstruction is  $L \approx 60$ , corresponding to the peak of the deflection power spectrum, where the S/N is of  $\mathcal{O} \sim 1$ . Figure 2.7 presents a summary plot of (Planck Collaboration *et al.* 2020a) new minimum variance lensing potential band powers together with a compilation of other recent measurements, and the previous results from Planck Collaboration *et al.* (2016). Lensing amplitude  $\hat{A}$  measures how well the estimated lensing potential power spectrum (reconstructed from the lensed CMB data) agrees with the lensing potential obtained from the fiducial cosmological model, with  $\hat{A} = 1$  for  $C_\ell^{\phi\phi}$  equal to the best fit  $\Lambda$ CDM model to the Planck temperature and polarization power spectra and the reconstructed lensing power. Over the multipole range ( $8 < L < 2048$ ), the measured lensing amplitude  $\hat{A}$  is,  $\hat{A}_{8 \rightarrow 2048}^{MV} = 0.995 \pm 0.026$ .

Gravitational lensing has now emerged as a powerful observational probe in cosmology. CMB lensing probes both the geometry and the growth of large scale structure of the universe and as such, precise measurements of its power spectrum can break the geometrical degeneracy affecting the primary CMB (Stompor and Efstathiou 1999; Howlett *et al.* 2012; Planck Collaboration *et al.* 2020a) and

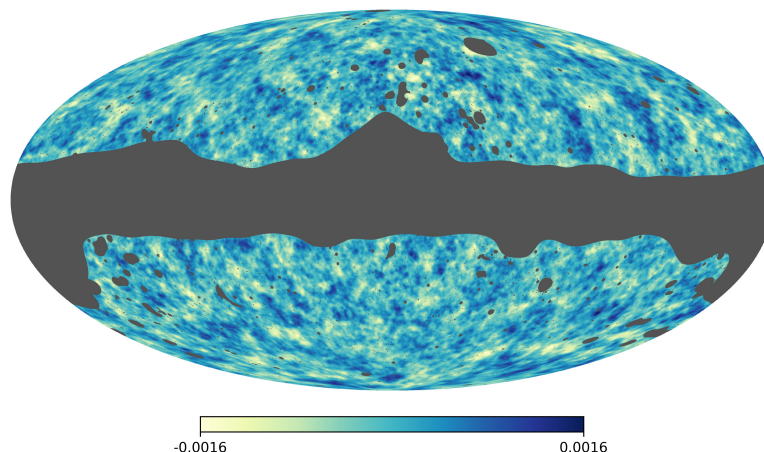


FIGURE 2.6: Mollweide projection in Galactic coordinates of the lensing-deflection reconstruction map from Planck Collaboration *et al.* (2020a) baseline minimum-variance (MV) analysis. Map represents the Wiener-filtered displacement-like scalar field with multipoles  $\hat{\alpha}_{LM}^{MV} = \sqrt{L(L+1)}\hat{\phi}_{LM}^{MV}$ , corresponding to the gradient mode (or  $E$ -mode) of the lensing deflection angle. Modes with  $L < 8$  have been filtered out.. This figure and caption has been taken from Planck Collaboration *et al.* (2020a).

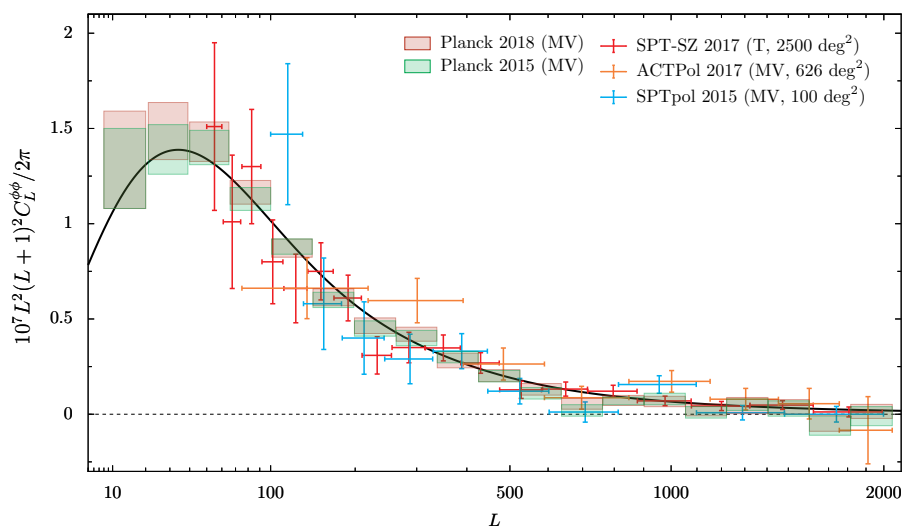


FIGURE 2.7: Planck 2018 lensing power-spectrum band powers (pink boxes) over the aggressive multipole range. The 2015 analysis band powers (green) were calculated assuming a slightly different fiducial model and have not been (linearly) corrected to the 2018 model. Also shown are recent measurements by the ACTPol (Sherwin *et al.* 2017), SPTpol (Story *et al.* 2015), and SPT-SZ (Simard *et al.* 2018) collaborations. The SPT-SZ measurement is not completely independent, since the SPT-SZ reconstruction also uses temperature data from Planck, but with subdominant weight over the smaller sky area used. The black line shows the lensing potential power spectrum for the  $\Lambda$ CDM best-fit parameters to the Planck 2018 likelihoods (Planck TT,TE,EE+lowE, which excludes the lensing reconstruction). This figure and caption has been taken from Planck Collaboration *et al.* (2020a).

tighten constraints on the sum of neutrino masses  $\sum m_\nu$  as well as on the amplitude of density fluctuations  $\sigma_8$  (Lesgourgues and Pastor 2006; Abazajian *et al.* 2015). Combination of galaxy and galaxy cluster strong lensing and the shear measurements from weak lensing of galaxies can also provide important constraints on the geometry of the Universe (Hand *et al.* 2015; Dark Energy Survey Collaboration *et al.* 2016; Hildebrandt *et al.* 2016; Omori *et al.* 2019).

Although such cross correlation studies between CMB and other data sets have been successful in improving constraints in cosmology, intriguingly, there is a modest level of discordance between the primary CMB power spectra from Planck and other cosmological probes within the  $\Lambda$ CDM model. For example, in the context of CMB lensing the amplitude of density fluctuations  $\sigma_8$  deduced from galaxy cluster counts and cosmic shear measurements is slightly lower than the value suggested by primary CMB Planck data (Hildebrandt *et al.* 2016; Hikage *et al.* 2019). Tensions within the Planck dataset are also emerging, for example the amount of lensing inferred from the smoothing of the acoustic peaks in the Planck CMB power spectra is larger than the one directly measured through the CMB lensing potential power spectrum (Planck Collaboration *et al.* 2020a). Now, the question is whether these tensions are due to some unaccounted systematics or they hint towards some new physics. To probe this question we can use measurements from different experiments which have uncorrelated systematics. Another way could be, to develop new statistical tools to analyse datasets than the traditionally used measures like hierarchy of correlations function or angular spectra. In this thesis we have employed recently introduced geometrical observables, Minkowski tensors to study the morphology of lensed CMB fields. These are the real space statistical tools which can be used to study the morphology and topology of cosmological random fields. In the next chapter, we will briefly review these statistics.

# Chapter 3

## Geometrical and Topological Observables for smooth random fields

### 3.1 Introduction

It is well known that statistical properties of Gaussian random fields can be studied entirely using their power spectrum or the two-point function: the latter being simply the lowest and first of an infinite hierarchy of correlation functions. The observed CMB data agree very well with Gaussian statistics at the precision level of currently available cosmological datasets. However, it is well established that most of the secondary anisotropies in CMB sourced by lensing or SZ-effect are not linear and produce non-Gaussian signatures. Also, it is well understood that a system evolving under gravitational instability becomes progressively more non-Gaussian, rendering the matter density field highly non-linear. Therefore, it is crucial to go

beyond two-point functions to understand the underlying complex physical processes fully. Most statistical analyses of CMB anisotropies are carried out using  $n$ -point functions in harmonic space, namely, the angular power spectrum, bispectrum, etc. Therefore, the need for going beyond the two-point function, such as in searches for non-Gaussian deviations, is served well by the next or next-to-next higher-order statistics. In some cases, such as when dealing with strongly non-Gaussian fields, to extract all statistical information, we need to calculate  $n$ -point functions to arbitrary order, which is not realistic for large cosmological datasets. It can be more profitable to employ real space statistical tools that can, in principle, encode all orders of  $n$ -point functions. In real space, the analysis of the rich geometrical and topological properties of excursion sets of smooth random fields provides a suite of statistical observables that can provide information that is complementary to Fourier or harmonic analysis. This chapter introduces such geometrical observables, Minkowski functionals (MFs) and Minkowski Tensors (MTs), to study the morphology and topology of two-dimensional random fields. In particular, we use these observables to quantify various morphological features and study physical phenomena like gravitational lensing of CMB fields, statistical isotropy of matter distribution inferred from CMB lensing. Our analysis of morphology of lensed CMB using MTs will be presented in later chapters.

## 3.2 Review of smooth random fields

In the following we give a review of smooth random fields defined on a manifold  $M$ , and their symmetry properties, namely, homogeneity and isotropy. The material covered here can be found in Adler (2010). Let us focus on two dimensional space  $M$ . Let us choose coordinates on  $M$  which we denote by  $\mathbf{x} = (x^1, x^2)$ . Let  $f(\mathbf{x})$  be a random variable at every point  $\mathbf{x} \in M$ , and whose probability distribution is given. The collection of random variables  $f(\mathbf{x})$  is called a random field on  $M$ .

Let the quantity  $C(\mathbf{x}, \mathbf{x}')$  be defined as the covariance between the random variables at  $\mathbf{x}$  and  $\mathbf{x}'$ , given by

$$C(\mathbf{x}, \mathbf{x}') = \left\langle (f(\mathbf{x}) - \mu_{\mathbf{x}})(f(\mathbf{x}') - \mu_{\mathbf{x}'}) \right\rangle, \quad (3.1)$$

where  $\mu_{\mathbf{x}}, \mu_{\mathbf{x}'}$  are the mean values of  $f$  at  $\mathbf{x}$  and  $\mathbf{x}'$ . The auto-covariance gives the variance of  $f$  at  $\mathbf{x}$ ,

$$C(\mathbf{x}, \mathbf{x}) = \sigma_{\mathbf{x}}^2. \quad (3.2)$$

*Homogeneity:* A random field is said to be homogeneous or stationary under a transformation  $\mathbf{x} \rightarrow \mathbf{x} + \mathbf{a}$ , if its covariance functions satisfies

$$C(\mathbf{x}, \mathbf{x}') = C(\mathbf{x} - \mathbf{x}'). \quad (3.3)$$

If  $f$  is homogeneous, then its mean is a constant function on  $R$ .

*Isotropy:* A field  $f$  is said to be isotropic if its covariance function is invariant under rotations, satisfying the condition

$$C(\mathbf{x}, \mathbf{x}') = C(|\mathbf{x} - \mathbf{x}'|). \quad (3.4)$$

So the covariance function depends only on the distance between the two points on  $M$ . Isotropic field is a special case of stationary or a homogeneous field.

*Derivatives of a random field:* If the covariance function is differentiable  $2k$  times, where  $k = 1, 2, \dots$  then the  $k^{\text{th}}$  derivative of the field exists at each point on  $M$ . If we are given that  $f$  is a homogeneous and isotropic field, then it follows that its derivatives are also homogeneous and isotropic fields.



*Ergodicity:* A homogeneous field is said to be ergodic if the ensemble expectation can be replaced by spatial average over a realization of the field.

$$\int dV P[f](\dots) \iff \frac{\int_M(\dots)}{\int_M}, \quad (3.5)$$

where  $dV$  is the infinitesimal volume element. This is an important property to assume in cosmology because we have one universe.

*Gaussian field:*  $f(\mathbf{x})$  is called a Gaussian field if the joint PDF of the random variables at  $k$  spatial locations, denoted by  $\mathcal{P}[f(\mathbf{x}_1), f(\mathbf{x}_2), \dots, f(\mathbf{x}_k)]$ , has the form

$$\mathcal{P}[f(\mathbf{x}_1), f(\mathbf{x}_2), \dots, f(\mathbf{x}_k)] = \frac{1}{N} \exp\left(-F^T C^{-1} F\right), \quad (3.6)$$

where  $F$  is the array given by

$$F \equiv (f(\mathbf{x}_1), f(\mathbf{x}_2), \dots, f(\mathbf{x}_k)) \quad (3.7)$$

$$C_{ij} = C(\mathbf{x}_i, \mathbf{x}_j), \quad (3.8)$$

$$N = \sqrt{(2\pi)^k \text{Det } C}, \quad (3.9)$$

with  $i, j = 1, \dots, k$ . If  $f$  is Gaussian then its partial derivatives are also Gaussian fields. The field and its derivatives at each point comprise a set of multivariate Gaussian random fields.

### 3.3 Minkowski functionals and Minkowski tensors for a single structure

We first define what we mean by a structure. Let  $R$  be a two-dimensional smooth manifold. For applications to cosmology fields we will consider the cases where  $R$  is either flat two-dimensional space  $\mathcal{R}^2$ , or the surface of the sphere  $\mathcal{S}^2$ . The

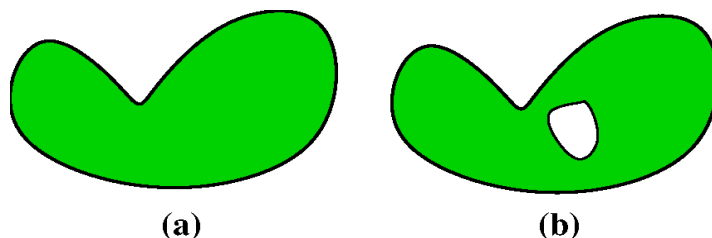


FIGURE 3.1: Examples of simply and doubly connected region. This figure demonstrates that a connected region or hole can be associated with a closed curve and hence count of structures is equivalent to count of closed curves.

word *structure* means a subset of  $R$  which is either a *connected region* or a *hole*. In figure 3.1 we show examples of connected regions and holes. Panel (a) shows a *simply* connected region. It has no hole inside it and has one closed curve as its boundary. Panel (b) shows a *doubly* connected region. It can be counted as one connected region and one hole. The boundary consists of two closed curves - one that encloses the connected region and the second encloses the hole. We can generalize further and identify each structure with one unique closed curve.

### 3.3.1 Minkowski functionals

Minkowski functionals (MFs) for a structure, or its associated curve  $C$ , on  $\mathcal{R}^2$  are defined as

$$V_0(\nu) = \int da, \quad (3.10)$$

$$V_1(\nu) = \frac{1}{4} \int_C ds, \quad (3.11)$$

$$V_2(\nu) = \frac{1}{2\pi} \int_C \kappa ds, \quad (3.12)$$

where  $da$  denote the infinitesimal area enclosed by the curve,  $ds$  be the infinitesimal arc length of the curve and  $\kappa$  the geodesic curvature of the curve.  $V_0$  is the area enclosed by the curve,  $V_1$  is the perimeter or the contour length and  $V_2$  is the Genus, that is equal to the difference between two Betti numbers,  $\beta_0$  and  $\beta_1$ .  $\beta_0$

is the number of connected regions while  $\beta_1$  is the number of disconnected regions (holes) within it. For CMB,  $\beta_0$  and  $\beta_1$  corresponds to the total number of hotspots and coldspots, respectively.

### 3.3.2 Minkowski tensors

The Minkowski tensors of rank (a,b) for a structure in a flat two-dimensional space are given by,

$$W_0^{a,0} = \int \vec{r}^a da, \quad (3.13)$$

$$W_1^{a,b} = \frac{1}{2} \int_C \vec{r}^a \otimes \hat{n}^b ds, \quad (3.14)$$

$$W_2^{a,b} = \frac{1}{2} \int_C \vec{r}^a \otimes \hat{n}^b \kappa ds, \quad (3.15)$$

where  $\vec{r}$  is the two dimensional position vector and  $\hat{n}$  is the unit normal to the curve. The tensor product of two vectors is defined to be the symmetric product  $(\vec{A} \otimes \vec{B}) = \frac{1}{2} (A_i B_j + A_j B_i)$ . The rank- zero MTs are standard scalar Minkowski functionals. The rank-1 MTs or vector counterparts of SMFs are translation covariant. For  $a + b = 2$ , we get total of seven rank-2 MTs:  $W_0^{2,0}$ ,  $W_1^{1,1}$ ,  $W_1^{2,0}$ ,  $W_1^{0,2}$ ,  $W_2^{1,1}$ ,  $W_2^{2,0}$ , and  $W_2^{0,2}$ . Out of these seven, we are interested in two of the MTs which are translationally invariant. They are,

$$W_2^{1,1} = \frac{1}{2} \int_C \vec{r} \otimes \hat{n} \kappa ds, \quad (3.16)$$

$$W_2^{0,2} = \frac{1}{2} \int_C \hat{n} \otimes \hat{n} \kappa ds. \quad (3.17)$$

$W_2^{1,1}$  (henceforth  $\mathcal{W}_1$ ) and  $W_2^{0,2}$  (henceforth  $\mathcal{W}_2$ ) are linearly independent and contains very useful additional information in comparison to scalar MFs as explained in the following subsections. These MTs can be generalised to curved manifolds. The notation in this section follows Chingangbam *et al.* (2017b). The contour

Minkowski tensor (henceforth CMT)  $\mathcal{W}_1$  and  $\mathcal{W}_2$  are defined for a smooth closed curve,  $C$ , on a general smooth two-dimensional manifold as,

$$\mathcal{W}_1 = \frac{1}{4} \int_C \hat{T} \otimes \hat{T} ds, \quad (3.18)$$

$$\mathcal{W}_2 = \frac{1}{2\pi} \int_C \hat{T} \otimes \hat{T} \kappa ds, \quad (3.19)$$

where  $ds$  is the infinitesimal arc length, and  $\hat{T}$  is the unit tangent vector at each point of the curve with the direction chosen to be one of the two possibilities, and  $\kappa$  denote the local curvature of the curve at particular point. The tensor product  $\otimes$  is defined as above. Both,  $\mathcal{W}_1$  and  $\mathcal{W}_2$  are  $2 \times 2$  matrix in two dimensions. These definitions are general and can be used for any smooth manifold with affine connection on it. The trace of  $\mathcal{W}_1$  and  $\mathcal{W}_2$  gives the scalar Minkowski functional,  $V_1$  and  $V_2$  respectively,

$$\text{Tr}(\mathcal{W}_1) = \frac{1}{4} \int_C ds = V_1, \quad (3.20)$$

$$\text{Tr}(\mathcal{W}_2) = \frac{1}{2\pi} \int_C \kappa ds = V_2. \quad (3.21)$$

where we have used  $|\hat{T}|^2 = 1$ .

We can express  $\mathcal{W}_1$  as

$$\mathcal{W}_1 = \begin{pmatrix} \tau + g_1 & g_2 \\ g_2 & \tau - g_1 \end{pmatrix}, \quad (3.22)$$

where

$$\tau = \frac{1}{2} \int_C ds, \quad (3.23)$$

$$g_1 = \frac{1}{2} \int_C (\hat{T}_1^2 - \hat{T}_2^2) ds, \quad (3.24)$$

$$g_2 = \int_C \hat{T}_1 \hat{T}_2 ds. \quad (3.25)$$

The pair  $(g_1, g_2)$  transforms as a rank-2 tensor under rotations. This can be expressed as

$$\begin{pmatrix} g_1 \\ g_2 \end{pmatrix} \rightarrow \begin{pmatrix} g'_1 \\ g'_2 \end{pmatrix} = \begin{pmatrix} \cos 2\theta & \sin 2\theta \\ -\sin 2\theta & \cos 2\theta \end{pmatrix} \begin{pmatrix} g_1 \\ g_2 \end{pmatrix}. \quad (3.26)$$

In a given coordinate system,  $g_1$  gives a measure of the anisotropic difference between the set of two components of the tangent vectors to the curve, while  $g_2$  gives a measure of how correlated the components of the tangent vectors are. Using  $g_1$  and  $g_2$  we can define the scalar  $g$  and the angle  $\varphi$  as

$$g \equiv \sqrt{g_1^2 + g_2^2}, \quad \varphi \equiv \tan^{-1} \left( \frac{g_1}{g_2} \right). \quad (3.27)$$

Here  $g$  represents the magnitude of the tensor while  $\varphi$  represents the direction of elongation or anisotropy with respect to the coordinate system.  $\tau$  and  $g$  are scalars under local rotations. Besides translation invariance  $\mathcal{W}_1$  is also invariant under parity transformations since all terms are quadratic. Moreover it transforms linearly under size scaling. The eigenvalues of  $\mathcal{W}_1$  are given by

$$\lambda_1 = \tau - g, \quad (3.28)$$

$$\lambda_2 = \tau + g. \quad (3.29)$$

Since  $\mathcal{W}_1$  is real and symmetric, the eigenvalues are real and positive. Further, we can show  $\tau \geq g$  and hence  $\lambda_1 < \lambda_2$ .

### 3.3.3 Alignment and shape parameters: $\alpha$ and $\beta$

The matrix  $\mathcal{W}_1$  carries information on the shape and alignment of structures. The eigenvalues  $\lambda_1$  and  $\lambda_2$  are real and positive; also, they are invariant under rotations.

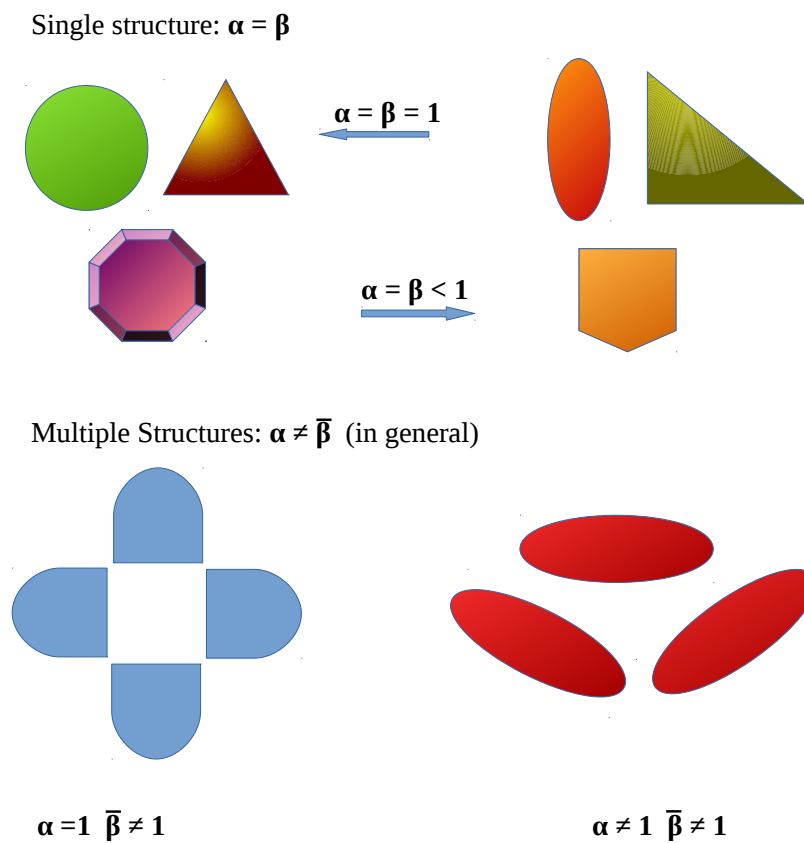


FIGURE 3.2:  $\alpha$  and  $\beta$  values for structures of different shapes and different spatial arrangement.

The *shape anisotropy parameter*  $\beta$  is defined to be the ratio of the eigenvalues,

$$\beta \equiv \frac{\lambda_1}{\lambda_2}. \tag{3.30}$$

$\beta$  lies between 0 and 1. It gives a measure of the intrinsic anisotropy of the curve. It is equal to one for a closed curve having  $m$ -fold symmetry with  $m \geq 3$ . Figure 3.2 shows examples of isotropic convex structures like circle, equilateral triangle, hexagon for which  $\beta = 1$ . Deviation of  $\beta$  from one indicates anisotropy of the curve like an ellipse, right triangle. Note that  $\beta$  is invariant under scaling the size of the curve. For distribution of many curves, let us denote  $\widetilde{\mathcal{W}}_1$  as the sum of  $\mathcal{W}_1$  over all structures, then we can define the *alignment parameter*,

$$\alpha \equiv \frac{\Lambda_1}{\Lambda_2}, \tag{3.31}$$

where  $\Lambda_1$  and  $\Lambda_2$  are the eigenvalues of  $\widetilde{\mathcal{W}}_1$  such that  $\Lambda_1 \leq \Lambda_2$ . By definition, we have  $0 \leq \alpha \leq 1$ .  $\alpha$  gives a measure of the orientation or the deviation from rotational symmetry in the distribution of curves. For randomly oriented structures with no preferred direction  $\alpha = 1$ , else  $\alpha$  lies between 0 and 1. For a single curve, we have  $\alpha = \beta$ . For many curves,  $\alpha$  gives the  $\beta$  value for the curve, resulting from translating and stacking all the curves such that their centroids overlap. While  $\bar{\beta}$  denotes the average of the  $\beta$  values of many curves.

### 3.4 Minkowski functionals and Minkowski tensors for smooth random fields.

Let us consider a smooth random field  $u$  defined on a two-dimensional space, for studying CMB we will consider random field on the surface of the unit sphere  $S^2$ , i.e.,  $u = u(\theta, \phi)$ . Consider all the points with the field value greater than or equal to some chosen threshold value ( $\nu$ ) of the field. This set is termed as the excursion set of the field at a particular threshold ( $\nu$ ), denoted by  $Q_\nu$ . The excursion set  $Q_\nu$  consists of the connected regions and holes. The boundaries, denoted by  $\partial Q_\nu$ , of these connected regions and holes form closed curves. These are the structures or the curves defined in section 3.3. Let  $d$  denote the infinitesimal area enclosed by a curve in an excursion set,  $ds$  be the infinitesimal arc length of the curve and  $\kappa$  the geodesic curvature of the curve, then the three scalar Minkowski functionals for the set  $Q_\nu \subseteq S^2$  are defined as follows,

$$V_0(\nu) = \int_{Q_\nu} da, \tag{3.32}$$

$$V_1(\nu) = \frac{1}{4} \int_{\partial Q_\nu} ds, \tag{3.33}$$

$$V_2(\nu) = \frac{1}{2\pi} \int_{\partial Q_\nu} \kappa ds. \tag{3.34}$$

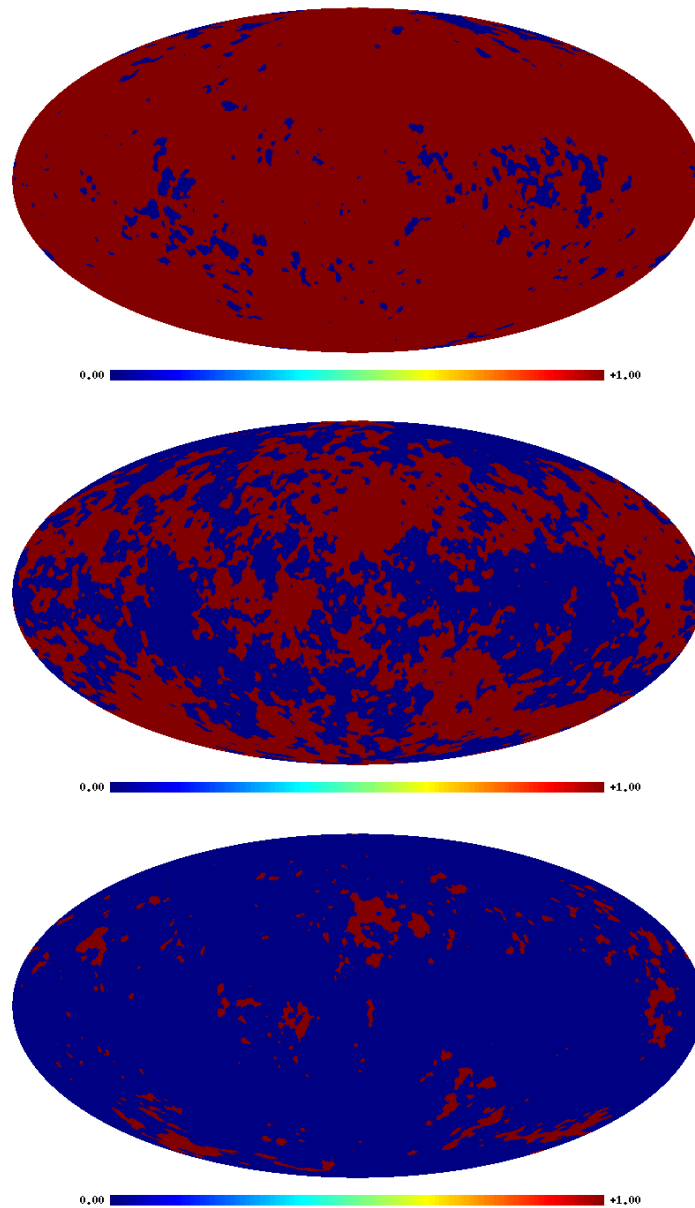


FIGURE 3.3: This figure shows the excursion set at three chosen  $\nu$  values of CMB temperature field on a 2-D surface of a sphere. Excursion set consists of red regions in the three panels. Red region in the top panel represents a multiply connected region with many holes. The threshold value for the three excursion sets (from left to right) are  $\nu = -1.5, 0, 1.5$ . Excursion sets vary systematically as a function of threshold, and their geometrical and topological properties are captured by MFs and MTs.



Each of these Minkowski functionals can be physically interpreted as:  $V_0$  is the area of the regions above the threshold, i.e., the total area of the excursion set,  $V_1$  is the perimeter of these regions, and  $V_2$  is the Genus, defined as the total number of connected components of the excursion above the threshold minus the total number of connected components below the threshold. The excursion set of a field will vary systematically with the field's threshold value depending on the field's statistical properties. The SMFs can capture these systematic variations, and thus they can be utilized to study properties of the field across different thresholds.

### 3.4.1 Analytical expressions for MFs of a Gaussian field

The SMFs and other geometrical characteristics of Gaussian random fields have been extensively studied in the literature. Analytical expressions for the average scalar Minkowski functionals of a Gaussian random field in arbitrary dimensions were derived by Tomita (1986). Consider  $u(\theta, \phi)$  to be a Gaussian random field then the analytic expression for the expectation value of the SMFs per unit area, in two-dimensional space, as a function of threshold  $\nu$  is given by,

$$V_0(\nu) = \frac{1}{2} \left[ 1 - \Theta \left( \frac{\nu}{\sqrt{2}} \right) \right], \quad (3.35)$$

$$V_1(\nu) = \frac{1}{8\sqrt{2}} \frac{\sigma_1}{\sigma_0} \exp \left( -\frac{\nu^2}{2} \right), \quad (3.36)$$

$$V_2(\nu) = \frac{1}{4\pi^{3/2}} \left( \frac{\sigma_1}{\sigma_0} \right)^2 \nu \exp(-\nu^2), \quad (3.37)$$

where,  $\Theta$  is the Gaussian error function given by  $\Theta(x) = \frac{2}{\sqrt{\pi}} \int_0^x dt \exp(-t^2)$ , and  $\sigma_1$  is the variance of the first derivative of the field.  $\sigma_0$  and  $\sigma_1$  can be calculated

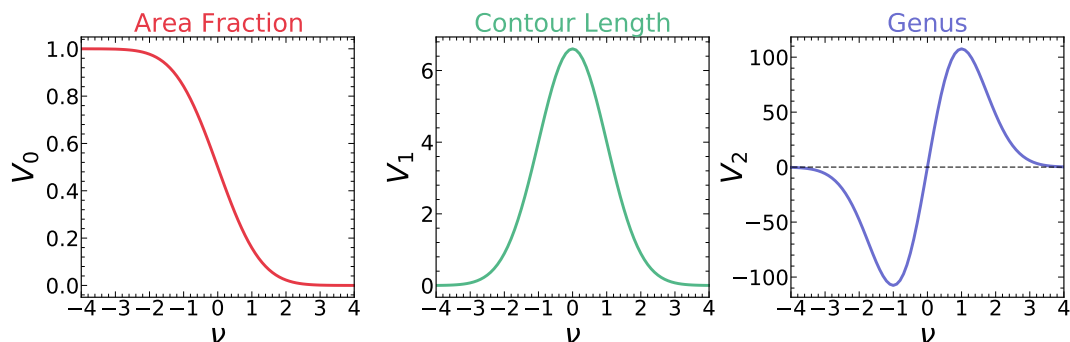


FIGURE 3.4: The three scalar Minkowski functionals for a Gaussian random field.

directly from the angular power spectrum,  $C_\ell$  as,

$$\sigma_0 = \sum_{\ell=1}^{\infty} (2\ell + 1) C_\ell, \quad (3.38)$$

$$\sigma_1 = \sum_{\ell=1}^{\infty} (2\ell + 1) C_\ell \frac{\ell(\ell + 1)}{2}. \quad (3.39)$$

### 3.4.2 Minkowski tensors of smooth random fields

We give here the definitions of the two Minkowski tensors  $\mathcal{W}_1$  and  $\mathcal{W}_2$  which were used for analysis in this thesis. Again consider a smooth random field  $u$  defined on unit sphere  $S^2$ , for which  $\mathcal{Q}_\nu$  denotes the excursion or level set at threshold value  $\nu$ . Let us assume the field  $u$  to be mean subtracted. Let the components of its first derivative be denoted by  $u_{;i}$ , where  $i = 1, 2$  and  $;$  represents the covariant derivative. As described in the previous section, the excursion set consists of a set of connected regions which may have one or more holes in them. The boundary of  $\mathcal{Q}_\nu$ , denoted by  $\partial\mathcal{Q}_\nu$ , consists of closed iso-field contours that enclose connected regions or holes. Let  $\widetilde{\mathcal{W}}_1$  and  $\widetilde{\mathcal{W}}_2$  denote the tensor sum over the  $\mathcal{W}_1$  and  $\mathcal{W}_2$  of all the curves for each  $\nu$ . They are given in terms of field values and its derivatives

as,

$$\left(\widetilde{\mathcal{W}}_1\right)_{ij} = \frac{1}{4} \int_{\partial \mathcal{Q}_\nu} ds \frac{1}{|\nabla u|^2} \mathcal{M}, \quad (3.40)$$

$$\left(\widetilde{\mathcal{W}}_2\right)_{ij} = \frac{1}{2\pi} \int_{\partial \mathcal{Q}_\nu} ds \frac{\kappa}{|\nabla u|^2} \mathcal{M}, \quad (3.41)$$

where geodesic curvature  $\kappa$  and matrix  $\mathcal{M}$  are given as

$$\mathcal{M} = \begin{pmatrix} u_{;2}^2 & -u_{;1}u_{;2} \\ -u_{;1}u_{;2} & u_{;1}^2 \end{pmatrix}, \quad \kappa = \frac{2u_{;1}u_{;2}u_{;12} - u_{;1}^2u_{;22} - u_{;2}^2u_{;11}}{|\nabla u|^3}. \quad (3.42)$$

These definitions follow from equations 3.18-3.19. The components of the tangent vector  $\hat{T}$  are given as,  $\hat{T}_i = \epsilon_{ij} \frac{u_{;j}}{|\nabla u|}$ , where  $\epsilon_{ij}$  is the antisymmetric tensor with  $\epsilon_{12} = 1$ .

## 3.5 Numerical computation of Minkowski functionals and Minkowski tensors

### 3.5.1 Minkowski functionals

We now describe a method to numerically compute scalar Minkowski functionals for smooth random fields defined above. This method was introduced by Schmalzing and Gorski (1998). The zeroth Minkowski functional  $V_0$ , i.e. the area, can be evaluated by integration of a Heaviside step function over the whole manifold  $R$  which is sphere ( $S^2$ ) in our case (for CMB),

$$V_0(\nu) = \int_{S^2} \Theta(u - \nu) da. \quad (3.43)$$

For computing  $V_1$  and  $V_2$ , line integrals in equations 3.33-3.34 can be converted to area integrals by inserting a delta function and appropriate jacobian as follow,

$$V_1(\nu) = \frac{1}{4} \int_{S^2} da \delta(u - \nu) |\nabla u|, \quad (3.44)$$

$$V_2(\nu) = \frac{1}{2\pi} \int_{S^2} da \delta(u - \nu) |\nabla u| \kappa. \quad (3.45)$$

All the three Minkowski functionals can be expressed as,

$$V_j(\nu) = \int_{S^2} da I_j, \quad (3.46)$$

with integrands  $I_j$  depending solely on the threshold  $\nu$ , field value  $u$ , its first and second order co-variant derivatives. In summary,

$$I_0 = \Theta(u - \nu), \quad (3.47)$$

$$I_1 = \frac{1}{4} \delta(u - \nu) \sqrt{u_{;1}^2 + u_{;2}^2}, \quad (3.48)$$

$$I_2 = \frac{1}{2\pi} \delta(u - \nu) \frac{2u_{;1}u_{;2}u_{;12} - u_{;1}^2u_{;22} - u_{;2}^2u_{;11}}{u_{;1}^2 + u_{;2}^2}. \quad (3.49)$$

In reality, we deal with a finite number of pixels or sample points in the excursion set. Hence, the delta function is replaced with a function of finite bin-width  $\Delta\nu$  as (Schmalzing and Gorski 1998; Chingangbam *et al.* 2017b),

$$\delta(u - \nu) = \begin{cases} \frac{1}{\Delta\nu}, & \text{if } u \in \left(\nu - \frac{\Delta\nu}{2}, \nu + \frac{\Delta\nu}{2}\right) \\ 0, & \text{otherwise,} \end{cases} \quad (3.50)$$

The bin width  $\Delta\nu$  is decided by the step size between the threshold values. And the integrals are replaced by summation over all the pixels as

$$V_j(\nu) = \frac{1}{N} \sum_{i=0}^{N_{\text{pix}}} w_i \mathcal{I}_j(x_i), \quad (3.51)$$

where  $x_i$  is the position vector of  $i^{\text{th}}$  pixel on the sphere, and  $\mathcal{I}_i$  are given by

equations 3.47-3.49. The variable  $w_i$  is the pixel weight which has value zero at pixels that are masked, and one otherwise.  $N$  is the count of all pixels having  $w_i = 1$ .

### 3.5.2 Discretization error for $V_1$ and $V_2$

To numerically compute scalar Minkowski functionals  $V_1$  and  $V_2$ , one needs to approximate  $\delta$  function with a appropriate discrete function of threshold bin width ( $\Delta\nu$ ). This introduces numerical error in the calculation of two SMFs. The residual error can be computed for a Gaussian random field as we know the exact analytical expression of the SMFs for the same. The numerically estimated SMFs can be written as  $V_j(\nu) = V_j^{an}(\nu) + R_j^{\Delta\nu}(\nu)$ , where  $R_j^{\Delta\nu}$  is the residual error due to discretization. Here, superscript  $\Delta\nu$  indicates the threshold bin size and the dependency of a residual error on it. The residual error  $R_j^{\Delta\nu}$ , is given by

$$R_j^{\Delta\nu}(\nu) = \frac{1}{\Delta\nu} \int_{\nu-\Delta\nu/2}^{\nu+\Delta\nu/2} ds V_j^{an}(s) - V_j^{an}(\nu). \quad (3.52)$$

Further exact expression of  $R_j^{\Delta\nu}(\nu)$  for  $V_1$  and  $V_2$  are given as

$$R_1^{\Delta\nu}(\nu) = \frac{1}{8} \sqrt{\frac{\pi}{2}} \frac{\sigma_1}{\sigma_0} \frac{1}{\Delta\nu} \left[ \operatorname{erf} \left( \frac{\nu + \Delta\nu/2}{\sqrt{2}\sigma_0} \right) - \operatorname{erf} \left( \frac{\nu - \Delta\nu/2}{\sqrt{2}\sigma_0} \right) \right] - V_1^{an}(\nu), \quad (3.53)$$

$$R_2^{\Delta\nu}(\nu) = \frac{1}{(2\pi)^{3/2}} \left( \frac{\sigma_1}{\sigma_0} \right)^2 \frac{1}{\Delta\nu} \left[ \exp \left( \frac{-(\nu - \Delta\nu/2)^2}{\sqrt{2}\sigma_0} \right) - \exp \left( \frac{-(\nu + \Delta\nu/2)^2}{\sqrt{2}\sigma_0} \right) \right] - V_2^{an}(\nu). \quad (3.54)$$

### 3.5.3 Methods for $\mathcal{W}_1$ and $\mathcal{W}_2$ numerical computation

#### 3.5.3.1 Method 1 - using field derivatives

In order to numerically calculate  $\widetilde{\mathcal{W}}_1$  and  $\widetilde{\mathcal{W}}_2$ , the line integral over the boundary of  $\mathcal{Q}_\nu$  in equations 3.40-3.41 can be transformed into an area integral by introducing a Jacobian to give

$$\widetilde{\mathcal{W}}_1 = \frac{1}{4} \int_{\mathcal{S}^2} da \delta(u - \nu) \frac{1}{|\nabla u|} \mathcal{M}, \quad (3.55)$$

$$\widetilde{\mathcal{W}}_2 = \frac{1}{2\pi} \int_{\mathcal{S}^2} da \delta(u - \nu) \frac{\kappa}{|\nabla u|} \mathcal{M}, \quad (3.56)$$

where  $da$  is the infinitesimal area element on  $\mathcal{S}^2$  and  $\delta(u - \nu)$  is the Dirac delta function. The  $\delta$ -function can be approximated as defined in equation 3.50. Other components of the two integrals have already been defined in the chapter above.

Equation 3.55 can be diagonalized, and the ratio of the eigenvalues give  $\alpha$ , by definition. *Note that we cannot obtain  $\beta$  from this method since it does not isolate individual curves at each  $\nu$ .*

When we work with finite resolution maps in the space of compact extent, such as the surface of a sphere, even for a field that is given to be statistically isotropic, we do not obtain  $\alpha$  to be precisely equal to one at each threshold even for a field which is given to be statistically isotropic.  $\alpha = 1$  is recovered only in the limit of the total perimeter tending to infinity. At threshold values close to zero, where the perimeter of  $\mathcal{Q}_\nu$  is the largest,  $\alpha$  is closest to one. For a random distribution of a few curves, the probability that they will be isotropically distributed is small. As a result, at higher  $|\nu|$ , the values of  $\alpha$  decrease from unity. Therefore, it is important to consider the threshold dependence of  $\alpha$  when searching for and interpreting results of statistical isotropy on finite resolution fields. This method has inherent numerical error coming from the discrete approximation of the delta function (Lim and Simon 2012). This numerical error has an analytic form and is a function of the threshold bin width and the smoothing scale. As shown in Chingangbam

*et al.* (2017b) the numerical error for the diagonal elements are similar in shape and amplitude for Gaussian isotropic fields (see figure 4 of the above reference). In order to make a rough estimate of the resulting error on  $\alpha$ , we express the diagonal elements of  $\overline{\mathcal{W}}_1$  as

$$\begin{aligned} (\overline{\mathcal{W}}_1)_{11}(\nu) &= a(\nu) + e(\nu) \\ (\overline{\mathcal{W}}_1)_{22}(\nu) &= b(\nu) + e(\nu), \end{aligned} \tag{3.57}$$

where  $a(\nu)$  and  $b(\nu)$  denote the true functional forms of the elements, and  $e(\nu)$  denotes the numerical error coming from the approximate  $\delta$  function. We have used  $a$  and  $b$  so as to keep the discussion general but they are expected to be comparable. The reason is that if  $u$  is a smooth isotropic field, then  $u_{;1}$  and  $u_{;2}$  are statistically identical fields and hence have the same variance. We have also used the same  $e(\nu)$  for the two matrix elements which means that we are ignoring possible statistical fluctuations between them. Further, we assume the off-diagonal element  $\overline{\mathcal{W}}_{12}$  to be zero. This is because the ensemble expectation of the correlation between  $u_{;1}$  and  $u_{;2}$  is expected to be zero since they are independent random fields. Then  $\alpha$  is given by

$$\alpha(\nu) \simeq \frac{(\overline{\mathcal{W}}_1)_{11}(\nu)}{(\overline{\mathcal{W}}_1)_{22}(\nu)} = \frac{a(\nu) + e(\nu)}{b(\nu) + e(\nu)} = \frac{a}{b} \left( 1 + \frac{e}{a} - \frac{e}{b} - \frac{e^2}{ab} + \mathcal{O}(e^3) \right), \tag{3.58}$$

where on the right hand side we have used  $|e/b| \ll 1$ . Since  $a \sim b$  the numerical error is of order  $\mathcal{O}(e^2)$ . Thus, this method of computation is well suited for applications where  $\alpha$  is used to extract physical information.

### 3.5.3.2 Method 2 - using identification of contours in pixel space

An alternative method of numerically reconstructing  $\mathcal{W}_1$  was adopted in Appleby *et al.* (2018a) (see also Ganesan and Chingangbam (2017)). In this section, we briefly review the approach.

The continuous field  $u$  is sampled on a uniformly spaced, two dimensional pixel grid

to generate a discrete function  $u_{ij}$ , where  $i, j$  denotes the  $i^{\text{th}}$ ,  $j^{\text{th}}$  pixel in the  $x_1, x_2$  coordinate space. For a given threshold  $\nu$ , we decompose the pixels as ‘inside’ the excursion set if  $u_{ij} > \nu$  and ‘outside’ if  $u_{ij} < \nu$ . We then apply the marching squares algorithm (Mantz *et al.* (2008); Lorensen and Cline (1987)) and linearly interpolate between any two adjacent ‘in’ and ‘out’ pixels to create a set of vertices at which  $u = \nu$ . Finally, these vertices are joined by line segments to create a boundary of constant threshold  $u = \nu$ . All topological quantities of interest can be deduced from the vertices and corresponding line segments that define the excursion set boundary, including the scalar and tensor Minkowski functionals.

In this discretized setup,  $\overline{\mathcal{W}}_1$  for the excursion set boundary  $\partial Q_\nu$  is approximated as

$$(\overline{\mathcal{W}}_1)_{ij} = \int_{\partial Q_\nu} \hat{e}_i \hat{e}_j = \sum_e |\vec{e}|^{-1} e_i e_j, \quad (3.59)$$

where  $\sum_e$  is the sum over all edges in the discretized boundary reconstruction and  $e_i$ ,  $|\vec{e}|$  are the length in the  $i^{\text{th}}$  direction, and total length, of an edge segment. This formalism of estimating  $\mathcal{W}_1$  for the polygonal structures in the excursion set is described in Schroder-Turk *et al.* (2010).

To construct  $\beta$  from a field, we must calculate  $\mathcal{W}_1$  for each individual connected component within the excursion set and also for every hole. To do so, we must not only assign each pixel  $u_{ij}$  as ‘in’ or ‘out’ of the excursion set, but also a unique identifier that informs which distinct connected region or hole the pixel belongs. This latter condition is achieved by using a simplified ‘friends-of-friends’ algorithm, assigning an initial pixel to an excursion set, then all adjacent pixels which satisfy  $u_{i'j'} > \nu$ . This is repeated until every ‘in’ pixel is assigned to an excursion set region. The procedure is then repeated for holes – regions outside the excursion set. Each edge segment to the excursion set boundary  $\vec{e}$  is associated with exactly one connected component, and one hole –  $\mathcal{W}_1$  is calculated for each sub-region as the sum over edge segments that define its boundary.

The principal source of error in using this method arises from the assumption that the field can be linearly interpolated between adjacent pixels. Critical points of a field are



intrinsically higher order quantities. Hence, the method will fail to accurately represent structures of size  $\sim \mathcal{O}(\Delta^2)$ , where  $\Delta$  is the resolution of the pixel grid. This issue is ameliorated by smoothing the field with scale  $R_G$ , and it was shown in Appleby *et al.* (2018a) that smoothing over five pixel lengths  $R_G > 5\Delta$  is sufficient to reduce the numerical error on the  $\mathcal{W}_1$  statistic to below 1% for threshold values in the range  $-4 < \nu < 4$ .

For calculating  $\beta$  for the CMB fields, we first project each hemisphere of the CMB maps onto a plane and then implement the above algorithm. We choose stereographic projection, as done in Ganesan and Chingangbam (2017) because it is a conformal mapping that preserves angles and shape of structures. However, it is essential to note that the sizes of structures are not preserved. The distortion is most prominent towards the outer edge of the hemisphere. Moreover, the distortion decreases as we probe smaller structures. A discussion of the effects of the stereographic projection on the structures can be found in Ganesan and Chingangbam (2017).

In the subsequent chapters, we do not attempt to correct the numerical error arising from this projection. We proceed to use this method of calculating  $\beta$  with the anticipation that the error will cancel out when we compare  $\beta$  for fields with a fixed realization seed but with varying physical input.

# Chapter 4

## Morphology of CMB fields-effect of weak gravitational lensing

### 4.1 Introduction

CMB photons have been deflected multiple times by gravitational potential wells they encounter along their path from the last scattering surface to an observer. The rms of the deflection angle in different sky directions can be estimated to be of the order of a few arcminutes. Lensing alters the statistical properties of primary CMB anisotropies in addition to adding power at small scales. It introduces non-Gaussianity, which can be probed using a four-point function as demonstrated in Bernardeau (1997). However, it is not necessarily the best indicator in terms of signal-to-noise ratio for an actual experiment. Weak gravitational lensing also causes shearing and magnification of the hotspots and coldspots of the CMB fields. By understanding the resulting distortion patterns, one may then, in principle, infer the integrated effect of the interaction between the CMB and the intervening matter distribution along each line of sight.

The morphological information encoded in the Minkowski tensors makes them well suited to probe the size and shape distortions of the structures of the CMB. Our work is similar in spirit to Bernardeau (1998) where the author analyzed the distortion induced by weak lensing on the ellipticity of hotspots and coldspots of CMB temperature. The definition of the ellipticity parameter used in Bernardeau (1998) was derived from the Hessian matrix of the field. The lensing effect was quantified by comparing the probability distribution function (PDF) of the ellipticity parameter of the lensed field and the unlensed field. It was found that the lensing broadens the ellipticity PDF, which implies that the structures, especially the peaks (or the extrema) in the field, are elongated due to the lens effect. We study the morphology of the cosmic microwave background temperature and polarization fields using the shape and alignment parameters,  $\beta$  and  $\alpha$ , that are constructed from the contour Minkowski tensor. The primary goal of this work is to understand the effect of weak gravitational lensing on the morphology of the CMB fields. In order to isolate different physical effects that can be potentially confused with the effect of lensing, we first study the effect of varying the cosmology on  $\alpha$  and  $\beta$  and show that they are relatively insensitive to variation of cosmological parameters. Next, we analyze the signatures of hemispherical anisotropy and show that such anisotropy in  $\alpha$  gets washed out at small angular scales and becomes pronounced only at large angular scales. For  $\beta$ , we find characteristic distortions which vary with the field threshold. We then study the effect of weak gravitational lensing using simulations of lensed temperature and  $E$  and  $B$  modes. We quantify the distortion induced in the fields across different angular scales. We find that lensing makes structures of all fields increasingly more anisotropic as we probe down to smaller scales. We find distinct behavior of morphological distortions as a function of the threshold for the different fields. The effect is small for temperature and  $E$  mode, while it is significantly large for  $B$  mode. Further, we find that lensing does not induce statistical anisotropy, as expected from the isotropic distribution of large scale structures of matter. We expect that the results obtained in this work will provide insights into the reconstruction of the lensing potential.

This chapter is organized as follows. In section 4.2.1 we show  $\alpha$  and  $\beta$  for Gaussian isotropic maps of CMB temperature and  $E$ - and  $B$ - modes. Then in section 4.2.2 we discuss their sensitivity to variation of cosmological parameters. Further, we investigate the effect of hemispherical anisotropy on  $\alpha$  and  $\beta$  in section 4.2.3. In section 4.3 we

give a brief overview of the method of simulation of lensed CMB maps using `LENSPIX`. Finally, we present our results for unlensed and lensed CMB fields and discuss the effect of lensing on the morphology of the fields in section 4.3.2. We end with a discussion of our results in section 4.4.

## 4.2 $\alpha$ and $\beta$ for CMB fields

We employ the contour Minkowski tensor ( $\mathcal{W}_1$ ) (defined in Chapter 3), which is one of the translation invariant Minkowski tensors, to capture the distortions in the alignment and anisotropy induced by lensing on the structures in the CMB temperature and polarization fields. Shape parameters  $\alpha$  and  $\beta$ , obtained from CMT, encapsulates the information about the statistical isotropy of the field and anisotropy of the structures in the field, respectively. The threshold dependence of  $\alpha$  and  $\beta$  for CMB temperature and  $E$  mode were previously studied in Ganesan and Chingambam (2017); Joby *et al.* (2019). Here we include  $B$  mode in our analysis and discuss the broad features of  $\alpha$  and  $\beta$  for the three fields for the standard  $\Lambda$ CDM cosmology with assumed Gaussianity and isotropy. We also discuss the dependence of their functional forms on the smoothing scale. In subsequent sections, we will use the symbol  $T$  to refer to CMB temperature maps. For the calculation of  $\alpha$  in this section and in section 4.3 we use method 1 described in section 3.5.3.1. For calculating  $\beta$  we use the method 2 described in section 3.5.3.2. All maps in this section are generated using `HEALPIX` (Górski *et al.* (2005)<sup>\*</sup>) and `CAMB` (Lewis *et al.* (2000)<sup>†</sup>). All error bars shown in this paper are the sample variance obtained from the number of maps of each field used. For  $\alpha$ , error bars are calculated using 500 simulations each of unlensed and lensed fields. The calculation of  $\beta$  is much more computationally intensive. Hence we use 200 simulations. We consider an ideal case ignoring contamination from instrumental noise, foreground emissions, and other effects for our study.

---

<sup>\*</sup><http://healpix.sourceforge.net/>

<sup>†</sup><https://camb.info/>

### 4.2.1 $\alpha$ and $\beta$ for Gaussian isotropic fields in $\Lambda$ CDM cosmology

In order to first have a visual and intuitive understanding of the number of structures and associated contour length for  $T, E, B$  fields, for the same values of  $\Lambda$ CDM parameters, and same smoothing angle  $\text{FWHM}=60'$ , we show one map of each field in figure 4.1. We can see that  $E$ -mode fluctuates the most on smaller scales, thus exhibiting a higher number of structures (hotspots and coldspots) than  $B$ -mode, which fluctuates the least. Since the value of  $\alpha$  is positively correlated with the total perimeter length, we can anticipate that  $\alpha$  will be highest for  $E$ -mode and lowest for  $B$ -mode, at all threshold values.

The plots of  $\alpha$  versus threshold,  $\nu$ , for simulated Gaussian isotropic CMB fields are shown in the top left panel of figure 4.2, for the same values of  $\Lambda$ CDM parameters, and same smoothing angle  $\text{FWHM}=20'$ . The plots are average over 500 realizations. We can see that  $\alpha$  for all three fields are symmetric about  $\nu = 0$ .  $E$ -mode has the largest values while  $B$ -mode is the smallest, in agreement with our expectation from the structure of the fields. Here, the value of the tensor-to-scalar ratio is  $r = 0.1$ . Note that change of  $r$  will not change the result for  $\alpha$  due to the fact that it scales only the field values by the same factor at all pixels, and we use normalized fields  $u$  for our calculations. Further, from the bottom left panel showing  $\alpha$  at  $\nu = 0$  as a function of the smoothing scale, we see that  $\alpha$  vary monotonically (almost linearly) with smoothing scale, while the slopes visually appear to be slightly different for the three fields. To quantify it we calculate the slopes. Their values and  $1\text{-}\sigma$  sample variance errors are obtained to be:

- $T$ :  $[-1.05 \pm (-0.23)] \times 10^{-4}$
- $E$ :  $[-0.92 \pm (-0.12)] \times 10^{-4}$
- $B$ :  $[-1.16 \pm (-0.11)] \times 10^{-4}$

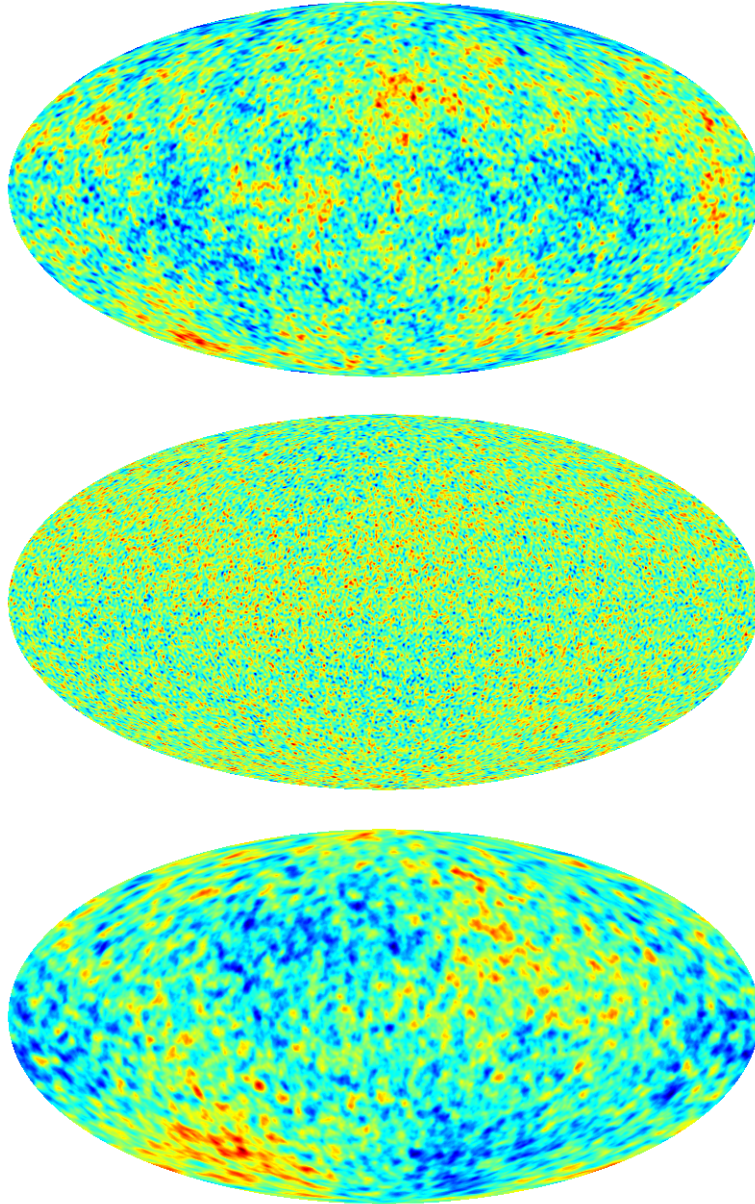


FIGURE 4.1: Maps of unlensed  $T$  (left),  $E$  (middle), and  $B$  (right) with tensor-to-scalar ratio  $r = 0.1$ . All maps are smoothed with  $\text{FWHM}=1^\circ$ . We have not put the colour scale since we wish to only draw visual attention to the fact that  $E$  mode has the highest number of structures per unit area, while  $B$  mode has the lowest. As a consequence  $\alpha$  is expected to be largest for  $E$  mode and lowest for  $B$  mode, at all threshold values. This expectation is corroborated by the top left panel of figure 4.2.

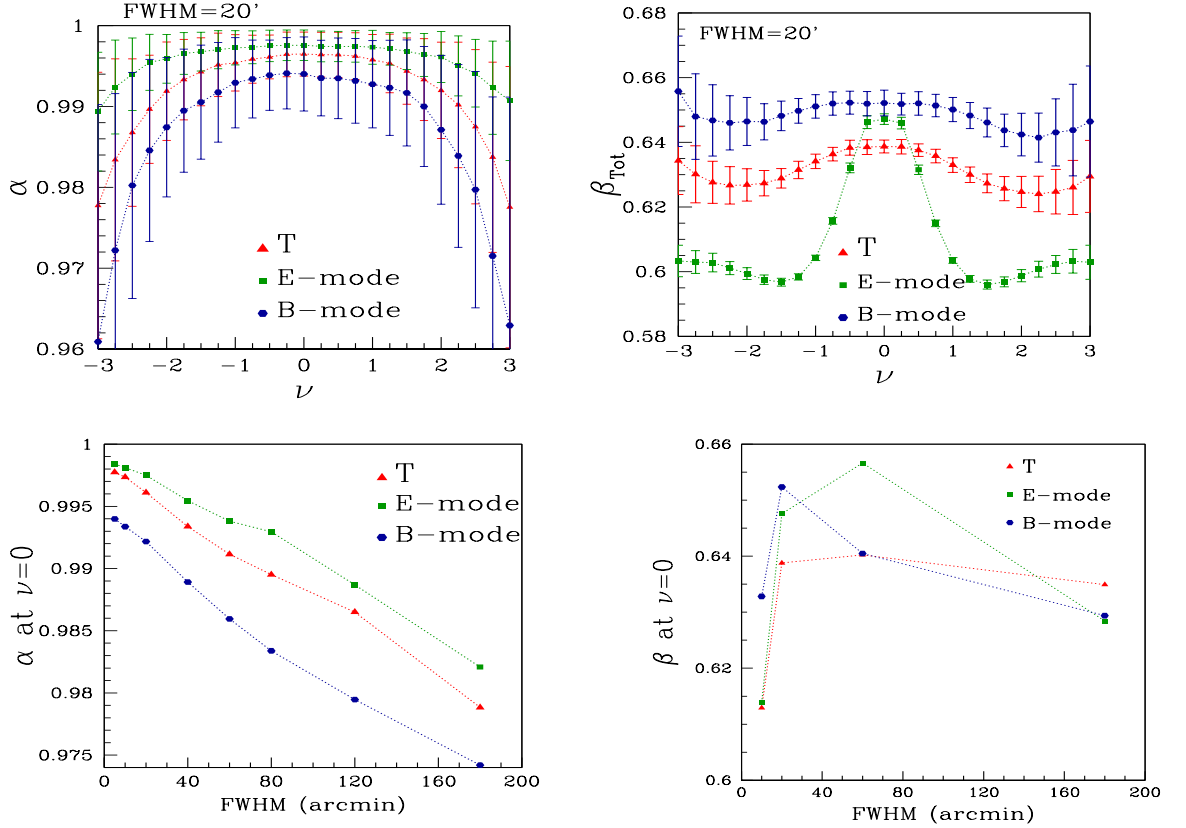


FIGURE 4.2: *Top left:*  $\alpha$  versus  $\nu$  for unlensed  $T$ ,  $E$  and  $B$  fields for the same smoothing angle  $\text{FWHM}=20'$ . *Bottom left:* Variation of  $\alpha$  at  $\nu=0$  as a function of the smoothing angle. Both the plots are average over 500 maps. *Top right:*  $\beta$  versus  $\nu$  for  $T$ ,  $E$  and  $B$  fields same smoothing scale as for  $\alpha$ . *Bottom right:* Variation of  $\beta$  at  $\nu=0$  as a function of the smoothing angle. The plots for  $\beta$  are average over 200 maps.

$B$ -mode has the steepest slope while  $E$ -mode has the shallowest. However, within the errors, the slopes for the three fields are comparable. The plots of  $\beta$  versus  $\nu$  for the same simulated maps and smoothing scale as for  $\alpha$  are shown in the top right panel of figure 4.2. Note that the  $\beta$  values shown here are the average over all the structures identified at each  $\nu$ . These plots are average over 200 realizations<sup>‡</sup>.  $\beta$  for all three fields are symmetric about  $\nu=0$ . The shapes are quite different.  $E$ -mode exhibits a relatively large variation of  $\beta$  across the threshold range, while the structures of  $B$ -mode are found to be the most isotropic across the entire threshold range. Again, by the same argument as  $\alpha$ ,  $\beta$  for  $B$ -mode will not change with  $r$ . The bottom right panel shows  $\beta$  at  $\nu=0$  as a function of the smoothing scale. We find that  $\beta$  does not show monotonic dependence

<sup>‡</sup>We use only 200 maps and not 500 as done for  $\alpha$  because the calculation of  $\beta$  is much more computationally expensive.

on smoothing scale as  $\alpha$ . We will further explore the dependence of the shape of  $\beta$  versus  $\nu$  on the smoothing scale in section 4.3.2.2.

## 4.2.2 Sensitivity of $\alpha$ and $\beta$ to variation of cosmological parameters

To cleanly isolate the effect of weak gravitational lensing on the morphology of the CMB, as encoded in  $\alpha$  and  $\beta$ , it is important first to understand the effects of various physical parameters which can be potentially confused with lensing. The effects of instrumental noise and residual foreground contamination were studied in Joby *et al.* (2019). For Gaussian fields, the system's physical properties, or in the context of cosmology, the cosmological parameters, enter the scalar/tensorial Minkowski Functionals in the amplitudes and are independent of the threshold dependence. The statistics of interest here,  $\alpha$  and  $\beta$  are ratios of eigenvalues which are non-linear functions of the matrix elements of  $\widetilde{\mathcal{W}}_1$ . For  $\alpha$ , it is reasonable to expect that the dependence on cosmology will 'mostly' cancel out, leaving behind a weak dependence arising from the non-linear terms of the eigenvalues. However, for  $\beta$ , it is not clear what to expect since it measures the anisotropy of individual structures.

We have computed  $\alpha$  and  $\beta$ , for unlensed  $T$ ,  $E$  and  $B$ , for different sets of cosmological parameters. We find that  $\alpha$  is relatively insensitive to variation of cosmological parameters, as anticipated above.  $\beta$ , on the other hand, is found to have characteristic dependence on  $\nu$  for varying cosmological parameters.

In order to test the sensitivity of  $\alpha$  and  $\beta$  to cosmology, we consider three different sets of cosmological parameters, in addition to the *fiducial*  $\Lambda$ CDM model. The value of the parameters for the models considered is given in Table 4.1. Model 1 has 95% cold dark matter and 5% baryons, keeping  $n_s$  the same as the fiducial model. Models 2 and 3 have different values of  $n_s$  while the matter density fractions are the same as the fiducial model. We assume a flat universe for all the models under consideration. We have chosen



Fiducial model	$\Omega_{\text{cdm}} = 0.228,$	$\Omega_{\text{b}} = 0.046,$	$\Omega_{\Lambda} = 0.726,$	$n_s = 0.960$
Model 1	$\Omega_{\text{cdm}} = 0.950,$	$\Omega_{\text{b}} = 0.050,$	$\Omega_{\Lambda} = 0.0,$	$n_s = 0.960$
Model 2	$\Omega_{\text{cdm}} = 0.228,$	$\Omega_{\text{b}} = 0.046,$	$\Omega_{\Lambda} = 0.726,$	$n_s = 0.50$
Model 3	$\Omega_{\text{cdm}} = 0.228$	$\Omega_{\text{b}} = 0.046,$	$\Omega_{\Lambda} = 0.726,$	$n_s = 0.30$

TABLE 4.1: Models with different values of cosmological parameters for which we compute  $\alpha$ . The input for the amplitude of primordial power spectrum and reionization history is the same in all the models. We assume curvature parameter,  $\Omega_k$ , is zero for all models. All models other than the fiducial one have unrealistic parameter values so as to magnify their effect in  $\alpha$  and  $\beta$ .

models with unrealistic parameters values far off from the fiducial model to exaggerate the effect on  $\alpha$  and  $\beta$ .

Let us denote the difference of  $\alpha$  between each non-standard model (superscript ‘mod’) and fiducial model (superscript ‘fid’) by

$$\Delta\alpha^{\text{mod}} \equiv \alpha^{\text{mod}} - \alpha^{\text{fid}}. \quad (4.1)$$

Then we normalize this quantity by the value of  $\alpha^{\text{fid}}$  at  $\nu = 0$ . The left column of figure 4.3 shows plots for normalized  $\Delta\alpha^{\text{mod}}$  for  $T$  and  $E$  and  $B$  modes. For  $T$  and  $E$  upper panels correspond to variation of matter content while lower panels correspond to variation of  $n_s$ . For  $B$ , we only vary the matter content and fix the tensor spectral index to be one. All plots are average over 500 realizations, and the error bars are the corresponding sample variance. The  $y$ -axis scales are the same for all plots.

*Effect of varying matter density fractions on  $\alpha$ :* We find that  $\Delta\alpha^{\text{mod}}$  for  $T$  and  $E$  are negligible, in agreement with our expectation. For  $B$ ,  $\Delta\alpha^{\text{mod}}$  is small but negative. This can be explained by the fact that the absence of dark energy decreases the luminosity distance to the last scattering surface, resulting in fewer structures per unit solid angle. Since the same reasoning applies to  $T$  and  $E$ , a similar negative value should also be

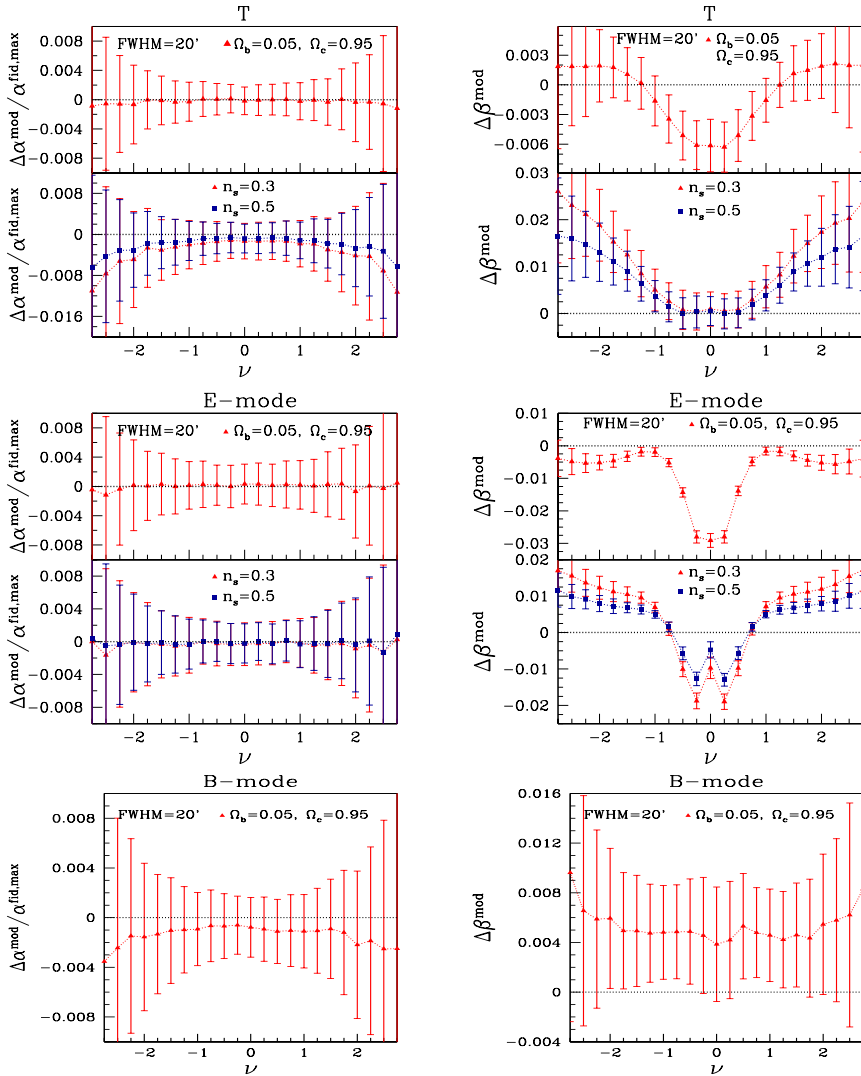


FIGURE 4.3: Deviations of  $\alpha$  (left column) and  $\beta$  (right column) for different cosmological models (listed in Table 4.1) from the ‘fiducial’  $\Lambda$ CDM model, for  $T$  (top),  $E$  (middle) and  $B$  mode (bottom) fields. The smoothing scale used is  $\text{FWHM}=20'$ . The upper panels in each plot show the effect of varying the matter density fraction, while the lower panels show the effect of varying  $n_s$ . For  $B$ -mode there is only one panel since we have fixed the tensor spectral index to be one. We have assumed a flat universe for all the cases.

obtained. However, due to the relatively larger number of structures of these two fields, the effect is not pronounced. We can safely assume that  $\alpha$  is insensitive to cosmology for a realistic range of matter fractions within PLANCK constraints.

*Effect of varying  $n_s$  on  $\alpha$ :* Lower values of  $n_s$  leads to reduced power in the primordial power spectrum for modes  $k > k_0$ , where  $k_0$  is the pivot scale which is chosen by CAMB to be  $0.05 \text{ Mpc}^{-1}$ . This implies a fewer number of structures on small-length scales. This is the reason why we obtain  $\Delta\alpha^{\text{mod}}$  negative, shown in the lower panels of the plots for  $T$  and  $E$  mode where smoothing scale  $\text{FWHM}=20'$  is sufficiently small scale. Again, as in the case of variation of matter fractions, for a realistic range of  $n_s$  within PLANCK constraints, the variation on  $\alpha$  is minimal, and we can safely ignore it.

Next we discuss the effect of cosmology on  $\beta$ . Let us denote

$$\Delta\beta^{\text{mod}} \equiv \beta^{\text{mod}} - \beta^{\text{fid}}, \quad (4.2)$$

where the superscripts have the same meaning as in the case of  $\alpha$ .

The right column of figure 4.3 shows plots for  $\Delta\beta^{\text{mod}}$  for  $T$  and  $E$  and  $B$  modes. For  $T$  and  $E$  upper panels correspond to variation of matter content while lower panels correspond to variation of  $n_s$ . Again, for  $B$ , we only vary the matter content and fix the tensor spectral index to be one. All plots are average over 300 realizations, and the error bars are the corresponding sample variance. Note that we have used different  $y$ -axis scales for the different models for the three fields. We find that  $\Delta\beta^{\text{mod}}$  has distinct shapes as the function of  $\nu$  for the different fields. For understanding this behavior, it is useful to remind ourselves that structures at different  $\nu$  correspond to different scales of clumpiness or emptiness. The distinct shapes of  $\Delta\beta^{\text{mod}}$  inform us that the anisotropy at different  $\nu$  is affected differently by variations in matter fractions. A comparison of the deviation amplitude for the three fields shows that  $E$ -mode has the highest level of deviations. These findings can be potentially helpful in inferring the properties of the universe.

### 4.2.3 Sensitivity of $\alpha$ and $\beta$ to Hemispherical anisotropy

We next consider the case of an anisotropic CMB temperature field modeled as

$$\tilde{T}(\hat{n}) = T^0(\hat{n}) \left( 1 + A \hat{k} \cdot \hat{n} \right), \quad (4.3)$$

$\hat{n}$  is the pixel direction,  $\hat{k}$  is the direction of anisotropy, and  $A$  is the amplitude of the anisotropy.  $T^0$  is the isotropic part of the field. This is the so-called dipolar modulation model of hemispherical anisotropy in the CMB described in Eriksen *et al.* (2004). Hemispherical power asymmetry implies that power extracted from two different hemispheres shows significant differences from one another. The significance of anisotropy is found to be  $3\sigma$  with the axis of maximum asymmetry having  $(\theta, \phi)$  pointing towards  $(115^\circ, 227^\circ)$  in galactic coordinates.

We have computed  $\alpha$  and  $\beta$  for different values of  $A$  and different smoothing scales. We find that  $\alpha$  is insensitive to it at small smoothing scales, and the input hemispherical anisotropy becomes noticeable in the threshold dependence of  $\alpha$  as we increase the smoothing scale.  $\beta$ , on the other hand, is found to have characteristic dependence on  $\nu$ .

To study the effect of hemispherical anisotropy, we calculate the differences  $\Delta\alpha^A \equiv \alpha^A - \alpha^I$  and  $\Delta\beta^A \equiv \beta^A - \beta^I$ , where the suffix A stands for the anisotropic case and I denotes the isotropic case. In the left panel of figure 4.4 we show  $\Delta\alpha^A$ , normalized by the value of  $\alpha^I$  at  $\nu = 0$ , for different smoothing scales, and for two values of the anisotropy strength,  $A = 0.1$  (upper panel) and  $A = 0.5$  (lower panel). The plots are average over 500 realizations of CMB maps. As expected,  $\Delta\alpha^A$  is larger for the greater value of the anisotropy strength parameter, i.e.,  $A$ . We observe that the effect of hemispherical anisotropy gets washed out at high resolution (small smoothing scale). This is because, at high resolution, the number of structures is very high. The effect of the anisotropy becomes noticeable at lower resolution. It is interesting to note that  $\Delta\alpha^A$  remains symmetric and that the difference is most pronounced at roughly  $|\nu| \sim 1$ .

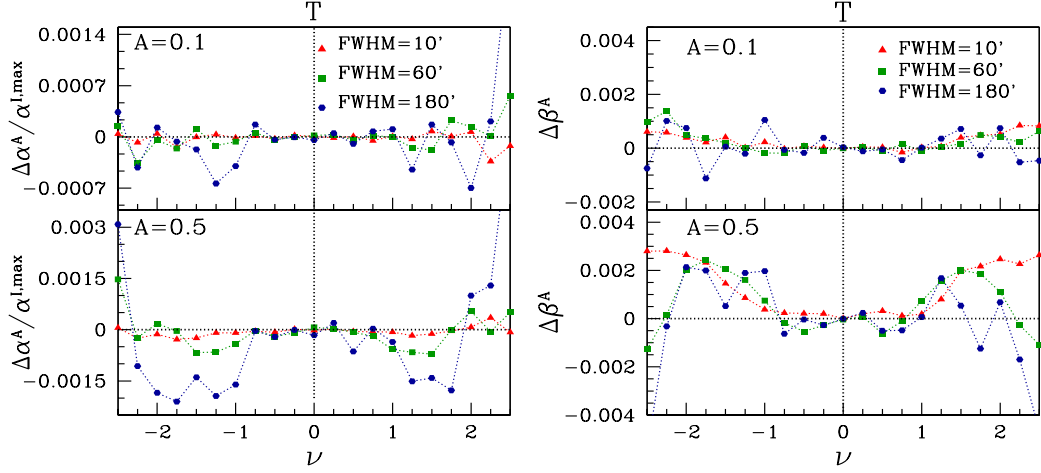


FIGURE 4.4: *Left:*  $\Delta\alpha^A$  for temperature field with input hemispherical anisotropy corresponding to  $A = 0.1$  and  $0.5$ , for three different smoothing scales at FWHM=10', 60' and 180'. All plots are average over 500 maps. We can see that the deviation in  $\alpha$  becomes distinguishable as we increase the smoothing scale. *Right:*  $\Delta\beta^A$  for the same fields, values of  $A$ , and smoothing scales as for  $\alpha$ . We have not added error bars since they are roughly one order of magnitude larger than the mean values, and hence they make the mean values difficult to discern visually.

The right panel of figure 4.4 shows  $\Delta\beta^A$  for the same smoothing scales and anisotropy strengths as for  $\alpha$ . The plots are average over 300 maps. Again as expected,  $\Delta\beta^A$  is larger for larger  $A$  value. We observe that  $\Delta\beta^A$  has roughly the same shape and amplitude across the threshold range  $-2.5 < \nu < 2.5$  for all smoothing scales. The positive values of  $\Delta\beta^A$  across this threshold range indicate that the structures are more anisotropic as a consequence of the anisotropy term in equation 4.3. The level of anisotropy is larger towards larger  $|\nu|$  albeit with larger error bars. Moreover, the statistical fluctuation increases for larger FWHM because the number of structures and corresponding total perimeter decreases with increasing FWHM. It is again interesting to note that  $\Delta\beta^A$  is symmetric. Our findings in this subsection suggest that  $\alpha$  and  $\beta$  are complementary, and together they can be a useful probe of departures from statistical isotropy of the universe.

## 4.3 Effect of weak lensing on the morphology of CMB fields

It is crucial to understand the properties of lensed CMB fields, especially the  $B$ -mode, so that in the future, it can be easily separated from the unlensed primordial  $B$ -mode. Since the lensed CMB observables are non-Gaussian, in addition to the power spectrum, we need other statistical measures to study their statistical properties. In the following subsections, we study the changes in the morphology of the CMB fields induced by lensing by using the contour Minkowski Tensor which can capture the information about shapes and the relative alignment of the structures. Having so far understood the dependence of  $\alpha$  and  $\beta$  on the smoothing scale and cosmological parameters and the effect of hemispherical anisotropy, we are now in a position to probe the effect of weak gravitational lensing. We first give a brief introduction to the method of simulations of lensed CMB maps, followed by a description of the results.

### 4.3.1 Simulation of lensed CMB maps

Weak lensing of CMB can be modeled very well using linear physics, and one can simulate full-sky lensed CMB maps in weak lensing approximation using `LENSPIX` (Lewis (2005)). Under the weak lensing approximation, this package implements a pixel remapping approach to mimic lensing effects on the CMB photons. The temperature or polarization field is shifted by the deflection vector as a function of position on the sphere's surface. Lensed temperature and polarization fields in a particular direction having coordinates  $(\theta, \phi)$  are given by unlensed fields in another direction  $(\theta', \phi')$  at the last scattering surface as,

$$\tilde{T}(\theta, \phi) = T(\theta', \phi'), \quad (4.4)$$

$$\tilde{P}(\theta, \phi) = \exp[-2i(\gamma - \delta)] P(\theta', \phi'), \quad (4.5)$$

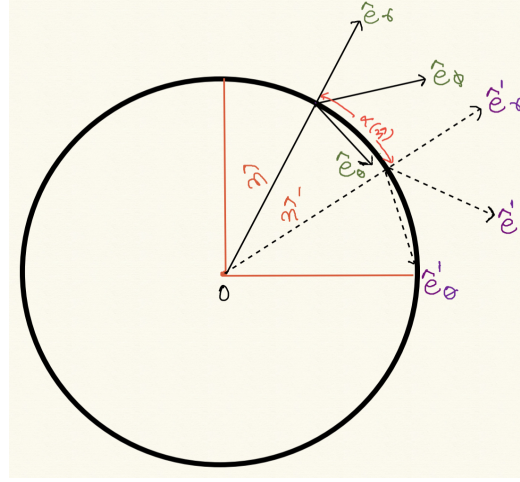


FIGURE 4.5: *Left:* We show here the lensing geometry.  $\hat{n}$  denotes the direction of observed lensed CMB and  $\hat{n}'$  denotes the corresponding unlensed CMB direction. *Right:* We show the unit vectors  $e_\theta, e_\phi, e'_\theta, e'_\phi$  and angle  $\gamma$  the spherical coordinate system is to be rotated to take into account the different direction of the coordinate vectors at the two points.

Here,  $P$  is the spin-2 polarization field given by the linear combination of  $Q$  and  $U$ ,  $\gamma$  is the angle (one of the Euler angle) by which the spherical coordinate system is to be rotated to take into account the different direction of the coordinate vectors at the two points as shown in figure 4.5, while applying pixel remapping for spin-2 polarization field in LENSPIX.  $\delta$  is the angle the deflection vector field makes with coordinate axis  $\hat{e}_\theta$ .

The angular coordinates corresponding to the original direction of the photon path  $(\theta', \phi')$ , are determined by the deflection field  $\vec{d}(\theta, \phi)$ ,

$$\cos \theta' = \cos d \cos \theta - \sin d \sin \theta \cos \delta, \quad (4.6)$$

$$\sin(\phi' - \phi) = \frac{\sin \delta \sin(d)}{\sin \theta'}, \quad (4.7)$$

where the deflection vector field is given by

$$\vec{d} \equiv \vec{\nabla} \Phi = d_\theta e_\theta + d_\phi e_\phi = d \cos \delta e_\theta + d \sin \delta e_\phi. \quad (4.8)$$

We have generated maps of lensed and unlensed  $T, E, B$  using LENSPIX. The theoretical input power spectra for lensing potential and unlensed  $T, E$ , and  $B$  fields were obtained

using the `CAMB` code. The input  $\Lambda$ CDM parameters are:  $\Omega_b h^2 = 0.0226$ ,  $\Omega_{cdm} h^2 = 0.1120$ ,  $H_0 = 70 \text{ km s}^{-1} \text{ Mpc}^{-1}$ ,  $\tau = 0.09$ , where the symbols have their usual meanings. Unless otherwise mentioned, all  $B$  mode maps have input value of tensor-to-scalar ratio  $r = 0.1$ . For calculations done with smoothing scales  $5'$  and higher we use maps for which the `HEALPIX` resolution parameter is  $N_{\text{side}} = 1024$  for both lensed and unlensed case. For large smoothing angles, we downgrade the maps to appropriate  $N_{\text{side}}$  values before smoothing them. For smoothing scales lower than  $5'$  we use  $N_{\text{side}} = 2048$ . Then we numerically compute the CMT for each smoothed map using the two methods described in Chapter 3. We rescale the field by the corresponding RMS value, so the typical threshold value is of order one. We choose the threshold range  $-4.0 < \nu < 4.0$  with 33 equally spaced bins for our calculations.

### 4.3.2 Morphological changes induced by lensing

Since lensing results in the remapping of the CMB field values at different pixels, we expect that it will lead to distortions of hotspots and coldspots. However, statistical isotropy is expected to be preserved, provided the distribution of the lensing potential remains isotropic. We quantify below the effect of lensing on the statistical isotropy parameter  $\alpha$  and the distortions induced for individual structures quantified by  $\beta$ . We note that while  $T$  is directly remapped by lensing,  $E$  and  $B$  are obtained from the directly remapped polarization components  $Q, U$  via non-local relations as outlined in Zaldarriaga (2001). This means that  $E$  and  $B$  at any point cannot be constructed by combining  $Q$  and  $U$  at that same point because any such linear combination (if invertible) would not be scalar under rotations. Hence, we do not expect similar distortion effects for all the fields.

The left and middle panels of the figure 4.6 show the difference of the lensed and unlensed angular power spectra,  $\Delta D_\ell$ , where  $D_\ell \equiv \ell(\ell + 1)C_\ell/2\pi$ , for  $T$  and  $E$ . The right panel



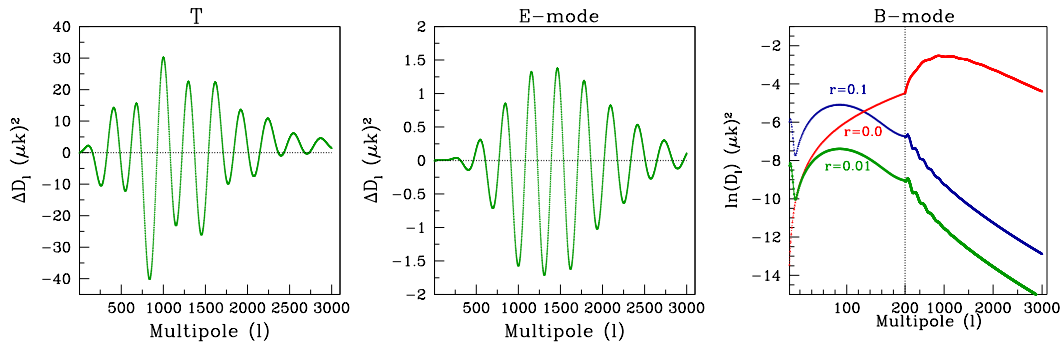


FIGURE 4.6: *Left*: Difference between lensed and unlensed angular power spectra for  $T$  used in our simulations. *Middle*: same for  $E$ . *Right*:  $D_\ell$  for primordial  $B$  with  $r = 0.1$  (blue) and  $r = 0.01$  (green), and lensed  $B$  corresponding to  $r = 0$  (red). We have used two different scales on the  $x$ -axis, with a dotted line serving as demarcation, in order to highlight the low  $\ell$  region.

shows  $D_\ell$  for  $B$ -mode for unlensed (primordial) case with  $r = 0.1$  (blue) and  $r = 0.01$  (green), and lensed case corresponding to  $r = 0$  (red). These plots serve the purpose of checking our simulations by comparing with known results, such as from Lewis *et al.* (2000). For  $B$ - mode, the amplitude of the unlensed power decreases linearly with  $r$ . For  $r = 0.1$ , we can see that the power of the lensed component dominates over the primordial component at scales  $\ell \gtrsim 150$  or larger than degree angular scales. For smaller values of  $r$ , the transition will take place at even larger angular scales. In the following subsections, we present our findings on the morphological changes of the CMB fields induced by lensing. We will find it useful to compare with the lensing effects on the power spectra when we interpret our results on the morphological changes.

#### 4.3.2.1 Effect of lensing on $\alpha$

We compute  $\alpha$  for unlensed and lensed maps for the three fields - temperature,  $E$ - and  $B$ - modes. The calculations are carried out for different smoothing scales in order to find out how the effect of lensing varies with scale. Let us denote the difference of  $\alpha$  between the lensed and unlensed maps by

$$\Delta\alpha(\nu) = \alpha^L(\nu) - \alpha^{UL}(\nu). \quad (4.9)$$

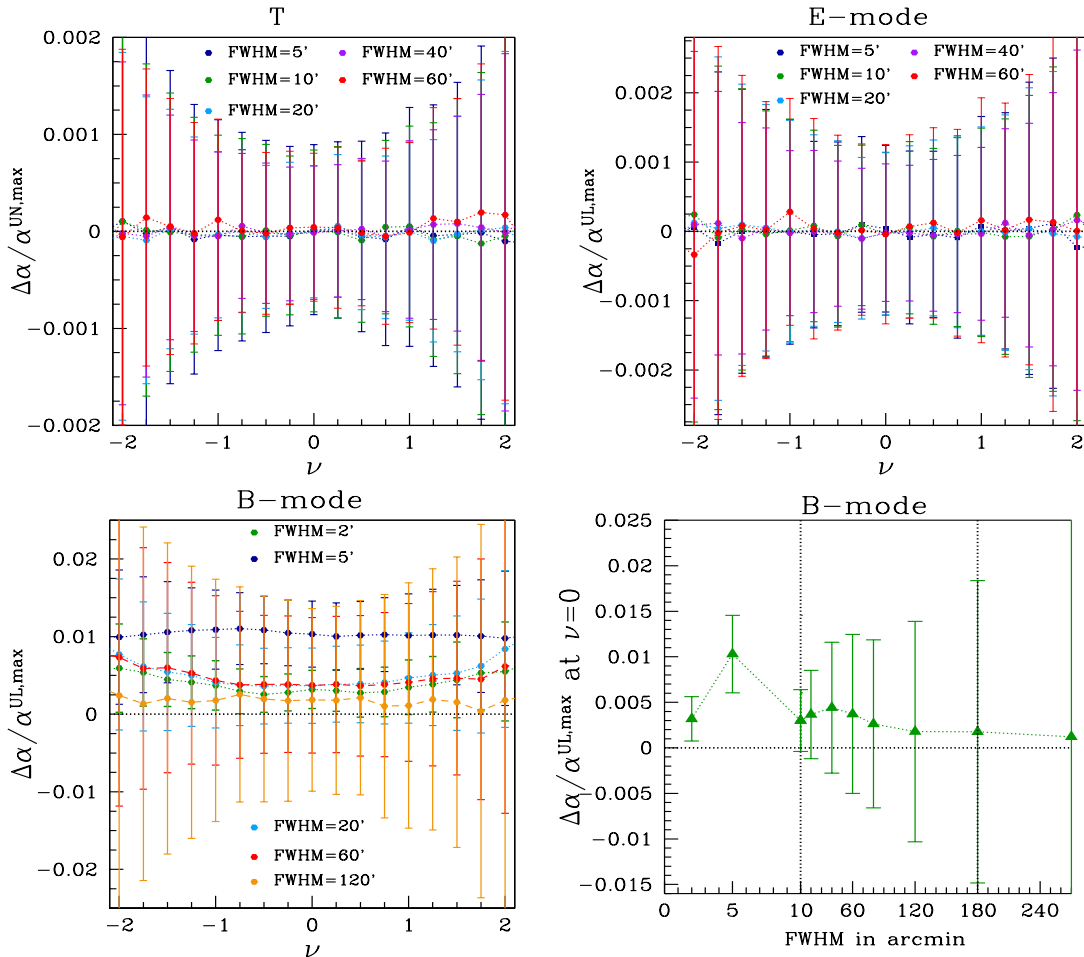


FIGURE 4.7: *Top panels:* Deviations  $\Delta\alpha$  between lensed and unlensed  $T$  (left),  $E$ -mode (right). *Bottom left panels:*  $\Delta\alpha$  for  $B$ -mode. All plots are average over 500 maps and the error bars are the standard deviation obtained from these maps. Note that the smoothing angles are different for the different fields. *Bottom right:*  $\Delta\alpha$  at  $\nu = 0$  as a function of smoothing angle, for  $B$ -mode, normalized by the magnitude of unlensed  $\alpha$  at  $\nu = 0$ . The range of the  $x$ -axis that is probed is between FWHM=2' to 270'. This range is subdivided into three different scales so as to highlight the behaviour at different scales. The locations of the scale transitions at FWHM=10' and 180' are marked by vertical dotted lines. Note the peak at FWHM $\sim$ 5'.

Let  $\alpha^{\text{UL,max}}$  denote the magnitude of the unlensed  $\alpha$  at  $\nu = 0$  where  $\alpha$  has the maximum value. The top panels of figure 4.7 show  $\Delta\alpha$  normalized by  $\alpha^{\text{UL,max}}$  as a function of  $\nu$  at various smoothing scales, for temperature and  $E$ -mode fields. The plots are averaged over 500 realizations. We find  $\Delta\alpha$  for  $T$  and  $E$  fluctuate about zero with error bars which show the consistency of  $\Delta\alpha$  being zero at all  $\nu$ , for all the smoothing scales considered here. Therefore, we do not obtain any systematic variation of  $\Delta\alpha$  with a smoothing scale.

Next, we consider the effect of lensing on the  $B$ -mode field. From the right panel of figure 4.6 we see that the angular power spectrum of the primordial  $B$ -mode peaks at around  $\ell \sim 80$ , which corresponds to roughly  $2^\circ$  angular scale. Beyond this scale, the power dissipates rapidly towards small angular scales. The lensing induced power leakage from  $E$  to  $B$  peaks at around  $\ell \sim 1000$ . For  $r = 0.1$  the lensing power dominates at scales smaller than  $1^\circ$ . This is manifest as structures in the  $B$ -mode field at corresponding angular scales. Consequently,  $\alpha$  for lensed  $B$  is expected to be larger than that of the unlensed value at all threshold values at scales dominated by the lensed signal. This is what we obtain, as seen in the bottom left panel of figure 4.7, where the primordial  $B$  mode maps have input  $r$  value 0.1. We find that  $\Delta\alpha$  is positive for all the smoothing scales that we have considered here. Further, we find that the effect of lensing becomes more pronounced as  $|\nu|$  increases. The error bars also increase as  $|\nu|$  increases since the total perimeter of excursion sets drops exponentially with increasing  $|\nu|$ . However, the functional form of the variation of  $\Delta\alpha$  with the smoothing scale is not clear from this plot.

To get a clear picture of how  $\Delta\alpha$  varies with the smoothing scale, we show the normalized  $\Delta\alpha$  at  $\nu = 0$  versus smoothing angle in the bottom right panel of figure 4.7. Note that on the  $x$ -axis, we have used three different linear scales with transitions at FWHM=10' and 180'. In the range between 2' and 10' we find that  $\Delta\alpha$  peaks around FWHM=5' which corresponds to a smoothing angle  $\theta_s \sim 5'/2\sqrt{2\ln 2} \sim 2.12'$ . This corresponds to the characteristic angular scale set by the typical size of the lensing potential. Notice

that the size of the error bars is smaller towards smaller angular scales, which indicates that the total perimeter of the structures increases towards smaller angles. In the range between 10' and 180,' we find that  $\Delta\alpha$  exhibits a mild increase that peaks at roughly  $FWHM=40'$ . The statistical significance decreases, as seen from the increase of the error bars resulting decrease in the perimeter. Further,  $\Delta\alpha$  decreases towards a large angle, as is expected from the fact that the lensing contribution to  $B$  mode becomes subdominant compared to the primordial part. However, we find a small but non-zero value even at 270' smoothing, possibly because lensing correlates signals at higher than degree scales.

### 4.3.2.2 Effect of lensing on $\beta$

Next, we quantify the distortion induced by lensing on individual structures. This information is captured by the  $\beta$  statistic. Again, the distortion effects are expected to be different for  $T$  and  $E$  and  $B$  fields because  $T$  is directly remapped by lensing, while for  $E$  and  $B$ , the effect is indirect via  $Q, U$ .

In the left panels of figure 4.8 we show the probability distribution function (PDF) of  $\beta$  obtained using all structures (hotspots and coldspots) at  $\nu = 0$ . The PDFs for lensed maps are shown in red and for unlensed in green. The top panel shows  $T$ , middle shows  $E$  and bottom shows  $B$ , for smoothing  $FWHM = 20'$ . The corresponding right panels show the difference between lensed and unlensed PDFs for three smoothing scales given by  $FWHM = 10', 20', 60'$ . We do not find a noticeable effect on the PDFs for  $T$  and  $E$  at the smoothing scales we have considered.  $B$ -mode, on the other hand, exhibits a relative shift of the peaks of the PDFs, indicating that lensed structures are more anisotropic.

To quantify the deviation in the average  $\beta$  induced by lensing let us denote

$$\Delta\beta(\nu) \equiv \beta^L(\nu) - \beta^{UL}(\nu). \quad (4.10)$$

$\Delta\beta(\nu)$  encapsulates the strength of the shear caused by lensing at different threshold

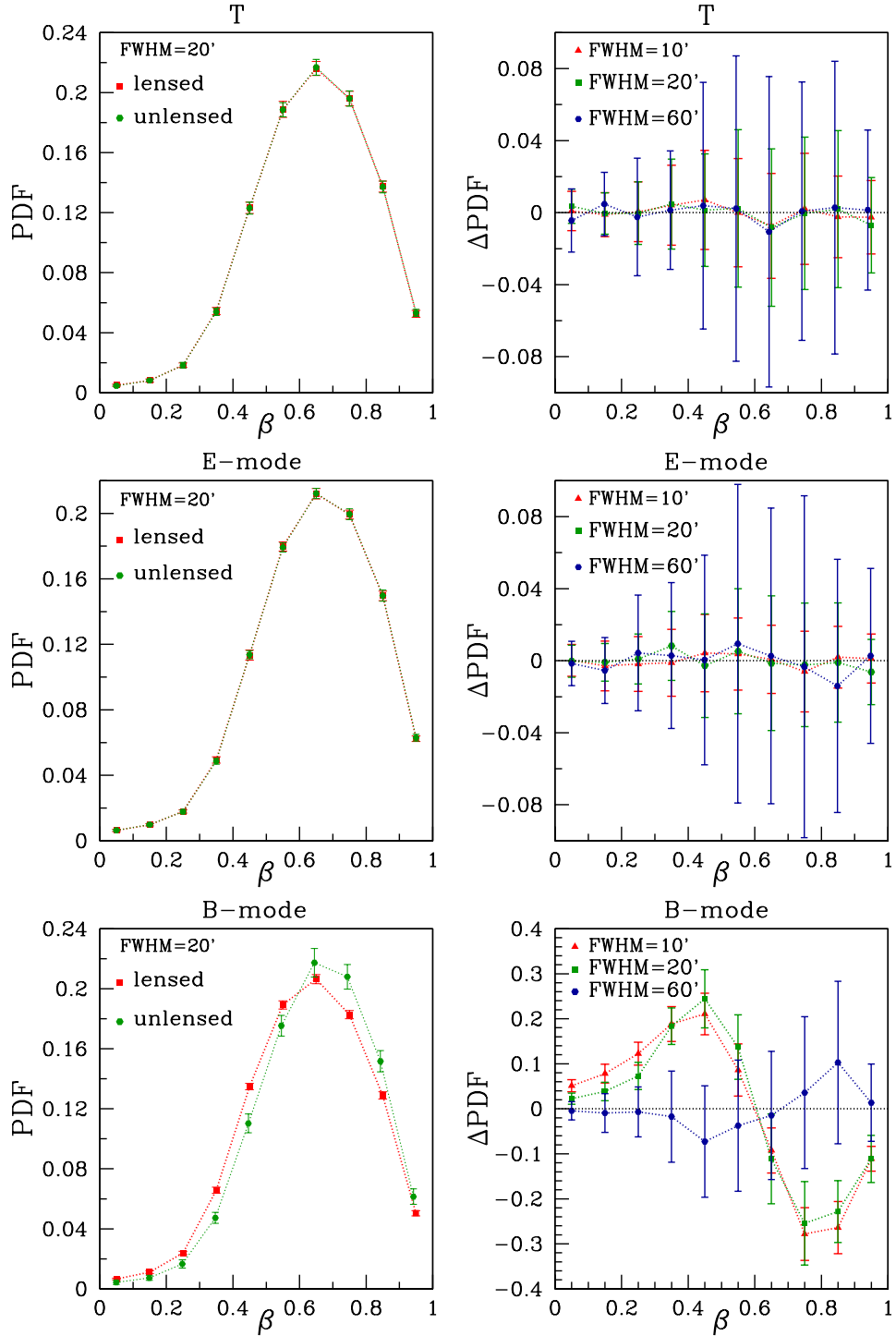


FIGURE 4.8: *Left panels:* PDFs of  $\beta$  for  $T$  (top),  $E$  (middle) and  $B$  (bottom), at  $\nu = 0$  for FWHM=20' for unlensed (green) and unlensed (red) cases. *Right panels:* The difference between lensed and unlensed PDFs for the three fields shown in the right panels. All plots are average over 200 maps and error bars are the standard deviations obtained from them.

levels. In the left panels of figure 4.9 we show  $\beta$  versus  $\nu$  for the lensed (red) and unlensed (green) maps, for  $T$  (left),  $E$  (middle) and  $B$  (right). The smoothing scales are the same as those in figure 4.8, namely, FWHM= 10', 20', 60'. We can see that  $\beta$  is symmetric about  $\nu = 0$  for both lensed and unlensed cases. The shape and amplitude of the curves vary significantly for all the three fields. Since we are dealing with smooth fields, it is reasonable to expect that at high values of  $|\nu|$ , the iso-field curves will follow the *curve shortening flow*<sup>§</sup>, under which the perimeter of the curves decreases and converge to the circular shape, and finally collapses to a single point of singularity at local maxima and minima. Therefore,  $\beta$  must tend towards one at sufficiently large  $\nu$ . The range of  $\nu$  in figure 4.9 is chosen to highlight comparison across different smoothing scales. Note that the RMS of the fields increases with a decrease in the smoothing scale. For FWHM=10',  $\beta$  has turning points beyond  $|\nu| \sim 3$  and does tend to one at large  $|\nu|$ .

The lensing distortions for  $T$  and  $E$  are not noticeable visually, while for  $B$ , the effect is very strong. The right panels of figure 4.9 show  $\Delta\beta$  corresponding to the respective left panels. We can discern a weak but distinct negative value of  $\Delta\beta$  for  $T$  that increases with a decrease of the smoothing scale. This implies that the lensing remapping causes structures to become statistically more anisotropic at all threshold levels. The effect becomes more pronounced as we probe down to smaller scales. For  $E$ -mode, the deviations remain consistent with zero.

$\Delta\beta$  for  $B$ -mode is large and exhibits wide variation with smoothing scale. The values are increasingly negative at smaller smoothing scales, where the lensing effect is strongest. At the relatively larger smoothing of  $1^\circ$  where we expect both primordial and lensed components to contribute to  $\beta$ , we find that  $\Delta\beta$  is positive for a symmetric range around  $\nu = 0$ , indicating that structures at these threshold ranges are more isotropic.

A comment regarding the impact of numerical errors arising from the stereographic projection on the interpretation of our results for  $\beta$  is in order at this point. Our results

---

<sup>§</sup>The nature of how the curves shorten with increasing  $|\nu|$  and finding the evolution equation that governs it is an interesting mathematical question in its own right. For example, for Gaussian fields, we know the perimeter decreases exponentially with increasing  $|\nu|$ . We will, however, not address it here and pursue it elsewhere.

suggest that the effect of lensing on  $T$  and  $E$  that is encapsulated in  $\beta$  is negligibly small at the smoothing scales that we have probed. To accurately calculate the effect, we stress that we should carry out the calculation directly on the sphere. For  $B$ , the distortion effects are large and increase with a decrease of the smoothing scale. Since these are structures that arise due to lensing, we conclude that this is a real signature of lensing-induced distortions. However, the importance of calculating  $\beta$  directly on the sphere cannot be overstated for precise quantification of lensing distortions.

## 4.4 Conclusion and discussion

The geometrical and topological properties of cosmological random fields are a vast source of physical information that has not yet been fully exploited. The applicability of analysis methods that rely on such pixel space properties depends on the availability of observational data, which are high resolution, cover a large field of view, and have a good signal-to-noise ratio. Rapid advances in observational technology and imaging are making such good quality data increasingly more available across a wide spectrum of length scales. Therefore, real pixel-based analysis methods can be expected to become more relevant and useful in the near future. This paper is the latest in a series of investigations that extend previously used pixel space methods of studying cosmological fields. Our focus in this work is to understand morphological changes induced in the fields of the CMB by gravitational lensing due to intervening matter distribution.

For our analysis, we have used shape parameters,  $\alpha$  and  $\beta$ , defined from the eigenvalues of the CMT, to capture the information about the statistical isotropy and the net anisotropy of distribution of structures of a field. We have used two calculation methods; the first one computes the CMT and hence,  $\alpha$  directly on the sphere. The second method, which is used to calculate  $\beta$ , is carried out on the flat plane after the stereographic projection of the fields. Before probing the effect of lensing on CMB fields, we have studied the effect of varying cosmology and hemispherical anisotropy on  $\alpha$  and  $\beta$ . The purpose of this exercise is to distinguish the effect of lensing from other physical phenomena that can mask its

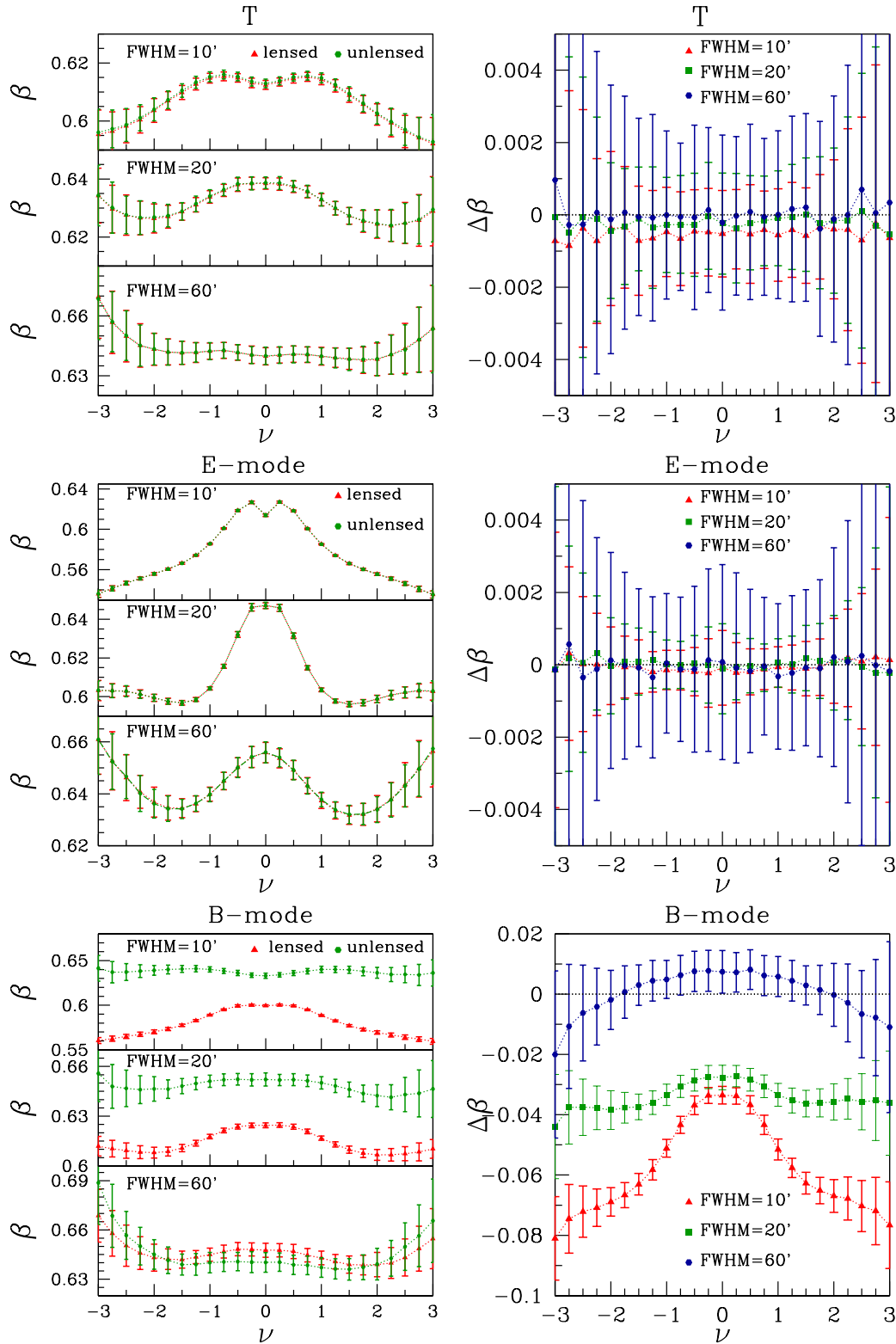


FIGURE 4.9: *Left panels:* Mean values of  $\beta$  for  $T$  (top),  $E$  (middle) and  $B$  (bottom) for FWHM=20' for unlensed (green) and unlensed (red) cases. *Right panels:* The difference between lensed and unlensed mean  $\beta$  values for the three fields shown in the top panels. All plots are average over 200 maps and error bars are the standard deviations obtained from them.



effects. We find  $\alpha$  to be insensitive to variation of cosmological parameters, but it can capture the hemispherical anisotropy in the CMB temperature field, especially at large angular scales.  $\beta$  for  $T$ ,  $E$ , and  $B$  fields show very distinct dependence on the cosmological models as well as hemispherical anisotropy. However, the cosmological parameter values that we have considered are far from the best fit values obtained from Planck data. It is not clear whether the distinct signatures in  $\beta$  can be used for constraining cosmology.

Minkowski tensors, particularly the CMT, provide a novel approach to quantify the effect of lensing on the CMB. We have carried out a detailed investigation of the distortion effects induced by lensing that is encapsulated in  $\alpha$  and  $\beta$  for all the CMB fields. We do not find signatures of lensing on  $\alpha$  in the range of scales studied for temperature and  $E$  mode. The coupling of  $E$ -mode and the  $B$ -mode, caused by lensing at smaller angular scales, manifest as positive values of the difference of  $\alpha$  between lensed and unlensed maps. We find that this difference peaks at around FWHM=5', corresponding to a smoothing angle of 2.12'. Further, we find that statistical isotropy is preserved for the lensed fields as is expected from isotropic large scale matter distribution in the Universe.

Next, we have quantified the distortions induced by lensing encapsulated by  $\beta$ . Our results imply that lensing makes structures more anisotropic across all threshold levels for CMB temperature. We find that the level of distortion increases towards smaller angular scales in the range of scales that we have studied. For  $E$  mode, we do not obtain a clear trend for the distortion effects.  $B$  mode, on the other hand, exhibits a very strong effect with increasing anisotropy at smaller scales. Our analysis here for  $\beta$  for all the fields is limited to relatively large angular scales ( $\geq 10'$ ) for two reasons: stereographic projections and limited computing resources. It will be useful to probe down to smaller scales of around 2' as done for  $\alpha$ .

The work presented in this chapter can be extended in the following directions. First, our results are based on pure simulations. For applications to observed data, we need to consider the effects of instrumental noise and residual foregrounds. Secondly, the computation of  $\beta$  should be done directly on the sphere without projection to the plane for accurate estimation. We are developing a numerical code for this purpose. Thirdly,

---

we should use the full suite of scalar and tensorial Minkowski functionals and Betti numbers for a comprehensive analysis of the lensing effects. Our approach differs from the previous use of scalar MFs in that we compute the geometry (namely, area, perimeter, and counts) of individual structures of the excursion sets and look at their statistics rather than simply their mean values. However, such calculations must be carried out directly on the sphere in order to avoid projection effects. We plan to use the results obtained here to guide a more profound understanding of the lensing deflection field or lensing potential field.

# Chapter 5

## Local patch analysis for testing statistical isotropy of the Planck convergence map

### 5.1 Introduction

The small but measurable effect of weak gravitational lensing on the cosmic microwave background radiation provides information about the large-scale distribution of matter in the universe. We use the all-sky distribution of matter, as represented by the *convergence map* that is inferred from CMB lensing measurement by Planck survey, to test the fundamental assumption of Statistical Isotropy (SI) of the universe. The assumption of SI of the CMB convergence field should be observationally verified since the detection of violation of SI could have profound implications for cosmology. Recently, (Marques *et al.* 2018) investigated SI of the Planck 2015 lensing convergence field using the local variance estimator and identified sky directions or outlier regions where the weak lensing

imprints anomalous signatures to the variance estimator revealed through a  $\chi^2$  analysis at a statistically significant level. The goal of this study is to carry out a similar analysis but using a different methodology. In our analysis, we use the  $\alpha$  statistic devised from the contour Minkowski tensor, a tensorial generalization of the scalar Minkowski functional, the contour length. In essence, the  $\alpha$  statistic captures the ellipticity of iso-field contours at any chosen threshold value of a smooth random field and provides a measure of anisotropy. The SI of the observed convergence map is tested against the suite of realistic simulations of the convergence map provided by the Planck collaboration. We first carry out a global analysis using the complete sky data after applying the galactic and point sources mask. We find that the observed data is consistent with SI. Further, we carry out a local search for departure from SI in small patches of the sky using  $\alpha$ . This analysis reveals several sky patches which exhibit deviations from simulations with statistical significance higher than 95% confidence level (CL). Our analysis indicates that the source of the anomalous behaviour of most of the outlier patches is the inaccurate estimation of noise. We identify two outlier patches that exhibit anomalous behaviour originating from departure from SI at higher than 95% CL. Most of the anomalous patches are found to be located roughly along the ecliptic plane or in proximity to the ecliptic poles.

This chapter is organized as follows. In section 5.2, we briefly review the method of the estimation of the convergence field followed by the Planck collaboration along with the data and the simulations used in our analysis. In section 5.3, we present our global and local analysis and the main results obtained. The chapter ends with the concluding remarks in section 5.4.

## 5.2 Data and Methodology

This section describes the set of observed data and simulations that we have used for our analysis, followed by explaining the statistical method used to test for SI of the convergence field.

### 5.2.1 The Planck convergence map: Observed data and Simulations

The Planck 2018 data release (Planck Collaboration *et al.* 2020a) provides the most significant measurement of the lensing potential and its power spectrum over about 70% of the sky.

*Observed data:* To reconstruct the lensing potential, the method employed (Carron and Lewis 2017) by the Planck team are based on quadratic estimators that use the features induced by the lensing process, such as the diverse correlations of the CMB temperature (T) and polarization (E and B) modes. The combination of these estimators in a minimum-variance (MV) estimator is used to reconstruct the CMB lensing potential,  $\psi^{MV}$ . The Planck 2015 lensing estimate was based on CMB temperature and polarization multipoles, i.e.,  $\psi^{TT}$ ,  $\psi^{EE}$ ,  $\psi^{TE}$ ,  $\psi^{TB}$ ,  $\psi^{EB}$  and a combination of all these five multipoles in the minimum variance quadratic estimator. However, the Planck 2018 estimate of the lensing potential differs from the previous release because it also includes the contribution from filtered B-modes,  $B^{WF}$ . The CMB data set used as input to the MV lensing estimator was the foreground cleaned map obtained by passing the raw Planck 2018 full mission frequency maps through the SMICA pipeline.

The reconstructed lensing potential estimate has a much red power spectrum, with most of its power on large angular scales. Cutting the maps with a red power spectrum in small portions can cause leakage issues. For this reason, we use in our analysis the convergence map,  $\kappa^{WF}$ , instead of the lensing potential map. The lensing convergence and its corresponding reconstruction noise have a much whiter power spectrum, especially on large angular scales as discussed in Bucher *et al.* (2012).

*Simulations:* Next, the simulations we use to perform our analysis are the set of 300 realizations of the convergence field, which constitutes the Planck Full Focal Plane (FFP10) simulations (Planck Collaboration *et al.* 2020b). These Monte Carlo realizations comprise a set of maps that incorporate the dominant instrumental effects (detector beam,

bandpass, and correlated noise properties), scanning (pointing and flags) and data analysis (map-making algorithm and implementation) effects.

Both the observed and simulation data sets of the convergence field are provided in the form of multipole expansion coefficients,  $\kappa_{\ell m}^{MV}$ , up to  $\ell_{max} = 4096$  in HEALPix (Górski *et al.* 2005) \* FITS format. We then generate convergence maps from these multipole expansion coefficients using HEALPix. The convergence field multipole coefficients are related to harmonic coefficients of the lensing potential by,

$$\kappa_{\ell m}^{MV} = \frac{\ell(\ell+1)}{2} \Psi_{\ell m}^{MV}. \quad (5.1)$$

The  $\kappa$  field reconstructed from observed data is highly noise-dominated, especially at small angular scales. The signal-to-noise ratio is  $S/N \approx 1$  at  $\ell = 60$ . For this reason, we will construct convergence maps by choosing map resolutions corresponding to the Healpix parameter  $N_{side} \leq 512$ . The largest multipole value is then chosen to be  $\ell_{max} = 2N_{side}$ . We do not downgrade the higher resolution map to required lower resolution. We just use  $\ell_{max}$  upto  $2N_{side}$  for the corresponding  $N_{side}$ . The maps constructed (both observed data and simulations) are then further processed following the steps given below.

- *Bandpass filtering:* We filter out  $\ell \leq 8$  modes as done in the Planck 2015 and 2018 lensing analysis. The reason is that the low  $\ell$  modes have high sensitivity to the mean-field subtraction. The form of the filter,  $F_\ell$ , is given by the following expression,

$$F_\ell = \frac{1}{2} \left\{ 1 + \tanh \left( \frac{\ell - \ell_0}{\Delta} \right) \right\}, \quad (5.2)$$

where  $\ell_0$  denotes the center of a chosen band of  $\ell$ , and  $\Delta$  denotes the bandwidth. We choose  $\ell_0 = 8$  and  $\Delta = 3$  to carry out our analysis. The bandpass filtered multipoles are then generated by multiplying  $\kappa_{\ell m}$ s of the input map with  $F_\ell$ .

- *Wiener filtering:* To mitigate the effect of noise, we apply Wiener filter to the spherical harmonic coefficients as employed in Bobin *et al.* (2013), as given by the

---

\*<http://healpix.sourceforge.net/>

following expression,

$$\kappa_{\ell m}^{WF} = \frac{C_{\ell}^{\kappa, fid}}{C_{\ell}^{\kappa, fid} + N_{\ell}^{\kappa}} \kappa_{\ell m}^{MV}. \quad (5.3)$$

Here  $C_{\ell}^{\kappa, fid}$  is the convergence power spectrum in the fiducial cosmological model, and  $N_{\ell}^{\kappa}$  is the reconstruction noise power spectrum.

- *Masking:* We further mask the convergence map using the lens reconstruction analysis mask (lens mask henceforth) provided among the lensing products, which has  $f_{\text{sky}} = 0.67$ . This is an improved mask over the 2015 weak lensing mask due to reduced point source contamination for the same sky fraction. We downgrade the lens mask to the lower resolution that is compatible with the resolution of the convergence map.

### 5.3 Analysis and results

In this section, we present our analysis of SI of the Planck convergence map using the  $\alpha$  statistic obtained from Contour Minkowski tensor ( $\widetilde{\mathcal{W}}_1$ ) discussed in Chapter 3.

In order to keep the terminology clear, we will refer to the convergence map obtained from Planck data as the *observed convergence map*. We first rescale the convergence field by its variance  $\sigma_0$ . This makes the rescaled field threshold range to be of order one. Then we compute  $\widetilde{\mathcal{W}}_1$ , and from it  $\alpha$ , for 33 equally spaced threshold bins, of width  $\Delta\nu = 0.25$ , ranging from  $-4.0 \leq \nu \leq 4.0$ .

*Minimizing numerical error due to mask boundaries:* In order to minimize numerical error near sharp mask boundaries that can arise due to harmonic transforms, we first mask the field using a downgraded lens mask which is then apodized using the same smoothing kernel as the convergence maps. As a result, the pixels near the boundary will now have values between zero and one. Then, we include only those pixels in our analysis that are sufficiently far away from the boundary for calculating  $\alpha$ . This is done using a parameter  $s_m$ , whose value lies between zero and one, and only pixels of the field

for which the corresponding smoothed lens mask has values greater than chosen value of  $s_m$  (0.98) are included. Since, as  $s_m$  increases towards one, the fraction of included pixels decreases, and hence the statistical significance of the results will decrease. Therefore, it is best to select an optimum value of  $s_m$  such that the numerical error is minimized and the statistical significance is maximized. A rough estimate shows that a smoothed mask pixel value greater than 0.89 roughly corresponds to  $> 2\theta_s$  distance from the mask boundary,  $\theta_s$  being the smoothing scale. Hence we use  $s_m = 0.89$  for our calculations.

### 5.3.1 Understanding the effects of bandpass filter and masking on $\alpha$ using ideal simulations

Before analyzing the observed data set and looking for subtle signatures of departure from SI in the universe, it is important to clearly understand the effects of masking and bandpass filtering on  $\alpha$  using ideal Gaussian isotropic maps of the convergence field. This step is important to isolate any physical phenomenon from the systematic effects. For this purpose, we simulate 300 Gaussian isotropic realizations of  $\kappa$  and then compute  $\alpha$  using the field derivative method outlined in chapter 3. The input lensing potential or convergence power spectrum is obtained from CAMB Lewis *et al.* (2000)<sup>†</sup>. The values of the input  $\Lambda$ CDM parameters are:  $\Omega_b h^2 = 0.02216$ ,  $\Omega_{cdm} h^2 = 0.1203$ ,  $H_0 = 67 \text{ km s}^{-1} \text{ Mpc}^{-1}$ ,  $\tau = 0.06$ ,  $n_s = 0.964$ ,  $A_s = 2.119 \times 10^{-9}$ , where the symbols have their usual meanings. These are the same fiducial cosmological parameters that are used as input for the Planck convergence simulations.

We compare  $\alpha$  as a function of the threshold for the full sky case with the corresponding  $\alpha$  obtained after (a) applying lens mask with  $s_m = 0.98$ , (b) no masking but band pass filtering, and (c) bandpass filtering and masking. In figure 5.1 we have shown  $\alpha$  for these three different cases. The four panels correspond to four different resolutions given by  $N_{\text{side}} = 64, 128, 256$  and  $512$ . The blue curves correspond to the full sky case, while the orange curves represent the masked case, red curves are for the bandpass filtered case

---

<sup>†</sup><https://camb.info/>



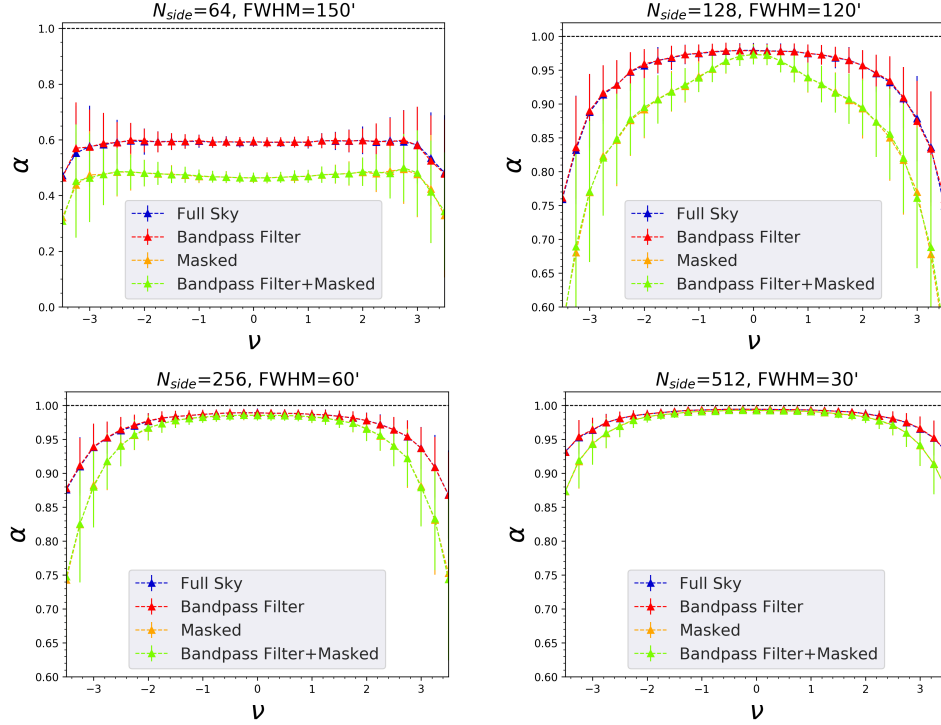


FIGURE 5.1: Mean values of  $\alpha$  and standard deviation obtained from isotropic Gaussian simulations of the convergence map for different resolutions  $N_{side} = 64, 128, 256$  and  $512$ . Different colors here represent  $\alpha$  calculated for full sky (blue), masked (orange), bandpass filtered (red), and masked plus band pass filtered (green).

with cut-off scale  $\ell_0 = 8$ , and the green curves represent the alpha for bandpass filtered and masked maps. We expect  $\alpha$  to be close to one at all thresholds considered here for the ideal case. We find that the ideal convergence field is isotropic as  $\alpha$  is close to one, which is as expected from the standard model of cosmology. Applying lens mask to the ideal  $\kappa$  field reduces the number of structures in the field, which leads to a drop in the value of  $\alpha$  at large thresholds. This effect is more prominent at lower resolutions, i.e.,  $N_{side} = 64, 128$ , where already the ideal field has few structures. We also note that the bandpass filtering does not affect the value of  $\alpha$ .

### 5.3.2 Quantifying the statistical significance of $\alpha$ and error bars

The  $\alpha$  statistic follows the Beta distribution given by the following expression,

$$P(\alpha) = \frac{\Gamma(a+b)}{\Gamma(a)\Gamma(b)} \alpha^{a-1} (1-\alpha)^{b-1},$$

where  $a > 0$ ,  $b > 0$  are parameters that depend on the cosmological model (see Chingangbam *et al.*). Hence the standard deviation of  $\alpha$ , which we denote by  $\sigma_\alpha$ , will not be equivalent to the usual 68% confidence interval. So, we first reconstruct the probability density function (PDF) of  $\alpha$  using the 300 FFP10 realizations and, using it, determine the confidence intervals as described below. Let  $\tilde{\alpha}^{\text{sim}}(\nu)$  denote the median value of  $\alpha$  at each threshold obtained from the simulations. Let the ranges of  $\alpha$  be given by  $\alpha_a = (\tilde{\alpha}^{\text{sim}} - \delta_-^{(j)})$  to  $\alpha_b = (\tilde{\alpha}^{\text{sim}} + \delta_+^{(j)})$ , which denotes the confidence intervals such that  $j = 1, 2, 3, \dots$  correspond to 68%, 95% and 99%, and so on, respectively. Then we determine  $\delta_-^{(j)}$  and  $\delta_+^{(j)}$  from the condition

$$\int_{\tilde{\alpha}^{\text{sim}} - \delta_-^{(j)}}^{\tilde{\alpha}^{\text{sim}}} d\alpha P(\alpha) = \int_{\tilde{\alpha}^{\text{sim}}}^{\tilde{\alpha}^{\text{sim}} + \delta_+^{(j)}} d\alpha P(\alpha) = p/2, \quad (5.4)$$

where  $p = 0.68, 0.95, 0.99$  for  $j = 1, 2, 3$ . We find that the difference between the mean and median values of  $\alpha$  is actually quite small in all cases. They differ at most by 1% at  $|\nu| \sim 3$  and this difference gets smaller towards  $|\nu| \sim 0$ .

To demonstrate, the left panel of figure 5.2 shows the reconstructed  $P(\alpha)$  for some selected  $\nu$  values, for  $N_{\text{side}} = 512$ . We observe that the maxima of the PDF for  $\nu = 0$  occurs at a smaller value of  $\alpha$  compared to  $\nu = 2$ . Moreover, there is no symmetry between positive and negative  $\nu$ . These are due to the presence of instrumental noise, foreground residuals, and other systematic effects. The panel on the right shows comparison of  $2\sigma_\alpha$  with  $\delta_-^{(2)}$  and  $\delta_+^{(2)}$ , calculated using  $p = 0.95$ . The values of the three quantities do not differ much. There is mild mismatch at higher  $|\nu|$  values where  $2\sigma_\alpha$  slightly underestimates  $\delta_-^{(2)}$  and overestimates  $\delta_+^{(2)}$ . We find similar behaviour for different values of  $N_{\text{side}}$ .

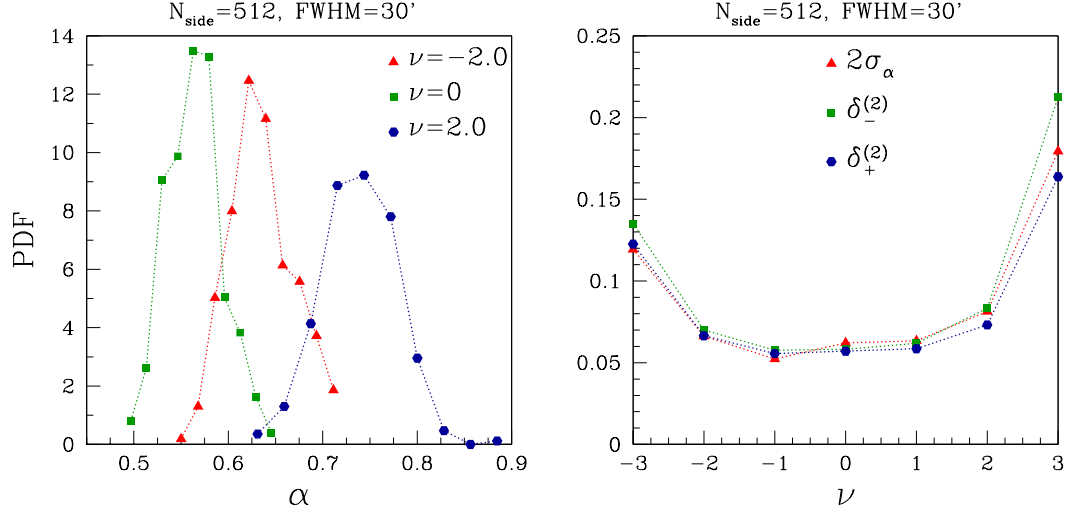


FIGURE 5.2: *Left:*  $P(\alpha)$  for some selected values of  $\nu$  for  $N_{\text{side}} = 512$ . *Right:*  $2\sigma_\alpha$  (red triangle),  $\delta_-^{(2)}$  (green square) and  $\delta_+^{(2)}$  (blue circle), for the same  $N_{\text{side}}$  as the left panel.

Let  $\alpha^{\text{obs}}$  denote the value of  $\alpha$  for the observed data, and let  $\tilde{\alpha}^{\text{sim}}$  mean/median  $\alpha$  value from 300 FFP10 simulations, then their difference  $\Delta\alpha$  is given by,

$$\Delta\alpha \equiv \alpha^{\text{obs}} - \tilde{\alpha}^{\text{sim}}. \quad (5.5)$$

Then in order to quantify the statistical significance of  $\Delta\alpha$  at each threshold we define the variable  $\tilde{\chi}^{(j)}$  as follows<sup>‡</sup>:

$$\tilde{\chi}^{(j)} = \begin{cases} \Delta\alpha/\delta_-^{(j)}, & \text{if } \Delta\alpha < 0, \\ \Delta\alpha/\delta_+^{(j)}, & \text{if } \Delta\alpha > 0. \end{cases} \quad (5.6)$$

If  $|\tilde{\chi}^{(j)}| > 1$  then it implies that  $\alpha^{\text{obs}}$  is outside the confidence interval corresponding to  $j$ . Since there can be unknown systematic or physical effects at different threshold levels, we choose to interpret  $\tilde{\chi}^{(j)}$  as a function of threshold, rather than condense the information of the threshold variation into a single value. It can be shown that the values of  $\alpha$  at neighboring thresholds are uncorrelated if the threshold bin size is sufficiently large. Our choice of  $\Delta\nu = 0.25$  is sufficiently large and hence  $\delta_-^{(j)}$  and  $\delta_+^{(j)}$  in the denominator of  $\tilde{\chi}^{(j)}$  captures the full covariance information.

<sup>‡</sup> $|\tilde{\chi}^{(1)}|$  reduces to the square root of the standard chi-squared statistic for Gaussian distribution.

An important point to keep in mind when we interpret our results is the following. Since a lower value of  $\alpha$  means a higher degree of alignment of structures, a significantly negative value of  $\Delta\alpha$ , and consequently of  $\tilde{\chi}^{(j)}$ , implies that the observed data has a higher level of anisotropy in comparison to the expectation from the median value of  $\tilde{\alpha}^{\text{sim}}$ . On the other hand, as seen in section 5.3.1,  $\alpha$  value for a generic field depends on the number of structures and is larger for a field with a higher number of structures. Therefore, a significantly large positive value of  $\Delta\alpha$  indicates anomalous behaviour but does not indicate a higher level of anisotropy.

Equipped with the understanding of the effects of masking and bandpass filtering on the ideal convergence field and the statistics of  $\alpha$ , we now focus on our stated goal of testing SI of the observed convergence map and the corresponding FFP10 simulations. In the following, we perform our analysis using two complementary approaches: (1) *global analysis*, where we calculate  $\alpha$  for the masked full-sky convergence maps, and (2) *local analysis*, where we calculate  $\alpha$  for non-overlapping small patches of the sky.

### 5.3.3 Global analysis

For the global analysis, we first construct the maps of the observed and FFP10 simulated convergence field following the steps outlined in section 5.2.1. For the masking, we use the conservative value of  $s_m = 0.98$ . The sky fraction for the full resolution ( $N_{\text{side}} = 2048$ ) mask is  $f_{\text{sky}} = 0.67$ . After apodizing the lens mask and then applying the  $s_m$  condition the sky fractions become  $f_{\text{sky}} = 0.48, 0.49, 0.53$  and  $0.60$  for  $N_{\text{side}} = 64, 128, 256$  and  $512$ , respectively. Then  $\alpha$  is calculated from each of the maps constructed as above. We will discuss the results for the cases with and without Wiener filtering.

We first discuss the results for the case without Wiener filtering. The  $\alpha$  and corresponding  $\tilde{\chi}^{(2)}$  values as functions of the field threshold are presented in the top row of figure. 5.3. The four panels correspond to  $N_{\text{side}} = 64, 128, 256$  and  $512$ , which are the same as in figure 5.1 with the same smoothing FWHM values. The  $\alpha$  values computed from the

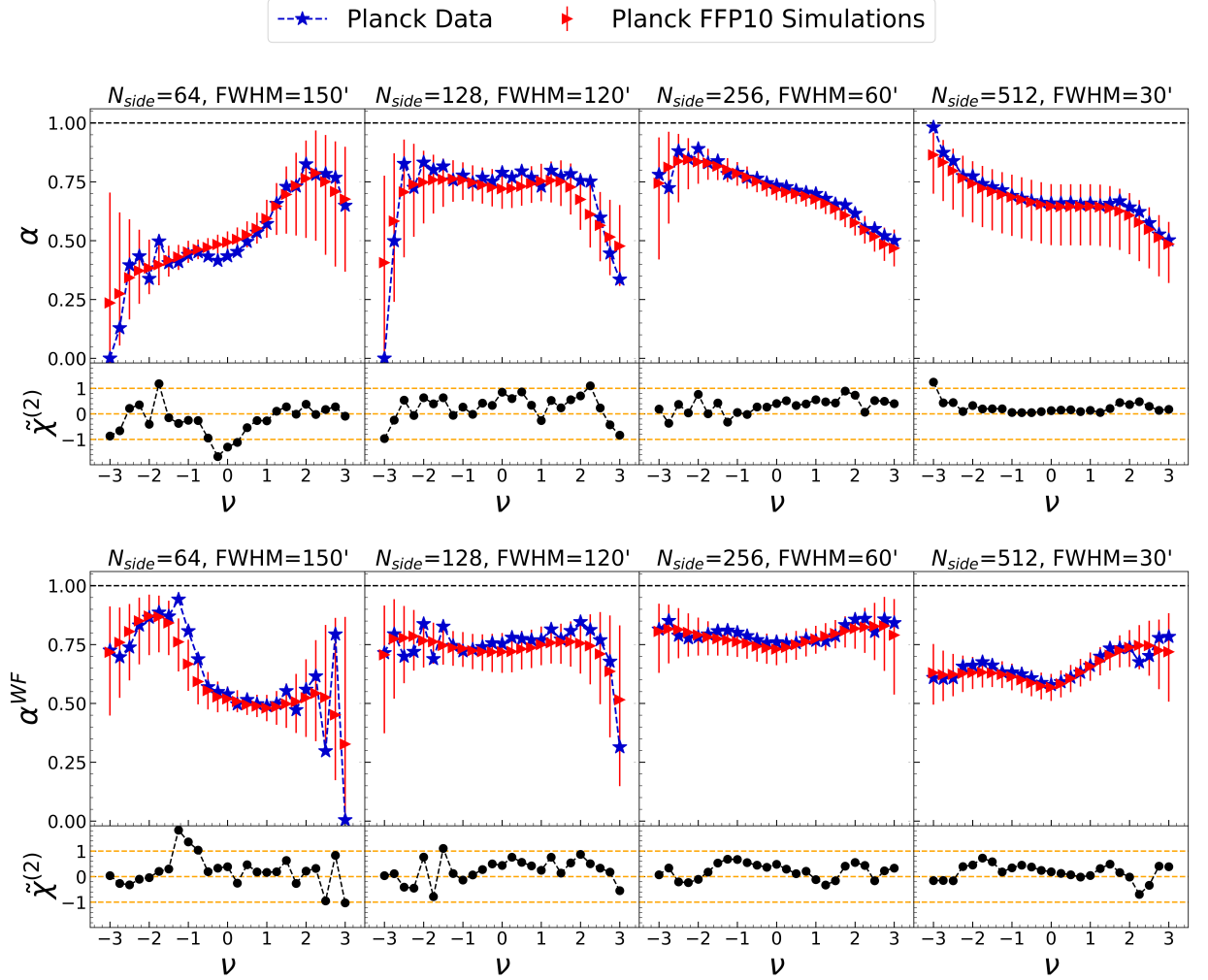


FIGURE 5.3: *Top row:* Upper panels show  $\alpha$  while lower panels show  $\tilde{\chi}^{(2)}$  for the Planck convergence map (blue stars) and FFP10 simulations (red triangles), without Wiener filtering, for different values of  $N_{side}$ . *Bottom row:* Same as first row but for Wiener filtered maps.

observed  $\kappa$  map are represented by blue stars, while the median value and error bars are given by  $\delta_-^{(2)}$  (lower) and  $\delta_+^{(2)}$  (upper) are shown in red. The black curves in the lower panels show  $\tilde{\chi}^{(2)}$ . We observe the following points:

- We find that  $\alpha$  values differ strongly in terms of amplitude as well as the shape of the threshold dependence between the FFP10 simulations and the ideal cases shown in figure 5.1. We observe a dip in the  $\alpha$  curve at around  $\nu = 0$ . Also, we note that  $\alpha$  is asymmetric about  $\nu = 0$ , unlike the case of ideal simulations. We find that the curve slopes down towards negative threshold values for  $N_{side} = 64$ , while

for higher resolution cases, the downward slope is towards positive thresholds. This difference can be attributed to the complex noise (arising from both instrument and lensing reconstruction) properties contributing to the observed data and the corresponding simulations.

- From the values of  $\tilde{\chi}^{(2)}$  we infer that there is good agreement between the observed data and FFP10 simulations for all the four cases except for some threshold values, particularly for  $N_{\text{side}} = 64$ .

Next, we discuss the results of the case with Wiener filtering. In the bottom row panels of figure 5.3, we show  $\alpha$  for the same observed data (blue stars) and simulations (red triangles) as in the top row. The superscript ‘WF’ refers to Wiener filter. Wiener filtering optimally weighs for the noise and is expected to suppress the modes with large noise contributions. We observe some changes in the results after applying the Wiener filter. For  $N_{\text{side}} = 64$ , we observe that the  $\alpha$  curve is now tilted toward the positive threshold values in contrast to the without Wiener filtering case. While for  $N_{\text{side}} = 256, 512$ , we find that  $\alpha$  becomes relatively more symmetric about  $\nu = 0$ , as the (large  $\ell$  values) modes with high noise contribution have been suppressed by the Wiener filter. Even though the shape of the  $\alpha$  curve obtained here also does not mimic the  $\alpha$  curve in the case of ideal Gaussian isotropic  $\kappa$  simulation, the observed  $\kappa$  is consistent with Planck isotropic simulations within  $2\sigma$ . Agreement between the corresponding values computed from observations and simulations implies that the observed maps are statistically isotropic. We also observe that  $\tilde{\chi}^{(2)}$  has positive values at most of the thresholds for almost all the  $N_{\text{side}}$  values considered here, in both with and without Wiener filtering case. The positive values of  $\tilde{\chi}^{(2)}$  indicate the presence of higher number of structures in the observed  $\kappa$  field than the corresponding simulated field.

We are guided by two factors to complement the global analysis by further analysis after restricting to smaller sky patches. The first is that any anomaly in localized sky regions can get washed out when  $\alpha$  is computed over larger regions. Secondly, we see some hints of an anomaly in the global analysis, which can be sharpened when analyzed over smaller

regions. Therefore, we expect the statistical significance of the positive values of  $\tilde{\chi}^{(2)}$  to get enhanced.

### 5.3.4 Local patch analysis

We now focus on analysis of small patches of the sky. We first pixellize the sky using a low value of the Healpix resolution parameter which we denote by  $N_{\text{side}}^{\text{local}}$ . Each pixel determined by  $N_{\text{side}}^{\text{local}}$  is referred to as a *patch*. We will work with  $N_{\text{side}}^{\text{local}} = 2$  and 4. For  $N_{\text{side}}^{\text{local}} = 2$  we get 48 patches, each patch having angular size  $(29.3^\circ)^2$ . For  $N_{\text{side}}^{\text{local}} = 4$  there are 192 patches and each patch has angular size  $(14.7^\circ)^2$ . We identify each patch by its pixel number in the ‘ring’ pixel numbering format in Healpix. Next, we pixellize the sky using a higher  $N_{\text{side}}$  value which we denote with a superscript ‘global’, by  $N_{\text{side}}^{\text{global}}$ . The number of pixels in each patch defined above is then given by  $N_{\text{pix}}^p = (N_{\text{side}}^{\text{global}}/N_{\text{side}}^{\text{local}})^2$ . We work with  $N_{\text{side}}^{\text{global}} = 128$  and 256. In each case we use the maximum multipole value of  $\kappa$  given by  $\ell_{\text{max}} \sim 2N_{\text{side}}^{\text{global}}$ . Therefore, the physical information encoded in the maps constructed with  $N_{\text{side}}^{\text{global}} = 128$  is contained in maps having  $N_{\text{side}}^{\text{global}} = 256$ , but the converse is not true. The values of  $N_{\text{side}}^{\text{local}}$  and  $N_{\text{side}}^{\text{global}}$  have been chosen keeping in mind that the SNR of the observed convergence map becomes increasingly smaller at high multipoles and that the patches should have good enough resolution for statistical analysis using morphological properties. Table 5.1 summarizes the values of  $N_{\text{side}}^{\text{local}}$  and  $N_{\text{side}}^{\text{global}}$  considered in our analysis, along with the relevant numbers of patches and pixels, and the angular sizes of patches.

The estimator of  $\tilde{\mathcal{W}}_1$ , which for the global analysis is given by equation 3.55 in chapter 3, is modified for each patch indexed by  $p$ , to the following form,

$$\bar{\mathcal{W}}_{1,p} = \frac{1}{N_p} \sum_{i=0}^{N_{\text{pix}}} \frac{w_{p,i}}{\Delta\nu} \mathcal{I}_i, \quad (5.7)$$

where the weight  $w_{p,i}$  has one if the pixel belongs to the  $p^{\text{th}}$  patch *and* if the apodized lens mask at that pixel has value  $> s_m$ , else it has value zero. The normalization  $N_p$

$N_{\text{side}}^{\text{local}}$	Total no of patches	Angular size of a patch	$N_{\text{side}}^{\text{global}}$	No of pixels in each patch
2	48	$(29.3^\circ)^2$	128	4096
			256	16384
4	192	$(14.7^\circ)^2$	128	1024
			256	4096

TABLE 5.1: Table showing the numbers of patches and their angular size, and number of pixels in each patch, for the values of  $N_{\text{side}}^{\text{global}}$  and  $N_{\text{side}}^{\text{local}}$  considered in our local analysis.

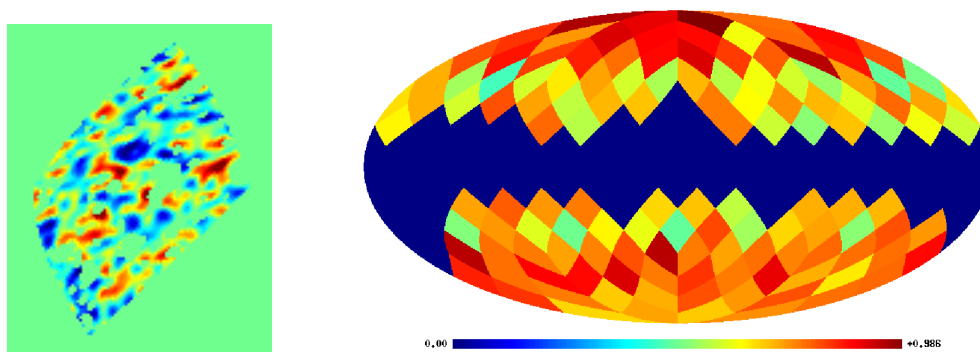


FIGURE 5.4: *Left:* An example of a patch of the  $\kappa$  map. *Right:* Map showing values of  $\alpha$  for sky patches at  $\nu = -0.5$ , with each patch being one of the 192 pixels given by  $N_{\text{side}}^{\text{local}} = 4$ . The value of  $N_{\text{side}}^{\text{global}}$  is 256 and the valid pixel fraction is  $p_{\text{frac}} = 0.6$ .

is now the count of pixels in each patch having  $w_{p,i} = 1$ . We also exclude patches that have a high percentage of masked regions. This is done by calculating the ratio,  $p_{\text{frac}}$ , of the number of pixels that are not masked (*valid* pixels,) to the total number of pixels in each patch. We choose  $p_{\text{frac}} = 0.6$ . Figure 5.4 visually demonstrates the local analysis. The left panel shows the  $\kappa$  field in one patch. The right panel shows a map of  $\alpha$  values for each patch computed from the observed convergence map, at threshold  $\nu = -0.5$  for the case of  $N_{\text{side}}^{\text{local}} = 4$  and  $N_{\text{side}}^{\text{global}} = 256$ .

*Identification of outlier patches:* We calculate  $\Delta\alpha$  for each patch at each threshold. Then we compute  $\tilde{\chi}^{(j)}(\nu)$ ,  $j = 1, 2, 3, \dots$ . At high thresholds, the excursion sets for a



typical patch consist of few structures, and hence the analysis of statistical significance can become unreliable. Therefore, we restrict the threshold range for identifying outlier patches to the conservative range  $-2 \leq \nu \leq 2$ . If  $|\tilde{\chi}^{(2)}(\nu)| > 1$  (equivalent to higher than  $2\sigma$ ) we consider the patch to be anomalous at that threshold. A patch can exhibit an anomaly at one or more threshold values. To identify a patch as an *outlier* for each value of  $N_{\text{side}}^{\text{local}}$  we demand that it satisfies *either* of the following two conditions:

1. It must show anomaly for both  $N_{\text{side}}^{\text{global}} = 128$  and  $256$ . This condition ensures that anomalous behaviour for  $N_{\text{side}}^{\text{global}} = 128$  is also manifested in the higher resolution case and that the anomaly is robust against variation of resolution.
2. For patches that are not common as above, they must be anomalous at three or more threshold values. This condition ensures that the anomaly is not just a statistical fluctuation.

The outlier patches that have been identified are listed in table 5.2. Patches shown in magenta have positive value of  $\tilde{\chi}^{(2)}(\nu)$ , while those in blue have negative value of  $\tilde{\chi}^{(2)}(\nu)$  at all anomalous thresholds. The patches that are *not* common between  $N_{\text{side}}^{\text{global}}=128$  and  $256$  are highlighted by the black boxes.

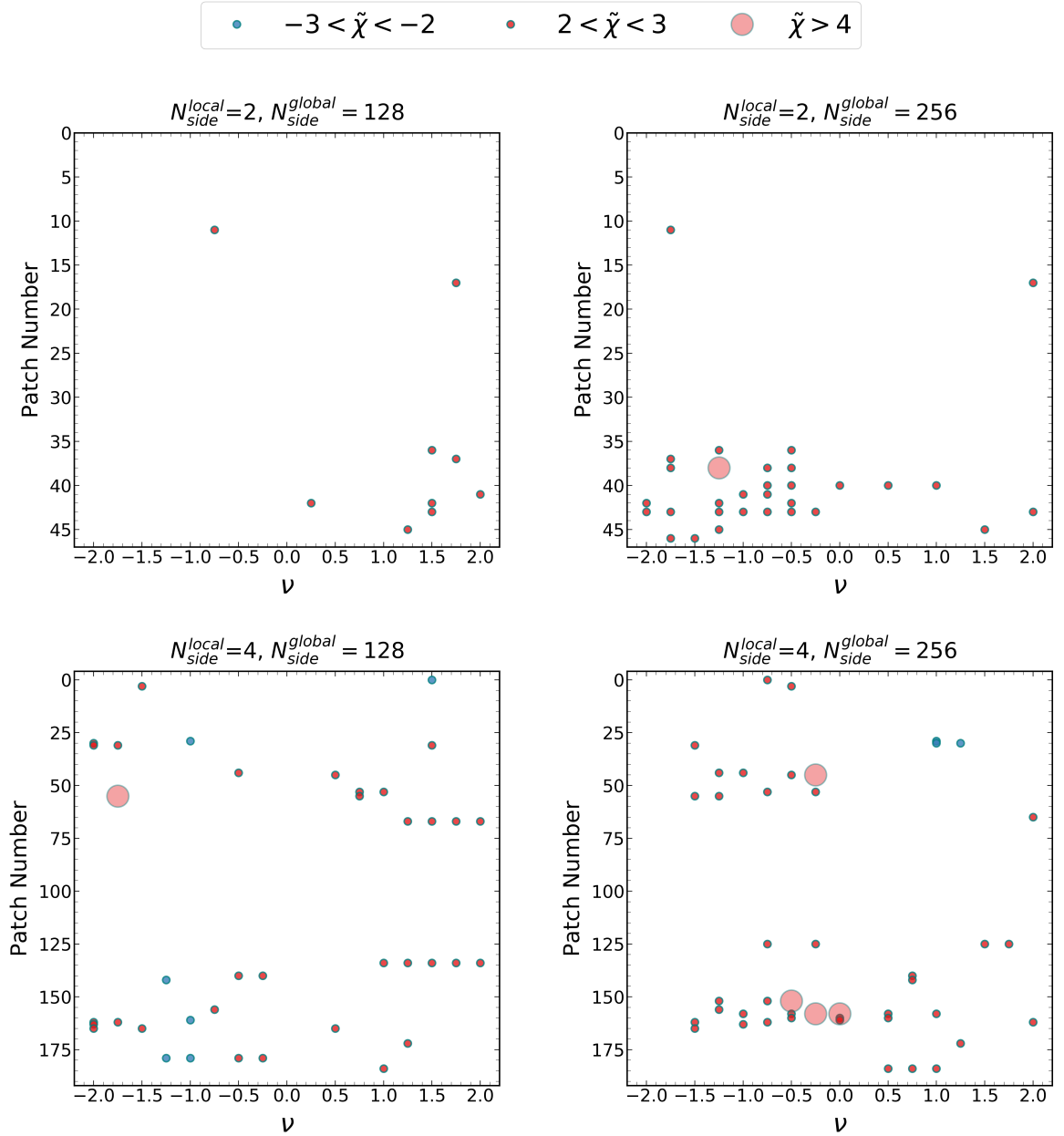
*Degree of anomaly:* We define a new statistic,  $\tilde{\chi}(\nu)$ , to measure the degree of statistical significance of  $\Delta\alpha$  for every outlier patch. It is defined to have value between 2 and 3 if  $\tilde{\chi}^{(2)} > 1$  and  $\tilde{\chi}^{(3)} < 1$ , between 3 and 4 if  $\tilde{\chi}^{(3)} > 1$  and  $\tilde{\chi}^{(4)} < 1$ , and so on. Figure 5.5 shows plots of  $\tilde{\chi}(\nu)$  for all the anomalous patches on the two dimensional space spanned by  $\nu$  and the patch identification numbers. The four panels correspond to the four combinations of  $N_{\text{side}}^{\text{local}}$  and  $N_{\text{side}}^{\text{global}}$ . Blue circles represent negative, while pink ones represent positive values of  $\tilde{\chi}$ . Larger sized circles denote larger values of  $|\tilde{\chi}|$ . There are no points having values  $3 < |\tilde{\chi}| < 4$  for any of the patches. There are no points in the central regions of the panels because these pixels lie in the masked region of the Galactic plane.

$N_{\text{side}}^{\text{local}}$	$N_{\text{side}}^{\text{global}}$	No of valid patches	No of outlier patches	Patch ids of outlier patches
2	128	28	8	11, 17, 36, 37, 41, 42, 43, 45
	256	29	11	11, 17, 36, 37, 38, 40, 41, 42, 43, 45, 46
4	128	123	22	0, 3, 29, 30, 31, 44, 45, 53, 55, 65, 67, 134, 140, 142, 156, 161, 162, 163, 165, 172, 179, 184
	256	121	23	0, 3, 29, 30, 31, 44, 45, 53, 55, 65, 125, 140, 142, 152, 156, 158, 160, 161, 162, 163, 165, 172, 184

TABLE 5.2: Table showing the numbers of anomalous patches, and their identification numbers. Patches shown in pink have positive value of  $\tilde{\chi}^{(2)}(\nu)$ , while those in blue have negative values of  $\tilde{\chi}^{(2)}(\nu)$  at all anomalous thresholds. The patches that are *not* common between  $N_{\text{side}}^{\text{global}}=128$  and 256 are highlighted by the black boxes.

We first discuss our findings for the case of  $N_{\text{side}}^{\text{local}} = 2$ . From table 5.2 and the top panels of figure 5.5 we observe the following points:

- The number of outlier patches for  $N_{\text{side}}^{\text{global}} = 128$  are 8. All of them have  $\tilde{\chi}$  value between 2 to 3 at one threshold values each, except patch id 42 which is anomalous at two threshold values.
- For  $N_{\text{side}}^{\text{global}} = 256$  there are 11 outlier patches. All the 8 patches identified in the case of  $N_{\text{side}}^{\text{global}} = 128$  form a subset of these. All the common patches have a  $\tilde{\chi}$  value between 2 to 3. Moreover, most of them are found to be anomalous at multiple

FIGURE 5.5:  $\tilde{\chi}$  values for outlier patches versus threshold.

threshold values (mostly on the negative side), as can be seen from a comparison of the top panels of figure 5.5. This confirms that the anomalous behaviour of the patches is not erased by variation of the resolution and that the anomaly is more evident in the case of the higher resolution. Note that the same value of the threshold will not correspond to the same actual field values for  $N_{side}^{global} = 128$  and 256, due to the field rescaling by the respective standard deviations. A patch exhibiting anomalous behaviour at some threshold will show similar behaviour at

a threshold value that is shifted with respect to the former. We can see this, for example, for patch id 11 which is anomalous at only one threshold, namely,  $\nu = 0.75$ , for  $N_{\text{side}}^{\text{global}} = 128$ , while for  $N_{\text{side}}^{\text{global}} = 256$  it is anomalous at  $\nu = -1.75$ . Moreover, the threshold shift need not be the same for all anomalous patches since the fields at the two different resolutions are different due to the inclusion of additional multipoles for the higher resolution.

- The 3 additional outlier patches found in the higher resolution case indicate new information regarding disagreement of the values of  $\kappa$  for multipoles higher than 256 between observed data and FFP10 simulations. Patch ids 40 and 46 have  $\tilde{\chi}$  values between 2 to 3, while patch id 38 is strongly anomalous with  $\tilde{\chi} > 4$ .

Next, we discuss  $N_{\text{side}}^{\text{local}} = 4$ . In this case what we are effectively doing is dividing each patch of  $N_{\text{side}}^{\text{local}} = 2$  into four equal parts and treating each part as a new patch. There is no new information compared to  $N_{\text{side}}^{\text{local}} = 2$  in terms of multipoles of  $\kappa$ . However, the information of anomalous nature of smaller sized regions can get washed out as components of larger regions since in that case,  $\alpha$  will capture the mean alignment of a larger number of structures. The analysis for  $N_{\text{side}}^{\text{local}} = 4$  can isolate such smaller anomalous regions. From table 5.2 and the bottom panels of figure 5.5 we observe the following points:

- The number of outlier patches for  $N_{\text{side}}^{\text{global}} = 128$  are 22, of which 5 have negative  $\tilde{\chi}$ . All the outliers have  $\tilde{\chi}$  values between 2 and 3, while 55 is strongly anomalous with  $\tilde{\chi} > 4$ .
- For  $N_{\text{side}}^{\text{global}} = 256$  we get 23 outliers, out of which 2 have negative  $\tilde{\chi}$  values. All the outliers have  $\tilde{\chi}$  values between 2 and 3, while 45, 152 and 158 are strongly anomalous with  $\tilde{\chi} > 4$ .
- There are 19 common patches. Out of these, we find that patch ids 0, 142 and 161 are anomalous at one threshold each, and the sign of  $\tilde{\chi}$  is different for different  $N_{\text{side}}^{\text{global}}$ . For this reason, we exclude them from the set of outlier patches.

*Sky locations of outlier patches:* Having identified the outlier patches for each value of  $N_{\text{side}}^{\text{local}}$ , we next examine these patches in further detail by visualising their location in the sky. The top row of figure 5.6 shows maps of outlier patches, with the different colours indicating the values of  $\tilde{\chi}$ , for  $N_{\text{side}}^{\text{local}} = 2$  for  $N_{\text{side}}^{\text{global}} = 128$  (left) and  $N_{\text{side}}^{\text{global}} = 256$  (right). The bottom row shows the same for  $N_{\text{side}}^{\text{local}} = 4$ . Dark blue corresponds to  $-3 < \tilde{\chi} < -2$ , yellow corresponds to  $2 < \tilde{\chi} < 3$  and maroon to  $\tilde{\chi} > 4$ . Patches ids in Healpix ring format is also indicated. All maps are shown using Mollweide projection in Galactic coordinates.

As seen in figure 5.6 all the outlier patches for  $N_{\text{side}}^{\text{local}} = 2$  and most of them for  $N_{\text{side}}^{\text{local}} = 4$  have positive  $\tilde{\chi}$ . As discussed in section 5.3.2, positive  $\tilde{\chi}$  is not an indication of a higher level of alignment between the structures. Rather, it indicates that the observed  $\kappa$  field in these patches has a higher number of structures than the simulations. Further, we observe a general trend of increase of statistical significance of anomaly for the higher resolution case for both  $N_{\text{side}}^{\text{local}} = 2$  and 4. For  $N_{\text{side}}^{\text{local}} = 2$ , the higher resolution case has three additional outlier patches, of which one (patch id 38) is very highly anomalous. For  $N_{\text{side}}^{\text{local}} = 4$ , the higher resolution case has two additional outlier patches (patch id 152 and 158), which are highly anomalous, while patch id 45 shows an increase of statistical significance of anomaly. It is useful to mention here that the addition of spatially uncorrelated noise to a given physical random field having some coherence length, in general, increases the number of small-scale structures of the combined field. Hence, positive values of  $\tilde{\chi}$  and the general trend for it to be higher for higher resolution correlate with the fact that the SNR of the observed convergence map decreases with increasing multipole. Therefore, while we cannot conclusively rule out other possibilities, our results strongly suggest that the anomalous behaviour of the outlier patches having positive  $\tilde{\chi}$  are caused by inadequate estimation of the instrumental noise.

We find two patches that have negative  $\tilde{\chi}$  (patch ids 29 and 179 in the bottom left panel of figure 5.6). These are patches where the structures in the observed  $\kappa$  map exhibit relative alignment that is significantly higher (lower value of  $\alpha$ ) than is expected from the simulations. Therefore we conclude that these two patches show a departure from SI at a higher than 95% confidence level. Of these, patch id 29 lies close to the ecliptic

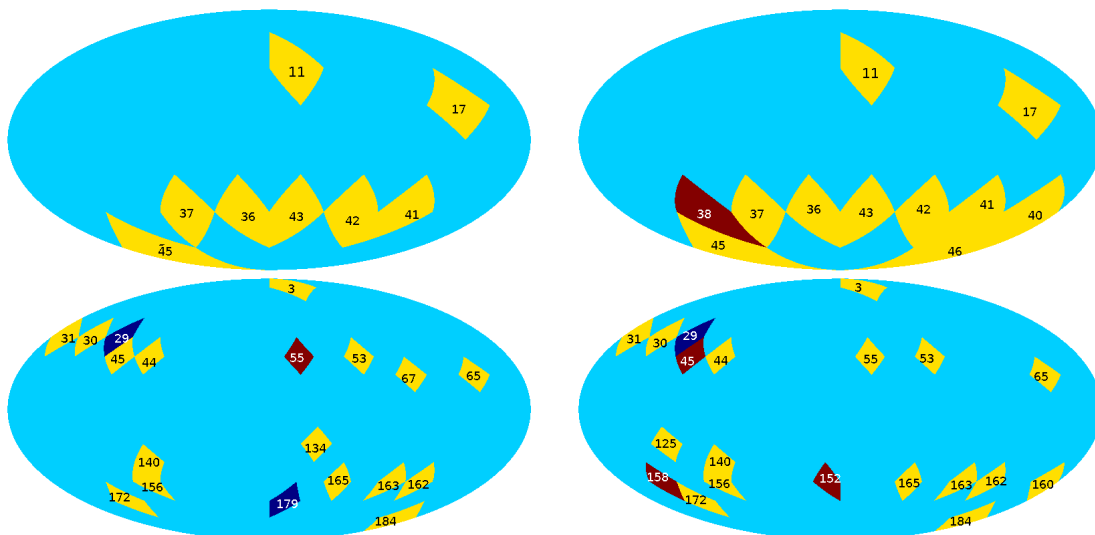


FIGURE 5.6: *Top*: Maps of showing outlier patches for  $N_{\text{side}}^{\text{local}} = 2$  for  $N_{\text{side}}^{\text{global}} = 128$  (left) and  $N_{\text{side}}^{\text{global}} = 256$  (right). The colors indicate the corresponding values of  $\tilde{\chi}$ . Dark blue corresponds to  $-3 < \tilde{\chi} < -2$ , yellow corresponds to  $2 < \tilde{\chi} < 3$  and maroon to  $\tilde{\chi} > 4$ . Patches are numbered in Healpix ring format. *Bottom*: Same as the top row but for  $N_{\text{side}}^{\text{local}} = 4$ . All maps are shown using Mollweide projection in Galactic coordinates.

north pole, while 179 is located close to the ecliptic plane.

We can visually see that several of the outlier patches obtained for  $N_{\text{side}}^{\text{local}} = 4$  are contained within the outlier patches of  $N_{\text{side}}^{\text{local}} = 2$ . Thus, as expected, by subdividing the patches of  $N_{\text{side}}^{\text{local}} = 2$  into smaller parts, we can further isolate or localize the anomalous regions. The regions corresponding to patch ids 29, 30, 31, 44 and 25 for  $N_{\text{side}}^{\text{local}} = 4$  are conspicuously absent for  $N_{\text{side}}^{\text{local}} = 2$ . This indicates that the alignment information has gotten washed out when  $\alpha$  is calculated over larger patch size.

Lastly, it is interesting to note that most outlier patches are located close to either the ecliptic north or south poles or the ecliptic plane. Patch ids 11 and 17 for  $N_{\text{side}}^{\text{local}} = 2$ , and correspondingly 53, 55 and 65 for  $N_{\text{side}}^{\text{local}} = 4$ , lie close to the masked regions (11 and 55 are close to the north Galactic spur) and are possibly contaminated by the residual foreground. It is also interesting to note that patch id 184 lies in the region of the WMAP cold spot.

## 5.4 Conclusion

In this work, we have carried out a statistical isotropy test using the observed Planck convergence map by comparing it with the FFP10 simulations provided by the Planck team. We use the  $\alpha$  statistic for the test, which measures the anisotropy of excursion sets of smooth random fields. We carry out the test using the global (masked) sky and for small sky patches. In order to focus on multipoles where the SNR of the observed convergence map is not too small, we restrict our analysis to  $N_{\text{side}} = 512$  in the global analysis and 256 in the local analysis. The local analysis is complementary to, but more effective than, the global one for detecting anisotropy or any anomalous behaviour of the field in localized sky regions. This is because the anomalous information can get washed out in carrying out the average over a larger set of structures. From the global analysis, we find that the observed data and simulations show good agreement but hint at the presence of some anomaly. Then using the local patch analysis, we identify several anomalous patches where the observed and simulated data show disagreement of the values of  $\alpha$  at statistical significance higher than 95% CL.

From the positive sign of the statistic  $\tilde{\chi}$ , we infer that the source of the anomalous behaviour of most of the outlier patches is an inaccurate estimation of noise. The locations of a majority of the anomalous patches that we have identified are close to either the ecliptic plane or the ecliptic poles. Further, we identify two outlier patches, which exhibit anomalous behaviour originating from departure from SI at higher than 95% CL. One of these is located near the north ecliptic pole, and the other is located close to the ecliptic plane. Though beyond the scope of this analysis, it will be interesting to examine these patches further and cross-correlate them with large-scale structure surveys.

Our local patch analysis is similar in spirit to the analysis carried out in Marques *et al.* (2018), though we use a different methodology. Their method uses the variance, and hence direct field values, computed from sky patches, while  $\alpha$  is constructed using the first derivative of the field and can be directly interpreted as the anisotropy of a curve. Therefore, the anomalous patches identified by our analysis need not be the same as those

identified using the variance. Comparison of figure 5.6 with figures 9 and 10 of Marques *et al.* (2018) shows that there are some patches in common, and both our analysis and theirs indicate that anomalous regions are more likely to occur near the ecliptic poles and ecliptic plane.

Our results broadly confirm that the universe is statistically isotropic on large scales by using a different method from the ones that have previously been used in the literature. We have argued that most of the anomalous regions we have identified can be well explained by inaccurate noise estimation. Hence our method and results will be useful for improved understanding of noise. Each of the anomalous regions, and in particular the two regions that exhibit statistically significant deviation from SI, are interesting for further probes and cross-correlation with large-scale structure surveys.



# Chapter 6

## Contour Minkowski tensor for Gaussian *anisotropic* fields\*

### 6.1 Introduction

The  $\Lambda$ CDM model which is currently the most widely accepted cosmological model rests on the assumption that the universe is statistically isotropic on large scales. It is then required to test this fundamental assumption using different observed data. This assumption of the universe has been directly tested employing different kinds of statistics and cosmological data, for instance, using CMB fields, x-ray background and radio sources, clustering properties of galaxies in large scale structure surveys such as Wiggle-Z and SDSS.

The alignment parameter  $\alpha$  obtained from the Contour Minkowski tensor  $\mathcal{W}_1$  can be used to test SI in cosmological fields. We have tested the Statistical Isotropy (SI) of

---

\*The work presented in this chapter is a part of a paper that will be submitted for publication soon.

the CMB lensing convergence field using the  $\alpha$  statistic as described in Chapter 5. The basic idea how it works is simple. Exact statistical isotropy implies that  $\alpha$  must be unity, which physically means that iso-field boundaries of excursion sets do not exhibit relative alignment. Any alignment will lead to  $\alpha < 1$  and the higher the deviation of value of  $\alpha$  from unity, higher is the degree of alignment. In practice, cosmological data is available on spatial regions of finite extent, such as a subset of flat space, or compact unbounded space such as the surface of the sphere. The finiteness of space combined with the resolution of sampling results in relative alignment of the iso-contours that is intrinsic to the sampling. Any real alignment due to a true departure from statistical isotropy will be in addition to this sampling effect.

We extend the results of Chingangbam *et al.* (2017b) focusing on the contour Minkowski tensor. We give an explicit construction for mapping any arbitrary shaped simple closed curve to an ellipse that is unique upto translations of its centroid. We also carry out a comparison of the shape parameters defined using the contour Minkowski tensor with the filamentarity parameter defined using two scalar Minkowski functionals - area and contour length, and demonstrate that they contain complementary shape information. We present the derivation of analytic expression for the contour Minkowski tensor for Gaussian anisotropic random fields. This work is a part of the full analysis done to understand the meaning of statistical isotropy of smooth random fields from geometrical perspective.

## 6.2 Mapping of a single arbitrary curve to an ellipse, uniqueness and shape anisotropy parameter

In this section we give an explicit construction for mapping any arbitrary shaped simple closed curve  $C$  to an ellipse that is unique upto translation of its centroid.

Consider a curve in 2-D manifold for which we compute CMT ( $\mathcal{W}_1$ ) using the method described in chapter 3. The eigenvalues of  $\mathcal{W}_1$  for an arbitrary curve are given by

$$\lambda_1 = \tau - g, \quad \lambda_2 = \tau + g. \quad (6.1)$$

These equations are same as defined in chapter 3 (equations 3.28 and 3.29). Since  $\mathcal{W}_1$  is real and symmetric, the eigenvalues are real and positive. Then we get  $\tau = (\lambda_1 + \lambda_2)/2$  and  $g = (\lambda_2 - \lambda_1)/2$ . Since  $g$  is positive we have  $\lambda_1 < \lambda_2$ .

For an ellipse whose principal axes are denoted by  $p$  and  $q$ , with  $p < q$  and are aligned along the coordinate axes, its  $\mathcal{W}_1$  is diagonal with the eigenvalues given by

$$\lambda_1 = (pq)^2 \int_0^{2\pi} \frac{\cos^2 t}{(p^2 \sin^2 t + q^2 \cos^2 t)^{3/2}} dt, \quad (6.2)$$

$$\lambda_2 = (pq)^2 \int_0^{2\pi} \frac{\cos^2 t}{(p^2 \cos^2 t + q^2 \sin^2 t)^{3/2}} dt. \quad (6.3)$$

Hence, given  $p, q$  we can determine  $\lambda_1, \lambda_2$ .

Now, the question that we are asking is - given  $\lambda_1, \lambda_2$  computed for an arbitrary closed curve, can we invert equations 6.2 and 6.3 to determine  $p, q$  of an ellipse corresponding to a curve, such that their perimeters are same. The perimeter of the ellipse is given by  $P = 4qE(\pi/2, e)$ , where  $e = \sqrt{1 - p^2/q^2}$  is the ellipticity, and  $E$  is the complete Elliptic integral of the second kind. We must also have  $P = (\lambda_1 + \lambda_2)/2$ . We know that  $E$  is a monotonous function of  $e$  which implies that there is a one-to-one invertible mapping between  $e, P$  and  $p, q$ . There must exist a one-to-one mapping from  $\lambda_1, \lambda_2$  to  $p, q$ . Therefore, for any arbitrary simple closed curve there is an unique ellipse corresponding to it. The ellipse is unique upto rotations and translations. If we include the orientation information about the curve contained in  $\varphi$ , the orientation of the ellipse also gets fixed.

Mapping of a curve to an unique ellipse can easily be generalized from flat 2-D to the surface of the sphere. An ellipse on the surface of the sphere, is defined as the locus of points which have the sum of the geodesic distances from the two loci constant.

Further, we know that  $\beta$  as defined in chapter 3, to be the ratio of the eigenvalues

$$\beta \equiv \frac{\lambda_1}{\lambda_2}. \quad (6.4)$$

quantify the anisotropy of a given arbitrary curve. We can expand  $\beta$  using equation 6.1 in terms of  $g/\tau$  as

$$\beta = \frac{\tau - g}{\tau + g} = 1 - 2\frac{g}{\tau} + 2\frac{g^2}{\tau^2} - \mathcal{O}\left(\frac{g^3}{\tau^3}\right). \quad (6.5)$$

The value of  $g$  lies between 0 and  $\infty$ , while  $\beta$  lies between zero and one. We get  $\beta$  equal to one for a closed curve having  $m$ -fold symmetry, with  $m \geq 3$ . Deviation of  $\beta$  from one, or  $g$  from zero indicates anisotropy of the curve as discussed in Chapter 3. Note that  $g$ , or  $g/\tau$ , or  $\beta$  are complementary measures of intrinsic anisotropy of the curve. Which among three is best suited for statistical analysis will be determined by the size of the standard deviation when applied to random fields. We have checked that for random fields, the statistical fluctuations of  $\beta$  are considerably smaller than that of  $g$ . This is due to cancellation of the fluctuations when taking ratio of the eigenvalues. Hence  $\beta$  is better suited as an anisotropy parameter. We are not showing here the relevant plots supporting this argument, but they will be part of the paper to be submitted soon.

### 6.2.1 Distribution of many curves and their relative alignment

We will now carry forward the idea of mapping of an arbitrary closed curve to an ellipse to describe the distribution of many such arbitrary shaped smooth simple curves.

For simplicity let us first consider two closed curves  $C'$  and  $C''$ . Let their CMTs be  $\mathcal{W}'_1$  and  $\mathcal{W}''_1$ . The tensor sum  $\widetilde{\mathcal{W}}_1 \equiv \mathcal{W}'_1 + \mathcal{W}''_1$  is

$$\widetilde{\mathcal{W}}_1 = \begin{pmatrix} (\tau' + g'_1) + (\tau'' + g''_1) & g'_2 + g''_2 \\ g'_2 + g''_2 & (\tau' - g'_1) + (\tau'' - g''_1) \end{pmatrix}, \quad (6.6)$$

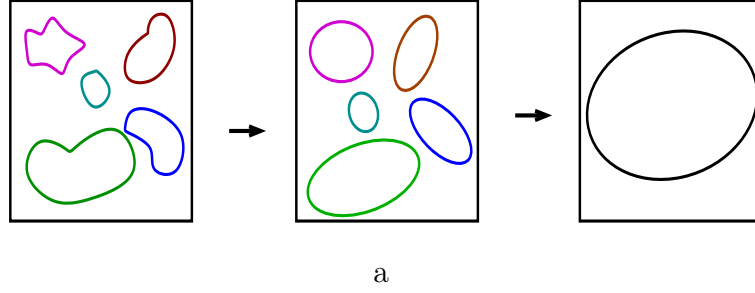


FIGURE 6.1: Schematic diagram for mapping from a distribution of curves (left panel) to a distribution of ellipses (a) in the middle panel to a single unique ellipse in the right panel.

Let us now define,

$$\tau \equiv (\tau' + \tau''), \quad g_1 \equiv (g_1' + g_1''), \quad g_2 \equiv (g_2' + g_2''), \quad (6.7)$$

$$\varphi \equiv \tan^{-1} \left( \frac{g_1}{g_2} \right). \quad (6.8)$$

Using the mapping between eigenvalues and principle axes of an ellipse described earlier we can construct the ellipse that corresponds to  $\widetilde{\mathcal{W}}_1$ . It is now straightforward to generalize the mapping for a distribution of many curves. Figure 6.1 shows a schematic diagram showing mapping of many curves to a final single ellipse. The middle panel in the figure shows a distribution of ellipses, each one corresponding to each arbitrary closed curve shown in the left panel. Mapping distribution of curves in left panel first to the distribution of ellipses in the middle panel and then finally to a single ellipse in the right panel, is equivalent to directly mapping distribution of arbitrary closed curves shown in left panel to a single ellipse.

*Alignment parameter:* Given a spatial distribution of many curves the relative alignment between the curves is encoded in the parameter,

$$\alpha \equiv \frac{\Lambda_1}{\Lambda_2}, \quad (6.9)$$

where  $\Lambda_1$  and  $\Lambda_2$  are the eigenvalues of  $\widetilde{\mathcal{W}}_1$  such that  $\Lambda_1 \leq \Lambda_2$ . By definition we have  $0 \leq \alpha \leq 1$ .  $\alpha$  gives a measure of the deviation from rotational symmetry in the distribution of structures. For randomly oriented structures with no preferred direction

$\alpha = 1$ . For  $\alpha < 1$ , its values gives the degree of anisotropy, while the direction information is contained in  $\varphi$  obtained from  $\widetilde{\mathcal{W}}_1$ . For a single curve we have  $\alpha = \beta$ . All this has already been described in Chapter 3, just for the completeness and aid the understanding of concepts presented in this chapter we are describing them here again.

Just as done for  $\beta$  we can expand  $\alpha$  in terms of  $g/\tau$  as

$$\alpha = \frac{\tau - g}{\tau + g} = 1 - 2\frac{g}{\tau} + 2\frac{g^2}{\tau^2} - \mathcal{O}\left(\frac{g^3}{\tau^3}\right). \quad (6.10)$$

This expression for  $\alpha$  shows that there can be degeneracy between the number of structures and the total perimeter, in the way  $\alpha$  captures the information of alignment. Any disproportionate change of  $\tau$  and  $g$  will make  $\alpha$  change, with the shift either towards one or towards zero determined by increase or decrease of their ratio.

### 6.3 Comparison with shape finders

Shapefinders comprise a set of geometric parameters derived from scalar Minkowski functionals to describe the geometry and topology of structures or individual objects (Sahni *et al.* 1998). MFs are themselves morphological descriptors; shapefinders can provide information about the characteristic dimensions of an object, for example, the filamentarity of a filament which is a part of the cosmic web. In this section, we compare the information contained in  $\alpha$  and  $\beta$  about the morphology of structures with that obtained from the shapefinders.

Using scalar MFs  $V_0$  (area enclosed by the curve) and  $V_1$  (contour length) one can define the *filamentarity* parameter (Sahni *et al.* 1998; Shandarin 2004; Bharadwaj *et al.* 2000):

$$F(\nu) = \frac{V_1^2 - V_0}{V_1^2 + V_0}. \quad (6.11)$$

$F$  gives a measure of the elongation or the filamentarity of a structure. Its value lies between 0 and 1.  $F$  value close to one implies highly elongated structure.

Now, we want to compare the information content encoded in three shape parameters  $F$ ,  $\alpha$  and  $\beta$ , i.e., how anisotropy of structures show up in each of these parameters.

To do so we have taken two simple examples of sums of Gaussian functions/fields given by

$$f(x, y) = \sum_{i=1}^n \exp \left\{ -\frac{(x - x_i)^2 + (y - y_i)^2}{2\sigma_i^2} \right\}, \quad (6.12)$$

such that the Gaussian peak locations  $x_i, y_i, \sigma_i$  are chosen depending on how we want to arrange the iso-contours. We have computed shape parameters  $\alpha$ ,  $\beta$  and  $F$  for the two Gaussian fields using the method 2 (using identification of contours in pixel space) described in chapter 3.

The top panels of figure 6.2 show two examples of  $f$  where  $x_i, y_i$  are arranged linearly (left) and curvilinearly (right). The figure shows systematic variation of the iso-contours shape, size and their number as a function of threshold value of the field. The bottom panels show  $\alpha$ ,  $\beta$  and  $F$  for the functions in the corresponding panel above. The thresholds at which the iso-contours percolate are marked by the dotted lines. We find that for both the cases  $F$  decreases only mildly as the contours shrink, till each fragmentation occurs where it exhibits discontinuity. This is as expected because the perimeter and area enclosed within it decrease proportionately. In particular  $F$  detects elongation of the structures but is not sensitive to whether a structure is linear or curved. Note that we do not show  $F$  for individual structures after fragmentation.  $\alpha$ , on the other hand, is strongly sensitive to the variation in the iso-contours with threshold. Therefore, it contains more information about the morphology (shape and distribution) of the curves compared to  $F$ . However, the caveat is that it will not sensitively distinguish a structure which is, say, mildly elliptical from one which is elongated but curved, such as the example on the right panel of figure 6.2. Therefore, for practical applications it will be best to use a combination of both  $F$  and  $\alpha$  to get complete morphological information about a structure. However, the knowledge of direction/orientation of the curve, encoded in  $\varphi$

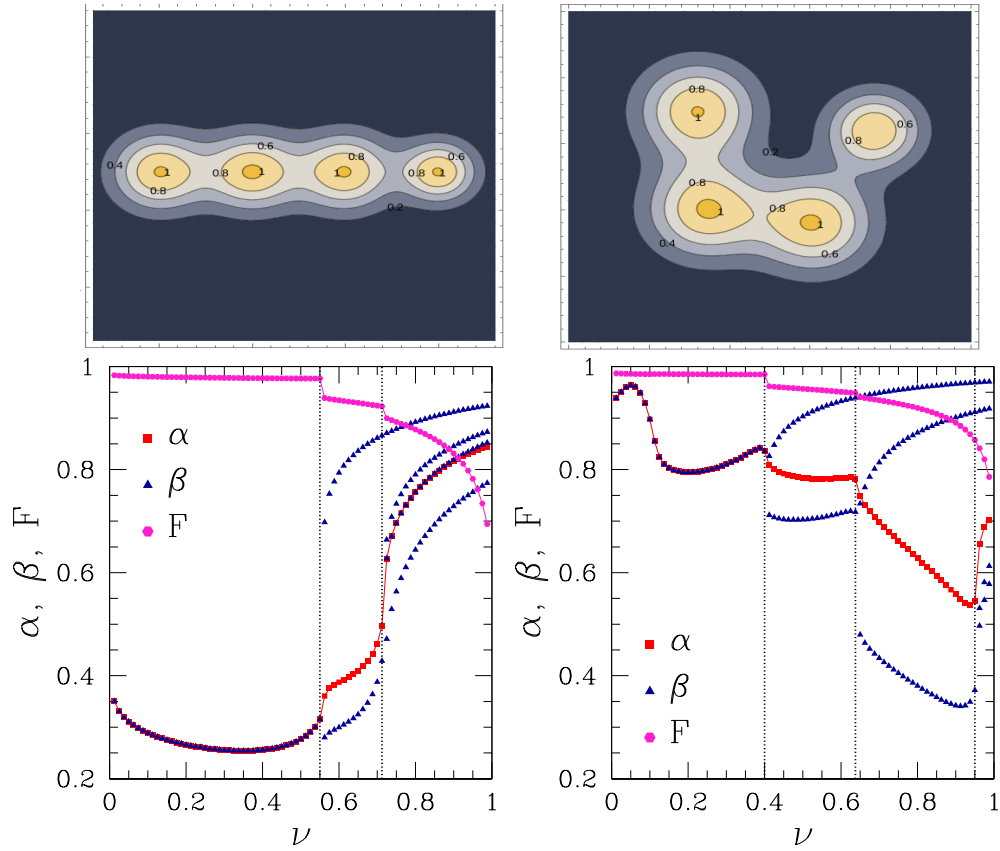


FIGURE 6.2: *Top*: Iso-contours for two functions given by eq. 6.12 with peak locations arranged linearly (left) and non-linearly (right). *Bottom*:  $F$ ,  $\alpha$  and  $\beta$  for individual structures after fragmentation versus threshold, for the corresponding function in the panel above. The percolation thresholds are indicated by the black dashed lines.

(equation 3.27) obtained from CMT is not contained in the scalar MFs.

It is also interesting to observe the behaviour of  $\beta$  for individual structures. As we can see in the bottom panels of figure 6.2, till the first fragmentation there is only structure and so  $\alpha = \beta$ . After each fragmentation threshold the blue curve for  $\beta$  bifurcates into two curves for each individual structure. We can track the evolution of morphology of each structure as a function of threshold.



## 6.4 Ensemble expectation value of $\widetilde{\mathcal{W}}_1$ for Gaussian anisotropic fields

Current observations indicate that cosmological fields are Gaussian and isotropic on large scales. However, on small scales, we see a deviation from both Gaussianity and isotropy. For example, the non-linear gravitational evolution of matter density field introduces non-Gaussianity on small scales. In order to employ MTs for probing anisotropy and non-Gaussianity of cosmological fields, it is desirable to derive analytic expressions, if possible, so that we can infer physical effects correctly when we compute them from observed data. As a first step, we have derived an analytic expression for the CMT for Gaussian anisotropic fields in two dimensions. Our results hold for fields in both flat and curved spaces.

Let us consider the random  $3 \times 1$  matrix  $\mathbf{X} \equiv (u, u_{;1}, u_{;2})$ . Each element is given to be Gaussian random variable. So the joint PDF of  $u, u_{;1}, u_{;2}$  is given by the Gaussian form

$$P_\nu(\mathbf{X}) = \frac{1}{\sqrt{2\pi \text{Det}\Sigma}} \exp\left(-\frac{1}{2}\mathbf{X}^T \Sigma^{-1} \mathbf{X}\right), \quad (6.13)$$

where  $\Sigma$  is the covariance matrix.

Given that the field  $u$  is homogeneous and *anisotropic* we model the covariance matrix as

$$\Sigma = \begin{pmatrix} \sigma_0^2 & 0 & 0 \\ 0 & \sigma_{u_1}^2 & 0 \\ 0 & 0 & \sigma_{u_2}^2 \end{pmatrix}, \quad (6.14)$$

where

$$\langle uu_{;i} \rangle = 0, \quad \langle u_{;i}^2 \rangle \equiv \sigma_{u_{;i}}^2 \equiv \sigma_{u_i}^2, \quad \langle u_{;1} u_{;2} \rangle = 0, \quad (6.15)$$

$i = 1, 2$ . The cross correlations  $\langle uu_i \rangle$  and  $\langle u_{;1}u_{;2} \rangle$  are zero even for anisotropic fields since the fields  $u, u_{;1}, u_{;2}$  are independent of each other, regardless of the nature or symmetry properties of the field.

In general  $\sigma_{u_{;1}}^2$  and  $\sigma_{u_{;2}}^2$  are function of the threshold. Such dependence can be due to the sampling effect. Hence, we consider threshold dependence of sigmas of the first derivatives of the field. However, we also assume that the sampling effect does not induce inhomogeneity and departure from Gaussian nature of the field. Then,  $P_\nu(\mathbf{X})$  becomes

$$P_\nu(\mathbf{X}) = \frac{1}{\sqrt{2\pi\sigma_0^2\sigma_{u_1}^2\sigma_{u_2}^2}} \exp \left\{ -\frac{1}{2} \left( \frac{u^2}{\sigma_0^2} + \frac{u_{;1}^2}{\sigma_{u_1}^2} + \frac{u_{;2}^2}{\sigma_{u_2}^2} \right) \right\}, \quad (6.16)$$

where the index  $\nu$  on  $P$  is to remind us that it can be dependent on  $\nu$  via  $\Sigma$ . On the RHS  $\nu$  is not explicitly written.

In the following we will use this PDF to discuss ensemble expectations of  $\widetilde{\mathcal{W}}_1$ .

### 6.4.1 Ensemble expectation of $\widetilde{\mathcal{W}}_1$

The ensemble expectation value of the  $(i, j)$  element of  $\widetilde{\mathcal{W}}_1$  at threshold  $\nu$  is obtained to be

$$\langle \widetilde{\mathcal{W}}_1 \rangle_{ij} = \int_{-\infty}^{\infty} du \int_{-\infty}^{\infty} du_1 \int_{-\infty}^{\infty} du_2 P_\nu(\mathbf{X}) \left( \widetilde{\mathcal{W}}_1 \right)_{ij} \quad (6.17)$$

$$= \frac{1}{N} \int du \delta(u - \nu) e^{-\frac{u^2}{2\sigma_0^2}} F_{ij} \quad (6.18)$$

$$= \frac{1}{N} e^{-\frac{\nu^2}{2\sigma_0^2}} F_{ij}. \quad (6.19)$$

where  $F_{ij}$  is given by

$$F_{ij} = \int_{-\infty}^{\infty} du_1 \int_{-\infty}^{\infty} du_2 \exp\left(-\frac{u_{;1}^2}{2\sigma_1^2} - \frac{u_{;2}^2}{2\sigma_2^2}\right) (\widetilde{\mathcal{W}}_1)_{ij} \quad (6.20)$$

The normalization factor  $\frac{1}{N}$  is

$$\frac{1}{N} = \frac{1}{\sqrt{2\pi \det \Sigma}} = \frac{1}{\sqrt{2\pi \sigma_0^2 \sigma_1^2 \sigma_2^2}}. \quad (6.21)$$

For 22 element we have :

$$F_{22} = \int_{-\infty}^{\infty} du_1 u_1^2 e^{-u_1^2/2\sigma_1^2} \int_{-\infty}^{\infty} du_2 e^{-u_2^2/2\sigma_2^2} \frac{1}{\sqrt{u_1^2 + u_2^2}}, \quad (6.22)$$

Carry out  $u_2$  integration first using the following integral (page 367 Gradsteyn & Ryzik)

$$\int_{-\infty}^{\infty} dx e^{-px^2} \frac{1}{\sqrt{a^2 + x^2}} = e^{a^2 p/2} K_0\left(\frac{a^2 p}{2}\right), \quad (6.23)$$

where

$$K_0(x) = \int_0^{\infty} \frac{\cos xt}{\sqrt{1+t^2}} dt \quad (6.24)$$

Using this we get,

$$F_{22} = \int_{-\infty}^{\infty} du_1 u_1^2 \exp\left[-\frac{u_1^2}{2\sigma_1^2} \left(1 - \frac{\sigma_1^2}{2\sigma_2^2}\right)\right] K_0\left(\frac{u_1^2}{4\sigma_2^2}\right) \quad (6.25)$$

$$= \int_0^{\infty} dt \frac{1}{\sqrt{1+t^2}} \int_{-\infty}^{\infty} du_1 u_1^2 \exp\left[-\frac{u_1^2}{2\sigma_1^2} \left(1 - \frac{\sigma_1^2}{2\sigma_2^2}\right)\right] \cos\left(\frac{u_1^2 t}{4\sigma_2^2}\right) \quad (6.26)$$

For carrying out  $u_1$  integral, we can use (page 507 Gradsteyn & Ryzik)

$$\int_{-\infty}^{\infty} dx x^2 \cos(Ax^2) e^{-Bx^2} = \frac{\sqrt{\pi}}{2B^{3/2}[(A/B)^2 + 1]^{3/4}} \cos\left(\frac{3}{2} \tan^{-1} \frac{A}{B}\right) \quad (6.27)$$

Here

$$A = \frac{t}{4\sigma_2^2} = at, \quad B = \frac{1}{2\sigma_1^2} \left(1 - \frac{\sigma_1^2}{2\sigma_2^2}\right). \quad (6.28)$$

Let

$$D = \frac{\sigma_2^2}{2\sigma_2^2 - \sigma_1^2} \left(\frac{\sigma_1}{\sigma_2}\right)^2, \quad (6.29)$$

then,

$$\frac{A}{B} = \frac{a}{B}t = Dt. \quad (6.30)$$

So,

$$F_{22} = \frac{\sqrt{\pi}}{2B^{3/2}} \int_0^\infty dt \frac{1}{\sqrt{1+t^2}} \frac{1}{(1+D^2t^2)^{3/4}} \cos\left(\frac{3}{2} \tan^{-1} Dt\right) \quad (6.31)$$

Let

$$\tan^{-1} Dt = y, \quad \Rightarrow t = \frac{1}{D} \tan y \quad (6.32)$$

$$dy = \frac{1}{1+D^2t^2} Ddt. \quad (6.33)$$

This gives,

$$F_{22} = \frac{\sqrt{\pi}}{2B^{3/2}D} \int_0^{\pi/2} dy \frac{1}{\sqrt{1+\tan^2 y/D^2}} (1+\tan^2 y)^{1/4} \cos\left(\frac{3}{2}y\right) \quad (6.34)$$

$$= \frac{\sqrt{\pi}}{2B^{3/2}} \underbrace{\int_0^{\pi/2} dy \frac{1}{\sqrt{D^2+\tan^2 y}} \frac{1}{\sqrt{\cos y}} \cos\left(\frac{3}{2}y\right)}_{\quad} \quad (6.35)$$

We can obtain other elements of  $F_{ij}$  by carrying out similar steps. Combining everything we finally obtain the expression for the ensemble expectation of  $\widetilde{\mathcal{W}}_1$  as,

$$\langle \widetilde{\mathcal{W}}_1 \rangle = \frac{2\sqrt{2}}{\sigma_0} \begin{pmatrix} A_1 f_1 & 0 \\ 0 & A_2 f_2 \end{pmatrix} e^{-\frac{\nu^2}{2\sigma_0^2}}, \quad (6.36)$$

where

$$A_1 = \frac{\sigma_{u_1}^2 \sigma_{u_2}^2}{(2\sigma_{u_2}^2 - \sigma_{u_1}^2)^{3/2}}, \quad A_2 = \frac{\sigma_{u_1}^2 \sigma_{u_2}^2}{(2\sigma_{u_1}^2 - \sigma_{u_2}^2)^{3/2}}. \quad (6.37)$$

The factor  $f_i$ , for  $i = 1, 2$ , is given by

$$f_i = \int_0^{\pi/2} dy \frac{1}{\sqrt{D_i^2 + \tan^2 y}} \frac{1}{\sqrt{\cos y}} \cos\left(\frac{3}{2}y\right), \quad (6.38)$$

with

$$D_1 = \frac{\sigma_{u_1}^2}{2\sigma_{u_2}^2 - \sigma_{u_1}^2}, \quad D_2 = \frac{\sigma_{u_2}^2}{2\sigma_{u_1}^2 - \sigma_{u_2}^2}. \quad (6.39)$$

From equation 6.36 we get  $g_2 = 0$ . Also, we can express  $\langle \tau \rangle$  and  $\langle g_1 \rangle$  as

$$\langle \tau(\nu) \rangle = \frac{\sqrt{2}}{\sigma_0} \left( A_1 f_1 + A_2 f_2 \right) e^{-\frac{\nu^2}{2\sigma_0^2}} \quad (6.40)$$

$$\langle g_1(\nu) \rangle = \frac{\sqrt{2}}{\sigma_0} \left( A_2 f_2 - A_1 f_1 \right) e^{-\frac{\nu^2}{2\sigma_0^2}}. \quad (6.41)$$

Equation 6.40 generalizes the well known expression for the second scalar MF, the contour length, for Gaussian isotropic fields to Gaussian but anisotropic fields.

If  $\sigma_{u_1}^2 = \sigma_{u_2}^2$ , then equation 6.36 gives

$$\langle \widetilde{\mathcal{W}}_1 \rangle = \frac{1}{8r_c} e^{-\nu^2/2} \times \mathbf{I} \times \mathcal{A}, \quad (6.42)$$

where  $\mathbf{I}$  is the identity matrix, and  $r_c$  is the correlation length of the field given by  $r_c = \sigma_0/\sigma_{u_1}$ . This is the expression obtained in Chingangbam *et al.* (2017b). Hence, we recover the result for a Gaussian isotropic field.

## 6.5 Conclusion

In this work we have addressed the question of statistical isotropy of smooth random fields in two dimensions from a geometrical perspective, building on our earlier work Chingangbam *et al.* (2017b). We use the CMT to construct a mapping of an arbitrary closed curve to an ellipse that is unique upto translations of the centroid. We show that the shape parameters that are defined using the CMT, and the filamentarity that is defined using the scalar MFs (area and the perimeter), carry complementary shape information. Therefore, using a combination of both will maximize extraction of shape information in practical applications. Next we focus on CMT for Gaussian anisotropic fields. We obtained an analytical expression for the ensemble expectation value of  $\widetilde{\mathcal{W}}_1$ . This will be useful to probe various physical processes that generate anisotropy in cosmological fields

like CMB. We plan to extend the analysis to address the question of geometrical meaning of statistical isotropy in three dimensional space.

# Chapter 7

## Constraining primordial non-Gaussianity using Minkowski tensors and Betti numbers\*

Morphological descriptors scalar MFs have been widely used to constrain primordial non-Gaussianity in CMB and large-scale structure datasets. The topological observables MTs and Betti numbers contain additional information in comparison to SMFs. Hence, we speculate that we can obtain significant improvement in constraints on  $f_{NL}$  parameter using MTs and Betti numbers. In this chapter, we discuss some investigations that are ongoing in this direction. We first briefly review the primordial non-Gaussianity sources and parametrization of a particular type of non-Gaussianity in section 7.1. This is followed by a brief outline of the simulations of non-Gaussian CMB maps in section 7.2. Further, we will present some preliminary results for this problem in the section 7.3 and discuss the further plans of this project in section 7.4.

---

\*This chapter contains material from paper in preparation

## 7.1 Review of primordial non-Gaussianity

Observations of cosmological fluctuations from CMB and large-scale structure strongly support the standard inflationary paradigm, predicting primordial fluctuations to be nearly scale-invariant, adiabatic, and Gaussian. However, all inflationary models that generate primordial perturbations predict a certain degree of primordial non-Gaussianity (PNG). The predicted degree of PNG is model-dependent. The amplitude of PNG is usually described in terms of a dimensionless nonlinearity parameter  $f_{NL}$ . Different models of inflation predict different amount of  $f_{NL}$ , starting from  $\mathcal{O}(1)$  to  $f_{NL} \sim 100$ . Non-Gaussianity from the simplest inflation models that are based on a slowly rolling scalar field is very small; however, a substantial class of more general models with, for example, multiple scalar fields, features in inflaton potential, nonadiabatic fluctuations, noncanonical kinetic terms, deviations from Bunch-Davies vacuum, among others generates substantially higher amounts of PNG. Two broad classes of PNG arising from various inflation models are: PNG of equilateral type (Alishahiha *et al.* 2004; Chen 2005; Langlois *et al.* 2008) and PNG of local type (Verde *et al.* 2000; Komatsu and Spergel 2001). Here, we focus on PNG of the local type, which has a simple form,

$$\Phi(r) = \Phi_L(r) + f_{NL}\Phi_{NL}(r), \quad (7.1)$$

where  $\Phi_{NL}$  is defined as

$$\Phi_{NL}(r) = \Phi_L^2(r) - \langle \Phi_L^2(r) \rangle. \quad (7.2)$$

Here  $\Phi$  is the non-Gaussian primordial gravitational potential which is the sum of two terms: linear part ( $\Phi_L$ ) and a non-linear ( $\Phi_{NL}$ ) part.  $\Phi$  sets the initial conditions for the theoretical calculation of CMB temperature and polarization anisotropies. Hence the signatures about PNG will be imprinted in the CMB fluctuations.

To capture non-Gaussianity in cosmological observations, we have to go beyond the two-point statistics, i.e., beyond two-point correlation function and its counterpart in Fourier



space, power spectrum. Small non-Gaussianity in the CMB motivates perturbative methods to characterize it, i.e. third, fourth moment (bispectrum, trispectrum, etc) are well motivated. The measurement of the bispectrum or the three-point correlation function of the CMB anisotropies is one of the most promising and clean ways of constraining primordial  $f_{NL}$ . Large-scale structure observations contain not only the PNG but also the late-time non-Gaussianity from gravitational instability and galaxy biasing, which potentially obscure the primordial signatures.

The tightest constraints on local type PNG are  $f_{NL} = -0.9 \pm 5.1$  at 68% CL from Planck 2018 measurements of the three-point correlation function of the CMB temperature and polarization anisotropies (Planck Collaboration *et al.* 2020d), and  $-51 < f_{NL} < 21$  at 95% CL from eBOSS DR14 data (Castorina *et al.* 2019). Foreground contamination, instrumental noise, and many secondary effects like weak lensing of CMB, late time integrated Sachs wolfe (ISW) effect, also generate non-Gaussian features in cosmological fields. Cosmic variance also introduces some NG due to the uniqueness of the observed CMB sky. PNG signal is mixed with all these other sources of NG. Hence the search for primordial non-Gaussianity is a challenging task.

To detect signatures of PNG in cosmological fields, we must use different statistical observables in real space and the Fourier domain. This approach is helpful since different statistical observables are sensitive to different aspects of non-Gaussianity, and hence they help disentangle PNG and non-Gaussianity from other sources. Commonly used observables in Fourier space to study NG signatures in CMB are bispectrum, trispectrum (Komatsu and Spergel 2001), the spherical Mexican hat wavelet, etc. Wavelets are kind of in between the Fourier domain and real space statistical tools which are used to investigate non-Gaussianity in cosmology. Real space statistics like skewness, kurtosis, Betti numbers, Minkowski functionals, and Minkowski tensors can provide complementary information on non-Gaussianity in cosmological fields. Minkowski functionals have been extensively studied and employed to investigate non-Gaussianity in CMB (Gott *et al.* 1990; Schmalzing and Gorski 1998; Novikov *et al.* 2000; Hikage *et al.* 2006; Chingangbam and Park 2009; Ducout *et al.* 2013; Chingangbam *et al.* 2017a; Buchert *et al.*

2017; Planck Collaboration *et al.* 2020d). Minkowski tensors (MTs) which are the tensor generalization of SMFs, carry extra degrees of freedom, i.e., additional information related to intrinsic anisotropy and alignment of structures as discussed in Chapter 3 of this thesis. It may be possible that MTs can constrain specific cosmological parameters better than possible with SMFs. Therefore, we plan to compare the constraints on PNG parameter  $f_{NL}$  obtained from MFs and MTs. We study imprints of PNG of local-type in CMB temperature and  $E$ -mode polarization fields.

## 7.2 Simulation of non-Gaussian CMB maps

In order to investigate non-Gaussianity in CMB using different statistical observables, one needs to first simulate high-resolution CMB maps containing non-Gaussianity. Here, we briefly describe the method first proposed by Liguori *et al.* (2003, 2007) and developed further in Elsner and Wandelt (2009) to generate CMB simulation with PNG. Below we outline the steps for simulating non-Gaussian CMB maps:

- Generate the multipole moments of a purely Gaussian gravitational potential  $\Phi_{L,\ell m}(r)$  as a function of the conformal distance in two steps,
  - Computation of radial correlation function or the covariance matrix of the gravitational potential given as

$$\begin{aligned} P_{\Phi\ell}(r_1, r_2) &\equiv \langle \Phi_{L,\ell_1 m_1}(r_1) \Phi_{L,\ell_2 m_2}^*(r_2) \rangle \\ &= 4\pi \delta_{\ell_1 \ell_2} \delta_{m_1 m_2} \int dk \frac{k^2 \mathcal{P}(k)}{2\pi^2} j_{\ell_1}(kr_1) j_{\ell_2}(kr_2), \end{aligned} \quad (7.3)$$

where  $\mathcal{P}(k)$  is the primordial power spectrum predicted by inflation.

- Then a random realization of the linear gravitational potential at distances  $\mathbf{r} = (r_1, r_2, r_3, \dots, r_n)$  is given by

$$\Phi_{L,\ell m}(r) = P_{\Phi\ell}^{1/2} \cdot \mathbf{g}, \quad (7.4)$$

where  $g$  is a vector of independent complex Gaussian random variables with zero mean and unit variance.

- Compute the inverse spherical harmonic transform to derive the corresponding expression in pixel space,  $\Phi_L(r)$ .
- Square the linear term  $\Phi_L$  and subtract the variance according to Eqn 7.2 to get the non-Gaussian potential  $\Phi_{NL}(r)$ .
- Transform to spherical harmonic space to obtain  $\Phi_{NL,\ell m}(r)$ .
- Solve the following integral

$$a_{L,\ell m}^X = \frac{(-i)^\ell}{2\pi^2} \int dk k^2 \Phi_{L,\ell m}(k) \Delta_\ell^X, \quad (7.5)$$

where  $\Delta_\ell^X$  is the radiation transfer function. Non-linear spherical harmonic coefficients ( $a_{NL,\ell m}^X$ ) are obtained by replacing the linear term,  $\Phi_{L,\ell m}$ , with the non-linear term  $\Phi_{NL,\ell m}$ .

- The spherical harmonic coefficients of a map with local-type primordial non-Gaussianity,  $f_{NL}$ , can be calculated as

$$a_{\ell m}^X = a_{L,\ell m}^X + f_{NL} \cdot a_{NL,\ell m}^X. \quad (7.6)$$

We use publicly available simulations by Elsner and Wandelt which were generated following the steps described above. The maximum resolution of these maps is fixed by the maximum multipole  $\ell_{max} = 1024$  and  $N_{side} = 512$ . These maps were simulated with the cosmological parameters obtained from WMAP + BAO + SN data:  $\Omega_\Lambda = 0.721$ ,  $\Omega_c h^2 = 0.1143$ ,  $\Omega_b h^2 = 0.02256$ ,  $n_s = 0.96$ ,  $A_s = 2.457 \times 10^{-9}$ .

### 7.3 Prospects of using Minkowski tensors and Betti numbers to constrain primordial non-Gaussianity

Topological observables like the genus and the betti numbers have been employed to study primordial non-Gaussianity in CMB and large scale structure data. Chingangbam *et al.* (2012) demonstrated that Betti numbers  $\beta_0$  and  $\beta_1$ , which are the count of hot spots and cold spots in the context of CMB, are sensitive to non-Gaussianity in CMB. They found the characteristic non-Gaussian deviation shapes of  $\beta_0$  and  $\beta_1$  for each distinct model of non-Gaussianity considered in their work. They also showed that the Betti numbers contain additional information compared to the genus and hence, are valuable statistical observables to probe non-Gaussianity. We will not show any results using Betti numbers. Nevertheless, we mention them as they complete the full set of morphological statistics. This work compares MFs and MTs to check if MTs can provide more information on PNG than MFs. Since MTs contain more degrees of freedom, we expect they can constrain PNG better than scalar MFs. We discuss our analysis below and present some preliminary results.

We have considered local-type PNG, which is parameterized by the  $f_{NL}$  parameter. We used Elsner's simulation to generate 1000 realizations of non-Gaussian CMB maps having local type PNG. We then compute MTs  $\mathcal{W}_1$  and  $\mathcal{W}_2$ , and their respective trace, which are the corresponding scalar MFs  $V_1$  and  $V_2$ . MTs and scalar MFs are computed for 33 equally spaced threshold bins from  $-4 \leq \nu \leq 4$  using the field derivative method outlined in Chapter 3. The resolution of the map we used is given by HEALPix resolution parameter,  $N_{side} = 512$ . We smoothed the maps with a Gaussian smoothing kernel having FWHM=30'. We have taken  $f_{NL} = 10$ .

We then compute  $\Delta\mathcal{W}$  and  $\Delta Tr$  which is the difference between MTs of non-Gaussian field and corresponding Gaussian field and are defined as,

$$(\Delta\mathcal{W}_1)_{ii} = (\mathcal{W}_1^{NG})_{ii} - (\mathcal{W}_1^G)_{ii}, \quad (7.7)$$

$$(\Delta\mathcal{W}_2)_{ii} = (\mathcal{W}_2^{NG})_{ii} - (\mathcal{W}_2^G)_{ii}, \quad (7.8)$$

$$\Delta Tr(\mathcal{W}_i) = Tr(\mathcal{W}_i^{NG}) - Tr(\mathcal{W}_i^G), \quad (7.9)$$

where  $i = 1, 2$ .

We now quantify the gain in information by comparing the signal to noise ( $S/N$ ), which is defined as the ratio of the mean and standard deviation of the quantities defined in equations 7.7-7.9. The standard deviation is given by sample variance of 1000 realizations used here. Our results are shown in figure 7.1. The top two panels show a comparison of  $S/N$  for individual elements of  $\Delta\mathcal{W}_i$ , where  $i = 1, 2$ , their trace and  $S/N$  of the diagonal elements of  $\mathcal{W}_1$  and  $\mathcal{W}_2$  combined in quadrature for the temperature field. We find that although  $S/N$  of the individual elements are no better than the  $S/N$  for the trace, the quadrature combination of the two diagonal elements gives  $S/N$  higher than that of the trace. So, using MTs,  $S/N$  increases by about 18%. However, we note that the gain is not uniform across the full threshold range. The bottom panels show the comparison of  $S/N$  for the  $E$ -mode polarization field. The results are similar to that for the temperature field. These are the preliminary results driving us to further pursue this analysis.

## 7.4 Summary and future work

MTs are a tensorial generalization of the scalar Minkowski functionals that have previously been used to probe non-Gaussianity in CMB and large-scale structure fields. MTs contain more independent degrees of freedom in comparison to MFs. Hence we speculate that they will provide tighter constraints on PNG parameter  $f_{NL}$ . We have used non-Gaussian simulations of CMB fields to compute non-Gaussian deviations of MFs and MTs and compare their statistical significance. We find  $\sim 18\%$  gain in  $S/N$  when

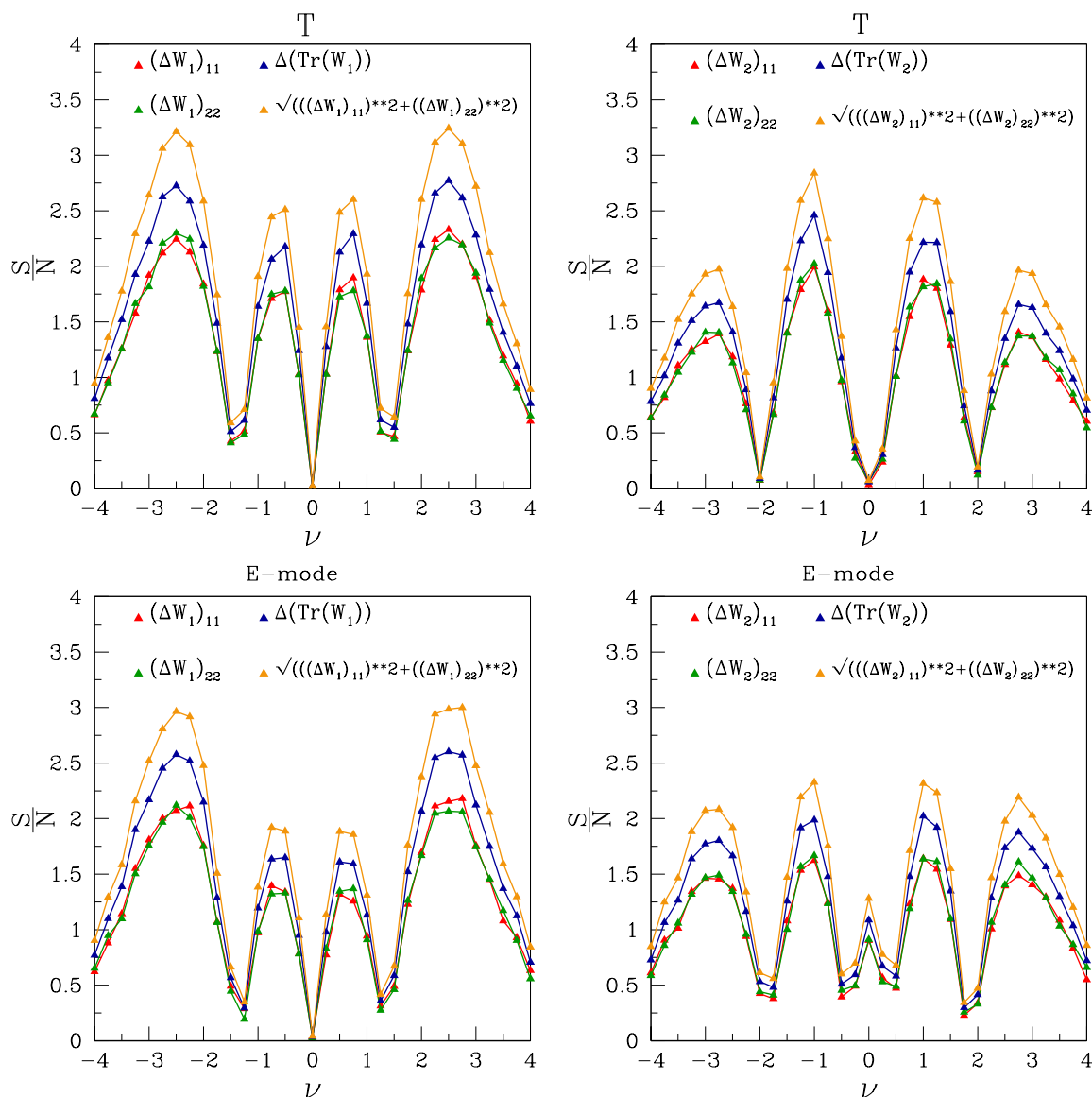


FIGURE 7.1: Comparison of  $S/N$  between MTs and SMFs (trace of MTs) for the temperature and  $E$ -mode polarization field.

the diagonal elements of  $\mathcal{W}_1$  and  $\mathcal{W}_2$  are combined in quadrature in comparison to their respective traces. This can be useful for improving constraints on the  $f_{NL}$  parameter.

The road map for future work is as follows:

- In our analysis, we have taken only one value of  $f_{NL}$  parameter. We will now repeat our analysis for different  $f_{NL}$  values that are consistent with the current constraints on  $f_{NL}$ , and see how the results will vary. This will inform us of any

potential dependence of  $S/N$  on  $f_{NL}$ .

- We will also consider different kinds of non-Gaussianity and check the sensitivity of our results to different types of NG.
- We have till now considered the ideal simulations with no real systematic effects like masking, noise, residual foreground contamination. We will now include these effects in our simulations and repeat the analysis to see if our method can be applied to real data to obtain a significant improvement of constraints on  $f_{NL}$ . We also plan to perform a Fisher matrix analysis to obtain constraints on  $f_{NL}$  using MTs and SMFs.
- Lastly, we will apply the method to Planck data to obtain constraints on  $f_{NL}$ .

# Chapter 8

## Summary, conclusions, and caveats

### 8.1 Key results and conclusions

- We have investigated the changes induced in the morphology of CMB fields, namely temperature fluctuations and E and B modes of polarization, which are sourced by gravitational lensing of CMB photons by large scale structures in the Universe. We use the recently introduced contour Minkowski Tensor  $\mathcal{W}_1$  and the shape parameters  $\alpha$  and  $\beta$ , to quantify the distortion induced by lensing in the shapes of the connected regions and the holes, and their relative alignment, which gives a measure of departure from statistical isotropy. The calculation of the alignment parameter  $\alpha$  was done by computing derivatives of the field which can be done directly on the sphere. We have verified that this method is very accurate and numerical error are well below sub-percent level. While for computing distortion parameter  $\beta$ , we carry out stereographic projection of the CMB fields on flat 2-D space and then compute  $\beta$  using the method described in Chapter.3. We use  $\alpha$  and  $\beta$  to quantify the morphological changes induced by lensing on the CMB fields. We find distinct behavior of morphological distortion as a function of threshold



for both temperature and polarization, namely  $E$  and  $B$  modes, of the CMB. We analyze the dependence on smoothing scale of the distortion and their complementary nature to the angular power spectrum. We find that lensing does not induce statistical anisotropy, which is as expected. We also found that lensing distorts the morphology of the structures in CMB, rendering them highly anisotropic.

- We have tested the cosmological principle by employing Contour Minkowski Tensor and hence computing  $\alpha$  parameter for the large scale matter distribution reconstructed using observations of lensed CMB fields by Planck mission. We have analysed the estimated Planck convergence map and the corresponding simulations from Planck 2018 data release. We compute  $\alpha$  for the convergence ( $\kappa$ ) map over full sky, we refer to this as the Global analysis. We find the convergence field to be statistically isotropic over the full sky. We also perform local analysis, where we compute  $\alpha$  for the convergence map by defining small patches/regions in the sky. From this analyses, we identified some anomalous regions/patches where data and simulations seem to disagree with more 95 % CL. This anomalous behavior of some regions in the can be attributed to to an inaccurate accounting for the estimated noise in the data. Hence, the local patch analysis suggests a powerful method for better understanding of noise.
- We use the CMT to construct a mapping of an arbitrary closed curve to an ellipse that is unique upto translations of the centroid. Using this idea we further study the distribution of many arbitrary shape curves each of which can be mapped to an unique ellipse. We also show that we can map this distribution of many ellipses to an unique one single ellipse, which is equivalent to the  $\alpha$  for the distribution of curves we started with. Next, we show that the shape parameters that are defined using the CMT, and the filamentarity that is defined using the scalar MFs (area and the perimeter), carry complementary shape information. Therefore, using a combination of both will maximize extraction of shape information in practical applications. Next we focus on CMT for Gaussian anisotropic fields. We obtained a analytical expression for the ensemble expectation value of  $\widetilde{\mathcal{W}}_1$ . This will be useful to probe various physical processes that generate anisotropy in cosmological fields like CMB.

- The last part of the thesis has focused on analyzing the prospects of constraining primordial non-Gaussianity in CMB fields using MTs and Betti numbers. MTs are a tensorial generalization of the scalar Minkowski functionals (MFs) which have previously been used to probe local-type primordial non-Gaussianity. MTs being the tensorial observables, contain more independent degrees of freedom. Hence, we expect that they will provide tighter constraints on primordial non-Gaussianity parameter  $f_{NL}$  in comparison to SMFs. In this analysis, we have used non-Gaussian simulations of CMB fields by Elsner Wandelt to compute non-Gaussian deviations of both MFs and MTs ( $\mathcal{W}_1$  and  $\mathcal{W}_2$ ) and compare their statistical significance. We find  $\sim 20\%$  gain in  $S/N$  in the case of MTs over MFs. We, therefore, demonstrate the gain in the signal to noise which can help improve the constraints on  $f_{NL}$ .

## 8.2 Future work

Below we give a list of future direction of investigation.

- We have studied the effect of weak gravitational lensing on morphology CMB temperature and polarization fields by generating their ideal lensed and unlensed simulations using LENSPIX. We did not add realistic instrumental effects such as masking, noise, and residual foregrounds to our simulated fields. Hence we plan to incorporate these effects and check their effects on our results. This analysis will be helpful to assess if we can employ real space observables like MTs on actual CMB data to detect CMB lensing. We have computed shape parameter  $\beta$  by projecting CMB fields on a flat 2-D plane in this work. We plan to develop a code to compute  $\beta$  directly on the surface of the sphere to avoid the errors introduced due to stereographic projection. Once we have the code which computes  $\beta$  directly on the sphere, we would like to obtain  $\beta$  distribution for the lensed CMB fields and study its cross-correlation with the lensing potential or the convergence map

inferred from lensed CMB observations. This analysis will be the first step towards inferring the lensing potential using morphological distortions of the CMB fields.

- We have identified some anomalous regions/patches in the sky by performing the local patch analysis of the Planck 2018 convergence field. Each of the anomalous regions, particularly the two regions that exhibit statistically significant deviation from statistical isotropy, is interesting for further probes and cross-correlation with large-scale structure surveys. This kind of investigation is beneficial in the wake of many upcoming large-scale structure surveys like EUCLID, Vera Rubin Observatory.
- We have outlined our method to constraint primordial non-Gaussianity (PNG) parameter  $f_{NL}$  in CMB fields using Minkowski tensors  $\mathcal{W}_1$  and  $\mathcal{W}_2$ . In the preliminary analysis, we find that MTs can provide statistically significant information on  $f_{NL}$ . We plan to extend our analysis by including instrumental systematics and check sensitivity of our results. Also, we will study other types of non-Gaussianity other than the local type PNG using MTs. Finally we will apply our methodology on Planck data and obtain constrain on  $f_{NL}$ . On the analytic front, we plan to derive analytic expression for the expectation value of MTs for a weakly non-Gaussian field.
- We have tried to understand some aspects of the meaning of homogeneity and isotropy of smooth random fields in 2-dimensional manifold from their geometrical properties. We have also derived analytic expression of the expectation value of CMT for a Gaussian anisotropic field. Although the cosmological fields are expected to be homogeneous, isotropic and Gaussian on large scales, on small scales we see deviation from both Gaussianity and isotropy. Thus, to employ MTs for probing anisotropy it is desirable to derive analytic expressions. We plan to extend this analysis to 3-D space.

# Bibliography

Abazajian, K. N., Arnold, K., Austermann, J., Benson, B. A., Bischoff, C., Bock, J., Bond, J. R., Borrill, J., Calabrese, E., Carlstrom, J. E., Carvalho, C. S., Chang, C. L., Chiang, H. C., Church, S., Cooray, A., Crawford, T. M., Dawson, K. S., Das, S., Devlin, M. J., Dobbs, M., Dodelson, S., Doré, O., Dunkley, J., Errard, J., Fraisse, A., Gallicchio, J., Halverson, N. W., Hanany, S., Hildebrandt, S. R., Hincks, A., Hlozek, R., Holder, G., Holzappel, W. L., Honscheid, K., Hu, W., Hubmayr, J., Irwin, K., Jones, W. C., Kamionkowski, M., Keating, B., Keisler, R., Knox, L., Komatsu, E., Kovac, J., Kuo, C. L., Lawrence, C., Lee, A. T., Leitch, E., Linder, E., Lubin, P., McMahon, J., Miller, A., Newburgh, L., Niemack, M. D., Nguyen, H., Nguyen, H. T., Page, L., Pryke, C., Reichardt, C. L., Ruhl, J. E., Sehgal, N., Seljak, U., Sievers, J., Silverstein, E., Slosar, A., Smith, K. M., Spergel, D., Staggs, S. T., Stark, A., Stompor, R., Vieregg, A. G., Wang, G., Watson, S., Wollack, E. J., Wu, W. L. K., Yoon, K. W. and Zahn, O., 2015, “Neutrino physics from the cosmic microwave background and large scale structure”, *Astroparticle Physics*, **63**, 66–80. [DOI], [ADS], [arXiv:1309.5383 [astro-ph.CO]]

Abazajian, Kevork, Addison, Graeme, Adshead, Peter, Ahmed, Zeeshan, Allen, Steven W., Alonso, David, Alvarez, Marcelo, Anderson, Adam, Arnold, Kam S., Baccigalupi, Carlo, Bailey, Kathy, Barkats, Denis, Barron, Darcy, Barry, Peter S., Bartlett, James G., Basu Thakur, Ritoban, Battaglia, Nicholas, Baxter, Eric, Bean, Rachel, Bebek, Chris, Bender, Amy N., Benson, Bradford A., Berger, Edo, Bhimani, Sanah, Bischoff, Colin A., Bleem, Lindsey, Bocquet, Sebastian, Boddy, Kimberly, Bonato, Matteo, Bond, J. Richard, Borrill, Julian, Bouchet, François R., Brown,

Michael L., Bryan, Sean, Burkhart, Blakesley, Buza, Victor, Byrum, Karen, Calabrese, Erminia, Calafut, Victoria, Caldwell, Robert, Carlstrom, John E., Carron, Julien, Cecil, Thomas, Challinor, Anthony, Chang, Clarence L., Chinone, Yuji, Cho, Hsiao-Mei Sherry, Cooray, Asantha, Crawford, Thomas M., Crites, Abigail, Cukierman, Ari, Cyr-Racine, Francis-Yan, de Haan, Tijmen, de Zotti, Gianfranco, Delabrouille, Jacques, Demarteau, Marcel, Devlin, Mark, Di Valentino, Eleonora, Dobbs, Matt, Duff, Shannon, Duivenvoorden, Adriaan, Dvorkin, Cora, Edwards, William, Eimer, Joseph, Errard, Josquin, Essinger-Hileman, Thomas, Fabbian, Giulio, Feng, Chang, Ferraro, Simone, Filippini, Jeffrey P., Flauger, Raphael, Flaugher, Brenna, Fraisse, Aurelien A., Frolov, Andrei, Galitzki, Nicholas, Galli, Silvia, Ganga, Ken, Gerbino, Martina, Gilchriese, Murdock, Gluscevic, Vera, Green, Daniel, Grin, Daniel, Grohs, Evan, Gualtieri, Riccardo, Guarino, Victor, Gudmundsson, Jon E., Habib, Salman, Haller, Gunther, Halpern, Mark, Halverson, Nils W., Hanany, Shaul, Harrington, Kathleen, Hasegawa, Masaya, Hasselfield, Matthew, Hazumi, Masashi, Heitmann, Katrin, Henderson, Shawn, Henning, Jason W., Hill, J. Colin, Hlozek, Renée, Holder, Gil, Holzappel, William, Hubmayr, Johannes, Huffenberger, Kevin M., Huffer, Michael, Hui, Howard, Irwin, Kent, Johnson, Bradley R., Johnstone, Doug, Jones, William C., Karkare, Kirit, Katayama, Nobuhiko, Kerby, James, Kernovsky, Sarah, Keskitalo, Reijo, Kisner, Theodore, Knox, Lloyd, Kosowsky, Arthur, Kovac, John, Kovetz, Ely D., Kuhlmann, Steve, Kuo, Chao-lin, Kurita, Nadine, Kusaka, Akito, Lahteenmaki, Anne, Lawrence, Charles R., Lee, Adrian T., Lewis, Antony, Li, Dale, Linder, Eric, Loverde, Marilena, Lowitz, Amy, Madhavacheril, Mathew S., Mantz, Adam, Matsuda, Frederick, Mauskopf, Philip, McMahon, Jeff, McQuinn, Matthew, Meerburg, P. Daniel, Melin, Jean-Baptiste, Meyers, Joel, Millea, Marius, Mohr, Joseph, Moncelsi, Lorenzo, Mroczkowski, Tony, Mukherjee, Suvodip, Münchmeyer, Moritz, Nagai, Daisuke, Nagy, Johanna, Namikawa, Toshiya, Nati, Federico, Natoli, Tyler, Negrello, Mattia, Newburgh, Laura, Niemack, Michael D., Nishino, Haruki, Nordby, Martin, Novosad, Valentine, O'Connor, Paul, Obied, Georges, Padin, Stephen, Pandey, Shivam, Partridge, Bruce, Pierpaoli, Elena, Pogosian, Levon, Pryke, Clement, Puglisi, Giuseppe, Racine, Benjamin, Raghunathan, Srinivasan, Rahlin, Alexandra, Rajagopalan, Sridhar, Raveri, Marco, Reichardt, Mark, Reichardt, Christian L., Remazeilles, Mathieu, Rocha, Graca, Roe, Natalie A., Roy, Anirban, Ruhl,

John, Salatino, Maria, Saliwanchik, Benjamin, Schaan, Emmanuel, Schillaci, Alessandro, Schmittfull, Marcel M., Scott, Douglas, Sehgal, Neelima, Shandera, Sarah, Sheehy, Christopher, Sherwin, Blake D., Shirokoff, Erik, Simon, Sara M., Slosar, Anze, Somerville, Rachel, Spergel, David, Staggs, Suzanne T., Stark, Antony, Stompor, Radek, Story, Kyle T., Stoughton, Chris, Suzuki, Aritoki, Tajima, Osamu, Teply, Grant P., Thompson, Keith, Timbie, Peter, Tomasi, Maurizio, Treu, Jesse I., Tristram, Matthieu, Tucker, Gregory, Umiltà, Caterina, van Engelen, Alexander, Vieira, Joaquin D., Vieregg, Abigail G., Vogelsberger, Mark, Wang, Gensheng, Watson, Scott, White, Martin, Whitehorn, Nathan, Wollack, Edward J., Kimmy Wu, W. L., Xu, Zhilei, Yasini, Siavash, Yeck, James, Yoon, Ki Won, Young, Edward and Zonca, Andrea, 2019, “CMB-S4 Science Case, Reference Design, and Project Plan”, *arXiv e-prints*, arXiv:1907.04473. [ADS], [arXiv:1907.04473 [astro-ph.IM]]

Ade, P. A. R., Akiba, Y., Anthony, A. E., Arnold, K., Atlas, M., Barron, D., Boettger, D., Borrill, J., Chapman, S., Chinone, Y., Dobbs, M., Elleflot, T., Errard, J., Fabbian, G., Feng, C., Flanigan, D., Gilbert, A., Grainger, W., Halverson, N. W., Hasegawa, M., Hattori, K., Hazumi, M., Holzzapfel, W. L., Hori, Y., Howard, J., Hyland, P., Inoue, Y., Jaehnig, G. C., Jaffe, A., Keating, B., Kermish, Z., Keskitalo, R., Kisner, T., Le Jeune, M., Lee, A. T., Linder, E., Leitch, E. M., Lungu, M., Matsuda, F., Matsumura, T., Meng, X., Miller, N. J., Morii, H., Moyerman, S., Myers, M. J., Navaroli, M., Nishino, H., Paar, H., Peloton, J., Quealy, E., Rebeiz, G., Reichardt, C. L., Richards, P. L., Ross, C., Schanning, I., Schenck, D. E., Sherwin, B., Shimizu, A., Shimmin, C., Shimon, M., Siritanasak, P., Smecher, G., Spieler, H., Stebor, N., Steinbach, B., Stompor, R., Suzuki, A., Takakura, S., Tomaru, T., Wilson, B., Yadav, A. and Zahn, O. [POLARBEAR Collaboration], 2014, “Measurement of the Cosmic Microwave Background Polarization Lensing Power Spectrum with the POLARBEAR Experiment”, *Phys. Rev. Lett.*, **113**, 021 301. [DOI]URL:  
<https://link.aps.org/doi/10.1103/PhysRevLett.113.021301>

Ade, P. A. R., Ahmed, Z., Aikin, R. W., Alexander, K. D., Barkats, D., Benton, S. J., Bischoff, C. A., Bock, J. J., Brevik, J. A., Buder, I., Bullock, E., Buza, V., Connors, J., Crill, B. P., Dowell, C. D., Dvorkin, C., Duband, L., Filippini, J. P., Fliescher, S., Golwala, S. R., Halpern, M., Harrison, S., Hasselfield, M., Hildebrandt, S. R., Hilton,

- G. C., Hristov, V. V., Hui, H., Irwin, K. D., Karkare, K. S., Kaufman, J. P., Keating, B. G., Kefeli, S., Kernasovskiy, S. A., Kovac, J. M., Kuo, C. L., Leitch, E. M., Lueker, M., Mason, P., Megerian, K. G., Netterfield, C. B., Nguyen, H. T., O’Brien, R., IV, R. W. Ogburn, Orlando, A., Pryke, C., Reintsema, C. D., Richter, S., Schwarz, R., Sheehy, C. D., Staniszewski, Z. K., Sudiwala, R. V., Teply, G. P., Thompson, K. L., Tolan, J. E., Turner, A. D., Vieregg, A. G., Weber, A. C., Willmert, J., Wong, C. L. and and, K. W. Yoon, 2015, “BICEP2/KECK ARRAY V: MEASUREMENTS OF FB-MODE POLARIZATION AT DEGREE ANGULAR SCALES AND 150 GHz BY THE KECK ARRAY”, *The Astrophysical Journal*, **811**(2), 126. [DOI]URL: <https://doi.org/10.1088/0004-637x/811/2/126>
- Adler, Robert J, 2010, *The Geometry of Random Fields*, Society for Industrial and Applied Mathematics. [DOI], [<https://epubs.siam.org/doi/pdf/10.1137/1.9780898718980>]URL: <https://epubs.siam.org/doi/abs/10.1137/1.9780898718980>
- Aghanim, Nabila, Majumdar, Subhabrata and Silk, Joseph, 2008, “Secondary anisotropies of the CMB”, *Reports on Progress in Physics*, **71**(6), 066902. [DOI]URL: <https://doi.org/10.1088/0034-4885/71/6/066902>
- Alesker, S., 1999, “Description of Continuous Isometry Covariant Valuations on Convex Sets”, *Geometriae Dedicata*, **74**(3), 241–248. [DOI]URL: <https://doi.org/10.1023/A:1005035232264>
- Alishahiha, Mohsen, Silverstein, Eva and Tong, David, 2004, “DBI in the sky: Non-Gaussianity from inflation with a speed limit”, *Physical Review D*, **70**(12), 123505. [DOI], [ADS], [arXiv:hep-th/0404084 [hep-th]]
- Alpher, Ralph A. and Herman, Robert, 1948, “Evolution of the Universe”, *Nature*, **162**(4124), 774–775. [DOI], [ADS]
- and P. A. R. Ade, Aguilar, M., Akiba, Y., Arnold, K., Baccigalupi, C., Barron, D., Beck, D., Bianchini, F., Boettger, D., Borrill, J., Chapman, S., Chinone, Y., Crowley, K., Cukierman, A., D’Aijner, R., Dobbs, M., Ducout, A., Elleflot, T., Errard, J., Fabbian, G., Feeney, S. M., Feng, C., Fujino, T., Galitzki, N., Gilbert, A., Goeckner-Wald, N., Groh, J. C., Hall, G., Halverson, N., Hamada, T., Hasegawa, M., Hazumi,

M., Hill, C. A., Howe, L., Inoue, Y., Jaehnig, G., Jaffe, A. H., Jeong, O., Kaneko, D., Katayama, N., Keating, B., Keskitalo, R., Kisner, T., Krachmalnicoff, N., Kusaka, A., Jeune, M. Le, Lee, A. T., Leitch, E. M., Leon, D., Linder, E., Lowry, L., Matsuda, F., Matsumura, T., Minami, Y., Montgomery, J., Navaroli, M., Nishino, H., Paar, H., Peloton, J., Pham, A. T. P., Poletti, D., Puglisi, G., Reichardt, C. L., Richards, P. L., Ross, C., Segawa, Y., Sherwin, B. D., Silva-Feaver, M., Siritanasak, P., Stebor, N., Stompor, R., Suzuki, A., Tajima, O., Takakura, S., Takatori, S., Tanabe, D., Teply, G. P., Tomaru, T., Tucker, C., Whitehorn, N. and Zahn, A., 2017, “A Measurement of the Cosmic Microwave Background B-mode Polarization Power Spectrum at Subdegree Scales from Two Years of polarbear Data”, *The Astrophysical Journal*, **848**(2), 121. [DOI]URL:

<https://doi.org/10.3847/1538-4357/aa8e9f>

Appleby, Stephen, Chingangbam, Pravabati, Park, Changbom, Hong, Sungwook E., Kim, Juhan and Ganesan, Vidhya, 2018a, “Minkowski Tensors in Two Dimensions: Probing the Morphology and Isotropy of the Matter and Galaxy Density Fields”, *Astrophys. J.*, **858**(2), 87. [DOI], [ADS], [arXiv:1712.07466 [astro-ph.CO]]

Appleby, Stephen, Chingangbam, Pravabati, Park, Changbom, Yogendran, K. P. and Joby, P. K., 2018b, “Minkowski Tensors in Three Dimensions: Probing the Anisotropy Generated by Redshift Space Distortion”, *Astrophys. J.*, **863**(2), 200. [DOI], [ADS], [arXiv:1805.08752 [astro-ph.CO]]

Appleby, Stephen, Kochappan, Joby P., Chingangbam, Pravabati and Park, Changbom, 2019, “Ensemble Average of Three-dimensional Minkowski Tensors of a Gaussian Random Field in Redshift Space”, *The Astrophysical Journal*, **887**(2), 128. [DOI]URL: <https://doi.org/10.3847/1538-4357/ab5057>

Beisbart, C., Buchert, T. and Wagner, H., 2001a, “Morphometry of spatial patterns”, *Physica A Statistical Mechanics and its Applications*, **293**, 592–604. [DOI], [ADS], [arXiv:astro-ph/0007459 [astro-ph]]

Beisbart, C., Valdarnini, R. and Buchert, T., 2001b, “The morphological and dynamical evolution of simulated galaxy clusters”, *Astron. Astrophys.*, **379**, 412–425. [DOI], [ADS], [arXiv:astro-ph/0109459 [astro-ph]]



- Beisbart, Claus, Dahlke, Robert, Mecke, Klaus and Wagner, Herbert, 2002, “Vector- and Tensor-Valued Descriptors for Spatial Patterns”, in *Morphology of Condensed Matter: Physics and Geometry of Spatially Complex Systems*, (Eds.) Mecke, Klaus, Stoyan, Dietrich, Springer Berlin Heidelberg, Berlin, Heidelberg. pp. 238–260. [DOI]URL: [https://doi.org/10.1007/3-540-45782-8\\_10](https://doi.org/10.1007/3-540-45782-8_10)
- Bernardeau, F., 1997, “Weak lensing detection in CMB maps.”, *Astron. Astrophys.*, **324**, 15–26. [ADS], [arXiv:astro-ph/9611012 [astro-ph]]
- Bernardeau, F., 1998, “Lens distortion effects on CMB maps”, *Astron. Astrophys.*, **338**, 767–776. [ADS], [arXiv:astro-ph/9802243 [astro-ph]]
- Bertschinger, Edmund, 1995, “COSMICS: Cosmological Initial Conditions and Microwave Anisotropy Codes”, *arXiv e-prints*, astro-ph/9506070. [ADS], [arXiv:astro-ph/9506070 [astro-ph]]
- Bharadwaj, Somnath, Sahni, Varun, Sathyaprakash, B. S., Shandarin, Sergei F. and Yess, Capp, 2000, “Evidence for Filamentarity in the Las Campanas Redshift Survey”, *Astrophys. J.*, **528**(1), 21–29. [DOI], [ADS], [arXiv:astro-ph/9904406 [astro-ph]]
- Bianchini, F., Bielewicz, P., Lapi, A., Gonzalez-Nuevo, J., Baccigalupi, C., de Zotti, G., Danese, L., Bourne, N., Cooray, A., Dunne, L., Dye, S., Eales, S., Ivison, R., Maddox, S., Negrello, M., Scott, D., Smith, M. W. L. and Valiante, E., 2015, “Cross-correlation between the CMB Lensing Potential Measured by Planck and High-z Submillimeter Galaxies Detected by the Herschel-Atlas Survey”, *Astrophys. J.*, **802**(1), 64. [DOI], [ADS], [arXiv:1410.4502 [astro-ph.CO]]
- BICEP2 Collaboration, Keck Array Collaboration, Ade, P. A. R., Ahmed, Z., Aikin, R. W., Alexander, K. D., Barkats, D., Benton, S. J., Bischoff, C. A., Bock, J. J., Bowens-Rubin, R., Brevik, J. A., Buder, I., Bullock, E., Buza, V., Connors, J., Crill, B. P., Duband, L., Dvorkin, C., Filippini, J. P., Fliescher, S., Grayson, J., Halpern, M., Harrison, S., Hildebrandt, S. R., Hilton, G. C., Hui, H., Irwin, K. D., Kang, J., Karkare, K. S., Karpel, E., Kaufman, J. P., Keating, B. G., Kefeli, S., Kernasovskiy, S. A., Kovac, J. M., Kuo, C. L., Leitch, E. M., Lueker, M., Megerian, K. G., Namikawa, T., Netterfield, C. B., Nguyen, H. T., O’Brient, R., Ogburn, R. W., IV, Orlando, A.,

Pryke, C., Richter, S., Schwarz, R., Sheehy, C. D., Staniszewski, Z. K., Steinbach, B., Sudiwala, R. V., Teply, G. P., Thompson, K. L., Tolan, J. E., Tucker, C., Turner, A. D., Vieregg, A. G., Weber, A. C., Wiebe, D. V., Willmert, J., Wong, C. L., Wu, W. L. K. and Yoon, K. W., 2016, “BICEP2/Keck Array VIII: Measurement of Gravitational Lensing from Large-scale B-mode Polarization”, *Astrophys. J.*, **833**(2), 228. [DOI], [ADS], [arXiv:1606.01968 [astro-ph.CO]]

BICEP2 Collaboration, Keck Array Collaboration, Ade, P. A. R., Ahmed, Z., Aikin, R. W., Alexander, K. D., Barkats, D., Benton, S. J., Bischoff, C. A., Bock, J. J., Bowens-Rubin, R., Brevik, J. A., Buder, I., Bullock, E., Buza, V., Connors, J., Cornelison, J., Crill, B. P., Crumrine, M., Dierickx, M., Duband, L., Dvorkin, C., Filipini, J. P., Fliescher, S., Grayson, J., Hall, G., Halpern, M., Harrison, S., Hildebrandt, S. R., Hilton, G. C., Hui, H., Irwin, K. D., Kang, J., Karkare, K. S., Karpel, E., Kaufman, J. P., Keating, B. G., Kefeli, S., Kernasovskiy, S. A., Kovac, J. M., Kuo, C. L., Larsen, N. A., Lau, K., Leitch, E. M., Lueker, M., Megerian, K. G., Moncelsi, L., Namikawa, T., Netterfield, C. B., Nguyen, H. T., O’Brient, R., Ogburn, R. W., Palladino, S., Pryke, C., Racine, B., Richter, S., Schillaci, A., Schwarz, R., Sheehy, C. D., Soliman, A., St. Germaine, T., Staniszewski, Z. K., Steinbach, B., Sudiwala, R. V., Teply, G. P., Thompson, K. L., Tolan, J. E., Tucker, C., Turner, A. D., Umiltà, C., Vieregg, A. G., Wandui, A., Weber, A. C., Wiebe, D. V., Willmert, J., Wong, C. L., Wu, W. L. K., Yang, H., Yoon, K. W. and Zhang, C., 2018, “Constraints on Primordial Gravitational Waves Using Planck, WMAP, and New BICEP2/Keck Observations through the 2015 Season”, *Physical Review L*, **121**(22), 221301. [DOI], [ADS], [arXiv:1810.05216 [astro-ph.CO]]

Blanchard, A. and Schneider, J., 1987, “Gravitational lensing effect on the fluctuations of the cosmic background radiation”, *Astron. Astrophys.*, **184**(1-2), 1–6. [ADS]

Bobin, J., Starck, J. L., Sureau, F. and Basak, S., 2013, “Sparse component separation for accurate cosmic microwave background estimation”, *Astron. Astrophys.*, **550**, A73. [DOI], [ADS], [arXiv:1206.1773 [astro-ph.CO]]

Bucher, Martin, Carvalho, Carla Sofia, Moodley, Kavilan and Remazeilles, Mathieu, 2012, “CMB lensing reconstruction in real space”, *Physical Review D*, **85**(4), 043016. [DOI], [ADS], [arXiv:1004.3285 [astro-ph.CO]]

- Buchert, Thomas, France, Martin J. and Steiner, Frank, 2017, “Model-independent analyses of non-Gaussianity in Planck CMB maps using Minkowski functionals”, *Classical and Quantum Gravity*, **34**(9), 094002. [DOI], [ADS], [arXiv:1701.03347 [astro-ph.CO]]
- Calabrese, M., Carbone, C., Fabbian, G., Baldi, M. and Baccigalupi, C., 2015, “Multiple lensing of the cosmic microwave background anisotropies”, *Journal of Cosmology and Astroparticle Physics*, **2015**(03), 049–049. [DOI]URL:  
<https://doi.org/10.1088/1475-7516/2015/03/049>
- Carron, Julien and Lewis, Antony, 2017, “Maximum a posteriori CMB lensing reconstruction”, *Physical Review D*, **96**(6), 063510. [DOI], [ADS], [arXiv:1704.08230 [astro-ph.CO]]
- Castorina, Emanuele, Hand, Nick, Seljak, Uroš, Beutler, Florian, Chuang, Chia-Hsun, Zhao, Cheng, Gil-Marín, Héctor, Percival, Will J., Ross, Ashley J., Choi, Peter Doohyun, Dawson, Kyle, de la Macorra, Axel, Rossi, Graziano, Ruggeri, Rossana, Schneider, Donald and Zhao, Gong-Bo, 2019, “Redshift-weighted constraints on primordial non-Gaussianity from the clustering of the eBOSS DR14 quasars in Fourier space”, , **2019**(9), 010. [DOI], [ADS], [arXiv:1904.08859 [astro-ph.CO]]
- Challinor, Anthony and Chon, Gayoung, 2002, “Geometry of weak lensing of CMB polarization”, *Phys. Rev. D*, **66**, 127301. [DOI]URL:  
<https://link.aps.org/doi/10.1103/PhysRevD.66.127301>
- Challinor, Anthony and Lewis, Antony, 2005, “Lensed CMB power spectra from all-sky correlation functions”, *Physical Review D*, **71**(10), 103010. [DOI], [ADS], [arXiv:astro-ph/0502425 [astro-ph]]
- Chen, Xingang, 2005, “Running non-Gaussianities in Dirac-Born-Infeld inflation”, *Phys. Rev. D*, **72**, 123518. [DOI]URL:  
<https://link.aps.org/doi/10.1103/PhysRevD.72.123518>
- Chingangbam, Prava, Yogendran, K P, Goyal, Priya and Appleby, Stephen, “Geometric meaning of statistical isotropy of smooth random fields: application to cosmological fields”. In prep.

- Chingangbam, Pravabati and Park, Changbom, 2009, “Statistical nature of non-Gaussianity from cubic order primordial perturbations: CMB map simulations and genus statistic”, , **2009**(12), 019. [DOI], [ADS], [arXiv:0908.1696 [astro-ph.CO]]
- Chingangbam, Pravabati and Park, Changbom, 2013, “Residual foreground contamination in the WMAP data and bias in non-Gaussianity estimation”, , **2013**(2), 031. [DOI], [ADS], [arXiv:1210.2250 [astro-ph.CO]]
- Chingangbam, Pravabati, Park, Changbom, Yogendran, K. P. and van de Weygaert, Rien, 2012, “Hot and Cold Spot Counts as Probes of Non-Gaussianity in the Cosmic Microwave Background”, *Astrophys. J.*, **755**(2), 122. [DOI], [ADS], [arXiv:1206.0436 [astro-ph.CO]]
- Chingangbam, Pravabati, Ganesan, Vidhya, Yogendran, K. P. and Park, Changbom, 2017a, “On Minkowski Functionals of CMB polarization”, *Physics Letters B*, **771**, 67–73. [DOI], [ADS], [arXiv:1705.04454 [astro-ph.CO]]
- Chingangbam, Pravabati, Yogendran, K. P., Joby, P. K., Ganesan, Vidhya, Appleby, Stephen and Park, Changbom, 2017b, “Tensor Minkowski Functionals for random fields on the sphere”, , **2017**(12), 023. [DOI], [ADS], [arXiv:1707.04386 [astro-ph.CO]]
- Choi, Steve K., Hasselfield, Matthew, Ho, Shuay-Pwu Patty, Koopman, Brian, Lungu, Marius, Abitbol, Maximilian H., Addison, Graeme E., Ade, Peter A. R., Aiola, Simone, Alonso, David, Amiri, Mandana, Amodeo, Stefania, Angile, Elio, Austermann, Jason E., Baildon, Taylor, Battaglia, Nick, Beall, James A., Bean, Rachel, Becker, Daniel T., Bond, J. Richard, Bruno, Sarah Marie, Calabrese, Erminia, Calafut, Victoria, Campusano, Luis E., Carrero, Felipe, Chesmore, Grace E., Cho, Hsiao-mei, Clark, Susan E., Cothard, Nicholas F., Crichton, Devin, Crowley, Kevin T., Darwish, Omar, Datta, Rahul, Denison, Edward V., Devlin, Mark J., Duell, Cody J., Duff, Shannon M., Duivenvoorden, Adriaan J., Dunkley, Jo, Dünner, Rolando, Essinger-Hileman, Thomas, Fankhanel, Max, Ferraro, Simone, Fox, Anna E., Fuzia, Brittany, Gallardo, Patricio A., Gluscevic, Vera, Golec, Joseph E., Grace, Emily, Gralla, Megan, Guan, Yilun, Hall, Kirsten, Halpern, Mark, Han, Dongwon, Hargrave, Peter, Henderson, Shawn, Hensley, Brandon, Hill, J. Colin, Hilton, Gene C., Hilton, Matt, Hincks, Adam D., Hložek, Renée, Hubmayr, Johannes, Huffenberger, Kevin M., Hughes,

- John P., Infante, Leopoldo, Irwin, Kent, Jackson, Rebecca, Klein, Jeff, Knowles, Kenda, Kosowsky, Arthur, Lakey, Vincent, Li, Dale, Li, Yaqiong, Li, Zack, Lokken, Martine, Louis, Thibaut, MacInnis, Amanda, Madhavacheril, Mathew, Maldonado, Felipe, Mallaby-Kay, Maya, Marsden, Danica, Maurin, Loïc, McMahon, Jeff, Menanteau, Felipe, Moodley, Kavilan, Morton, Tim, Naess, Sigurd, Namikawa, Toshiya, Nati, Federico, Newburgh, Laura, Nibarger, John P., Nicola, Andrina, Niemack, Michael D., Nolta, Michael R., Orłowski-Sherer, John, Page, Lyman A., Pappas, Christine G., Partridge, Bruce, Phakathi, Phumlani, Prince, Heather, Puddu, Roberto, Qu, Frank J., Rivera, Jesus, Robertson, Naomi, Rojas, Felipe, Salatino, Maria, Schaan, Emmanuel, Schillaci, Alessandro, Schmitt, Benjamin L., Sehgal, Neelima, Sherwin, Blake D., Sierra, Carlos, Sievers, Jon, Sifon, Cristobal, Sikhosana, Precious, Simon, Sara, Spergel, David N., Staggs, Suzanne T., Stevens, Jason, Storer, Emilie, Sunder, Dhaneshwar D., Switzer, Eric R., Thorne, Ben, Thornton, Robert, Trac, Hy, Treu, Jesse, Tucker, Carole, Vale, Leila R., Van Engelen, Alexander, Van Lanen, Jeff, Vavagiakis, Eve M., Wagoner, Kasey, Wang, Yuhan, Ward, Jonathan T., Wollack, Edward J., Xu, Zhilei, Zago, Fernando and Zhu, Ningfeng, 2020, “The Atacama Cosmology Telescope: a measurement of the Cosmic Microwave Background power spectra at 98 and 150 GHz”, , **2020**(12), 045. [DOI], [ADS], [arXiv:2007.07289 [astro-ph.CO]]
- Condon, J. J., Cotton, W. D., Greisen, E. W., Yin, Q. F., Perley, R. A., Taylor, G. B. and Broderick, J. J., 1998, “The NRAO VLA Sky Survey”, *Astron. J.*, **115**(5), 1693–1716. [DOI], [ADS]
- Cooray, Asantha and Sheth, Ravi, 2002, “Halo models of large scale structure”, *Phys. Rep.*, **372**(1), 1–129. [DOI], [ADS], [arXiv:astro-ph/0206508 [astro-ph]]
- Coulson, D., Crittenden, R. G. and Turok, N. G., 1994, “Polarization and anisotropy of the microwave sky”, *Physical Review L*, **73**(18), 2390–2393. [DOI], [ADS], [arXiv:astro-ph/9406046 [astro-ph]]
- Crittenden, Robert, Davis, Richard L. and Steinhardt, Paul J., 1993, “Polarization of the Microwave Background Due to Primordial Gravitational Waves”, *Astrophys. J. Lett.*, **417**, L13. [DOI], [ADS], [arXiv:astro-ph/9306027 [astro-ph]]

Dark Energy Survey Collaboration, Abbott, T., Abdalla, F. B., Aleksić, J., Allam, S., Amara, A., Bacon, D., Balbinot, E., Banerji, M., Bechtol, K., Benoit-Lévy, A., Bernstein, G. M., Bertin, E., Blazek, J., Bonnett, C., Bridle, S., Brooks, D., Brunner, R. J., Buckley-Geer, E., Burke, D. L., Caminha, G. B., Capozzi, D., Carlsen, J., Carnero-Rosell, A., Carollo, M., Carrasco-Kind, M., Carretero, J., Castander, F. J., Clerkin, L., Collett, T., Conselice, C., Crocce, M., Cunha, C. E., D’Andrea, C. B., da Costa, L. N., Davis, T. M., Desai, S., Diehl, H. T., Dietrich, J. P., Dodelson, S., Doel, P., Drlica-Wagner, A., Estrada, J., Etherington, J., Evrard, A. E., Fabbri, J., Finley, D. A., Flaugher, B., Foley, R. J., Fosalba, P., Frieman, J., García-Bellido, J., Gaztanaga, E., Gerdes, D. W., Giannantonio, T., Goldstein, D. A., Gruen, D., Gruendl, R. A., Guarnieri, P., Gutierrez, G., Hartley, W., Honscheid, K., Jain, B., James, D. J., Jeltema, T., Jouvel, S., Kessler, R., King, A., Kirk, D., Kron, R., Kuehn, K., Kuropatkin, N., Lahav, O., Li, T. S., Lima, M., Lin, H., Maia, M. A. G., Makler, M., Manera, M., Maraston, C., Marshall, J. L., Martini, P., McMahon, R. G., Melchior, P., Merson, A., Miller, C. J., Miquel, R., Mohr, J. J., Morice-Atkinson, X., Naidoo, K., Nielsen, E., Nichol, R. C., Nord, B., Ogando, R., Ostrovski, F., Palmese, A., Papadopoulos, A., Peiris, H. V., Peoples, J., Percival, W. J., Plazas, A. A., Reed, S. L., Refregier, A., Romer, A. K., Roodman, A., Ross, A., Roza, E., Rykoff, E. S., Sadeh, I., Sako, M., Sánchez, C., Sanchez, E., Santiago, B., Scarpine, V., Schubnell, M., Sevilla-Noarbe, I., Sheldon, E., Smith, M., Smith, R. C., Soares-Santos, M., Sobreira, F., Soumagnac, M., Suchyta, E., Sullivan, M., Swanson, M., Tarle, G., Thaler, J., Thomas, D., Thomas, R. C., Tucker, D., Vieira, J. D., Vikram, V., Walker, A. R., Wechsler, R. H., Weller, J., Wester, W., Whiteway, L., Wilcox, H., Yanny, B., Zhang, Y. and Zuntz, J., 2016, “The Dark Energy Survey: more than dark energy - an overview”, *Mon. Not. Roy. Astron. Soc.*, **460**(2), 1270–1299. [DOI], [ADS], [arXiv:1601.00329 [astro-ph.CO]]

Das, Sudeep, Sherwin, Blake D., Aguirre, Paula, Appel, John W., Bond, J. Richard, Carvalho, C. Sofia, Devlin, Mark J., Dunkley, Joanna, Dünner, Rolando, Essinger-Hileman, Thomas, Fowler, Joseph W., Hajian, Amir, Halpern, Mark, Hasselfield, Matthew, Hincks, Adam D., Hlozek, Renée, Huffenberger, Kevin M., Hughes, John P., Irwin, Kent D., Klein, Jeff, Kosowsky, Arthur, Lupton, Robert H., Marriage, Tobias A., Marsden, Danica, Menanteau, Felipe, Moodley, Kavilan, Niemack, Michael D.,

- Nolta, Michael R., Page, Lyman A., Parker, Lucas, Reese, Erik D., Schmitt, Benjamin L., Sehgal, Neelima, Sievers, Jon, Spergel, David N., Staggs, Suzanne T., Swetz, Daniel S., Switzer, Eric R., Thornton, Robert, Visnjic, Katerina and Wollack, Ed, 2011, “Detection of the Power Spectrum of Cosmic Microwave Background Lensing by the Atacama Cosmology Telescope”, *Physical Review L*, **107**(2), 021301. [DOI], [ADS], [arXiv:1103.2124 [astro-ph.CO]]
- Ducout, A., Bouchet, F. R., Colombi, S., Pogosyan, D. and Prunet, S., 2012, “Non-Gaussianity and Minkowski functionals: forecasts for Planck”, *Monthly Notices of the Royal Astronomical Society*, **429**(3), 2104–2126. [DOI], [https://academic.oup.com/mnras/article-pdf/429/3/2104/3214532/sts483.pdf]URL: <https://doi.org/10.1093/mnras/sts483>
- Ducout, A., Bouchet, F. R., Colombi, S., Pogosyan, D. and Prunet, S., 2013, “Non-Gaussianity and Minkowski functionals: forecasts for Planck”, *Mon. Not. Roy. Astron. Soc.*, **429**(3), 2104–2126. [DOI], [ADS], [arXiv:1209.1223 [astro-ph.CO]]
- Elsner, Franz and Wandelt, Benjamin D., 2009, “Improved Simulation of Non-Gaussian Temperature and Polarization Cosmic Microwave Background Maps”, *Astrophys. J. Suppl.*, **184**(2), 264–270. [DOI], [ADS], [arXiv:0909.0009 [astro-ph.CO]]
- Eriksen, H. K., Hansen, F. K., J.Banday, A., Gorski, K. M. and Lilje, P. B., 2004, “Erratum: “Asymmetries in the Cosmic Microwave Background Anisotropy Field” (ApJ, 605, 14 [2004])”, *The Astrophysical Journal*, **609**(2), 1198–1199. [DOI]URL: <https://doi.org/10.1086/421972>
- Fantaye, Y, Baccigalupi, C, Leach, S.M and Yadav, A.P.S, 2012, “CMB lensing reconstruction in the presence of diffuse polarized foregrounds”, *Journal of Cosmology and Astroparticle Physics*, **2012**(12), 017–017. [DOI]URL: <https://doi.org/10.1088/1475-7516/2012/12/017>
- Feng, Chang, Aslanyan, Grigor, Manohar, Aneesh V., Keating, Brian, Paar, Hans P. and Zahn, Oliver, 2012, “Measuring gravitational lensing of the cosmic microwave background using cross correlation with large scale structure”, *Phys. Rev. D*, **86**, 063 519. [DOI]URL: <https://link.aps.org/doi/10.1103/PhysRevD.86.063519>

- Fixsen, D. J., Cheng, E. S., Gales, J. M., Mather, J. C., Shafer, R. A. and Wright, E. L., 1996, “The Cosmic Microwave Background Spectrum from the Full COBE FIRAS Data Set”, *Astrophys. J.*, **473**, 576. [DOI], [ADS], [arXiv:astro-ph/9605054 [astro-ph]]
- GAMOW, G., 1948, “The Evolution of the Universe”, *Nature*, **162**(4122), 680–682. [DOI]URL:  
<https://doi.org/10.1038/162680a0>
- Ganesan, Vidhya and Chingangbam, Pravabati, 2017, “Tensor Minkowski Functionals: first application to the CMB”, , **2017**(6), 023. [DOI], [ADS], [arXiv:1608.07452 [astro-ph.CO]]
- Górski, K. M., Hivon, E., Banday, A. J., Wandelt, B. D., Hansen, F. K., Reinecke, M. and Bartelmann, M., 2005, “HEALPix: A Framework for High-Resolution Discretization and Fast Analysis of Data Distributed on the Sphere”, *Astrophys. J.*, **622**(2), 759–771. [DOI], [ADS], [arXiv:astro-ph/0409513 [astro-ph]]
- Gott, J. Richard, III, Melott, Adrian L. and Dickinson, Mark, 1986, “The Sponge-like Topology of Large-Scale Structure in the Universe”, *Astrophys. J.*, **306**, 341. [DOI], [ADS]
- Gott, J. Richard, III, Park, Changbom, Juskiewicz, Roman, Bies, William E., Bennett, David P., Bouchet, Francois R. and Stebbins, Albert, 1990, “Topology of Microwave Background Fluctuations: Theory”, *Astrophys. J.*, **352**, 1. [DOI], [ADS]
- Guth, Alan H., 1981, “Inflationary universe: A possible solution to the horizon and flatness problems”, *Phys. Rev. D*, **23**, 347–356. [DOI]URL:  
<https://link.aps.org/doi/10.1103/PhysRevD.23.347>
- Hand, Nick, Leauthaud, Alexie, Das, Sudeep, Sherwin, Blake D., Addison, Graeme E., Bond, J. Richard, Calabrese, Erminia, Charbonnier, Aldée, Devlin, Mark J., Dunkley, Joanna, Erben, Thomas, Hajian, Amir, Halpern, Mark, Harnois-Déraps, Joachim, Heymans, Catherine, Hildebrandt, Hendrik, Hincks, Adam D., Kneib, Jean-Paul, Kosowsky, Arthur, Makler, Martin, Miller, Lance, Moodley, Kavilan, Moraes, Bruno, Niemack, Michael D., Page, Lyman A., Partridge, Bruce, Sehgal, Neelima, Shan, Huanyuan, Sievers, Jonathan L., Spergel, David N., Staggs, Suzanne T., Switzer,



- Eric R., Taylor, James E., Van Waerbeke, Ludovic, Welker, Charlotte and Wollack, Edward J., 2015, “First measurement of the cross-correlation of CMB lensing and galaxy lensing”, *Physical Review D*, **91**(6), 062001. [DOI], [ADS], [arXiv:1311.6200 [astro-ph.CO]]
- Hanson, D., Hoover, S., Crites, A., Ade, P. A. R., Aird, K. A., Austermann, J. E., Beall, J. A., Bender, A. N., Benson, B. A., Bleem, L. E., Bock, J. J., Carlstrom, J. E., Chang, C. L., Chiang, H. C., Cho, H. M., Conley, A., Crawford, T. M., de Haan, T., Dobbs, M. A., Everett, W., Gallicchio, J., Gao, J., George, E. M., Halverson, N. W., Harrington, N., Henning, J. W., Hilton, G. C., Holder, G. P., Holzzapfel, W. L., Hrubes, J. D., Huang, N., Hubmayr, J., Irwin, K. D., Keisler, R., Knox, L., Lee, A. T., Leitch, E., Li, D., Liang, C., Luong-Van, D., Marsden, G., McMahon, J. J., Mehl, J., Meyer, S. S., Mocuano, L., Montroy, T. E., Natoli, T., Nibarger, J. P., Novosad, V., Padin, S., Pryke, C., Reichardt, C. L., Ruhl, J. E., Saliwanchik, B. R., Sayre, J. T., Schaffer, K. K., Schulz, B., Smecher, G., Stark, A. A., Story, K. T., Tucker, C., Vanderlinde, K., Vieira, J. D., Viero, M. P., Wang, G., Yefremenko, V., Zahn, O. and Zemcov, M., 2013, “Detection of B-Mode Polarization in the Cosmic Microwave Background with Data from the South Pole Telescope”, *Physical Review L*, **111**(14), 141301. [DOI], [ADS], [arXiv:1307.5830 [astro-ph.CO]]
- Hanson, Duncan, Challinor, Anthony and Lewis, Antony, 2010, “Weak lensing of the CMB”, *General Relativity and Gravitation*, **42**(9), 2197–2218. [DOI], [ADS], [arXiv:0911.0612 [astro-ph.CO]]
- Hanson, Duncan, Challinor, Anthony, Efstathiou, George and Bielewicz, Pawel, 2011, “CMB temperature lensing power reconstruction”, *Phys. Rev. D*, **83**, 043005. [DOI]URL:  
<https://link.aps.org/doi/10.1103/PhysRevD.83.043005>
- Hazumi, M. *et al.*, 2019, “LiteBIRD: A Satellite for the Studies of B-Mode Polarization and Inflation from Cosmic Background Radiation Detection”, *J. Low Temp. Phys.*, **194**(5-6), 443–452. [DOI]
- Hikage, Chiaki, Schmalzing, Jens, Buchert, Thomas, Suto, Yasushi, Kayo, Issha, Taruya, Atsushi, Vogele, Michael S., Hoyle, Fiona, Gott, J. Richard, III and Brinkmann, Jon,

2003, “Minkowski Functionals of SDSS Galaxies I : Analysis of Excursion Sets”, *Pub. Astron. Soc. Japan*, **55**, 911–931. [DOI], [ADS], [arXiv:astro-ph/0304455 [astro-ph]]

Hikage, Chiaki, Komatsu, Eiichiro and Matsubara, Takahiko, 2006, “Primordial Non-Gaussianity and Analytical Formula for Minkowski Functionals of the Cosmic Microwave Background and Large-Scale Structure”, *Astrophys. J.*, **653**(1), 11–26. [DOI], [ADS], [arXiv:astro-ph/0607284 [astro-ph]]

Hikage, Chiaki, Oguri, Masamune, Hamana, Takashi, More, Surhud, Mandelbaum, Rachel, Takada, Masahiro, Käñhlinger, Fabian, Miyatake, Hironao, Nishizawa, Atsushi J, Aihara, Hiroaki, Armstrong, Robert, Bosch, James, Coupon, Jean, Ducout, Anne, Ho, Paul, Hsieh, Bau-Ching, Komiyama, Yutaka, Lanusse, Franãgois, Leauthaud, Alexie, Lupton, Robert H, Medezinski, Elinor, Mineo, Sogo, Miyama, Shoken, Miyazaki, Satoshi, Murata, Ryoma, Murayama, Hitoshi, Shirasaki, Masato, Sifãšn, Cristãşbal, Simet, Melanie, Speagle, Joshua, Spergel, David N, Strauss, Michael A, Sugiyama, Naoshi, Tanaka, Masayuki, Utsumi, Yousuke, Wang, Shiang-Yu and Yamada, Yoshihiko, 2019, “Cosmology from cosmic shear power spectra with Subaru Hyper Suprime-Cam first-year data”, *Publications of the Astronomical Society of Japan*, **71**(2). [DOI], [https://academic.oup.com/pasj/article-pdf/71/2/43/28463847/psz010.pdf]URL:

<https://doi.org/10.1093/pasj/psz010>. 43

Hildebrandt, H, Viola, M, Heymans, C, Joudaki, S, Kuijken, K, Blake, C, Erben, T, Joachimi, B, Klaes, D, Miller, L, Morrison, C B, Nakajima, R, Verdoes Kleijn, G, Amon, A, Choi, A, Covone, G, de Jong, J T A, Dvornik, A, Fenech Conti, I, Grado, A, Harnois-Dãraps, J, Herbonnet, R, Hoekstra, H, Käñhlinger, F, McFarland, J, Mead, A, Merten, J, Napolitano, N, Peacock, J A, Radovich, M, Schneider, P, Simon, P, Valentijn, E A, van den Busch, J L, van Uitert, E and Van Waerbeke, L, 2016, “KiDS-450: cosmological parameter constraints from tomographic weak gravitational lensing”, *Monthly Notices of the Royal Astronomical Society*, **465**(2), 1454–1498. [DOI], [https://academic.oup.com/mnras/article-pdf/465/2/1454/24243465/stw2805.pdf]URL:

<https://doi.org/10.1093/mnras/stw2805>

- Hinshaw, G., Nolta, M. R., Bennett, C. L., Bean, R., Doré, O., Greason, M. R., Halpern, M., Hill, R. S., Jarosik, N., Kogut, A., Komatsu, E., Limon, M., Odegard, N., Meyer, S. S., Page, L., Peiris, H. V., Spergel, D. N., Tucker, G. S., Verde, L., Weiland, J. L., Wollack, E. and Wright, E. L., 2007, “Three-Year Wilkinson Microwave Anisotropy Probe (WMAP) Observations: Temperature Analysis”, *Astrophys. J. Suppl.*, **170**(2), 288–334. [DOI], [ADS], [arXiv:astro-ph/0603451 [astro-ph]]
- Hirata, Christopher M. and Seljak, Uroš, 2003, “Analyzing weak lensing of the cosmic microwave background using the likelihood function”, *Phys. Rev. D*, **67**, 043001. [DOI]URL:  
<https://link.aps.org/doi/10.1103/PhysRevD.67.043001>
- Hirata, Christopher M. and Seljak, Uroš, 2003, “Reconstruction of lensing from the cosmic microwave background polarization”, *Physical Review D*, **68**(8), 083002. [DOI], [ADS], [arXiv:astro-ph/0306354 [astro-ph]]
- Ho, Shirley, Hirata, Christopher, Padmanabhan, Nikhil, Seljak, Uros and Bahcall, Neta, 2008, “Correlation of CMB with large-scale structure. I. Integrated Sachs-Wolfe tomography and cosmological implications”, *Physical Review D*, **78**(4), 043519. [DOI], [ADS], [arXiv:0801.0642 [astro-ph]]
- Howlett, Cullan, Lewis, Antony, Hall, Alex and Challinor, Anthony, 2012, “CMB power spectrum parameter degeneracies in the era of precision cosmology”, *Journal of Cosmology and Astroparticle Physics*, **2012**(04), 027–027. [DOI]URL:  
<https://doi.org/10.1088/1475-7516/2012/04/027>
- Hu, Wayne, 2000, “Weak lensing of the CMB: A harmonic approach”, *Phys. Rev. D*, **62**, 043007. [DOI]URL:  
<https://link.aps.org/doi/10.1103/PhysRevD.62.043007>
- Hu, Wayne, 2001, “Mapping the Dark Matter through the Cosmic Microwave Background Damping Tail”, *Astrophys. J. Lett.*, **557**(2), L79–L83. [DOI], [ADS], [arXiv:astro-ph/0105424 [astro-ph]]

- Hu, Wayne and Okamoto, Takemi, 2002, “Mass Reconstruction with Cosmic Microwave Background Polarization”, *Astrophys. J.*, **574**(2), 566–574. [DOI], [ADS], [arXiv:astro-ph/0111606 [astro-ph]]
- Hu, Wayne and White, Martin, 1997, “A CMB polarization primer”, *New Astronomy*, **2**(4), 323–344. [DOI], [ADS], [arXiv:astro-ph/9706147 [astro-ph]]
- Joby, P. K., Chingangbam, Pravabati, Ghosh, Tuhin, Ganesan, Vidhya and Ravikumar, C. D., 2019, “Search for anomalous alignments of structures in Planck data using Minkowski Tensors”, , **2019**(1), 009. [DOI], [ADS], [arXiv:1807.01306 [astro-ph.CO]]
- Kapahtia, Akanksha, Chingangbam, Pravabati, Appleby, Stephen and Park, Changbom, 2018, “A novel probe of ionized bubble shape and size statistics of the epoch of reionization using the contour Minkowski Tensor”, *Journal of Cosmology and Astroparticle Physics*, **2018**(10), 011–011. [DOI]URL:  
<https://doi.org/10.1088/1475-7516/2018/10/011>
- Kapahtia, Akanksha, Chingangbam, Pravabati and Appleby, Stephen, 2019, “Morphology of 21cm brightness temperature during the Epoch of Reionization using Contour Minkowski Tensor”, , **2019**(9), 053. [DOI], [ADS], [arXiv:1904.06840 [astro-ph.CO]]
- Kapahtia, Akanksha, Chingangbam, Pravabati, Ghara, Raghunath, Appleby, Stephen and Choudhury, Tirthankar Roy, 2021, “Prospects of constraining reionization model parameters using Minkowski tensors and Betti numbers”, *Journal of Cosmology and Astroparticle Physics*, **2021**(05), 026. [DOI]URL:  
<https://doi.org/10.1088/1475-7516/2021/05/026>
- Keisler, R., Reichardt, C. L., Aird, K. A., Benson, B. A., Bleem, L. E., Carlstrom, J. E., Chang, C. L., Cho, H. M., Crawford, T. M., Crites, A. T., de Haan, T., Dobbs, M. A., Dudley, J., George, E. M., Halverson, N. W., Holder, G. P., Holzzapfel, W. L., Hoover, S., Hou, Z., Hrubes, J. D., Joy, M., Knox, L., Lee, A. T., Leitch, E. M., Lueker, M., Luong-Van, D., McMahon, J. J., Mehl, J., Meyer, S. S., Millea, M., Mohr, J. J., Montroy, T. E., Natoli, T., Padin, S., Plagge, T., Pryke, C., Ruhl, J. E., Schaffer, K. K., Shaw, L., Shirokoff, E., Spieler, H. G., Staniszewski, Z., Stark, A. A., Story, K., van Engelen, A., Vanderlinde, K., Vieira, J. D., Williamson, R. and Zahn, O., 2011,

“A MEASUREMENT OF THE DAMPING TAIL OF THE COSMIC MICROWAVE BACKGROUND POWER SPECTRUM WITH THE SOUTH POLE TELESCOPE”,

*The Astrophysical Journal*, **743**(1), 28. [DOI]URL:

<https://doi.org/10.1088/0004-637x/743/1/28>

Kesden, Michael, Cooray, Asantha and Kamionkowski, Marc, 2003, “Lensing reconstruction with CMB temperature and polarization”, *Phys. Rev. D*, **67**, 123 507. [DOI]URL:

<https://link.aps.org/doi/10.1103/PhysRevD.67.123507>

Knox, Lloyd and Song, Yong-Seon, 2002, “Limit on the Detectability of the Energy Scale of Inflation”, *Physical Review L*, **89**(1), 011303. [DOI], [ADS], [arXiv:astro-ph/0202286 [astro-ph]]

Kochappan, Joby P., Sen, Aparajita, Ghosh, Tuhin, Chingangbam, Pravabati and Basak, Soumen, 2021, “Application of the contour Minkowski tensor and  $\mathcal{D}$  statistic to the Planck  $E$ -mode data”, *Phys. Rev. D*, **103**, 123 523. [DOI]URL:

<https://link.aps.org/doi/10.1103/PhysRevD.103.123523>

Komatsu, E., Spergel, D. N. and Wandelt, B. D., 2005, “Measuring Primordial Non-Gaussianity in the Cosmic Microwave Background”, *Astrophys. J.*, **634**(1), 14–19. [DOI], [ADS], [arXiv:astro-ph/0305189 [astro-ph]]

Komatsu, Eiichiro and Spergel, David N., 2001, “Acoustic signatures in the primary microwave background bispectrum”, *Physical Review D*, **63**(6), 063002. [DOI], [ADS], [arXiv:astro-ph/0005036 [astro-ph]]

Kovac, J. M., Leitch, E. M., Pryke, C., Carlstrom, J. E., Halverson, N. W. and Holzzapfel, W. L., 2002, “Detection of polarization in the cosmic microwave background using DASI”, *Nature*, **420**(6917), 772–787. [DOI], [ADS], [arXiv:astro-ph/0209478 [astro-ph]]

Langlois, David, Renaux-Petel, Sébastien, Steer, Danièle A. and Tanaka, Takahiro, 2008, “Primordial perturbations and non-Gaussianities in DBI and general multifield inflation”, *Phys. Rev. D*, **78**, 063 523. [DOI]URL:

<https://link.aps.org/doi/10.1103/PhysRevD.78.063523>

Lee, Adrian, Abitbol, Maximilian H., Adachi, Shunsuke, Ade, Peter, Aguirre, James, Ahmed, Zeeshan, Aiola, Simone, Ali, Aamir, Alonso, David, Alvarez, Marcelo A., Arnold, Kam, Ashton, Peter, Atkins, Zachary, Austermann, Jason, Awan, Humna, Baccigalupi, Carlo, Baildon, Taylor, Baleato Lizancos, Anton, Barron, Darcy, Battaglia, Nick, Battye, Richard, Baxter, Eric, Bazarko, Andrew, Beall, James A., Bean, Rachel, Beck, Dominic, Beckman, Shawn, Beringue, Benjamin, Bhandarkar, Tanay, Bhimani, Sanah, Bianchini, Federico, Boada, Steven, Boettger, David, Bolland, Boris, Bond, J. Richard, Borrill, Julian, Brown, Michael L., Bruno, Sarah Marie, Bryan, Sean, Calabrese, Erminia, Calafut, Victoria, Calisse, Paolo, Carron, Julien, Carl, Fred. M., Cayuso, Juan, Challinor, Anthony, Chesmore, Grace, Chinone, Yuji, Chluba, Jens, Cho, Hsiao-Mei Sherry, Choi, Steve, Clark, Susan, Clarke, Philip, Contaldi, Carlo, Coppi, Gabriele, Cothard, Nicholas F., Coughlin, Kevin, Coulton, Will, Crichton, Devin, Crowley, Kevin D., Crowley, Kevin T., Cukierman, Ari, D'Ewart, John M., Dünner, Rolando, de Haan, Tijmen, Devlin, Mark, Dicker, Simon, Dober, Bradley, Duell, Cody J., Duff, Shannon, Duivenvoorden, Adri, Dunkley, Jo, El Bouhargani, Hamza, Errard, Josquin, Fabbian, Giulio, Feeney, Stephen, Fergusson, James, Ferraro, Simone, Fluxa, Pedro, Freese, Katherine, Frisch, Josef C., Frolov, Andrei, Fuller, George, Galitzki, Nicholas, Gallardo, Patricio A., Galvez Gherzi, Jose Tomas, Gao, Jiansong, Gawiser, Eric, Gerbino, Martina, Gluscevic, Vera, Goeckner-Wald, Neil, Golec, Joseph, Gordon, Sam, Gralla, Megan, Green, Daniel, Grigorian, Arpi, Groh, John, Groppi, Chris, Guan, Yilun, Gudmundsson, Jon E., Halpern, Mark, Han, Dongwon, Hargrave, Peter, Harrington, Kathleen, Hasegawa, Masaya, Hasselfield, Matthew, Hattori, Makoto, Haynes, Victor, Hazumi, Masashi, Healy, Erin, Henderson, Shawn W., Hensley, Brandon, Hervias-Caimapo, Carlos, Hill, Charles A., Hill, J. Colin, Hilton, Gene, Hilton, Matt, Hincks, Adam D., Hinshaw, Gary, Hložek, Renee, Ho, Shirley, Ho, Shuay-Pwu Patty, Hoang, Thuong D., Hoh, Jonathan, Hotinli, Selim C., Huang, Zhiqi, Hubmayr, Johannes, Huffenberger, Kevin, Hughes, John P., Ijjas, Anna, Ikape, Margaret, Irwin, Kent, Jaffe, Andrew H., Jain, Bhuvnesh, Jeong, Oliver, Johnson, Matthew, Kaneko, Daisuke, Karpel, Ethan D., Katayama, Nobuhiko, Keating, Brian, Keskitalo, Reijo, Kisner, Theodore, Kiuchi, Kenji, Klein, Jeff, Knowles, Kenda, Kofman, Anna, Koopman, Brian, Kosowsky,

Arthur, Krachmalnicoff, Nicoletta, Kusaka, Akito, La Plante, Paul, Lashner, Jacob, Lee, Adrian, Lee, Eunseong, Lewis, Antony, Li, Yaqiong, Li, Zack, Limon, Michele, Linder, Eric, Liu, Jia, Lopez-Caraballo, Carlos, Louis, Thibaut, Lungu, Marius, Madhavacheril, Mathew, Mak, Daisy, Maldonado, Felipe, Mani, Hamdi, Mates, Ben, Matsuda, Frederick, Maurin, Loïc, Mauskopf, Phil, May, Andrew, McCallum, Nialh, McCarrick, Heather, McKenney, Chris, McMahan, Jeff, Meerburg, P. Daniel, Mertens, James, Meyers, Joel, Miller, Amber, Mirmelstein, Mark, Moodley, Kavilan, Moore, Jenna, Munchmeyer, Moritz, Munson, Charles, Murata, Masaaki, Naess, Sigurd, Namikawa, Toshiya, Nati, Federico, Navaroli, Martin, Newburgh, Laura, Nguyen, Ho Nam, Nicola, Andrina, Niemack, Mike, Nishino, Haruki, Nishinomiya, Yume, Orłowski-Scherer, John, Pagano, Luca, Partridge, Bruce, Perrotta, Francesca, Phakathi, Phumlani, Piccirillo, Lucio, Pierpaoli, Elena, Pisano, Giampaolo, Poletti, Davide, Puddu, Roberto, Puglisi, Giuseppe, Raum, Chris, Reichardt, Christian L., Remazeilles, Mathieu, Rephaeli, Yoel, Riechers, Dominik, Rojas, Felipe, Rotti, Aditya, Roy, Anirban, Sadeh, Sharon, Sakurai, Yuki, Salatino, Maria, Sathyanarayana Rao, Mayuri, Saunders, Lauren, Schaan, Emmanuel, Schmittfull, Marcel, Sehgal, Neelima, Seibert, Joseph, Seljak, Uros, Shellard, Paul, Sherwin, Blake, Shimon, Meir, Sierra, Carlos, Sievers, Jonathan, Sifon, Cristobal, Sikhosana, Precious, Silva-Feaver, Maximiliano, Simon, Sara M., Sinclair, Adrian, Smith, Kendrick, Sohn, Wuhyun, Sonka, Rita, Spergel, David, Spisak, Jacob, Staggs, Suzanne T., Stein, George, Stevens, Jason R., Stompor, Radek, Suzuki, Aritoki, Tajima, Osamu, Takakura, Satoru, Teply, Grant, Thomas, Daniel B., Thorne, Ben, Thornton, Robert, Trac, Hy, Treu, Jesse, Tsai, Calvin, Tucker, Carole, Ullom, Joel, Vagnozzi, Sunny, van Engelen, Alexander, Van Lanen, Jeff, Van Winkle, Daniel D., Vavagiakis, Eve M., Vergès, Clara, Vissers, Michael, Wagoner, Kasey, Walker, Samantha, Wang, Yuhan, Ward, Jon, Westbrook, Ben, Whitehorn, Nathan, Williams, Jason, Williams, Joel, Wollack, Edward, Xu, Zhilei, Yasini, Siavash, Young, Edward, Yu, Byeonghee, Yu, Cyndia, Zago, Fernando, Zannoni, Mario, Zhang, Hezi, Zheng, Kaiwen, Zhu, Ningfeng and Zonca, Andrea, 2019, “The Simons Observatory”, in *Bulletin of the American Astronomical Society*, 51, [ADS], [arXiv:1907.08284 [astro-ph.IM]]

Lesgourgues, Julien, 2011, “The Cosmic Linear Anisotropy Solving System (CLASS) I: Overview”, *arXiv e-prints*, arXiv:1104.2932. [ADS], [arXiv:1104.2932 [astro-ph.IM]]

- Lesgourgues, Julien and Pastor, Sergio, 2006, “Massive neutrinos and cosmology”, *Phys. Rep.*, **429**(6), 307–379. [DOI], [ADS], [arXiv:astro-ph/0603494 [astro-ph]]
- Lewis, Antony, 2005, “Lensed CMB simulation and parameter estimation”, *Physical Review D*, **71**(8), 083008. [DOI], [ADS], [arXiv:astro-ph/0502469 [astro-ph]]
- Lewis, Antony and Challinor, Anthony, 2006, “Weak gravitational lensing of the CMB”, *Phys. Rep.*, **429**(1), 1–65. [DOI], [ADS], [arXiv:astro-ph/0601594 [astro-ph]]
- Lewis, Antony, Challinor, Anthony and Lasenby, Anthony, 2000, “Efficient Computation of Cosmic Microwave Background Anisotropies in Closed Friedmann-Robertson-Walker Models”, *Astrophys. J.*, **538**(2), 473–476. [DOI], [ADS], [arXiv:astro-ph/9911177 [astro-ph]]
- Liguori, M., Matarrese, S. and Moscardini, L., 2003, “High-Resolution Simulations of Non-Gaussian Cosmic Microwave Background Maps in Spherical Coordinates”, *Astrophys. J.*, **597**(1), 57–65. [DOI], [ADS], [arXiv:astro-ph/0306248 [astro-ph]]
- Liguori, Michele, Yadav, Amit, Hansen, Frode K., Komatsu, Eiichiro, Matarrese, Sabino and Wandelt, Benjamin, 2007, “Temperature and polarization CMB maps from primordial non-Gaussianities of the local type”, *Physical Review D*, **76**(10), 105016. [DOI], [ADS], [arXiv:0708.3786 [astro-ph]]
- Lim, Eugene A. and Simon, Dennis, 2012, “Can we detect Hot or Cold spots in the CMB with Minkowski Functionals?”, *JCAP*, **01**, 048. [DOI], [arXiv:1103.4300 [astro-ph.CO]]
- Linde, A.D., 1982, “A new inflationary universe scenario: A possible solution of the horizon, flatness, homogeneity, isotropy and primordial monopole problems”, *Physics Letters B*, **108**(6), 389–393. [DOI]URL:  
<https://www.sciencedirect.com/science/article/pii/0370269382912199>
- Lorensen, William E. and Cline, Harvey E., 1987, “Marching Cubes: A High Resolution 3D Surface Construction Algorithm”, *SIGGRAPH Comput. Graph.*, **21**(4), 163–169. [DOI]URL:  
<https://doi.org/10.1145/37402.37422>



- Lyth, David H., 1997, “What Would We Learn by Detecting a Gravitational Wave Signal in the Cosmic Microwave Background Anisotropy?”, *Physical Review L*, **78**(10), 1861–1863. [DOI], [ADS], [arXiv:hep-ph/9606387 [hep-ph]]
- Mantz, Hubert, Jacobs, Karin and Mecke, Klaus, 2008, “Utilizing Minkowski functionals for image analysis: a marching square algorithm”, *Journal of Statistical Mechanics: Theory and Experiment*, **2008**(12), P12015. [DOI]URL:  
<https://doi.org/10.1088/1742-5468/2008/12/p12015>
- Manzotti, A., Story, K. T., Wu, W. L. K., Austermann, J. E., Beall, J. A., Bender, A. N., Benson, B. A., Bleem, L. E., Bock, J. J., Carlstrom, J. E., Chang, C. L., Chiang, H. C., Cho, H.-M., Citron, R., Conley, A., Crawford, T. M., Crites, A. T., de Haan, T., Dobbs, M. A., Dodelson, S., Everett, W., Gallicchio, J., George, E. M., Gilbert, A., Halverson, N. W., Harrington, N., Henning, J. W., Hilton, G. C., Holder, G. P., Holzzapfel, W. L., Hoover, S., Hou, Z., Hrubes, J. D., Huang, N., Hubmayr, J., Irwin, K. D., Keisler, R., Knox, L., Lee, A. T., Leitch, E. M., Li, D., McMahon, J. J., Meyer, S. S., Mocalanu, L. M., Natoli, T., Nibarger, J. P., Novosad, V., Padin, S., Pryke, C., Reichardt, C. L., Ruhl, J. E., Saliwanchik, B. R., Sayre, J. T., Schaffer, K. K., Smecher, G., Stark, A. A., Vanderlinde, K., Vieira, J. D., Viero, M. P., Wang, G., Whitehorn, N., Yefremenko, V. and Zemcov, M., 2017, “CMB Polarization B-mode Delensing with SPTpol and Herschel”, *The Astrophysical Journal*, **846**(1), 45. [DOI]URL:  
<https://doi.org/10.3847/1538-4357/aa82bb>
- Marian, Laura and Bernstein, Gary M., 2007, “Detectability of CMB tensor  $B$  modes via delensing with weak lensing galaxy surveys”, *Phys. Rev. D*, **76**, 123009. [DOI]URL:  
<https://link.aps.org/doi/10.1103/PhysRevD.76.123009>
- Marques, G. A., Novaes, C. P., Bernui, A. and Ferreira, I. S., 2018, “Isotropy analyses of the Planck convergence map”, *Mon. Not. Roy. Astron. Soc.*, **473**(1), 165–172. [DOI], [ADS], [arXiv:1708.09793 [astro-ph.CO]]
- Mather, J. C., Cheng, E. S., Cottingham, D. A., Eplee, R. E., Jr., Fixsen, D. J., Hewagama, T., Isaacman, R. B., Jensen, K. A., Meyer, S. S., Noerdlinger, P. D., Read, S. M., Rosen, L. P., Shafer, R. A., Wright, E. L., Bennett, C. L., Boggess,

- N. W., Hauser, M. G., Kelsall, T., Moseley, S. H., Jr., Silverberg, R. F., Smoot, G. F., Weiss, R. and Wilkinson, D. T., 1994, “Measurement of the Cosmic Microwave Background Spectrum by the COBE FIRAS Instrument”, *Astrophys. J.*, **420**, 439. [DOI], [ADS]
- McDonald, Patrick, Scherrer, Robert J. and Walker, Terry P., 2000, “Cosmic microwave background constraint on residual annihilations of relic particles”, *Phys. Rev. D*, **63**, 023001. [DOI]URL:  
<https://link.aps.org/doi/10.1103/PhysRevD.63.023001>
- Mecke, K. R., Buchert, T. and Wagner, H., 1994, “Robust morphological measures for large-scale structure in the Universe”, *Astron. Astrophys.*, **288**, 697–704. [ADS], [arXiv:astro-ph/9312028 [astro-ph]]
- Metcalf, R. Benton and Silk, Joseph, 1997, “Gravitational Magnification of the Cosmic Microwave Background”, *Astrophys. J.*, **489**(1), 1–6. [DOI], [ADS], [arXiv:astro-ph/9708059 [astro-ph]]
- Miyamoto, Koichi, Sekiguchi, Toyokazu, Tashiro, Hiroyuki and Yokoyama, Shuichiro, 2014, “CMB distortion anisotropies due to the decay of primordial magnetic fields”, *Physical Review D*, **89**(6), 063508. [DOI], [ADS], [arXiv:1310.3886 [astro-ph.CO]]
- Namikawa, Toshiya, Hanson, Duncan and Takahashi, Ryuichi, 2013, “Bias-hardened CMB lensing”, *Monthly Notices of the Royal Astronomical Society*, **431**(1), 609–620. [DOI], [https://academic.oup.com/mnras/article-pdf/431/1/609/18243508/stt195.pdf]URL:  
<https://doi.org/10.1093/mnras/stt195>
- Novikov, D., Schmalzing, J. and Mukhanov, V. F., 2000, “On non-Gaussianity in the cosmic microwave background”, *Astron. Astrophys.*, **364**, 17–25. [ADS], [arXiv:astro-ph/0006097 [astro-ph]]
- Okamoto, Takemi and Hu, Wayne, 2003, “Cosmic microwave background lensing reconstruction on the full sky”, *Physical Review D*, **67**(8), 083002. [DOI], [ADS], [arXiv:astro-ph/0301031 [astro-ph]]

Omori, Y., Chown, R., Simard, G., Story, K. T., Aylor, K., Baxter, E. J., Benson, B. A., Bleem, L. E., Carlstrom, J. E., Chang, C. L., Cho, H-M., Crawford, T. M., Crites, A. T., de Haan, T., Dobbs, M. A., Everett, W. B., George, E. M., Halverson, N. W., Harrington, N. L., Holder, G. P., Hou, Z., Holzappel, W. L., Hrubes, J. D., Knox, L., Lee, A. T., Leitch, E. M., Luong-Van, D., Manzotti, A., Marrone, D. P., McMahon, J. J., Meyer, S. S., Mocanu, L. M., Mohr, J. J., Natoli, T., Padin, S., Pryke, C., Reichardt, C. L., Ruhl, J. E., Sayre, J. T., Schaffer, K. K., Shirokoff, E., Staniszewski, Z., Stark, A. A., Vanderlinde, K., Vieira, J. D., Williamson, R. and Zahn, O., 2017, "A 2500 deg<sup>2</sup>CMB Lensing Map from Combined South Pole Telescope and Planck Data", *The Astrophysical Journal*, **849**(2), 124. [DOI]URL:

<https://doi.org/10.3847/1538-4357/aa8d1d>

Omori, Y., Baxter, E. J., Chang, C., Kirk, D., Alarcon, A., Bernstein, G. M., Bleem, L. E., Cawthon, R., Choi, A., Chown, R., Crawford, T. M., Davis, C., De Vicente, J., DeRose, J., Dodelson, S., Eifler, T. F., Fosalba, P., Friedrich, O., Gatti, M., Gaztanaga, E., Giannantonio, T., Gruen, D., Hartley, W. G., Holder, G. P., Hoyle, B., Huterer, D., Jain, B., Jarvis, M., Krause, E., MacCrann, N., Miquel, R., Prat, J., Rau, M. M., Reichardt, C. L., Rozo, E., Samuroff, S., Sánchez, C., Secco, L. F., Sheldon, E., Simard, G., Troxel, M. A., Vielzeuf, P., Wechsler, R. H., Zuntz, J., Abbott, T. M. C., Abdalla, F. B., Allam, S., Annis, J., Avila, S., Aylor, K., Benson, B. A., Bertin, E., Bridle, S. L., Brooks, D., Burke, D. L., Carlstrom, J. E., Carnero Rosell, A., Carrasco Kind, M., Carretero, J., Castander, F. J., Chang, C. L., Cho, H. M., Crites, A. T., Crocce, M., Cunha, C. E., da Costa, L. N., de Haan, T., Desai, S., Diehl, H. T., Dietrich, J. P., Dobbs, M. A., Everett, W. B., Fernandez, E., Flaugher, B., Frieman, J., García-Bellido, J., George, E. M., Gruendl, R. A., Gutierrez, G., Halverson, N. W., Harrington, N. L., Hollowood, D. L., Honscheid, K., Holzappel, W. L., Hou, Z., Hrubes, J. D., James, D. J., Jeltema, T., Kuehn, K., Kuropatkin, N., Lima, M., Lin, H., Lee, A. T., Leitch, E. M., Luong-Van, D., Maia, M. A. G., Manzotti, A., Marrone, D. P., Marshall, J. L., Martini, P., McMahon, J. J., Melchior, P., Menanteau, F., Meyer, S. S., Mocanu, L. M., Mohr, J. J., Natoli, T., Ogando, R. L. C., Padin, S., Plazas, A. A., Pryke, C., Romer, A. K., Roodman, A., Ruhl, J. E., Rykoff, E. S., Sanchez, E., Scarpine, V., Schaffer, K. K., Schindler, R., Sevilla-Noarbe, I., Shirokoff, E., Smith, M., Smith, R. C., Soares-Santos, M., Sobreira, F., Staniszewski, Z., Stark, A. A.,

- Story, K. T., Suchyta, E., Swanson, M. E. C., Tarle, G., Thomas, D., Vanderlinde, K., Vieira, J. D., Vikram, V., Walker, A. R., Weller, J., Williamson, R., Wu, W. L. K., Zahn, O., DES Collaboration and SPT Collaboration, 2019, “Dark Energy Survey Year 1 Results: Cross-correlation between Dark Energy Survey Y1 galaxy weak lensing and South Pole Telescope+Planck CMB weak lensing”, *Physical Review D*, **100**(4), 043517. [DOI], [ADS], [arXiv:1810.02441 [astro-ph.CO]]
- Osborne, Stephen J., Hanson, Duncan and Doré, Olivier, 2014, “Extragalactic foreground contamination in temperature-based CMB lens reconstruction”, *Journal of Cosmology and Astroparticle Physics*, **2014**(03), 024–024. [DOI]URL:  
<https://doi.org/10.1088/1475-7516/2014/03/024>
- Park, Changbom, Pranav, Pratyush, Chingangbam, Pravabati, van de Weygaert, Rien, Jones, Bernard, Vegter, Gert, Kim, Inkang, Hidding, Johan and Hellwing, Wojciech A., 2013, “Betti Numbers of Gaussian Fields”, *Journal of Korean Astronomical Society*, **46**(3), 125–131. [DOI], [ADS], [arXiv:1307.2384 [astro-ph.CO]]
- Peiris, Hiranya V. and Spergel, David N., 2000, “Cross-Correlating the Sloan Digital Sky Survey with the Microwave Sky”, *The Astrophysical Journal*, **540**(2), 605–613. [DOI]URL:  
<https://doi.org/10.1086/309373>
- Penzias, A. A. and Wilson, R. W., 1965, “A Measurement of Excess Antenna Temperature at 4080 Mc/s.”, *Astrophys. J.*, **142**, 419–421. [DOI], [ADS]
- Perotto, L., Bobin, J., Plaszczynski, S., Starck, J.-L. and Lavabre, A., 2010, “Reconstruction of the cosmic microwave background lensing for Planck”, *A&A*, **519**, A4. [DOI]URL:  
<https://doi.org/10.1051/0004-6361/200912001>
- Planck Collaboration, Ade, P. A. R., Aghanim, N., Armitage-Caplan, C., Arnaud, M., Ashdown, M., Atrio-Barandela, F., Aumont, J., Baccigalupi, C., Banday, A. J., Barreiro, R. B., Bartlett, J. G., Basak, S., Battaner, E., Benabed, K., Benoît, A., Benoit-Lévy, A., Bernard, J. P., Bersanelli, M., Bielewicz, P., Bobin, J., Bock, J. J., Bonaldi, A., Bonavera, L., Bond, J. R., Borrill, J., Bouchet, F. R., Bridges, M., Bucher, M.,

Burigana, C., Butler, R. C., Cardoso, J. F., Catalano, A., Challinor, A., Chamballu, A., Chiang, H. C., Chiang, L. Y., Christensen, P. R., Church, S., Clements, D. L., Colombi, S., Colombo, L. P. L., Couchot, F., Coulais, A., Crill, B. P., Curto, A., Cuttaia, F., Danese, L., Davies, R. D., Davis, R. J., de Bernardis, P., de Rosa, A., de Zotti, G., Déchelette, T., Delabrouille, J., Delouis, J. M., Désert, F. X., Dickinson, C., Diego, J. M., Dole, H., Donzelli, S., Doré, O., Douspis, M., Dunkley, J., Dupac, X., Efstathiou, G., Enßlin, T. A., Eriksen, H. K., Finelli, F., Forni, O., Frailis, M., Franceschi, E., Galeotta, S., Ganga, K., Giard, M., Giardino, G., Giraud-Héraud, Y., González-Nuevo, J., Górski, K. M., Gratton, S., Gregorio, A., Gruppuso, A., Gudmundsson, J. E., Hansen, F. K., Hanson, D., Harrison, D., Henrot-Versillé, S., Hernández-Monteagudo, C., Herranz, D., Hildebrandt, S. R., Hivon, E., Ho, S., Hobson, M., Holmes, W. A., Hornstrup, A., Hovest, W., Huffenberger, K. M., Jaffe, A. H., Jaffe, T. R., Jones, W. C., Juvela, M., Keihänen, E., Keskitalo, R., Kisner, T. S., Kneissl, R., Knoche, J., Knox, L., Kunz, M., Kurki-Suonio, H., Lagache, G., Lähteenmäki, A., Lamarre, J. M., Lasenby, A., Laureijs, R. J., Lavabre, A., Lawrence, C. R., Leahy, J. P., Leonardi, R., León-Tavares, J., Lesgourgues, J., Lewis, A., Liguori, M., Lilje, P. B., Linden-Vørnle, M., López-Caniiego, M., Lubin, P. M., Macías-Pérez, J. F., Maffei, B., Maino, D., Mandolesi, N., Mangilli, A., Maris, M., Marshall, D. J., Martin, P. G., Martínez-González, E., Masi, S., Massardi, M., Matarrese, S., Matthai, F., Mazzotta, P., Melchiorri, A., Mendes, L., Mennella, A., Migliaccio, M., Mitra, S., Miville-Deschênes, M. A., Moneti, A., Montier, L., Morgante, G., Mortlock, D., Moss, A., Munshi, D., Murphy, J. A., Naselsky, P., Nati, F., Natoli, P., Netterfield, C. B., Nørgaard-Nielsen, H. U., Noviello, F., Novikov, D., Novikov, I., Osborne, S., Oxborrow, C. A., Paci, F., Pagano, L., Pajot, F., Paoletti, D., Partridge, B., Pasian, F., Patanchon, G., Perdureau, O., Perotto, L., Perrotta, F., Piacentini, F., Piat, M., Pierpaoli, E., Pietrobon, D., Plaszczynski, S., Pointecouteau, E., Polenta, G., Ponthieu, N., Popa, L., Poutanen, T., Pratt, G. W., Prézeau, G., Prunet, S., Puget, J. L., Pullen, A. R., Rachen, J. P., Rebolo, R., Reinecke, M., Remazeilles, M., Renault, C., Ricciardi, S., Riller, T., Ristorcelli, I., Rocha, G., Rosset, C., Roudier, G., Rowan-Robinson, M., Rubiño-Martín, J. A., Rusholme, B., Sandri, M., Santos, D., Savini, G., Scott, D., Seiffert, M. D., Shellard, E. P. S., Smith, K., Spencer, L. D., Starck, J. L., Stolyarov, V., Stompor, R., Sudiwala, R., Sunyaev, R., Sureau, F., Sutton, D., Suur-Uski, A. S.,

Sygnet, J. F., Tauber, J. A., Tavagnacco, D., Terenzi, L., Toffolatti, L., Tomasi, M., Tristram, M., Tucci, M., Tuovinen, J., Umama, G., Valenziano, L., Valiviita, J., Van Tent, B., Vielva, P., Villa, F., Vittorio, N., Wade, L. A., Wandelt, B. D., White, M., White, S. D. M., Yvon, D., Zacchei, A. and Zonca, A., 2014a, “Planck 2013 results. XVII. Gravitational lensing by large-scale structure”, *Astron. Astrophys.*, **571**, A17. [DOI], [ADS], [arXiv:1303.5077 [astro-ph.CO]]

Planck Collaboration, Ade, P. A. R., Aghanim, N., Armitage-Caplan, C., Arnaud, M., Ashdown, M., Atrio-Barandela, F., Aumont, J., Baccigalupi, C., Banday, A. J., Barreiro, R. B., Bartlett, J. G., Battaner, E., Benabed, K., Benoît, A., Benoit-Lévy, A., Bernard, J.-P., Bersanelli, M., Bielewicz, P., Bobin, J., Bock, J. J., Bonaldi, A., Bond, J. R., Borrill, J., Bouchet, F. R., Bridges, M., Bucher, M., Burigana, C., Butler, R. C., Calabrese, E., Cappellini, B., Cardoso, J.-F., Catalano, A., Challinor, A., Chamballu, A., Chary, R.-R., Chen, X., Chiang, H. C., Chiang, L.-Y., Christensen, P. R., Church, S., Clements, D. L., Colombi, S., Colombo, L. P. L., Couchot, F., Coulais, A., Crill, B. P., Curto, A., Cuttaia, F., Danese, L., Davies, R. D., Davis, R. J., de Bernardis, P., de Rosa, A., de Zotti, G., Delabrouille, J., Delouis, J.-M., Désert, F.-X., Dickinson, C., Diego, J. M., Dolag, K., Dole, H., Donzelli, S., Doré, O., Douspis, M., Dunkley, J., Dupac, X., Efstathiou, G., Elsner, F., Enßlin, T. A., Eriksen, H. K., Finelli, F., Forni, O., Frailis, M., Fraisse, A. A., Franceschi, E., Gaier, T. C., Galeotta, S., Galli, S., Ganga, K., Giard, M., Giardino, G., Giraud-Héraud, Y., Gjerløw, E., González-Nuevo, J., Górski, K. M., Gratton, S., Gregorio, A., Gruppuso, A., Gudmundsson, J. E., Haissinski, J., Hamann, J., Hansen, F. K., Hanson, D., Harrison, D., Henrot-Versillé, S., Hernández-Monteagudo, C., Herranz, D., Hildebrandt, S. R., Hivon, E., Hobson, M., Holmes, W. A., Hornstrup, A., Hou, Z., Hovest, W., Huffenberger, K. M., Jaffe, A. H., Jaffe, T. R., Jewell, J., Jones, W. C., Juvela, M., Keihänen, E., Keskitalo, R., Kisner, T. S., Kneissl, R., Knoche, J., Knox, L., Kunz, M., Kurki-Suonio, H., Lagache, G., Lähteenmäki, A., Lamarre, J.-M., Lasenby, A., Lattanzi, M., Laureijs, R. J., Lawrence, C. R., Leach, S., Leahy, J. P., Leonardi, R., León-Tavares, J., Lesgourgues, J., Lewis, A., Liguori, M., Lilje, P. B., Linden-Vørnle, M., López-Caniego, M., Lubin, P. M., Macías-Pérez, J. F., Maffei, B., Maino, D., Mandolesi, N., Maris, M., Marshall, D. J., Martin, P. G., Martínez-González, E., Masi, S., Massardi, M., Matarrese, S., Matthai, F., Mazzotta, P., Meinhold, P. R., Melchiorri, A., Melin, J.-B., Mendes, L.,

Menegoni, E., Mennella, A., Migliaccio, M., Millea, M., Mitra, S., Miville-Deschênes, M.-A., Moneti, A., Montier, L., Morgante, G., Mortlock, D., Moss, A., Munshi, D., Murphy, J. A., Naselsky, P., Nati, F., Natoli, P., Netterfield, C. B., Nørgaard-Nielsen, H. U., Noviello, F., Novikov, D., Novikov, I., O'Dwyer, I. J., Osborne, S., Oxborrow, C. A., Paci, F., Pagano, L., Pajot, F., Paladini, R., Paoletti, D., Partridge, B., Pasian, F., Patanchon, G., Pearson, D., Pearson, T. J., Peiris, H. V., Perdureau, O., Perotto, L., Perrotta, F., Pettorino, V., Piacentini, F., Piat, M., Pierpaoli, E., Pietrobon, D., Plaszczynski, S., Platania, P., Pointecouteau, E., Polenta, G., Ponthieu, N., Popa, L., Poutanen, T., Pratt, G. W., Prézeau, G., Prunet, S., Puget, J.-L., Rachen, J. P., Reach, W. T., Rebolo, R., Reinecke, M., Remazeilles, M., Renault, C., Ricciardi, S., Riller, T., Ristorcelli, I., Rocha, G., Rosset, C., Roudier, G., Rowan-Robinson, M., Rubiño-Martín, J. A., Rusholme, B., Sandri, M., Santos, D., Savelainen, M., Savini, G., Scott, D., Seiffert, M. D., Shellard, E. P. S., Spencer, L. D., Starck, J.-L., Stolyarov, V., Stompor, R., Sudiwala, R., Sunyaev, R., Sureau, F., Sutton, D., Suur-Uski, A.-S., Sygnet, J.-F., Tauber, J. A., Tavagnacco, D., Terenzi, L., Toffolatti, L., Tomasi, M., Tristram, M., Tucci, M., Tuovinen, J., Türler, M., Umaga, G., Valenziano, L., Valiviita, J., Van Tent, B., Vielva, P., Villa, F., Vittorio, N., Wade, L. A., Wandelt, B. D., Wehus, I. K., White, M., White, S. D. M., Wilkinson, A., Yvon, D., Zacchei, A. and Zonca, A., 2014b, "Planck 2013 results. XVI. Cosmological parameters", *A&A*, **571**, A16. [DOI]URL:

<https://doi.org/10.1051/0004-6361/201321591>

Planck Collaboration, Ade, P. A. R., Aghanim, N., Arnaud, M., Ashdown, M., Aumont, J., Baccigalupi, C., Banday, A. J., Barreiro, R. B., Bartlett, J. G., Bartolo, N., Basak, S., Battaner, E., Benabed, K., Benoît, A., Benoit-Lévy, A., Bernard, J. P., Bersanelli, M., Bielewicz, P., Bock, J. J., Bonaldi, A., Bonavera, L., Bond, J. R., Borrill, J., Bouchet, F. R., Boulanger, F., Bucher, M., Burigana, C., Butler, R. C., Calabrese, E., Cardoso, J. F., Catalano, A., Challinor, A., Chamballu, A., Chiang, H. C., Christensen, P. R., Church, S., Clements, D. L., Colombi, S., Colombo, L. P. L., Combet, C., Couchot, F., Coulais, A., Crill, B. P., Curto, A., Cuttaia, F., Danese, L., Davies, R. D., Davis, R. J., de Bernardis, P., de Rosa, A., de Zotti, G., Delabrouille, J., Désert, F. X., Diego, J. M., Dole, H., Donzelli, S., Doré, O., Douspis, M., Ducout, A., Dunkley, J., Dupac, X., Efstathiou, G., Elsner, F., Enßlin, T. A., Eriksen, H. K.,

Fergusson, J., Finelli, F., Forni, O., Frailis, M., Fraisse, A. A., Franceschi, E., Frejsel, A., Galeotta, S., Galli, S., Ganga, K., Giard, M., Giraud-Héraud, Y., Gjerløw, E., González-Nuevo, J., Górski, K. M., Gratton, S., Gregorio, A., Gruppuso, A., Gudmundsson, J. E., Hansen, F. K., Hanson, D., Harrison, D. L., Henrot-Versillé, S., Hernández-Monteagudo, C., Herranz, D., Hildebrandt, S. R., Hivon, E., Hobson, M., Holmes, W. A., Hornstrup, A., Hovest, W., Huffenberger, K. M., Hurier, G., Jaffe, A. H., Jaffe, T. R., Jones, W. C., Juvela, M., Keihänen, E., Keskitalo, R., Kisner, T. S., Kneissl, R., Knoche, J., Kunz, M., Kurki-Suonio, H., Lagache, G., Lähteenmäki, A., Lamarre, J. M., Lasenby, A., Lattanzi, M., Lawrence, C. R., Leonardi, R., Lesgourgues, J., Levrier, F., Lewis, A., Liguori, M., Lilje, P. B., Linden-Vørnle, M., López-Caniego, M., Lubin, P. M., Macías-Pérez, J. F., Maggio, G., Maino, D., Mandolesi, N., Mangilli, A., Maris, M., Martin, P. G., Martínez-González, E., Masi, S., Matarrese, S., McGehee, P., Meinhold, P. R., Melchiorri, A., Mendes, L., Mennella, A., Migliaccio, M., Mitra, S., Miville-Deschênes, M. A., Moneti, A., Montier, L., Morgante, G., Mortlock, D., Moss, A., Munshi, D., Murphy, J. A., Naselsky, P., Nati, F., Natoli, P., Netterfield, C. B., Nørgaard-Nielsen, H. U., Noviello, F., Novikov, D., Novikov, I., Oxborrow, C. A., Paci, F., Pagano, L., Pajot, F., Paoletti, D., Pasian, F., Patanchon, G., Perdereau, O., Perotto, L., Perrotta, F., Pettorino, V., Piacentini, F., Piat, M., Pierpaoli, E., Pietrobon, D., Plaszczynski, S., Pointecouteau, E., Polenta, G., Popa, L., Pratt, G. W., Prézeau, G., Prunet, S., Puget, J. L., Rachen, J. P., Reach, W. T., Rebolo, R., Reinecke, M., Remazeilles, M., Renault, C., Renzi, A., Ristorcelli, I., Rocha, G., Rosset, C., Rossetti, M., Roudier, G., Rowan-Robinson, M., Rubiño-Martín, J. A., Rusholme, B., Sandri, M., Santos, D., Savelainen, M., Savini, G., Scott, D., Seiffert, M. D., Shellard, E. P. S., Spencer, L. D., Stolyarov, V., Stompor, R., Sudiwala, R., Sunyaev, R., Sutton, D., Suur-Uski, A. S., Sygnet, J. F., Tauber, J. A., Terenzi, L., Toffolatti, L., Tomasi, M., Tristram, M., Tucci, M., Tuovinen, J., Valenziano, L., Valiviita, J., Van Tent, B., Vielva, P., Villa, F., Wade, L. A., Wandelt, B. D., Wehus, I. K., White, M., Yvon, D., Zacchei, A. and Zonca, A., 2016, “Planck 2015 results. XV. Gravitational lensing”, *Astron. Astrophys.*, **594**, A15. [DOI], [ADS], [arXiv:1502.01591 [astro-ph.CO]]

Planck Collaboration, Aghanim, N., Akrami, Y., Ashdown, M., Aumont, J., Baccigalupi, C., Ballardini, M., Banday, A. J., Barreiro, R. B., Bartolo, N., Basak, S., Benabed,



K., Bernard, J. P., Bersanelli, M., Bielewicz, P., Bock, J. J., Bond, J. R., Borrill, J., Bouchet, F. R., Boulanger, F., Bucher, M., Burigana, C., Calabrese, E., Cardoso, J. F., Carron, J., Challinor, A., Chiang, H. C., Colombo, L. P. L., Combet, C., Crill, B. P., Cuttaia, F., de Bernardis, P., de Zotti, G., Delabrouille, J., Di Valentino, E., Diego, J. M., Doré, O., Douspis, M., Ducout, A., Dupac, X., Efstathiou, G., Elsner, F., Enßlin, T. A., Eriksen, H. K., Fantaye, Y., Fernandez-Cobos, R., Finelli, F., Forastieri, F., Frailis, M., Fraisse, A. A., Franceschi, E., Frolov, A., Galeotta, S., Galli, S., Ganga, K., Génova-Santos, R. T., Gerbino, M., Ghosh, T., González-Nuevo, J., Górski, K. M., Gratton, S., Gruppuso, A., Gudmundsson, J. E., Hamann, J., Handley, W., Hansen, F. K., Herranz, D., Hivon, E., Huang, Z., Jaffe, A. H., Jones, W. C., Karakci, A., Keihänen, E., Keskitalo, R., Kiiveri, K., Kim, J., Knox, L., Krachmalnicoff, N., Kunz, M., Kurki-Suonio, H., Lagache, G., Lamarre, J. M., Lasenby, A., Lattanzi, M., Lawrence, C. R., Le Jeune, M., Levrier, F., Lewis, A., Liguori, M., Lilje, P. B., Lindholm, V., López-Caniego, M., Lubin, P. M., Ma, Y. Z., Macías-Pérez, J. F., Maggio, G., Maino, D., Mandolesi, N., Mangilli, A., Marcos-Caballero, A., Maris, M., Martin, P. G., Martínez-González, E., Matarrese, S., Mauri, N., McEwen, J. D., Melchiorri, A., Mennella, A., Migliaccio, M., Miville-Deschênes, M. A., Molinari, D., Moneti, A., Montier, L., Morgante, G., Moss, A., Natoli, P., Pagano, L., Paoletti, D., Partridge, B., Patanchon, G., Perrotta, F., Pettorino, V., Piacentini, F., Polastri, L., Polenta, G., Puget, J. L., Rachen, J. P., Reinecke, M., Remazeilles, M., Renzi, A., Rocha, G., Rosset, C., Roudier, G., Rubiño-Martín, J. A., Ruiz-Granados, B., Salvati, L., Sandri, M., Savelainen, M., Scott, D., Sirignano, C., Sunyaev, R., Suur-Uski, A. S., Tauber, J. A., Tavagnacco, D., Tenti, M., Toffolatti, L., Tomasi, M., Trombetti, T., Valiviita, J., Van Tent, B., Vielva, P., Villa, F., Vittorio, N., Wandelt, B. D., Wehus, I. K., White, M., White, S. D. M., Zacchei, A. and Zonca, A., 2020a, “Planck 2018 results. VIII. Gravitational lensing”, *Astron. Astrophys.*, **641**, A8. [DOI], [ADS], [arXiv:1807.06210 [astro-ph.CO]]

Planck Collaboration, Aghanim, N., Akrami, Y., Ashdown, M., Aumont, J., Baccigalupi, C., Ballardini, M., Banday, A. J., Barreiro, R. B., Bartolo, N., Basak, S., Benabed, K., Bernard, J. P., Bersanelli, M., Bielewicz, P., Bond, J. R., Borrill, J., Bouchet, F. R., Boulanger, F., Bucher, M., Burigana, C., Calabrese, E., Cardoso, J. F., Carron, J., Challinor, A., Chiang, H. C., Colombo, L. P. L., Combet, C., Couchot, F., Crill, B. P.,

Cuttaia, F., de Bernardis, P., de Rosa, A., de Zotti, G., Delabrouille, J., Delouis, J. M., Di Valentino, E., Diego, J. M., Doré, O., Douspis, M., Ducout, A., Dupac, X., Efstathiou, G., Elsner, F., Enßlin, T. A., Eriksen, H. K., Falgarone, E., Fantaye, Y., Finelli, F., Frailis, M., Fraisse, A. A., Franceschi, E., Frolov, A., Galeotta, S., Galli, S., Ganga, K., Génova-Santos, R. T., Gerbino, M., Ghosh, T., González-Nuevo, J., Górski, K. M., Gratton, S., Gruppuso, A., Gudmundsson, J. E., Handley, W., Hansen, F. K., Henrot-Versillé, S., Herranz, D., Hivon, E., Huang, Z., Jaffe, A. H., Jones, W. C., Karakci, A., Keihänen, E., Keskitalo, R., Kiiveri, K., Kim, J., Kisner, T. S., Krachmalnicoff, N., Kunz, M., Kurki-Suonio, H., Lagache, G., Lamarre, J. M., Lasenby, A., Lattanzi, M., Lawrence, C. R., Levrier, F., Liguori, M., Lilje, P. B., Lindholm, V., López-Caniego, M., Ma, Y. Z., Macías-Pérez, J. F., Maggio, G., Maino, D., Mandolesi, N., Mangilli, A., Martin, P. G., Martínez-González, E., Matarrese, S., Mauri, N., McEwen, J. D., Melchiorri, A., Mennella, A., Migliaccio, M., Miville-Deschênes, M. A., Molinari, D., Moneti, A., Montier, L., Morgante, G., Moss, A., Mottet, S., Natoli, P., Pagano, L., Paoletti, D., Partridge, B., Patanchon, G., Patrizzii, L., Perdureau, O., Perrotta, F., Pettorino, V., Piacentini, F., Puget, J. L., Rachen, J. P., Reinecke, M., Remazeilles, M., Renzi, A., Rocha, G., Roudier, G., Salvati, L., Sandri, M., Savelainen, M., Scott, D., Sirignano, C., Sirri, G., Spencer, L. D., Sunyaev, R., Suur-Uski, A. S., Tauber, J. A., Tavagnacco, D., Tenti, M., Toffolatti, L., Tomasi, M., Tristram, M., Trombetti, T., Valiviita, J., Vansyngel, F., Van Tent, B., Vibert, L., Vielva, P., Villa, F., Vittorio, N., Wandelt, B. D., Wehus, I. K. and Zonca, A., 2020b, “Planck 2018 results. III. High Frequency Instrument data processing and frequency maps”, *Astron. Astrophys.*, **641**, A3. [DOI], [ADS], [arXiv:1807.06207 [astro-ph.CO]]

Planck Collaboration, Aghanim, N., Akrami, Y., Ashdown, M., Aumont, J., Baccigalupi, C., Ballardini, M., Banday, A. J., Barreiro, R. B., Bartolo, N., Basak, S., Battye, R., Benabed, K., Bernard, J.-P., Bersanelli, M., Bielewicz, P., Bock, J. J., Bond, J. R., Borrill, J., Bouchet, F. R., Boulanger, F., Bucher, M., Burigana, C., Butler, R. C., Calabrese, E., Cardoso, J.-F., Carron, J., Challinor, A., Chiang, H. C., Chluba, J., Colombo, L. P. L., Combet, C., Contreras, D., Crill, B. P., Cuttaia, F., de Bernardis, P., de Zotti, G., Delabrouille, J., Delouis, J.-M., Di Valentino, E., Diego, J. M., Doré, O., Douspis, M., Ducout, A., Dupac, X., Dusini, S., Efstathiou, G., Elsner, F., Enßlin, T. A., Eriksen, H. K., Fantaye, Y., Farhang, M., Fergusson, J., Fernandez-Cobos,

R., Finelli, F., Forastieri, F., Frailis, M., Fraisse, A. A., Franceschi, E., Frolov, A., Galeotta, S., Galli, S., Ganga, K., Génova-Santos, R. T., Gerbino, M., Ghosh, T., González-Nuevo, J., Górski, K. M., Gratton, S., Gruppuso, A., Gudmundsson, J. E., Hamann, J., Handley, W., Hansen, F. K., Herranz, D., Hildebrandt, S. R., Hivon, E., Huang, Z., Jaffe, A. H., Jones, W. C., Karakci, A., Keihänen, E., Keskitalo, R., Kiiveri, K., Kim, J., Kisner, T. S., Knox, L., Krachmalnicoff, N., Kunz, M., Kurki-Suonio, H., Lagache, G., Lamarre, J.-M., Lasenby, A., Lattanzi, M., Lawrence, C. R., Le Jeune, M., Lemos, P., Lesgourgues, J., Levrier, F., Lewis, A., Liguori, M., Lilje, P. B., Lilley, M., Lindholm, V., López-Caniego, M., Lubin, P. M., Ma, Y.-Z., Macías-Pérez, J. F., Maggio, G., Maino, D., Mandolesi, N., Mangilli, A., Marcos-Caballero, A., Maris, M., Martin, P. G., Martinelli, M., Martínez-González, E., Matarrese, S., Mauri, N., McEwen, J. D., Meinhold, P. R., Melchiorri, A., Mennella, A., Migliaccio, M., Millea, M., Mitra, S., Miville-Deschênes, M.-A., Molinari, D., Montier, L., Morgante, G., Moss, A., Natoli, P., Nørgaard-Nielsen, H. U., Pagano, L., Paoletti, D., Partridge, B., Patanchon, G., Peiris, H. V., Perrotta, F., Pettorino, V., Piacentini, F., Polastri, L., Polenta, G., Puget, J.-L., Rachen, J. P., Reinecke, M., Remazeilles, M., Renzi, A., Rocha, G., Rosset, C., Roudier, G., Rubiño-Martín, J. A., Ruiz-Granados, B., Salvati, L., Sandri, M., Savelainen, M., Scott, D., Shellard, E. P. S., Sirignano, C., Sirri, G., Spencer, L. D., Sunyaev, R., Suur-Uski, A.-S., Tauber, J. A., Tavagnacco, D., Tenti, M., Toffolatti, L., Tomasi, M., Trombetti, T., Valenziano, L., Valiviita, J., Van Tent, B., Vibert, L., Vielva, P., Villa, F., Vittorio, N., Wandelt, B. D., Wehus, I. K., White, M., White, S. D. M., Zacchei, A. and Zonca, A., 2020c, “Planck 2018 results - VI. Cosmological parameters”, *A&A*, **641**, A6. [DOI]URL:

<https://doi.org/10.1051/0004-6361/201833910>

Planck Collaboration, Akrami, Y., Arroja, F., Ashdown, M., Aumont, J., Baccigalupi, C., Ballardini, M., Banday, A. J., Barreiro, R. B., Bartolo, N., Basak, S., Benabed, K., Bernard, J. P., Bersanelli, M., Bielewicz, P., Bond, J. R., Borrill, J., Bouchet, F. R., Bucher, M., Burigana, C., Butler, R. C., Calabrese, E., Cardoso, J. F., Casaponsa, B., Challinor, A., Chiang, H. C., Colombo, L. P. L., Combet, C., Crill, B. P., Cuttaia, F., de Bernardis, P., de Rosa, A., de Zotti, G., Delabrouille, J., Delouis, J. M., Di Valentino, E., Diego, J. M., Doré, O., Douspis, M., Ducout, A., Dupac, X., Dusini, S., Efstathiou, G., Elsner, F., Enßlin, T. A., Eriksen, H. K., Fantaye, Y., Fergusson,

J., Fernandez-Cobos, R., Finelli, F., Frailis, M., Fraisse, A. A., Franceschi, E., Frolov, A., Galeotta, S., Galli, S., Ganga, K., Génova-Santos, R. T., Gerbino, M., González-Nuevo, J., Górski, K. M., Gratton, S., Gruppuso, A., Gudmundsson, J. E., Hamann, J., Handley, W., Hansen, F. K., Herranz, D., Hivon, E., Huang, Z., Jaffe, A. H., Jones, W. C., Jung, G., Keihänen, E., Keskitalo, R., Kiiveri, K., Kim, J., Krachmalnicoff, N., Kunz, M., Kurki-Suonio, H., Lamarre, J. M., Lasenby, A., Lattanzi, M., Lawrence, C. R., Le Jeune, M., Levrier, F., Lewis, A., Liguori, M., Lilje, P. B., Lindholm, V., López-Caniego, M., Ma, Y. Z., Macías-Pérez, J. F., Maggio, G., Maino, D., Mandolesi, N., Marcos-Caballero, A., Maris, M., Martin, P. G., Martínez-González, E., Matarrese, S., Mauri, N., McEwen, J. D., Meerburg, P. D., Meinhold, P. R., Melchiorri, A., Mennella, A., Migliaccio, M., Miville-Deschênes, M. A., Molinari, D., Moneti, A., Montier, L., Morgante, G., Moss, A., Münchmeyer, M., Natoli, P., Oppizzi, F., Pagano, L., Paoletti, D., Partridge, B., Patanchon, G., Perrotta, F., Pettorino, V., Piacentini, F., Polenta, G., Puget, J. L., Rachen, J. P., Racine, B., Reinecke, M., Remazeilles, M., Renzi, A., Rocha, G., Rubiño-Martín, J. A., Ruiz-Granados, B., Salvati, L., Savelainen, M., Scott, D., Shellard, E. P. S., Shiraishi, M., Sirignano, C., Sirri, G., Smith, K., Spencer, L. D., Stanco, L., Sunyaev, R., Suur-Uski, A. S., Tauber, J. A., Tavagnacco, D., Tenti, M., Toffolatti, L., Tomasi, M., Trombetti, T., Valiviita, J., Van Tent, B., Vielva, P., Villa, F., Vittorio, N., Wandelt, B. D., Wehus, I. K., Zacchei, A. and Zonca, A., 2020d, “Planck 2018 results. IX. Constraints on primordial non-Gaussianity”, *Astron. Astrophys.*, **641**, A9. [DOI], [ADS], [arXiv:1905.05697 [astro-ph.CO]]

Planck Collaboration, Akrami, Y., Arroja, F., Ashdown, M., Aumont, J., Baccigalupi, C., Ballardini, M., Banday, A. J., Barreiro, R. B., Bartolo, N., Basak, S., Benabed, K., Bernard, J.-P., Bersanelli, M., Bielewicz, P., Bock, J. J., Bond, J. R., Borrill, J., Bouchet, F. R., Boulanger, F., Bucher, M., Burigana, C., Butler, R. C., Calabrese, E., Cardoso, J.-F., Carron, J., Challinor, A., Chiang, H. C., Colombo, L. P. L., Combet, C., Contreras, D., Crill, B. P., Cuttaia, F., de Bernardis, P., de Zotti, G., Delabrouille, J., Delouis, J.-M., Di Valentino, E., Diego, J. M., Donzelli, S., Doré, O., Douspis, M., Ducout, A., Dupac, X., Dusini, S., Efstathiou, G., Elsner, F., Enßlin, T. A., Eriksen, H. K., Fantaye, Y., Fergusson, J., Fernandez-Cobos, R., Finelli, F., Forastieri, F., Frailis, M., Franceschi, E., Frolov, A., Galeotta, S., Galli, S., Ganga, K., Gauthier, C.,

Génova-Santos, R. T., Gerbino, M., Ghosh, T., González-Nuevo, J., Górski, K. M., Gratton, S., Gruppuso, A., Gudmundsson, J. E., Hamann, J., Handley, W., Hansen, F. K., Herranz, D., Hivon, E., Hooper, D. C., Huang, Z., Jaffe, A. H., Jones, W. C., Keihänen, E., Keskitalo, R., Kiiveri, K., Kim, J., Kisner, T. S., Krachmalnicoff, N., Kunz, M., Kurki-Suonio, H., Lagache, G., Lamarre, J.-M., Lasenby, A., Lattanzi, M., Lawrence, C. R., Le Jeune, M., Lesgourgues, J., Levrier, F., Lewis, A., Liguori, M., Lilje, P. B., Lindholm, V., López-Caniego, M., Lubin, P. M., Ma, Y.-Z., Macías-Pérez, J. F., Maggio, G., Maino, D., Mandolesi, N., Mangilli, A., Marcos-Caballero, A., Maris, M., Martin, P. G., Martínez-González, E., Matarrese, S., Mauri, N., McEwen, J. D., Meerburg, P. D., Meinhold, P. R., Melchiorri, A., Mennella, A., Migliaccio, M., Mitra, S., Miville-Deschênes, M.-A., Molinari, D., Moneti, A., Montier, L., Morgante, G., Moss, A., Münchmeyer, M., Natoli, P., Nørgaard-Nielsen, H. U., Pagano, L., Paoletti, D., Partridge, B., Patanchon, G., Peiris, H. V., Perrotta, F., Pettorino, V., Piacentini, F., Polastri, L., Polenta, G., Puget, J.-L., Rachen, J. P., Reinecke, M., Remazeilles, M., Renzi, A., Rocha, G., Rosset, C., Roudier, G., Rubiño-Martín, J. A., Ruiz-Granados, B., Salvati, L., Sandri, M., Savelainen, M., Scott, D., Shellard, E. P. S., Shiraishi, M., Sirignano, C., Sirri, G., Spencer, L. D., Sunyaev, R., Suur-Uski, A.-S., Tauber, J. A., Tavagnacco, D., Tenti, M., Toffolatti, L., Tomasi, M., Trombetti, T., Valiviita, J., Van Tent, B., Vielva, P., Villa, F., Vittorio, N., Wandelt, B. D., Wehus, I. K., White, S. D. M., Zacchei, A., Zibin, J. P. and Zonca, A., 2020e, “Planck 2018 results - X. Constraints on inflation”, *A&A*, **641**, A10. [DOI]URL:  
<https://doi.org/10.1051/0004-6361/201833887>

Pranav, Pratyush, van de Weygaert, Rien, Vegter, Gert, Jones, Bernard J. T., Adler, Robert J., Feldbrugge, Job, Park, Changbom, Buchert, Thomas and Kerber, Michael, 2019, “Topology and geometry of Gaussian random fields I: on Betti numbers, Euler characteristic, and Minkowski functionals”, *Mon. Not. Roy. Astron. Soc.*, **485**(3), 4167–4208. [DOI], [ADS], [arXiv:1812.07310 [astro-ph.CO]]

Pratten, Geraint and Munshi, Dipak, 2012, “Non-Gaussianity in large-scale structure and Minkowski functionals”, *Mon. Not. Roy. Astron. Soc.*, **423**(4), 3209–3226. [DOI], [ADS], [arXiv:1108.1985 [astro-ph.CO]]

- Rees, M. J., 1968, “Polarization and Spectrum of the Primeval Radiation in an Anisotropic Universe”, *Astrophys. J. Lett.*, **153**, L1. [DOI], [ADS]
- Reichardt, C. L., Ade, P. A. R., Bock, J. J., Bond, J. R., Brevik, J. A., Contaldi, C. R., Daub, M. D., Dempsey, J. T., Goldstein, J. H., Holzappel, W. L., Kuo, C. L., Lange, A. E., Lueker, M., Newcomb, M., Peterson, J. B., Ruhl, J., Runyan, M. C. and Staniszewski, Z., 2009, “High-Resolution CMB Power Spectrum from the Complete ACBAR Data Set”, *Astrophys. J.*, **694**(2), 1200–1219. [DOI], [ADS], [arXiv:0801.1491 [astro-ph]]
- Riess, Adam G., Yuan, Wenlong, Macri, Lucas M., Scolnic, Dan, Brout, Dillon, Casertano, Stefano, Jones, David O., Murakami, Yukei, Breuval, Louise, Brink, Thomas G., Filippenko, Alexei V., Hoffmann, Samantha, Jha, Saurabh W., Kenworthy, W. D’arcy, Mackenty, John, Stahl, Benjamin E. and Zheng, Weikang, 2021, “A Comprehensive Measurement of the Local Value of the Hubble Constant with 1 km/s/Mpc Uncertainty from the Hubble Space Telescope and the SH0ES Team”, *arXiv e-prints*, arXiv:2112.04510. [ADS], [arXiv:2112.04510 [astro-ph.CO]]
- Sahni, Varun, Sathyaprakash, B. S. and Shandarin, Sergei F., 1998, “Shapefinders: A New Shape Diagnostic for Large-Scale Structure”, *Astrophys. J. Lett.*, **495**(1), L5–L8. [DOI], [ADS], [arXiv:astro-ph/9801053 [astro-ph]]
- Santos, Larissa, Wang, Kai and Zhao, Wen, 2016, “Probing the statistical properties of CMB B-mode polarization through Minkowski functionals”, , **2016**(7), 029. [DOI], [ADS], [arXiv:1510.07779 [astro-ph.CO]]
- Schmalzing, Jens and Gorski, Krzysztof M., 1998, “Minkowski functionals used in the morphological analysis of cosmic microwave background anisotropy maps”, *Mon. Not. Roy. Astron. Soc.*, **297**(2), 355–365. [DOI], [ADS], [arXiv:astro-ph/9710185 [astro-ph]]
- Schröder-Turk, G. E., Mickel, W., Kapfer, S. C., Schaller, F. M., Breidenbach, B., Hug, D. and Mecke, K., 2013, “Minkowski tensors of anisotropic spatial structure”, *New Journal of Physics*, **15**(8), 083028. [DOI], [ADS], [arXiv:1009.2340 [cond-mat.soft]]

Schroder-Turk, G.E., KAPFER, S., BREIDENBACH, B., BEISBART, C. and MECKE, K., 2010, “Tensorial Minkowski functionals and anisotropy measures for planar patterns”, *Journal of Microscopy*, **238**(1), 57–74. [DOI], [https://onlinelibrary.wiley.com/doi/pdf/10.1111/j.1365-2818.2009.03331.x]URL: https://onlinelibrary.wiley.com/doi/abs/10.1111/j.1365-2818.2009.03331.x

Seljak, Uros, 1996, “Gravitational Lensing Effect on Cosmic Microwave Background Anisotropies: A Power Spectrum Approach”, *Astrophys. J.*, **463**, 1. [DOI], [ADS], [arXiv:astro-ph/9505109 [astro-ph]]

Seljak, Uros and Zaldarriaga, Matias, 1996, “A Line-of-Sight Integration Approach to Cosmic Microwave Background Anisotropies”, *Astrophys. J.*, **469**, 437. [DOI], [ADS], [arXiv:astro-ph/9603033 [astro-ph]]

Seljak, Uroš and Zaldarriaga, Matias, 1997, “Signature of Gravity Waves in the Polarization of the Microwave Background”, *Physical Review L*, **78**(11), 2054–2057. [DOI], [ADS], [arXiv:astro-ph/9609169 [astro-ph]]

Shandarin, Sergei F., 2004, “Morphological statistics of the cosmic web”, in *IAU Colloq. 195: Outskirts of Galaxy Clusters: Intense Life in the Suburbs*, (Ed.) Diaferio, Antonaldo, [DOI], [ADS], [arXiv:astro-ph/0405303 [astro-ph]]

Shandarin, Sergei F., Feldman, Hume A., Xu, Yongzhong and Tegmark, Max, 2001, “Morphological Measures of nonGaussianity in CMB Maps”, *arXiv e-prints*, astro-ph/0107136. [ADS], [arXiv:astro-ph/0107136 [astro-ph]]

Sherwin, Blake D., Das, Sudeep, Hajian, Amir, Addison, Graeme, Bond, J. Richard, Crichton, Devin, Devlin, Mark J., Dunkley, Joanna, Gralla, Megan B., Halpern, Mark, Hill, J. Colin, Hincks, Adam D., Hughes, John P., Huffenberger, Kevin, Hlozek, Renée, Kosowsky, Arthur, Louis, Thibaut, Marriage, Tobias A., Marsden, Danica, Menanteau, Felipe, Moodley, Kavilan, Niemack, Michael D., Page, Lyman A., Reese, Erik D., Sehgal, Neelima, Sievers, Jon, Sifón, Cristóbal, Spergel, David N., Staggs, Suzanne T., Switzer, Eric R. and Wollack, Ed, 2012, “The Atacama Cosmology Telescope: Cross-correlation of cosmic microwave background lensing and quasars”, *Phys. Rev. D*, **86**,

083006. [DOI]URL:

<https://link.aps.org/doi/10.1103/PhysRevD.86.083006>

Sherwin, Blake D., van Engelen, Alexander, Sehgal, Neelima, Madhavacheril, Mathew, Addison, Graeme E., Aiola, Simone, Allison, Rupert, Battaglia, Nicholas, Becker, Daniel T., Beall, James A., Bond, J. Richard, Calabrese, Erminia, Datta, Rahul, Devlin, Mark J., Dünner, Rolando, Dunkley, Joanna, Fox, Anna E., Gallardo, Patricio, Halpern, Mark, Hasselfield, Matthew, Henderson, Shawn, Hill, J. Colin, Hilton, Gene C., Hubmayr, Johannes, Hughes, John P., Hincks, Adam D., Hlozek, Renée, Huffenberger, Kevin M., Koopman, Brian, Kosowsky, Arthur, Louis, Thibaut, Maurin, Loïc, McMahon, Jeff, Moodley, Kavilan, Naess, Sigurd, Nati, Federico, Newburgh, Laura, Niemack, Michael D., Page, Lyman A., Sievers, Jonathan, Spergel, David N., Staggs, Suzanne T., Thornton, Robert J., Van Lanen, Jeff, Vavagiakis, Eve and Wolack, Edward J., 2017, “Two-season Atacama Cosmology Telescope polarimeter lensing power spectrum”, *Physical Review D*, **95**(12), 123529. [DOI], [ADS], [arXiv:1611.09753 [astro-ph.CO]]

Shirasaki, Masato, Yoshida, Naoki, Hamana, Takashi and Nishimichi, Takahiro, 2012, “Probing Primordial Non-Gaussianity with Weak-lensing Minkowski Functionals”, *Astrophys. J.*, **760**(1), 45. [DOI], [ADS], [arXiv:1204.4981 [astro-ph.CO]]

Silk, Joseph, 1968, “Cosmic Black-Body Radiation and Galaxy Formation”, *Astrophys. J.*, **151**, 459. [DOI], [ADS]

Simard, G., Omori, Y., Aylor, K., Baxter, E. J., Benson, B. A., Bleem, L. E., Carlstrom, J. E., Chang, C. L., Cho, H-M., Chown, R., Crawford, T. M., Crites, A. T., de Haan, T., Dobbs, M. A., Everett, W. B., George, E. M., Halverson, N. W., Harrington, N. L., Henning, J. W., Holder, G. P., Hou, Z., Holzzapfel, W. L., Hrubes, J. D., Knox, L., Lee, A. T., Leitch, E. M., Luong-Van, D., Manzotti, A., McMahon, J. J., Meyer, S. S., Mocuano, L. M., Mohr, J. J., Natoli, T., Padin, S., Pryke, C., Reichardt, C. L., Ruhl, J. E., Sayre, J. T., Schaffer, K. K., Shirokoff, E., Staniszewski, Z., Stark, A. A., Story, K. T., Vanderlinde, K., Vieira, J. D., Williamson, R. and Wu, W. L. K., 2018, “Constraints on Cosmological Parameters from the Angular Power Spectrum of a Combined



2500 deg<sup>2</sup> SPT-SZ and Planck Gravitational Lensing Map”, *The Astrophysical Journal*, **860**(2), 137. [DOI]URL:

<https://doi.org/10.3847/1538-4357/aac264>

Smith, Kendrick M., Zahn, Oliver and Doré, Olivier, 2007, “Detection of gravitational lensing in the cosmic microwave background”, *Physical Review D*, **76**(4), 043510. [DOI], [ADS], [arXiv:0705.3980 [astro-ph]]

Smoot, G. F., Bennett, C. L., Kogut, A., Wright, E. L., Aymon, J., Boggess, N. W., Cheng, E. S., de Amici, G., Gulkis, S., Hauser, M. G., Hinshaw, G., Jackson, P. D., Janssen, M., Kaita, E., Kelsall, T., Keegstra, P., Lineweaver, C., Loewenstein, K., Lubin, P., Mather, J., Meyer, S. S., Moseley, S. H., Murdock, T., Rokke, L., Silverberg, R. F., Tenorio, L., Weiss, R. and Wilkinson, D. T., 1992, “Structure in the COBE Differential Microwave Radiometer First-Year Maps”, *Astrophys. J. Lett.*, **396**, L1. [DOI], [ADS]

Stompor, R. and Efstathiou, G., 1999, “Gravitational lensing of cosmic microwave background anisotropies and cosmological parameter estimation”, *Monthly Notices of the Royal Astronomical Society*, **302**(4), 735–747. [DOI], [https://academic.oup.com/mnras/article-pdf/302/4/735/18631312/302-4-735.pdf]URL:

<https://doi.org/10.1046/j.1365-8711.1999.02174.x>

Story, K. T., Hanson, D., Ade, P. A. R., Aird, K. A., Austermann, J. E., Beall, J. A., Bender, A. N., Benson, B. A., Bleem, L. E., Carlstrom, J. E., Chang, C. L., Chiang, H. C., Cho, H-M., Citron, R., Crawford, T. M., Crites, A. T., de Haan, T., Dobbs, M. A., Everett, W., Gallicchio, J., Gao, J., George, E. M., Gilbert, A., Halverson, N. W., Harrington, N., Henning, J. W., Hilton, G. C., Holder, G. P., Holzappel, W. L., Hoover, S., Hou, Z., Hrubes, J. D., Huang, N., Hubmayr, J., Irwin, K. D., Keisler, R., Knox, L., Lee, A. T., Leitch, E. M., Li, D., Liang, C., Luong-Van, D., McMahon, J. J., Mehl, J., Meyer, S. S., Mocuano, L., Montroy, T. E., Natoli, T., Nibarger, J. P., Novosad, V., Padin, S., Pryke, C., Reichardt, C. L., Ruhl, J. E., Saliwanchik, B. R., Sayre, J. T., Schaffer, K. K., Smecher, G., Stark, A. A., Tucker, C., Vanderlinde, K., Vieira, J. D., Wang, G., Whitehorn, N., Yefremenko, V. and Zahn,

O., 2015, “A MEASUREMENT OF THE COSMIC MICROWAVE BACKGROUND GRAVITATIONAL LENSING POTENTIAL FROM 100 SQUARE DEGREES OF SPTPOL DATA”, *The Astrophysical Journal*, **810**(1), 50. [DOI]URL: <https://doi.org/10.1088/0004-637x/810/1/50>

Sugai, H., Ade, P. A. R., Akiba, Y., Alonso, D., Arnold, K., Aumont, J., Austermann, J., Baccigalupi, C., Banday, A. J., Banerji, R., Barreiro, R. B., Basak, S., Beall, J., Beckman, S., Bersanelli, M., Borrill, J., Boulanger, F., Brown, M. L., Bucher, M., Buzzelli, A., Calabrese, E., Casas, F. J., Challinor, A., Chan, V., Chinone, Y., Cliche, J.-F., Columbro, F., Cukierman, A., Curtis, D., Danto, P., de Bernardis, P., de Haan, T., De Petris, M., Dickinson, C., Dobbs, M., Dotani, T., Duband, L., Ducout, A., Duff, S., Duivenvoorden, A., Duval, J.-M., Ebisawa, K., Elleflot, T., Enokida, H., Erikssen, H. K., Errard, J., Essinger-Hileman, T., Finelli, F., Flauger, R., Franceschet, C., Fuskeland, U., Ganga, K., Gao, J.-R., GAlnova-Santos, R., Ghigna, T., Gomez, A., Gradziel, M. L., Grain, J., Grupp, F., Gruppuso, A., Gudmundsson, J. E., Halverson, N. W., Hargrave, P., Hasebe, T., Hasegawa, M., Hattori, M., Hazumi, M., Henrot-Versille, S., Herranz, D., Hill, C., Hilton, G., Hirota, Y., Hivon, E., Hlozek, R., Hoang, D.-T., Hubmayr, J., Ichiki, K., Iida, T., Imada, H., Ishimura, K., Ishino, H., Jaehnig, G. C., Jones, M., Kaga, T., Kashima, S., Kataoka, Y., Katayama, N., Kawasaki, T., Keskitalo, R., Kibayashi, A., Kikuchi, T., Kimura, K., Kisner, T., Kobayashi, Y., Kogiso, N., Kogut, A., Kohri, K., Komatsu, E., Komatsu, K., Konishi, K., Krachmalnicoff, N., Kuo, C. L., Kurinsky, N., Kushino, A., Kuwata-Gonokami, M., Lamagna, L., Lattanzi, M., Lee, A. T., Linder, E., Maffei, B., Maino, D., Maki, M., Mangilli, A., MartAnez-Gonzalez, E., Masi, S., Mathon, R., Matsumura, T., Mennella, A., Migliaccio, M., Minami, Y., Mistuda, K., Molinari, D., Montier, L., Morgante, G., Mot, B., Murata, Y., Murphy, J. A., Nagai, M., Nagata, R., Nakamura, S., Namikawa, T., Natoli, P., Nerval, S., Nishibori, T., Nishino, H., Nomura, Y., Noviello, F., OSullivan, C., Ochi, H., Ogawa, H., Ohsaki, H., Ohta, I., Okada, N., Okada, N., Pagano, L., Paiella, A., Paoletti, D., Patanchon, G., Piacentini, F., Pisano, G., Polenta, G., Poletti, D., Prouve, T., Puglisi, G., Rambaud, D., Raum, C., Realini, S., Remazeilles, M., Roudil, G., Rubio-Martn, J. A., Russell, M., Sakurai, H., Sakurai, Y., Sandri, M., Savini, G., Scott, D., Sekimoto, Y., Sherwin, B. D., Shinozaki, K., Shiraishi, M., Shirron, P., Signorelli, G., Smecher, G., Spizzi, P., Stever, S. L.,

Stompor, R., Sugiyama, S., Suzuki, A., Suzuki, J., Switzer, E., Takaku, R., Takakura, H., Takakura, S., Takeda, Y., Taylor, A., Taylor, E., Terao, Y., Thompson, K. L., Thorne, B., Tomasi, M., Tomida, H., Trappe, N., Tristram, M., Tsuji, M., Tsujimoto, M., Tucker, C., Ullom, J., Uozumi, S., Utsunomiya, S., Van Lanen, J., Vermeulen, G., Vielva, P., Villa, F., Vissers, M., Vittorio, N., Voisin, F., Walker, I., Watanabe, N., Wehus, I., Weller, J., Westbrook, B., Winter, B., Wollack, E., Yamamoto, R., Yamasaki, N. Y., Yanagisawa, M., Yoshida, T., Yumoto, J., Zannoni, M. and Zonca, A., 2020, “Updated Design of the CMB Polarization Experiment Satellite LiteBIRD”, *Journal of Low Temperature Physics*, **199**(3-4), 1107–1117. [DOI]URL:  
<http://link.springer.com/10.1007/s10909-019-02329-w>

Tomita, Hiroyuki, 1986, “Statistical Properties of Random Interface System”, *Progress of Theoretical Physics*, **75**(3), 482–495. [DOI], [<https://academic.oup.com/ptp/article-pdf/75/3/482/5403230/75-3-482.pdf>]URL:  
<https://doi.org/10.1143/PTP.75.482>

van Engelen, A., Keisler, R., Zahn, O., Aird, K. A., Benson, B. A., Bleem, L. E., Carlstrom, J. E., Chang, C. L., Cho, H. M., Crawford, T. M., Crites, A. T., de Haan, T., Dobbs, M. A., Dudley, J., George, E. M., Halverson, N. W., Holder, G. P., Holzzapfel, W. L., Hoover, S., Hou, Z., Hrubes, J. D., Joy, M., Knox, L., Lee, A. T., Leitch, E. M., Lueker, M., Luong-Van, D., McMahon, J. J., Mehl, J., Meyer, S. S., Millea, M., Mohr, J. J., Montroy, T. E., Natoli, T., Padin, S., Plagge, T., Pryke, C., Reichardt, C. L., Ruhl, J. E., Sayre, J. T., Schaffer, K. K., Shaw, L., Shirokoff, E., Spieler, H. G., Staniszewski, Z., Stark, A. A., Story, K., Vanderlinde, K., Vieira, J. D. and Williamson, R., 2012, “A MEASUREMENT OF GRAVITATIONAL LENSING OF THE MICROWAVE BACKGROUND USING SOUTH POLE TELESCOPE DATA”, *The Astrophysical Journal*, **756**(2), 142. [DOI]URL:  
<https://doi.org/10.1088/0004-637x/756/2/142>

Verde, Licia, Wang, Limin, Heavens, Alan F. and Kamionkowski, Marc, 2000, “Large-scale structure, the cosmic microwave background and primordial non-Gaussianity”, *Monthly Notices of the Royal Astronomical Society*, **313**(1), 141–147. [DOI], [<https://academic.oup.com/mnras/article-pdf/313/1/141/18409614/313-1-141.pdf>]URL:

<https://doi.org/10.1046/j.1365-8711.2000.03191.x>

Vogeley, Michael S., Park, Changbom, Geller, Margaret J., Huchra, John P. and Gott, J. Richard, III, 1994, “Topological Analysis of the CfA Redshift Survey”, *Astrophys. J.*, **420**, 525. [DOI], [ADS]

Wu, W. L. K., Mocanu, L. M., Ade, P. A. R., Anderson, A. J., Austermann, J. E., Avva, J. S., Beall, J. A., Bender, A. N., Benson, B. A., Bianchini, F., Bleem, L. E., Carlstrom, J. E., Chang, C. L., Chiang, H. C., Citron, R., Corbett Moran, C., Crawford, T. M., Crites, A. T., de Haan, T., Dobbs, M. A., Everett, W., Gallicchio, J., George, E. M., Gilbert, A., Gupta, N., Halverson, N. W., Harrington, N., Henning, J. W., Hilton, G. C., Holder, G. P., Holzzapfel, W. L., Hou, Z., Hrubes, J. D., Huang, N., Hubmayr, J., Irwin, K. D., Knox, L., Lee, A. T., Li, D., Lowitz, A., Manzotti, A., McMahon, J. J., Meyer, S. S., Millea, M., Montgomery, J., Nadolski, A., Natoli, T., Nibarger, J. P., Noble, G. I., Novosad, V., Omori, Y., Padin, S., Patil, S., Pryke, C., Reichardt, C. L., Ruhl, J. E., Saliwanchik, B. R., Sayre, J. T., Schaffer, K. K., Sievers, C., Simard, G., Smecher, G., Stark, A. A., Story, K. T., Tucker, C., Vanderlinde, K., Veach, T., Vieira, J. D., Wang, G., Whitehorn, N. and Yefremenko, V., 2019, “A Measurement of the Cosmic Microwave Background Lensing Potential and Power Spectrum from 500 deg<sup>2</sup> of SPTpol Temperature and Polarization Data”, *Astrophys. J.*, **884**(1), 70. [DOI], [ADS], [arXiv:1905.05777 [astro-ph.CO]]

Zaldarriaga, Matias, 2001, “Nature of the E-B decomposition of CMB polarization”, *Physical Review D*, **64**(10), 103001. [DOI], [ADS], [arXiv:astro-ph/0106174 [astro-ph]]

Zaldarriaga, Matias and Seljak, Uroš, 1999, “Reconstructing projected matter density power spectrum from cosmic microwave background”, *Phys. Rev. D*, **59**, 123507. [DOI]URL:

<https://link.aps.org/doi/10.1103/PhysRevD.59.123507>

Zaldarriaga, Matias and Seljak, Uroš, 1997, “All-sky analysis of polarization in the microwave background”, *Physical Review D*, **55**(4), 1830–1840. [DOI], [ADS], [arXiv:astro-ph/9609170 [astro-ph]]

Zaldarriaga, Matias and Seljak, Uroš, 1998, “Gravitational lensing effect on cosmic microwave background polarization”, *Physical Review D*, **58**(2), 023003. [DOI], [ADS], [arXiv:astro-ph/9803150 [astro-ph]]

Zaldarriaga, Matias, Seljak, Uroš and Bertschinger, Edmund, 1998, “Integral Solution for the Microwave Background Anisotropies in Nonflat Universes”, *The Astrophysical Journal*, **494**(2), 491–502. [DOI]URL:  
<https://doi.org/10.1086/305223>